UNIVERSITY OF MINNESOTA

This is to certify that I have examined this copy of a doctoral thesis by

Alex A. Volinsky

and have found that it is complete and satisfactory in all respects, and that any and all revisions required by the final examination committee have been made.

William W. Gerberich

Name of Faculty Adviser

Signature of Faculty Adviser

Date

GRADUATE SCHOOL

The Role of Geometry and Plasticity in Thin, Ductile Film Adhesion

A THESIS
SUBMITTED TO THE FACULTY OF THE GRADUATE SCHOOL OF THE
UNIVERSITY OF MINNESOTA
BY

Alex A. Volinsky

IN PARTIAL FULFILLMENT OF THE REQUIREMENTS
FOR THE DEGREE OF
DOCTOR OF PHILOSOPHY

William W. Gerberich, Adviser

October 2000

© Copyright 2000 by Alex A. Volinsky
All Right Reserved

ACKNOWLEDGEMENTS

I would like to thank my parents for their continuous support during my years in the Graduate School. Without their love and support this would not be possible.

I would like to thank the people and institutions that supported me during my years at the Graduate School at the University of Minnesota. In particular, I would like to acknowledge:

The financial support from the U.S. Department of Energy under grant DE-FG02/96ER45574, from Sandia National Lab at Livermore and from Motorola Digital DNA Labs.

I would like to thank Dr. Neville R. Moody for his leadership and support, staff members at Sandia National Laboratories, Livermore CA: W. Miles Clift and Bernice E. Mills, Dorrance E. McLean and Douglas Medlin, Douglas A. Chinn.

Thanks to Motorolans I had a pleasure to work with in Arizona:

Interconnect Systems Lab: Vijay Sarihan, Lei Mercado, Jaynal Molla, Russell Lee, Betty H. Yeung, Owen Fay, Beth Keser, Li Miller; Process and Materials Characterization Joe B. Vella, Paddy Padmanabhan, Indira S. Adhihetty, Stefan Zollner, Atul Konkar, Himansu Yapa, Bob Carpenter, Lester Casoose, Michael Kottke, Larry Rice, Ha Le; Physical Science Research Lab: John D'urso, Jeffrey Baker, Steven Smith, Tony Botta, Eric Newlin.

Prof. Ronald Gibala of the University of Michigan has provided valued input for my research.

I would like to specially thank my coworkers at the University of Minnesota:

John C. Nelson, David F. Bahr, Michael Kriese, Donald Kramer, Natalia Tymiak, John Jungk and Min Li. Some of the results and data presented in this thesis are obtained with their collaboration and support.

Finally, I would like to thank my advisor, professor William W. Gerberich for the extremely valuable guidance and support he has provided during my years in Graduate School.

ABSTRACT

Thin film adhesion is a very important property not only for the microelectronics and magnetic recording industries, but also for emerging technologies such as data transmission through optical switches dependent on microelectomechanical systems (MEMS). In general, films that adhere well to the substrate are desired. However, spontaneous delamination may occur at any time due to crack growth between thin film and the substrate.

This dissertation considers the superlayer indentation test for quantitatively measuring the practical work of adhesion of thin, ductile films. Deposition of a highly stressed hard superlayer on top of the film of interest adds additional stress to the delamination process, and prevents out of plane displacements of the film, suppressing plastic pile-up around the indenter. The technique is extremely useful since it is applied to the as-deposited, as-processed thin films, without changing the interfacial chemistry and film microstructure/properties. Adhesion results of metal-ceramic interfaces are discussed. One of the most important mechanisms that contribute to the thin film practical work of adhesion is the plasticity occurring in a process zone in the vicinity of the delamination boundary. A quantitative model to characterize the contributions of plastic energy dissipation is introduced to rationalize experimental adhesion assessments. This model incorporates the functional dependence of the film thickness and constitutive properties. Orders of magnitude increases in the practical work of adhesion were both observed and predicted. Temperature effects on thin film mechanical properties and adhesion are also considered.

TABLE OF CONTENTS

ACKNOWLEDGEMENTS i
ABSTRACT ii
TABLE OF CONTENTS iii
LIST OF TABLES vi
LIST OF FIGURES vii
CHAPTER 1. INTRODUCTION AND OVERVIEW 1
1.1 THIN FILM ADHESION 2
DEFINITION OF ADHESION 2
Thermodynamic Work Of Adhesion 2
Practical Work Of Adhesion 3
SELECTED RESULTS FROM LINEAR ELASTIC FRACTURE MECHANICS 5
Fracture Criterion 5
Mode Mixity (Phase) Angle Ψ 6
THIN FILM ADHESION TESTS 10
Superlayer Test 10
Indentation Tests 14
Superlayer Indentation Test 18
Scratch Tests 22
Bulge And Blister Tests 26
Sandwich Specimen Tests 28
1.2 MATERIALS CONSIDERATIONS 31
MODERN METALLIC INTERCONNECTS 31
Advantages Of Copper As An Interconnect Material 32
Electromigration In Metallic Interconnects 32
Electromigration In Cu Interconnects 36
Electromigration And Stress 37
Complications Associated With Cu As An Interconnect Material 38
Underlayer Materials For Cu Interconnects 39
1.3 THIN FILM PROCESSING AND CHARACTERIZATION 41
Sputter Deposition 41
Microstructure Of PVD Thin Films 42
Stresses In Thin Films 46
Residual Stress Measurements 47
Stress-driven Thin Film Fracture 48
CHAPTER 2. THIN FILM MICROSTRUCTURE AND MECHANICAL PROPERTIES DETERMINATION 51
2.1 THIN FILM MICROSTRUCTURE 51
Cu Thin Film Grain Orientation 51
Cu Thin Film Grain Size 52
2.2 THIN FILM MECHANICAL PROPERTIES 56
Nanoindentation For Thin Film Mechanical Properties Determination 56
Nanoindentation Apparatus 58
Thin Film Yield Stress 61
Sputter Deposited Cu Thin Film Mechanical Properties 62
Electroplated Cu Thin Film Mechanical Properties 67
Stress Relaxation In Copper Thin Films 73
CHAPTER 3. PLASTICITY EFFECT ON Cu THIN FILM ADHESION 76
3.1 THEORETICAL CONSIDERATION 76
Upper Bound Plastic Strip Model 76
Crack Tip Plastic Zone Size Estimate 80
3.2 Cu THIN FILM ADHESION 82
Sample Preparation 82

Adhesion Assessment 87
Radial Multilayer Cracking 88
Ti Underlayer....90
Cu Film Adhesion Results....92
Sources Of Elevated Interfacial Toughness....98
Bond Strength And Phase Angle Estimates....102
CHAPTER 4. BRITTLE-TO-DUCTILE TRANSITION (BDT) IN Cu FILMS. 111
4.1 ELEVATED TEMPERATURE INDENTATION EXPERIMENTS....111
Elevated Temperature Experimental Setup 111
Thin Film Constitutive Properties At Elevated Temperatures....114
Cu Adhesion At Elevated Temperatures 119
4.2 THEORETICAL MODELING 122
Dislocation Free Zone (DFZ) Model....123
DFZ Model Validation 129
CHAPTER 5. THIN FILM FRACTURE ACOUSTIC EMISSION....134
Acoustic Emission Signal....134
5.1 EXPERIMENTAL PROCEDURE....135
Acoustic Emission Setup....135
5.2 ACOUSTIC EMISSION DURING THIN FILM FRACTURE 136
Acoustic Emission During Cu And Cu/Ti Film Fracture 136
Acoustic Emission Energy Trends....139
CHAPTER 6. THIN FILM FRACTURE CHARACTERIZATION 143
6.1 "INSIDE THE BLISTER"....143
Microscopy Characterization....143
Crack Arrest (Fiducial) Marks....144
6.2 SLOW CRACK GROWTH ANALYSIS 147
Crack Tip Opening Angle Measurement....147
Slow Crack Growth Approach....147
6.3 FRACTURE SURFACE AUGER ANALYSIS 149
Fracture Interface Determination....149
Electron Beam Surface Damage....152
6.4 FIDUCIAL MARKS CHARACTERIZATION 154
Fiducial Mark Auger Analysis....155
Carbon Contamination Source....156
Fiducial Mark Morphology 160
6.5 PETAL-SHAPED BLEED-THROUGH MARKS 166
Petal-shaped Marks Discoveries....166
Petal-shaped Bleed-through Marks Source....169
CHAPTER 7. ALUMINUM FILM ADHESION....171
7.1 Al FILMS EXPERIMENTS....171
Al Film Deposition....171
Al Film Characterization 172
Al Adhesion Measurements....173
Superlayer Residual Stress 173
Al Film Adhesion Results....176
Modified Plastic Strip Model 182
7.2 CONTAMINATION EFFECT ON Al FILM ADHESION 183
Al Films On Cu And C Underlayers....183
Al Film Adhesion On Cu And C Underlayers....184
CHAPTER 8. SUMMARY AND RECOMMENDATIONS....191
SUMMARY 191
RECOMMENDATIONS....194
Constitutive Properties Determination In Extreme Environments....194
Radial Cracking....194
Phase Angle Determination For The Superlayer Test 195
Double Indentation 195

Environmental Fracture Effects 197
Superlayer Indentation Test Adhesion Measurement Automation 198
Acoustic Emission Thin Film Fracture Analysis 198
Fracture Characterization 199
Other Thin Film Systems 200
APPENDIX 202
EXCEL SPREADSHEET FOR THE SUPERLAYER INDENTATION TEST ADHESION DETERMINATION 202
REFERENCES 205

LIST OF TABLES

Table 1. Comparison of underlayer materials for copper interconnects. 41
Table 2. Zone structures of evaporated and sputtered coatings [12]. 44
Table 3. Sputtered Cu film grain size and yield stress. 64
Table 4. Sputtering deposition parameters. 84
Table 5. Cu film interfacial fracture characteristics. 106
Table 6. Experimental values of k_{Ii}/σ_{ys} and K_I/σ_{ys} obtained from k_{Ii}=0.27 MPa·m$^{1/2}$ and K_I from average G_I values obtained for each test temperature. 128
Table 7. Experimental values of k_{Ii}/σ_{ys} and K_I/σ_{ys} obtained from k_{Ii}=0.27 MPa·m$^{1/2}$ and K_I from average G_I values obtained for each film thickness. 128
Table 8. Al film hardness and grain size [161]. 172
Table 9. Materials parameters for the superlayer spreadsheet (Cells A1 through M11). 202
Table 10. Spreadsheet Input parameters for each indent (Cells A26 through M38). 203
Table 11. Calculated G values (Cells BM28 through BR50). 203

LIST OF FIGURES

Figure 1. Contact angle measurement schematic....3
Figure 2. Modes of fracture: a) Mode I opening mode; b) Mode II sliding mode; c) Mode III tearing mode....5
Figure 3. Interfacial fracture toughness as a function of the mode mixity angle....8
Figure 4. Phenomenological functions for $\Gamma(\psi)$....9
Figure 5. Superlayer test schematics....12
Figure 6. Film decohesion in the superlayer test....12
Figure 7. a) No buckling during indentation; b) double-buckling during indentation; c) single-buckling after the indenter tip removal....15
Figure 8. Optical micrographs of indentation iduced blisters with (right) and without (left) a W superlayer....19
Figure 9. Effect of W superlayer thickness (500 MPa compressive residual stress) on the energy available for crack extension....20
Figure 10. Load-displacement curve and corresponding delamination in a 120 nm thick Cu film on SiO_2....21
Figure 11. Schematic of the precracked line scratch test (PLST)....24
Figure 12. Strain energy release rate for the Precracked Line Scratch Test (PLST)....25
Figure 13. Schematic of unstable crack growth during buckling for the PLST....25
Figure 14. Bulge test schematics....26
Figure 15. Sandwich specimen tests schematics: a) Modified K_{IC} sample; b) Brazil-nut sample; c) 4-point bent (UCSB) sample....29
Figure 16. “Electron wind” force....35
Figure 17. Narrow (bamboo) and wide lines....35
Figure 18. Slow surface diffusion vs. grain boundary fast diffusion....35
Figure 19. Simplified schematic of RF sputtering system....42
Figure 20. Zone model for thin films. {Schematic reproduced from Hentzell [113]}....44
Figure 21. Structural zones and physical processes schematics for sputtering. {Schematic reproduced from Thornton [114]}....45
Figure 22. Residual stress map of 1 um W film on a 6” Si wafer....49
Figure 23. Telephone cord delamination of highly compressed W thin film....50
Figure 24. AFM height image of a 200 nm thick sputtered Cu film with a cross-section, showing grain size measurement. {taken by N.I. Tymiak}....53
Figure 25. SEM micrograph of a 3 um thick Cu film on Ti. {taken by N.I. Tymiak}....54
Figure 26. Height and deflection AFM images of sputter deposited 500 nm thick Cu film [144]....55
Figure 27. AFM images of electroplated Cu films (100 nm Z range)....55
Figure 28. Focused Ion Beam images of electroplated Cu films of different thickness (45° tilt)....56
Figure 29. Nanoindenter schematic....59
Figure 30. Comparison of indentation instruments....59
Figure 31. Indentation curves for a 200 nm Cu film....63
Figure 32. Substrate effect correction. Cu film hardness, H_f is determined from the best fit to the experimental data....64
Figure 33. Yield stress dependence on the grain size for sputtered Cu films....65
Figure 34. Plastic zone size evaluation for yield stress determination. An AFM image of an indent into a 200 nm Cu film with a corresponding cross-sectional analysis [147]....66
Figure 35. Cu film yield stress based on the hardness and plastic zone size measurements along with theoretical predictions. Annealed Cu data is taken from [107]....66
Figure 36. Electroplated 200 nm Cu film hardness as a function of the indentation depth....69
Figure 37. Electroplated Cu elastic modulus and yield stress as a function of film thickness....69
Figure 38. Electroplated Cu yield stress compared to the annealed Cu yield stress from [107] and theoretical prediction from equation (2.7)....70
Figure 39. Electroplated Cu yield stress as a function of grain size....71
Figure 40. Cu yield stress fit using classical Hall-Petch relationship....71
Figure 41. Cu yield stress fit using film thickness....72
Figure 42. Temperature cycling of 1 μm copper film on silicon. {Schematic after M.D. Thouless}....74

Figure 43. Electroplated Cu yield stress and strain energy release rate upper bound as a function of film thickness. 79
Figure 44. Electroplated Cu yield stress and strain energy release rate upper bound for small film thicknesses. 79
Figure 45. Superlayer indentation schematic. Plastic zones. 81
Figure 46. Thin film stack schematic. 83
Figure 47. Step profilometry for film thickness determination. 84
Figure 48. Energy yield spectrum of RBS analysis of W/Cu film. 85
Figure 49. SEM micrograph of a film cross-section. 86
Figure 50. Residual stress levels in the Cu and Ti/Cu films. 86
Figure 51. Nomarski contrast optical image of a series of indentations in a 1 um thick Cu film with W superlayer. 87
Figure 52. Load-displacement curves and corresponding delaminations for a 100 nm thick Cu film without Ti underlayer. 89
Figure 53. Radial cracking contribution to the increase in the contact area. 89
Figure 54. SEM micrograph of Ti underlayer. 91
Figure 55. Cross-sectional TEM of the SiO_2/Ti/Cu/W stack {image taken by D. Medlin, Sandia National Lab}. 91
Figure 56. Ti underlayer X-Ray spectra obtained in TEM {D. Medlin, SNL} 92
Figure 57. An interfacial energy relationship to the film thickness: theoretical upper bound solution (top solid line) and experimental strain energy release rates. 94
Figure 58. Crack tip plastic zone estimates for Cu films. Straight line corresponds to the plastic zone size equal to the film thickness. 95
Figure 59. Cu film practical work of adhesion as a function of film thickness. 96
Figure 60. Crack tip plastic zone for Cu films with and without Ti underlayer. Plastic strip model estimates. ...97
Figure 61. Strain energy release rate as a function of normalized delamination radius for Cu films. 98
Figure 62. Strain energy release rate as a function of normalized delamination radius for Cu films with Ti underlayer. 99
Figure 63. Indentation induced delamination in a 100 nm Cu film with and without Ti underlayer. 100
Figure 64. Load-displacement curves corresponding to delaminations in Figure 63. 100
Figure 65. Substrate constraint effect in an 80 nm thick Cu film. 101
Figure 66. Interfacial shear stress and bond stress dependence on the Cu film thickness. 105
Figure 67. Effect of the relative Cu film thickness on the mode mixity. Solid line is a theoretical prediction from [29]. 108
Figure 68. Cu film bond strength. 108
Figure 69. Heater assembly components. 112
Figure 70. Load-displacement curves reflecting sample motion during indentation. 113
Figure 71. Elastic modulus as a function of indentation depth for Au films at different testing temperatures...116
Figure 72. Hardness as a function of indentation depth for Au films at different testing temperatures. 116
Figure 73. Yield stress variations of Cu and Au thin films. 117
Figure 74. Hardness of a Pt-passivated Cu film as a function of test temperature. 118
Figure 75. Indentation induced delaminations in a 500 nm thick Cu film at ambient and room temperatures alongside the corresponding indentation curves. 119
Figure 76. Temperature effects on interfacial toughness for 80 and 500 nm thick Cu films. 120
Figure 77. Indentation induced delaminations in an 80 nm thick Cu film at ambient and room temperatures alongside the corresponding indentation curves. 121
Figure 78. A physical picture corresponding to local crack tip stress intensity, k_I just above a dislocation emission value, k_{Ie}. 124
Figure 79. Evaluation of an assumption of a constant DFZ radius. 126
Figure 80. Shielding dislocations at a Mode I crack tip under a far-field K_I in an Fe-3wt%Si single crystal loaded in ⟨100⟩. Single dislocations affect the near-tip local stress intensity, k_{tip}, while the superdislocation representing the far-field plasticity is associated with K_I. 127
Figure 81. Theoretical predictions (equation (4.9)) for ductile-to-brittle transition in Fe-3wt%Si as compared to experimental data [188]. 128
Figure 82. Temperature effects on interfacial toughness for 80 nm thick Cu film. Solid and dashed lines correspond to experimental results and theoretical prediction, respectively. 130

Figure 83. Temperature effects on interfacial toughness for a 500 nm thick Cu film. Solid and dashed lines correspond to experimental results and theoretical prediction, respectively. 131
Figure 84. Schematic of an indentation induced delamination. For a strong interface plastic zone around an indenter and crack tip plastic zone may interact. 131
Figure 85. Comparison of experimental strain energy release rates and theoretical predictions as given by both an upper bound and a more precise DFZ model. 132
Figure 86. Strain energy release rate as a function of the normalized delamination radius for a 500 nm Cu film. 133
Figure 87. Parameters of a burst-type acoustic emission signal. 134
Figure 88. Schematic of the AE experimental setup 135
Figure 89. a) Load-displacement curve and acoustic emission events for a Ti/Cu/W indentation; b) Nomarski optical image of the corresponding blister. 136
Figure 90. Acoustic emission signals during Ti/Cu/W indentation. Signals are put on the same time scale. 137
Figure 91. Total AE energy vs. rise time for Cu film with a Ti underlayer. 138
Figure 92. Total AE energy vs. rise time for Cu film without a Ti underlayer. 138
Figure 93. Total AE energy for the films with Ti underlayer. 139
Figure 94. Strain energy release rate for the films with Ti underlayer. 140
Figure 95. Total true acoustic emission energy as a function of load. 141
Figure 96. Optical micrographs of the removed blister. Substrate (left) and tape (right) sides. 143
Figure 97. a) Optical image of a blister; b) SEM image of the area underneath the removed blister in a); c) SEM image of a crack arrest mark. 145
Figure 98. Element concentration profile along with the SEM image identifying analyzed areas. 146
Figure 99. Contact and deflection AFM images of the crack arrest mark. 146
Figure 100. Crack opening displacement angle measurement. θ_1 is the angle measured from the blister angle without its removal, θ_2 is the angle measured from the crack arrest mark geometry. 147
Figure 101. Auger spectrum obtained from the substrate side. 150
Figure 102. Auger spectrum obtained from the removed Cu film. 151
Figure 103. AES scans on the tape and substrate sides for a Cu film on Ti/SiO_2 along with element concentrations. 152
Figure 104. AFM image of the Ti/SiO_2 surface damage due to electron beam scanning. 153
Figure 105. SEM micrographs of Cu 120 nm fiducial marks on the substrate a) and on the tape b) sides. 154
Figure 106. AES scan superimposed on the enlarged SEM image from Figure 101b. 155
Figure 107. SEM micrograph of the removed TiWN film. 157
Figure 108. SEM micrograph of a GaAs fracture surface upon TiWN film removal. 158
Figure 109. Carbon X-ray map corresponding to the SEM image in Figure 108. 158
Figure 110. SEM micrograph with the corresponding carbon X-ray map of the delaminated TiWN film. 159
Figure 111. Center of the blister from Figure 105b. 161
Figure 112. Contact mode AFM height (300 nm Z range) and deflection images of an 80 nm Cu blister. 162
Figure 113. Fiducial mark schematics. 162
Figure 114. AFM height and deflection images of the fiducial mark left on SiO_2. 163
Figure 115. AFM height and deflection images of partially removed blister, showing fiducial mark underneath. 164
Figure 116. 3D AFM image of the fiducial mark in Ti/Cu film. 164
Figure 117. Contact AFM height and deflection images of the small blister indent into a 40 nm Cu/Ti film. No fiducial marks are present. 165
Figure 118. Stains around an indentation into $SiO_2/Cr/Cu/W$ film stack. 166
Figure 119. Petal-shaped marks around radial cracks. 167
Figure 120. Petal-shaped marks seen in the SEM. 167
Figure 121. Auger depth concentration profiles taken on the petal-shaped mark from Figure 120. 168
Figure 122. Auger depth concentration profiles taken on the W surface outside the blister area. 168
Figure 123. Sheet resistance and reflectance of Al films as a function of film thickness. 173
Figure 124. Load-displacement curves and corresponding blister delaminations for a 40 nm thick Al film with compressive and tensile W superlayers. 175
Figure 125. Load-displacement curves and corresponding blister delaminations for a 2 μm thick Al film with compressive and tensile W superlayers. 175
Figure 126. R-curve for a 1 um thick Al film. 177

Figure 127. Strain energy release rate dependence on the phase angle for a 500 nm tick Al film. Solid line is a theoretical prediction from either equation (1.20) or equation (1.21), assuming λ=0 and Γ_0=4 J/m^2.........178
Figure 128. Al thin film adhesion with residual tensile and compressive residual stresses in the W superlayer. Modified Plastic Strip Model is equation (7.4)..........179
Figure 129. Plane strain a) and plane stress b) normalized strain energy release rate as a function of distance from the indentation for films with residual tensile and compressive residual stresses..........179
Figure 130. Schematic of the plastic pile-up without interfacial delamination in Al film..........180
Figure 131. Indentation into TiW/Cu/TiW film stack. 181
Figure 132. SEM image of the FIB cross-section of an indent in Figure 131, showing no interfacial delamination {courtesy of Motorola}. 182
Figure 133. Al film contamination stack schematic. 184
Figure 134. Al film adhesion with Cu and C underlayers. 185
Figure 135. Load-displacement curves with corresponding delaminations in a 340 nm thick Al film on Cu with different superlayers. 186
Figure 136. Indentation-induced telephone cord delaminations in a Cu/Al 500 nm thick film..........187
Figure 137. Blister delaminations of a 2 um thick Al film on Cu with the compressive (left image) and tensile (right image) stress in the w superlayer. 187
Figure 138. Al film spallation and circumferential cracking (Al 340 nm film on Cu, 1 um W 100 MPa tensile residual stress). 188
Figure 139. Schematic of a bilayer film bending due to the residual stress in each layer. 189
Figure 140. Indentation-induced blisters in a 2 um thick Al film on the carbon underlayer. 190
Figure 141. Load-displacement curve for the 2 um thick Al film on carbon..........190
Figure 142. Double indentation into a 120 nm Cu film along with the corresponding blister delamination......197
Figure 143. Optical micrograph of the FIB cut in a 120 nm Cu film blister. 199
Figure 144. SEM image of the fracture zone underneath the indenter. 200

CHAPTER 1. INTRODUCTION AND OVERVIEW

A modern integrated circuit (IC) contains more than 200 million transistors. This rapid growth in the microelectronics industry for the past several years requires very fine interconnects with thin metal lines within one chip. There is a tendency to increase the number of transistors while lowering the chip's dimensions and reducing the power consumption. Aluminum interconnects in the microelectronic devices are now pushed to their dimensional limits due to reliability (electromigration and stress migration) problems. Copper, having a higher conductivity and better electromigration properties is replacing aluminum in integrated circuits. It is also beneficial to use a material with the low dielectric constant (K) to fill the space between Cu interconnect lines in order to reduce the amount of cross talk between interconnects and place them closer to each other. Basically, it is the whole materials system that needs to be changed with the introduction of Cu metallization.

The barrier of poor low-K materials and copper adhesion and diffusion into a silicon substrate has been challenging and was only recently overcome by IBM and Motorola. This still needs to be optimized before a full-scale incorporation of copper interconnects into mass production is a routine. In addition, Cu might also bring up other potential problems, requiring a thorough study to ensure IC reliability.

For the above-mentioned reliability, it is essential to know the thin film adhesion and to be able to measure it quantitatively. In general, films that are well adhered to the substrate are desired, though spontaneous delamination may occur at any time due to crack growth between thin film and the substrate. Linear Elastic Fracture Mechanics (LEFM) is the discipline that provides quantitative answers to specific problems of crack propagation due to stresses in different structures. It can be also applied in the case of thin films. Though there is no standard adhesion test for thin films, there are certain universal approaches that can be applied for measuring film adhesion. At this point it is important to define what we mean by adhesion.

1.1 THIN FILM ADHESION

DEFINITION OF ADHESION

Thermodynamic Work Of Adhesion

From a thermodynamic standpoint the true work of adhesion of the interface is the amount of energy required to create free surfaces from the bonded materials:

$$W_A = \gamma_f + \gamma_s - \gamma_{fs} \quad (1.1),$$

where γ_f and γ_s are the specific surface energies of the film and the substrate respectively, γ_{fs} is the energy of the interface (Figure 1). The true work of adhesion is an intrinsic property of the film/substrate pair; it depends on the type of bonding between the film and the substrate, and the level of initial surface contamination.

The true work of adhesion can be measured by the contact angle technique [1, 3]. If the tested material particle is in thermal equilibrium on a substrate, then:

$$\gamma_{fs} = \gamma_s - \gamma_f \cos\Theta \quad (1.2),$$

where Θ is the contact angle between the particle free surface and the substrate (Figure 1). The work of adhesion now can be expressed with the Young-Dupré equation:

$$W_A = \gamma_f + \gamma_s - \gamma_{fs} = \gamma_f (1 + \cos\Theta) \quad (1.3).$$

Particles in thermodynamic equilibrium can be obtained by the Sessile drop method [3] or by annealing [1, 3]. In case of the easily oxidized particles such as Cu, annealing must be performed in vacuum. When the surface energy of the film γ_f is known at a given temperature T_0, at any temperature T it would be:

$$\gamma_f(T) \approx \gamma_f(T_0) + (T - T_0)\left(\frac{\partial \gamma_f}{\partial T}\right)_{T=T_0} \quad (1.4).$$

Solving equations (1.3) and (1.4) for the annealing temperature gives the value of the true (thermodynamic) adhesive energy. In most of the cases annealing has to be performed in vacuum in order to avoid oxidation. If crystallographic faceting occurs upon cooling, a different technique is used to assess the work of adhesion, based on the aspect ratio measurements of the equilibrated crystals [5, 6]. Usually both results from contact angle and

aspect ratio measurements agree well for metallic films [7]. Contact angle distribution can be obtained from the SEM, or AFM image analysis [7].

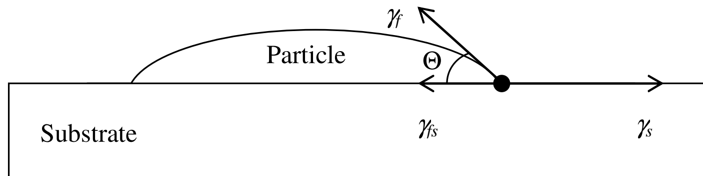

Figure 1. Contact angle measurement schematic.

Lipkin and others [7] measured 0.9 J/m^2 for the thermodynamic work of adhesion of gold on sapphire. Furuya and coworkers [3] calculated adhesive energies of Cu/SiO_2, Cu/TiN and Cu/TiW interfaces using the contact angle technique with the two latter values being more than double the Cu/SiO_2 value of 0.8 J/m^2 as discussed later. The true work of adhesion is a constant for a given film/substrate pair, and for metals on ceramic is typically a small number on the order of 1-2 J/m^2.

For the idealized case of Griffith fracture [8] the interfacial toughness, Γ_i, is assumed to be equal to the thermodynamic work of adhesion, W_A: $\Gamma_i = W_A$. In practice, even brittle fracture is accompanied by some sort of energy dissipation either through plastic deformation at the crack tip [9], or friction. In this regard, even relatively thin films on the order of 100 nm can exhibit plasticity during interfacial fracture resulting in an elevated work of fracture.

Practical Work Of Adhesion

Most of the test methods measure adhesion by delaminating thin films from the substrate. While debonding from the substrate, the thin film and/or the substrate usually experience plastic deformation, so it is difficult to extract the true adhesive energy from the total energy measured. What is measured is the practical work of adhesion, or interfacial toughness:

$$W_{A,P} = W_A + U_f + U_s + U_{fric} \qquad (1.5),$$

where U_f and U_s is the energy spent in plastic deformation of the film and the substrate respectively, and U_{fric} are the energy losses due to friction. Although the last three terms appear to be simply additive, it should be noted that both $U_f(W_A)$ and $U_s(W_A)$ are functions of the true work of adhesion [10] and in many cases $U_{fric}(W_A)$ will be as well.

The fracture mechanics approach uses the strain energy release rate, or the crack driving force as a measure of the practical work of adhesion:

$$G = \pm \frac{\partial U}{\partial A} = R \quad (1.6),$$

where U is the total energy of the system, and A is the crack area, and R is the resistance to crack propagation. We will consider the tests to determine G, and later consider various resistance terms and several possible ways to interpret that resistance, e.g. phase angle, friction and plastic energy dissipation.

Most adhesion tests empirically infer the adhesive strength by subjecting the specimen to some external load and measuring the critical value at which it fails [11]. While still useful for routine quality control, these tests do not measure the interface fracture toughness Γ_i, since the strain energy release rate usually can't be deconvoluted from the work of the external load. There are several qualitative adhesion tests such as the scotch tape or the peel test [12, 13]. These tests are usually easy and fast to perform, but they do not provide accurate values of adhesion. In the scotch tape test for example a piece of adhesive tape is attached to the tested film and then pulled off at 180°. "Bad" adhesion is indicated if the film is removed with the tape, conversely, "good" adhesion is indicated if the film remains attached to the substrate. The ideal test should simulate the practical situation as closely as possible, while also being able to extract the value of strain energy release rate. The method must explicitly account for contribution of the residual stress to the decohesion process. If the actual structure is to experience only low service temperature upon fabrication, using high homologous temperature processing steps in test specimen preparation, such as diffusion bonding, is not desirable, since it severely alters interface adhesion properties [14]. One of the goals of this thesis was to further develop a thin film technique, which avoids the need of diffusion bonding. One of the ways to evaluate the practical work of adhesion is by applying linear elastic fracture mechanics (LEFM), using a number of possible specimen types as detailed below.

SELECTED RESULTS FROM LINEAR ELASTIC FRACTURE MECHANICS

Mechanical behavior of many materials can change considerably with the presence of a crack. In most cases a film debonds from the substrate by crack growth. The discipline that accounts for crack propagation due to stresses in different geometric configurations is known as linear elastic fracture mechanics (LEFM).

Fracture Criterion

When the driving force (strain energy release rate), G exceeds the material's resistance to crack growth Γ_i, the crack propagates (Griffith criterion) [15]:

$$G \geq \Gamma_i \qquad (1.7).$$

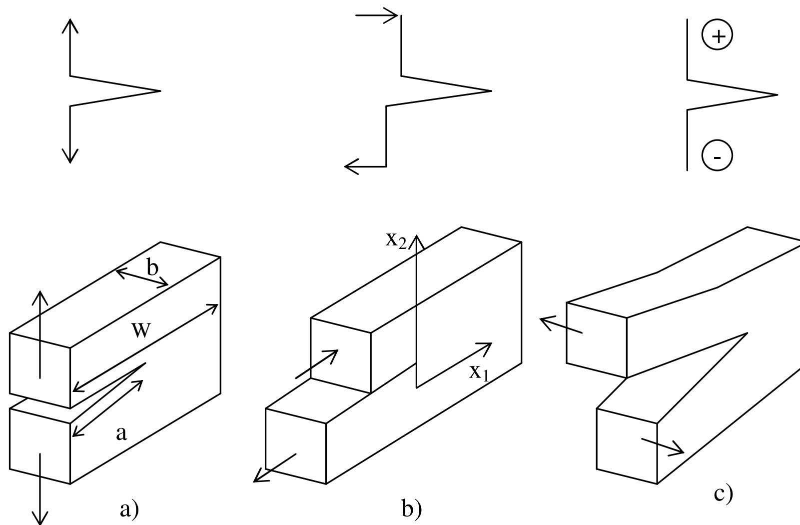

Figure 2. Modes of fracture: a) Mode I opening mode; b) Mode II sliding mode; c) Mode III tearing mode.

The stress intensity factor, K is defined for three modes of loading (Figure 2):

$$K_I = \sigma_{22}^{\infty}\sqrt{\pi a} \quad K_{II} = \sigma_{12}^{\infty}\sqrt{\pi a} \quad K_{III} = \sigma_{23}^{\infty}\sqrt{\pi a} \qquad (1.8),$$

where a is the crack length, σ_{ij}^{∞} are stresses far from the crack tip [16]. Irwin's stress intensity approach for crack growth states that the crack will propagate when the applied stress intensity K is greater than the critical stress intensity of the material K_C:

$$K \geq K_C \qquad (1.9).$$

Stored elastic strain energy is released by crack growth, which creates new surface. Strain energy release rate G is defined as in equation (1.6):

$$G = \pm\frac{\partial U}{\partial A} = \pm\frac{1}{b}\frac{\partial U}{\partial a} \qquad (1.10),$$

where U is the elastic strain energy of the body, A is the area created by the crack growth and b is the constant thickness of the specimen, and a is the crack length (Figure 2). For the fixed load condition the plus sign should be used, for the fixed grips condition the minus sign should be used in equations (1.6) and (1.10) [15].

The Griffith and stress intensity approaches were combined by Irwin [17]:

$$G = \frac{K_I^2(1-\nu^2) + K_{II}^2(1-\nu^2) + K_{III}^2(1+\nu)}{E} \qquad (1.11),$$

where E is the Young's modulus, ν is the Poisson's ratio of the material. Unpassivated thin films bonded to substrates with different elastic properties are considered to be in a plane strain state, giving rise to a mixture of mode I and mode II loading with K_{III}=0.

Mode Mixity (Phase) Angle Ψ

The phase (or mode mixity) angle describes the symmetry of the stress field and fully specifies K for homogeneous materials:

$$\Psi = tan^{-1}(K_{II}/K_I) \qquad (1.12),$$

$$K = K_I + iK_{II} = |K|e^{i\Psi} \qquad (1.13),$$

so that for plane strain:

$$G = \frac{|K|^2}{E}(1 - \nu^2) \quad (1.14).$$

The phase angle Ψ represents a measure of the ratio of shear to opening displacement acting on the debond crack surface. For pure mode I loading $\Psi = 0°$ since there is no shear, and for pure mode II loading it is 90°since there is no opening. In the fracture mechanics approach the critical strain energy release rate, G_C, at final instability is equal to the resistance term, R, which is equivalent to the practical work of adhesion $W_{A,P}$ from (1.5). It is recognized here that subcritical crack growth can and often does occur in these thin film systems. In this case $G_I < G_{IC}$ and yet crack growth occurs, often by some environmentally-enhanced degradation process.

Interfacial fracture mechanics considers an interface between two different isotropic materials. The complex stress intensity factor for bimaterials can be expressed as [18]:

$$K = (K_1 + iK_2) = \left(\frac{P}{\sqrt{h}} - i\frac{M}{h^{3/2}}\right)\frac{p}{\sqrt{2}} h^{-i\varepsilon} e^{i\omega} \quad (1.15),$$

where h is the film thickness, M is the bending moment due to load P, ω is a real angular function, $p = \sqrt{(1-\alpha)/(1-\beta^2)}$, and ε is a bimaterial real constant:

$$\varepsilon = (1/2\pi)\, ln\left[(1-\beta)/(1+\beta)\right] \quad (1.16).$$

Dundurs parameters α and β for plane strain are [19]:

$$\alpha = \frac{(\mu_1/\mu_2)(1-\upsilon_1) - (1-\upsilon_2)}{(\mu_1/\mu_2)(1-\upsilon_2) + (1-\upsilon_1)}$$
$$\beta = \frac{1}{2}\frac{(\mu_1/\mu_2)(1-2\upsilon_2) - (1-2\upsilon_1)}{(\mu_1/\mu_2)(1-\upsilon_1) + (1-\upsilon_2)} \quad (1.17).$$

For bimaterials the phase angle Ψ is:

$$\Psi = tan^{-1}\left[\frac{Ph\, sin\,\omega - 2\sqrt{3}M\, cos\,\omega}{Ph\, cos\,\omega + 2\sqrt{3}M\, sin\,\omega}\right] \quad (1.18),$$

and the strain energy release rate G is related to the interface stress intensity factor K as:

$$G = \frac{1-\beta^2}{E(1-\alpha)}|K|^2 \quad (1.19),$$

where E is the thin film elastic modulus.

The amount of energy dissipation depends on the mode mixity (phase angle), a relative measure of the amount of shear and normal stress components at the crack tip. The idea of the mode mixity effect is presented in Figure 3. The amount of energy dissipation is higher in pure shear compared to the pure opening fracture mode. There are results in the literature, both experimental and theoretical that exhibit similar behavior [20-24]. The most realistic phenomenological descriptions of the functional dependence of the interfacial toughness on the mode mixity are given by Hutchinson and Suo [24]:

$$\Gamma(\psi) = \Gamma_0\left[1+tan^2\{\psi(1-\lambda)\}\right] \qquad (1.20),$$

$$\Gamma(\psi) = \Gamma_0\left[1+(1-\lambda)tan^2\{\psi\}\right] \qquad (1.21),$$

where Γ_0 is the mode I interfacial toughness for ψ=0; and λ is an adjustable parameter (Figure 4). Note that there is no mode mixity dependence for the ideally brittle material (λ=0), and both solutions collapse into one for λ=0 and λ=1. Strictly speaking, there is always a mode mixity effect in the case of a crack propagating along the interface between two dissimilar materials due to a mismatch in their elastic properties [19].

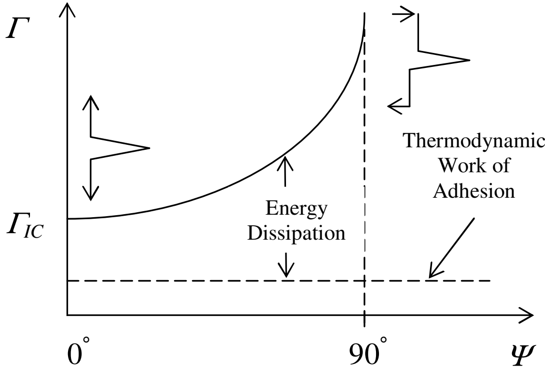

Figure 3. Interfacial fracture toughness as a function of the mode mixity angle.

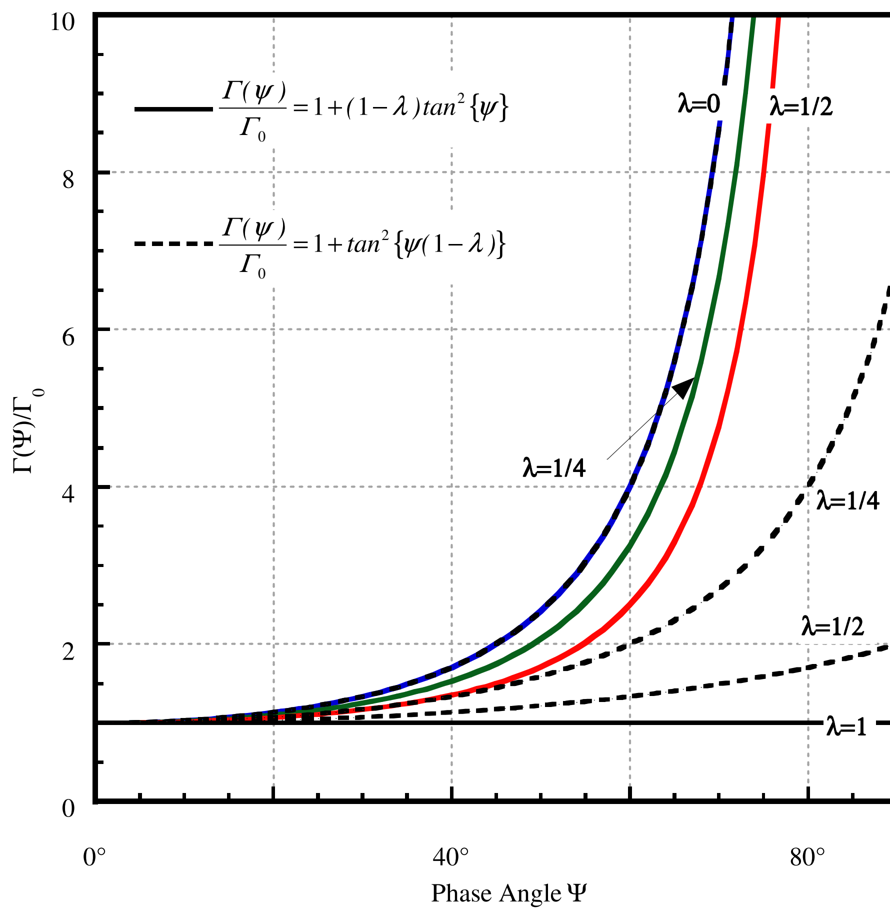

Figure 4. Phenomenological functions for $\Gamma(\psi)$.

In the case of a weakly bonded film on the substrate the interface will be the most likely crack path, although there are cases when the crack can kink either into the substrate or into the film itself [24]. The crack path depends on the phase angle, residual stress and the modulus mismatch between the film and the substrate. When testing thin film adhesion, knowledge of the fracture interface and the phase angle is necessary in order to interpret the results correctly. Interface toughness is strongly dependent on Ψ (Figure 3), so it is useful to measure adhesion over a wide range of phase angles, and preferably at $\Psi = 0°$, since it is the minimum value of adhesion, which is important for design considerations.

There is also a link between the thermodynamic work of adhesion (W_A) and the interfacial toughness (Γ_i). For example, when the thin film yield stress is low, and W_A is high, ductile fracture is the most likely mechanism. Conversely, brittle fracture occurs when the film yield stress is high, and the true adhesion is low [1, 25-27]. In the case of a metal film on a brittle substrate, one may improve the interfacial toughness by decreasing the film yield stress (annealing), or by using the underlayers that may increase the W_A term. At this point we will consider different techniques for measuring the interfacial fracture toughness of thin films.

THIN FILM ADHESION TESTS

There are more than a hundred different methods for measuring thin film adhesion that employ different sample geometries. Some tests use the as-deposited films, some require patterning, but one thing is common for all the tests: Since measuring adhesion requires breaking the interface, all tests use some driving force or stored energy to achieve thin film delamination. The energy may come from external mechanical force imposed on the film, or it can be stored in the film itself (through the internal film stress).

Superlayer Test

A test based upon internally developed stresses was proposed by Bagchi and coworkers [28]. Here, residual tensile stresses in a thin line drive its delamination from a thick substrate. The non-dimensional steady state strain energy release rate for a narrow thin line after crack initiation is:

$$G_{ss}E_f / \sigma_f^2 h_f = 1/2 \qquad (1.22),$$

where E_f is the Young's modulus of the film, h_f is the film thickness, σ_f is the residual stress in the film. The corresponding phase angle in this case is about 52° [28]. For a wide line (width greater than thickness) the residual stress is biaxial and the strain energy release rate is:

$$G_{ss}E_f / \sigma_f^2 h_f = 1 - \nu_f \qquad (1.23),$$

where ν_f is the Poisson's ratio of the film. For a typical film thickness of a micron and a 100 MPa residual stress, the stress-induced energy release rate is small, on the order of 0.1 J/m^2. Most interfaces in microelectronic devices have higher debond energies, so decohesion is not possible under these conditions. G_{ss} should be substantially increased without changing the phase angle. One of the ways to achieve this is by increasing the resulting film thickness by putting a thick overlayer (superlayer) on top of the tested structure. For Cu interconnects a Cr superlayer was found to work the best [14, 28, 29]. The superlayer increases the film total thickness and elevates the total residual stress without changing the tested interface. It is deposited at ambient temperatures (by electron beam evaporation or sputter deposition) and does not react with the tested Cu film; on the other hand it has high residual tensile stresses upon deposition. Figure 5 illustrates the test schematically. First a thin carbon release layer is thermally evaporated and patterned using the bilayer photolithography technique. This layer acts like a precrack for the test structure. Its width is at least twice the Cu film thickness to avoid edge effects on the energy release rate.

In the second step the film of interest (Cu) and the superlayer (Cr) are deposited and patterned to form strips perpendicular to the carbon lines. In order to produce a range of strain energy release rates for a given sample, the superlayer thickness is varied. The metal bilayer structure is cut by wet etching or ion milling during the third step. If the strain energy release rate exceeds the adhesion energy, the strips decohere. This gives the upper bound for the thin film adhesion. If the films stay attached, the adhesion energy was not exceeded and a superlayer thickness must be increased. This procedure gives the lower and upper bounds, bracketing the real adhesion value.

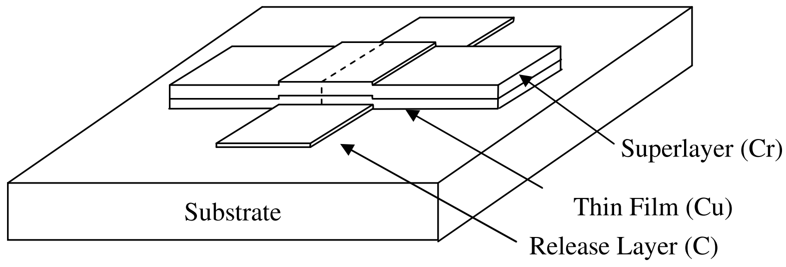

Figure 5. Superlayer test schematics.

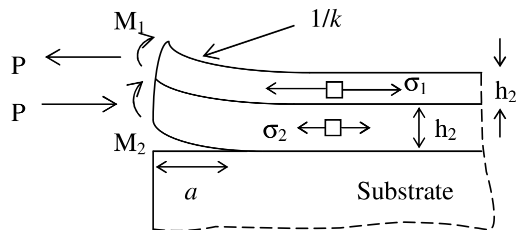

Figure 6. Film decohesion in the superlayer test.

The debond energy G is determined by the critical superlayer thickness [28]:

$$G = \sum_i \frac{\sigma_i^2 h_i}{E_i^{'}} - \sum_i \frac{1}{E_i^{'}} \left[\frac{P^2}{h_i} + \frac{12 M_i^2}{h_i^3} \right]$$

$$P = k \left[\frac{E_1^{'} h_1^3 + E_2^{'} h_2^3}{6(h_1 + h_2)} \right]$$

$$k = \frac{6(h_1 + h_2)(\varepsilon_1 - \varepsilon_2)}{h_1^2 + E_2^{'} h_2^3 / E_1^{'} h_1 + E_1^{'} h_1^3 / E_2^{'} h_2 + h_2^2 + 3(h_1 + h_2)^2} \qquad (1.24),$$

$$M_i = E_i^{'} k$$

where i=1, 2 refer to the two materials in the bilayer, $h_1=h_c$, $E^{'}_i$ are the biaxial elastic moduli, $E^{'}_I = E_i/(1-\nu_i)$, the load P is associated with the residual tension stress σ_i in each layer, k is the curvature of the debonded layer, ε_i are misfit strains: $\varepsilon_I = \sigma_i/E^{'}_i$, M_i are the bending moments along the centerline of each layer due to the load P (Figure 6).

A similar idea of using the superlayer residual stress to drive thin film delamination was employed by Kinbara et al [30] to debond Ti films with a Ni superlayer. Finite element analysis has been used to calculate the stress distribution in the test structure. Normal stress was used as the adhesion measurement, so the mode mixity effects are not taken into account.

In the case of the residual compressive stress in the line, it may buckle, relieving the stress. The interfacial toughness is calculated then [24, 31]:

$$G = \left[\frac{(1-\nu^2)h}{2E} \right] (\sigma - \sigma_B)(\sigma + 3\sigma_B) \qquad (1.25),$$

where σ_B is the buckling stress in equation (1.29), and σ is the stress in the line, which can be calculated from the buckle height, d [24]:

$$\sigma = \sigma_B \left[\frac{3}{4} \left(\frac{d}{h} \right)^2 + 1 \right] \qquad (1.26).$$

Zhuk et al [32] have measured practical work of adhesion in thin polymer films using the superlayer test, and related it to the true work of adhesion from the contact angle

measurements. Xu et al have used a 1 um Cr superlayer with a 1 GPa residual stress to form cracks at the end of microlithographed strips [33].

Though the superlayer test gives accurate adhesion energy values, the testing technique is rather tedious. Several superlayer thicknesses have to be deposited before the lower and the upper bounds of adhesion could be extracted. The phase angle is also limited to 50° [28, 29].

Indentation Tests

Nanoindentation is normally used for measuring thin film mechanical properties such as the elastic modulus and hardness [34], which are also useful for modeling the film fracture behavior. In the case of a brittle, weakly bonded film, indentation can be used to delaminate the film from the substrate, thus measuring the thin film interfacial strength [35-41]. Basically, the cone (plane stress) and the wedge (plane strain) are the two most popular indenter geometries for measuring brittle thin film adhesion by indentation. Marshall and Evans [35] provide the analysis for the conical indentation-induced thin film delamination. The strain energy release rate is:

$$\frac{GE_f}{(1-\nu_f)} = \tfrac{1}{2}h\sigma_I^2(1+\nu_f) + (1-\alpha)(h\sigma_R^2) - (1-\alpha)h(\sigma_I - \sigma_B)^2 \qquad (1.27),$$

where E_f and ν_f are the thin film's Young's modulus and Poisson ratio respectively, h is the film thickness, σ_R is the residual stress in the film. Here, a sharp diamond tip is indented into the tested thin film, and plastically deforms a volume of $2V_I$ (Figure 7a) Indentation causes nucleation and propagation of the interfacial crack. If the indenter is driven deep enough, so that the crack reaches its critical buckling length, the film double buckles (Figure 7b) during indentation. If the crack length did not reach its critical buckling length on each side of the indenter, single buckling might occur upon tip removal (Figure 7c). When the tip is removed, the film under indenter is no longer under constraint, so it may form a single buckle even in the initial double-buckling case.

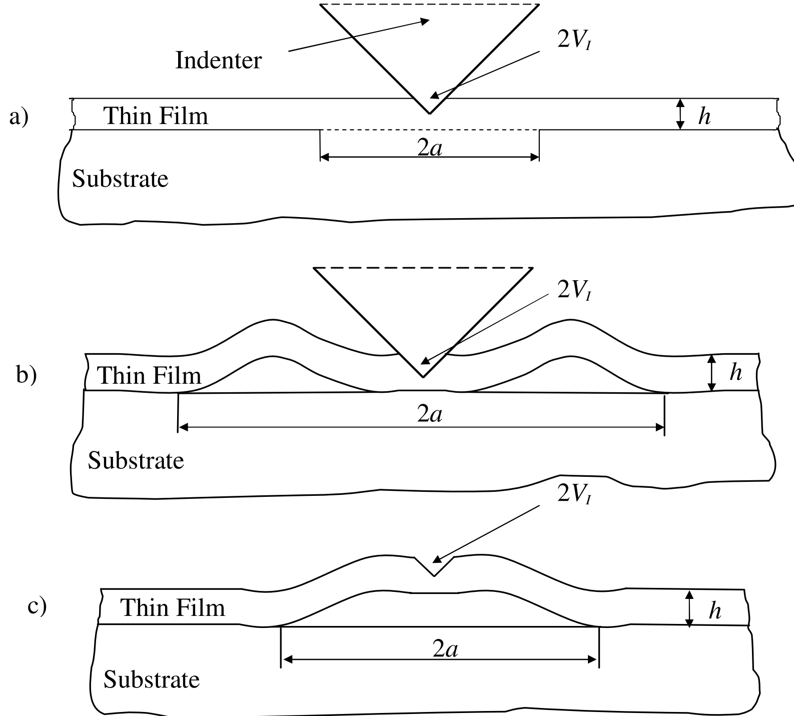

Figure 7. a) No buckling during indentation; b) double-buckling during indentation; c) single-buckling after the indenter tip removal.

The indentation stress, σ_I can be calculated by using the indenter tip geometry:

$$\sigma_I = \frac{V_I E_f}{2\pi h a^2 (1-\nu_f)} \qquad (1.28).$$

The indentation volume, V_I can be calculated from the plastic indentation depth using the tip geometry, and the crack length, a can be directly measured by using microscopy of profilometry techniques. If the crack is driven far enough by the indenter (Figure 7b or c), the film can buckle, giving rise to the last term in (1.27) through the Euler buckling stress

$$\sigma_B = \frac{\mu^2 h^2 E_f}{12 a^2 (1-\nu_f)} \qquad (1.29),$$

where μ is a constant, which depends on the boundary condition (μ^2 = 14.68 for single buckling, and μ^2 = 42.67 for annular double buckling). The term α is equal to one if the film

is not buckled, otherwise it represents the slope of the buckling load versus the edge displacement on buckling:

$$\alpha = 1 - \frac{1}{1 + 0.902(1 - \nu_f)} \quad (1.30).$$

Note that in the case of non-buckling fracture (α = 1), delamination is only driven by the indentation stress, and the residual stress does not come into play.

A simpler model is presented by Rosenfeld et al [42] for thick films with low elastic modulus:

$$G = \frac{2(1-\nu_f^2)\sigma_{rx}^2 h}{E_f}\left(\frac{1}{1+\nu_f + (a/x)^2(1-\nu_f)}\right)^2 \quad (1.31),$$

where σ_{rx} is the radial stress at the indenter contact radius, a is the crack radius and x is the indenter contact radius. If the film hardness, H, is constant through the film thickness, then the contact radius can be expressed through the indentation load with $x=(P/H)^{1/2}$. Applying the Tresca yield criterion, the radial stress σ_{rx} can be expressed through the film hardness H, and the strain energy release rate from equation (1.31) becomes:

$$G = \frac{0.627H^2 h(1-\nu_f^2)}{E_f}\frac{1}{\left[1+\nu_f + 2(1-\nu_f)Ha^2/P\right]^2} \quad (1.32).$$

The idea of expressing the strain energy release rate is very promising, since the load is continuously recorded during the indentation process, although the model does not account for the thin film residual stress and buckling. It can be applied to relatively thick films (>10 μm), where hardness does not change with the film thickness.

A microwedge wedge indentation test (MWIT) has been proposed by De Boer and Gerberich for thin metal lines [37, 38]. Here, a diamond wedge is indented perpendicular to the line to cause its debonding. Approach, similar to [35] is employed, where the plastic volume is assumed to transform into the film elastic displacement at the crack tip:

$$G = \frac{E_f' V_0^2}{2b^2 h a^2} \quad (1.33),$$

where V_0 is the half of the total indentation volume, a is the crack length, b is the line width, and E_f' is the plane strain elastic modulus of the film: $E_f' = E_f/(1-\nu_f^2)$. The test accounts for the line buckling, and appropriate solutions are available [37].

A similar wedge indentation test has been applied by Vlassak et al to measure adhesion of hard films on ductile substrates [40]. It is based on the model for the plane strain wedge indentation into a brittle continuous film on a ductile substrate:

$$G = \frac{(1-\nu_f^2)\sigma_{xx}h}{2E_f} \qquad (1.34),$$

where σ_{xx} is the stress in the film, perpendicular to the wedge line:

$$\sigma_{xx} = \sigma_R - \nu_f\left(\frac{E_f}{1-\nu_f^2}\right)\frac{W^2 \tan\beta}{\pi a^2} \qquad (1.35).$$

Here, σ_R is the residual stress in the film, W is the half width of the wedge indentation, β is the inclination of the face of the wedge to the surface of the film, and a is the crack length.

The advantage of the wedge indenter geometry is the weaker $1/a^2$ dependence in equation (1.33) compared to $1/a^4$ for the axisymmetric case (equations (1.27) and (1.32)), which leads to less experimental scatter. The problem with the wedge indentation is the alignment. Usually, wedges are not perfectly symmetric, and it is also extremely hard to align the wedge perpendicular to the plane of the thin film. Misalignment causes asymmetric crack growth on both sides of the wedge. This effect has been observed on both the micro and macro scales [37, 43]. A new revision of the wedge indentation test is provided in [44].

A relatively new idea of a cross-sectional indentation for thin film delamination has been proposed by Sanchez et al [45]. An indentation is made into the substrate cross-section, close to the film interface, which causes the film to debond. The energy release rate can be calculated by knowing the maximum film deflection, u_0:

$$G = \frac{Eh^3u_0^2}{12(a-b)^2}(1-\lambda)^4(2F+\lambda F') \qquad (1.36),$$

where a and b are the delamination and contact radii respectively, $\lambda = a/b$, and F is defined as:

$$F(\lambda) = \frac{2\ln\lambda + \frac{1+\lambda}{1-\lambda}\ln^2\lambda}{\left[(1+\lambda)\ln\lambda + 2(1-\lambda)\right]^2} \qquad (1.37),$$

and $F' = dF/d\lambda$. This test is particularly useful, since the film is not indented directly, and the crack initiates in the brittle substrate, which limits the amount of plastic deformation.

Unfortunately, indentation tests on thin films of interest cannot often be used directly in the case of ductile films on brittle substrates. A ductile strongly adhered film would form a

plastic pile-up around the indenter rather than delaminate from the substrate. Even if the film debonds from the substrate, delaminations are not reproducible, and plastic pile-up has to be taken into account anyways. Such problems have been solved with the introduction of the superlayer indentation technique.

Superlayer Indentation Test

Kriese and Gerberich [46] have combined the idea of the superlayer test with the indentation test. Deposition of a hard film, capable of storing sufficient amounts of elastic energy over the film of interest, can result in multilayer debonding [29], producing larger delamination radii (Figure 8). It also acts like a capping layer, preventing plastic flow of the underlying film in the vertical direction, adding normal stresses at the interfacial crack tip [47]. Presence of the overlayer provides an additional driving force for de-adhesion as shown in Figure 8. For the superlayer indentation test a sharp indenter also provides additional stress for crack initiation/propagation at the interface.

A modified Marshall and Evans analysis was used [35], and the laminate theory was employed in order to calculate the necessary terms in equation (1.27) for the bilayer [46]. In the case of a highly compressed superlayer, the indentation stress is being added to the residual stress, so multiple superlayer depositions are avoided. Blanket films can be tested in the as-deposited, as-processed conditions; no pattern transfer is necessary. When an indenter penetrates through a bilayer, it causes film debonding and blister formation, which can be seen afterwards in an optical microscope with Nomarski contrast (Figure 8 and Figure 9).

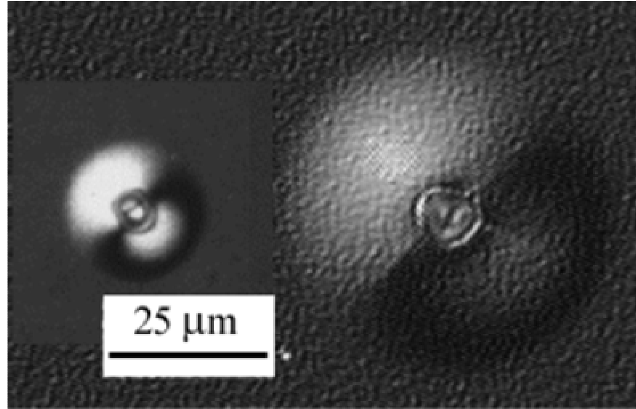

Figure 8. Optical micrographs of indentation iduced blisters with (right) and without (left) a W superlayer.

Properties of the films such as elastic modulus, Poisson's ratio, as well as the tip angle and radius are needed for an adhesion assessment. Generally speaking, there are two measurements that are necessary for strain energy release rate calculations. From the standpoint of blister formation, both indentation depth and blister diameter are required. Blister diameter is measured in the optical microscope with Nomarski contrast. Using the Oliver-Pharr method [34], inelastic indentation depth, δ_{pl}, is calculated from:

$$P = A(\delta - \delta_{pl})^m \qquad (1.38),$$

where P and δ are the load and displacement from the 65% of the unloading slope of the load-displacement curve respectively (Figure 10), A and m are fitting parameters. The indentation volume, V_I, is calculated from the inelastic depth by using the tip geometry. The indentation stress can be calculated from equation (1.28), assuming the conservation of volume.

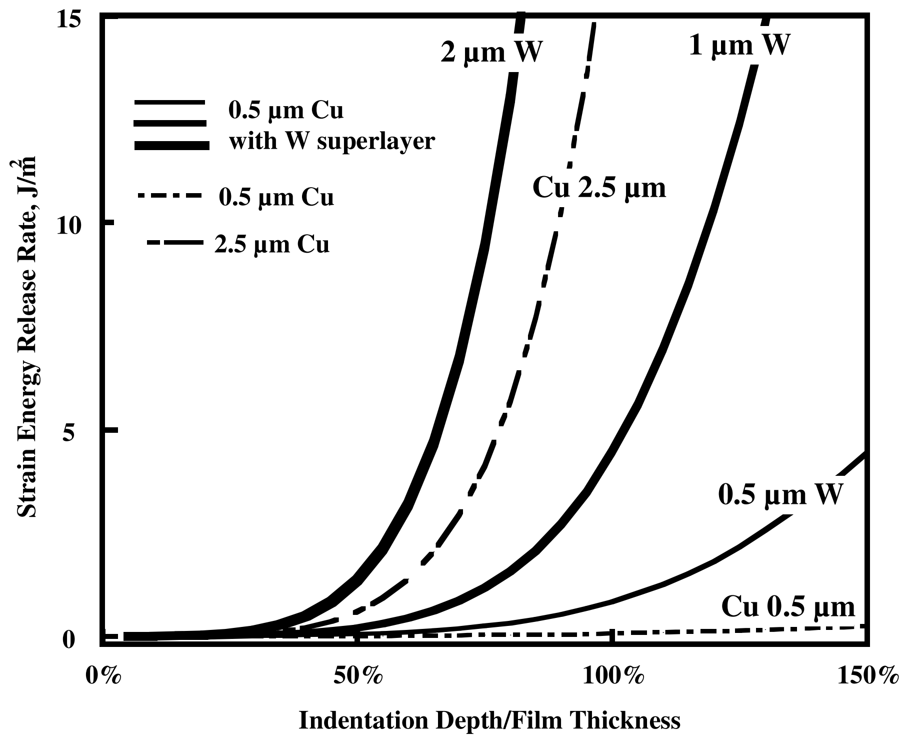

Figure 9. Effect of W superlayer thickness (500 MPa compressive residual stress) on the energy available for crack extension.

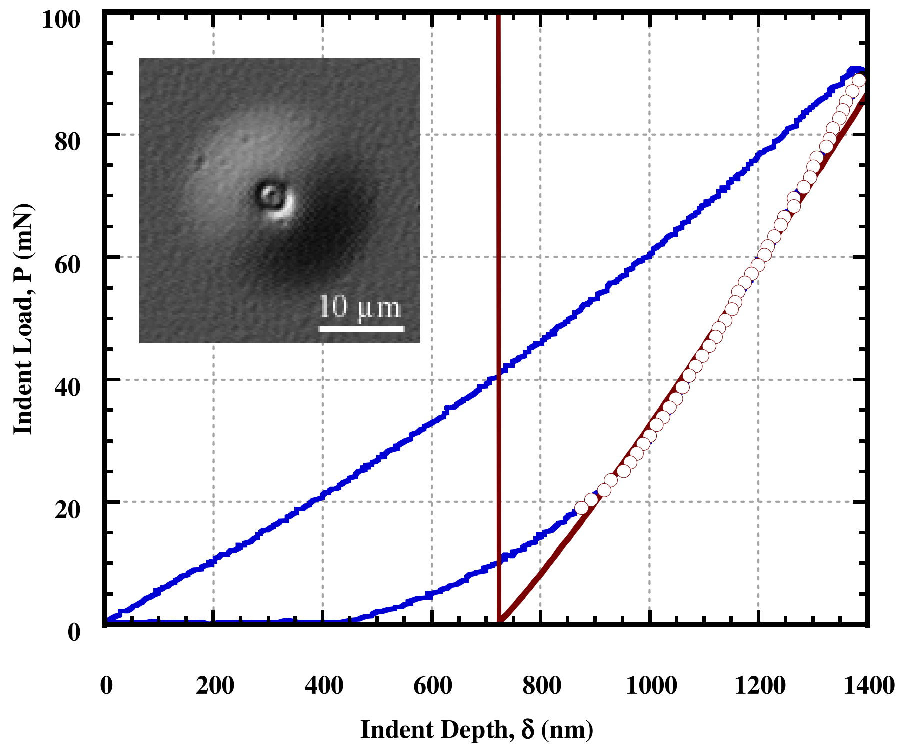

Figure 10. Load-displacement curve and corresponding delamination in a 120 nm thick Cu film on SiO_2.

The solution for the buckling stress in the bilayer is also provided in [46]. There are two different cases of buckling in the indentation-induced delamination. If the crack is driven far enough, the film may buckle around the indenter when the tip is in contact with the film (double or annular buckling). The film may also buckle back upon the tip retrieval from the film (single buckling), when the total crack length exceeds the critical buckling length. The appropriate strain energy release rate, G can be determined according to the following rule:

$G=G_{\text{nonbuckled}}$ if the total stresses in the film never exceed double or single buckling stresses;

$G=G_{\text{nonbuckled}}$ if G exceeds G_{single}, but the stress is not sufficient for the double buckling to happen;

$G=G_{\text{double}}$ if double buckling occurs and G exceeds G_{single};

$G=G_{\text{single}}$ if none of above conditions occurs.

The advantage of the superlayer indentation test is that it provides interfacial toughness measurements over a wide range of phase angles. Prior to buckling the phase angle is equal to the real angular function, ω, and at the onset of buckling a rapid decrease occurs.

The superlayer indentation test is the primary method for adhesion studies in this thesis.

Scratch Tests

In a typical scratch test a stylus or a diamond tip is drawn across the film surface. The test could be treated as a combination of two operations: normal indentation and horizontal tip motion. A vertical increasing load is applied to the tip during scratching until the coating detaches from the substrate. The minimum critical load P_{cr} at which delamination occurs is used as a measure of the practical work of adhesion [48, 49]:

$$P_{cr} = \frac{\pi r^2}{2}\left(\frac{2EW_{A,P}}{h}\right)^{1/2} \quad (1.39),$$

where r is the contact radius and h is the film thickness. This analysis is applicable only when the tensile stress normal to the film surface drives delamination.

Venkataraman, et al. developed a model for estimating the energy per unit area G_0 stored in the film from the scratch elastic stress distribution [50, 51], which was modified later to account for residual stresses in the film [52]:

$$G_0 = \frac{(1-\nu^2)\sigma_r^2 h}{2E} + \sum\left(\frac{(1-\nu^2)\bar{\tau}_{ij}^2 h}{2\mu} + \frac{(1-\nu^2)\bar{\sigma}_{ij}^2 h}{2E}\right) \quad (1.40),$$

where the first term comes from the contribution of the residual stress σ_r, $\bar{\tau}_{ij}$ and $\bar{\sigma}_{ij}$ are the average elastic shear and normal stresses in the delaminated film, h is the film thickness, μ is the film shear modulus. $\bar{\tau}_{ij}$ and $\bar{\sigma}_{ij}$ could be determined from the scratch trace geometry observed in SEM.

For a symmetric scratch trace, the strain energy release rate could be found using a circular blister analysis [52]:

$$G_0 = \frac{(1-\nu)h\sigma^2}{E}(1-\alpha)\left(1-\frac{\sigma_B}{\sigma}\right)^2 \quad (1.41),$$

where α is defined by equation (1.30) and σ_B is the Euler buckling stress, defined by equation (1.29) for a circular blister with $\mu=\pi$ [24].

M. de Boer, et al. adjusted the original scratch test for fine line structures [53, 54]. A schematic of the new test, precracked line scratch test (PLST) is shown in Figure 11. A thin metal line on a substrate is pushed with the asymmetric diamond wedge from its end. The thin line has a processed precrack in the form of a carbon layer, which makes it a real fracture mechanics specimen. The carbon layer is similar to that of the superlayer test of Bagchi and Evans [28, 29]. The precrack portion of the line is deformed elastically in the beginning of the test until the crack propagates. When the crack reaches its critical buckling length at a certain critical load, P_{cr}, the film buckles. At the point of buckling the strain energy release rate can be calculated as:

$$G = \frac{\sigma^2 h}{2E_f^{'}} = \frac{\left(P_{cr} - P_{fric}\right)^2}{2b^2 h E_f^{'}} \quad (1.42).$$

Here σ is the stress in the cracked portion of the line, b is the line width, P_{cr} and P_{fric} are the critical buckling load and the friction load respectively, which are measured experimentally.

The test is applicable to the hard lines, capable of bearing a load to the crack tip without plastically deforming; it was originally carried out on W thin lines on oxidized silicon wafers. The phase angle just prior to buckling is 52.7°, and decreases rapidly after buckling due to the increased normal stress component. Post-buckling solutions for the strain energy release rate are provided in [37, 39 and 43].

The mechanics for the PLST has been modeled using the macroscopic setup of a polycarbonate line bonded to steel with cyanoacrylate [43**Error! Reference source not found.**]. This allowed a construction of the stain energy release curve throughout the whole test, before and after the line buckling (Figure 12). Prior to the line buckling an R-curve behavior is observed, when the strain energy release rate increases with the crack length. At the point of buckling there is an unstable crack growth, since the strain energy release rate, G, exceeds interfacial fracture toughness, $\Gamma(\psi)$(Figure 13). This situation is analogous to the circular blister buckling [24]: at a certain level of stress, σ_{buckle}, and a certain crack length, a_1, line starts to buckle, at which point the interfacial fracture toughness drops under the influence of the phase angle decrease. The crack arrests at a_2 when the strain energy release rate and the interfacial fracture toughness are again in the equilibrium. At this point fracture is dominated by the mode I stress component, and continues to grow stably until the total line decohesion [43**Error! Reference source not found.**].

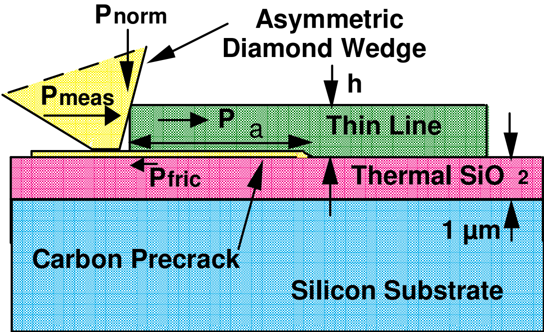

Figure 11. Schematic of the precracked line scratch test (PLST).

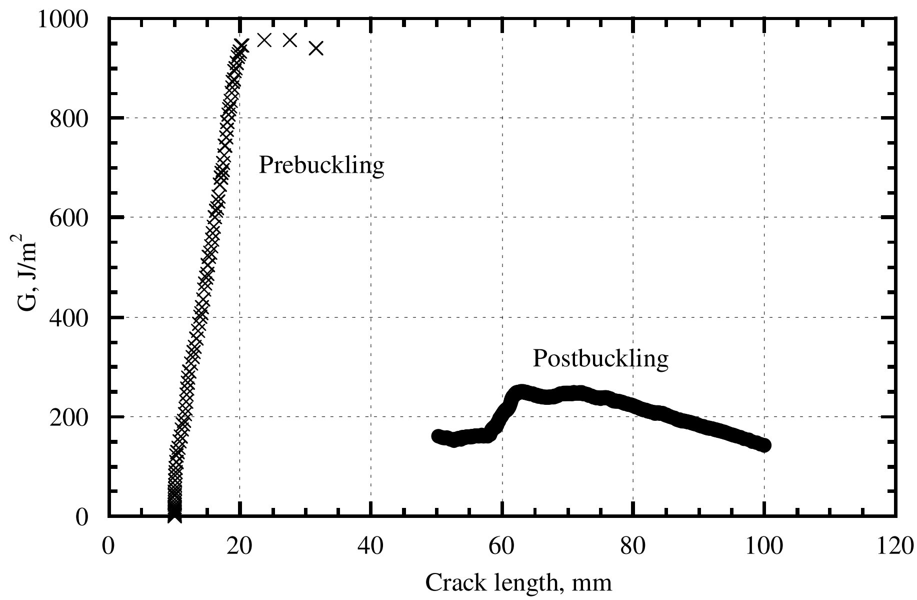

Figure 12. Strain energy release rate for the Precracked Line Scratch Test (PLST).

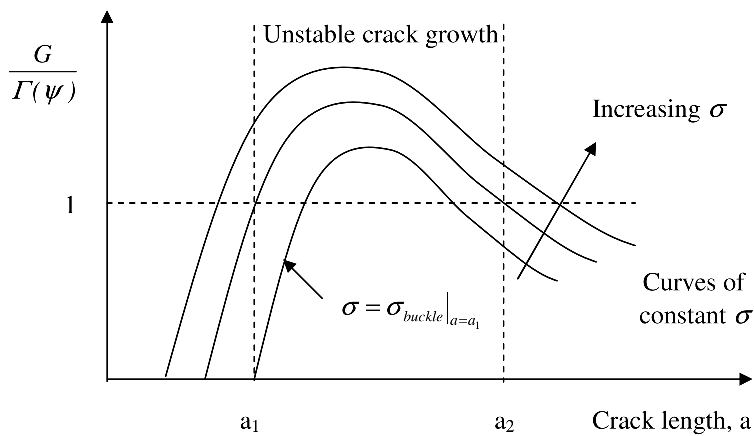

Figure 13. Schematic of unstable crack growth during buckling for the PLST.

The PLST allows measuring the interfacial fracture toughness over a wide range of phase angles, although it may not work with ductile metals such as Cu, Al and Au. For this test to work, the material must transfer the stress down to the crack tip without plastically deforming. This problem may be solved by using a stiff hard superlayer on top of the film of interest, just like in the superlayer indentation test.

Bulge And Blister Tests

The bulge test is analogous to uniaxial tension for bulk materials and has been developed for measuring mechanical properties of thin films. In the bulge test a freestanding thin film "window" is pressurized on one side, causing it to deflect (Figure 14). A stress-strain curve could be constructed from measured pressure, P, and film deflection δ.

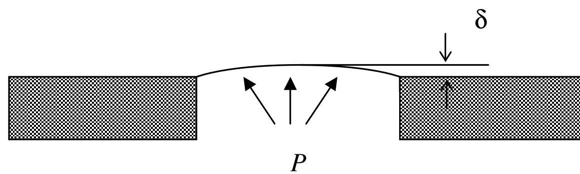

Figure 14. Bulge test schematics.

The pressure-deflection curve is a function of sample geometry, its mechanical properties and residual stress. A spherical cap model was initially used for stress and strain determination in the bulge test [55]:

$$\sigma = \frac{P r^2}{4\delta h} \text{ and } \varepsilon = \frac{2}{3r^2}\delta^2 + A \tag{1.43}$$

where δ is the total bulge height, h is the film thickness, r is the bulge radius, and A is the term which accounts for initial stress in the film and for slack films is: $2\delta_0/3r^2$, with δ_0 the height due to the slack in the film. For taut films $A=\sigma_0/E'$, where σ_0 is the initial tensile stress in the film, E' is the biaxial modulus of the tested film.

The relation between pressure P and deflection δ may be expressed, based on the cap model:

$$P = \frac{c_1\sigma_0 h}{ar^2} + \frac{c_2 Eh}{r^4(1-\nu)}\delta^3 \quad (1.44),$$

where c_1 and c_2 are are geometric parameters of the bulge form. Vlassak, et al. showed the validity of equation (1.44) for square and rectangular membranes using an energy minimization technique [55].

The spherical cap model assumes an equi-biaxial state of stress and strain in the bulged film, which is not true since the film is clamped and there is no circumferential strain at the edge. There is also an uncertainty in measuring the initial bulge height in the beginning of pressurizing. Finite element analysis was conducted to overcome such problems [55-58] for measurement of biaxial modulus and Poisson's ratio. Mechanics for the blister test is also given in [24]. A disadvantage of this method lay in its difficult specimen preparation, if the film is too thin (< 2 μm), it may wrinkle due to the residual stress relief upon being made freestanding [57].

The blister test is similar to the bulge test with the only difference that the pressure is being increased until the film starts to debond from the substrate, forming a blister. The crack extension force (strain energy release rate) for the blister test is given as in [59]:

$$G = P\delta\frac{k_v}{\pi}\left(\frac{4+5\varphi}{4+4\varphi}\right) \quad (1.45),$$

where coefficient k_v accounts for the shape of the blister and is about 1.62 for circular window and 1.94 for square window; φ is given as: $\varphi = \frac{c_2 E_f^{'}}{c_1\sigma_0}\left(\frac{\delta}{r}\right)^2$.

Blister tests are often invalid in the case of thin ductile films due to film yielding before decohesion. In order to prevent film yielding, a hard elastic superlayer may be deposited on top of the film of interest, similar to the superlayer indentation technique. The superlayer can be deposited directly on the freestanding film without causing its wrinkling. Another problem with the blister test is that the crack often does not propagate uniformly along the perimeter of the blister, making it harder to interpret the results. A transition between blister bending and stretching is discussed in [60]. For a homogeneous system the phase angle range in the blister test is between -40 and -90°. A comprehensive analysis of mode mixity in the blister test is presented in [61].

Sandwich Specimen Tests

For the sandwich type of test a macroscopic fracture mechanics sample is made with a thin film incorporated into the test structure. This is typically done through diffusion bonding, which can alter both the film microstructure and the interfacial adhesion, since the bonding takes a long time (several hours) and occurs at high temperatures, close to the melting point. Usually it acts as an annealing step during the sample preparation, which may not happen in the actual film processing. As a result these types of measurements often do not apply to the films in the as-deposited state. These tests are modifications of classical fracture mechanics tests, for which mechanics has been developed. For an isotropic material the crack tends to grow in the opening mode I, but in the case of an interface, the crack tends to grow along the interface, that's why it is important to quantify interfacial fracture toughness as a function of mode mixity.

Different geometries are possible, so only the most common ones will be considered. The simplest example is the modified K_{IC} specimen [63, 64], where a thin film is bonded between the two pieces of a compact tension sample [62] (Figure 15a). Another version of this test is the double cantilever test, where a thin film is bonded between the two rigid elastic plates. For the K_{IC} test the interfacial fracture toughness can be expressed in the form:

$$K = \frac{P_Q}{B\sqrt{W}} f(a/W) \qquad (1.46),$$

where P_Q is the load determined from the load-displacement curve, B is the specimen thickness, W is the specimen width as defined in Figure 15a, $f(a/W)$ is a function of a and W which is defined in the standard for the homogeneous material [62]. McNaney et al provide the elastic compliance solution for the modified compact tension as well as the four-point bend specimens [65, 66].

In the case of the double cantilever test, the strain energy release rate can be expressed as [67, 69]:

$$G = \frac{12P^2 a_0}{EB^2H^3}\left[1 + AH/a_0 + B(H/a_0)^2\right] \qquad (1.47),$$

where P is the fracture load, a_0 is the precrack length, and H is the half the specimen height (Figure 15a), A and B are the proportionality coefficients ($A \approx 1.3$ and $B \approx 0.5$).

It turns out that the presence of a thin middle layer does not shift the phase angle much as compared to the homogeneous case as long as the middle layer is thin compared to the total sample thickness 2*H* [63]. The importance of both tests is that they provide the interfacial toughness at almost zero mode mixity angle.

Another test, which uses sandwich structure, is the Brazil disk test. Brazil disk test is schematically shown in Figure 15b. A thin film is bonded in-between two pieces of a disk of radius *R*. The crack of the length *2a* is present in the interface. Load *P* is applied at a certain compression angle Θ to the crack axis. Mode mixity is varied by changing the compression angle Θ. Pure mode I conditions are achieved when $\Theta = 0°$ and pure mode II when $\Theta \cong 25°$ [70].

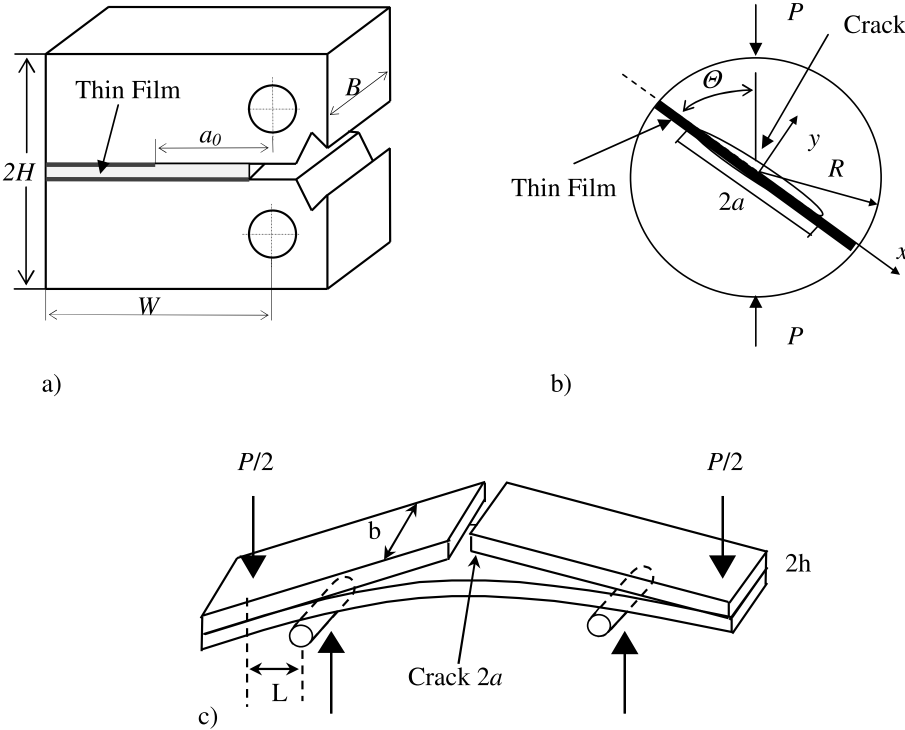

Figure 15. Sandwich specimen tests schematics: a) Modified K_{IC} sample; b) Brazil-nut sample; c) 4-point bent (UCSB) sample.

Atkinson et al presented explicit formulae for K_I and K_{II} valid for any crack orientation in the homogeneous Brazil disk [71, 72]:

$$K_I = \frac{PN_I}{Rb}\sqrt{\frac{a}{\pi}}$$
$$K_{II} = \frac{PN_{II}}{Rb}\sqrt{\frac{a}{\pi}} \quad (1.48),$$

where P is the load applied in compression, a is half the crack length, b is the disk thickness, N_I and N_{II} are non-dimensional functions of the relative crack size, (a/R), and the compression angle Θ.

O'Dowd and coworkers provided stress intensity solution for a bimaterial Brazil disk [70]:

$$K = \frac{YP}{2R}\sqrt{2a}(2a)^{-i\varepsilon}e^{i\Psi} \quad (1.49),$$

where Y is a dimensionless geometric factor, ε is the bimaterial real constant as in equation (1.16). The dependence of Ψ and Y on the compression angle Θ is not known. Since the crack has two tips, the stress intensity factors at each tip would also be different, so Ψ and Y must be provided for each crack tip. Brazil disk mechanics for orthotropic materials as well as a FEM model are discussed in [73]. Mechanics for a Brazil-nut-sandwich specimen (Figure 15b) and different failure types are considered in [74]. The advantage of the test is the ability to change the phase angle by rotating the sample relative to the axis of the applied load.

The last type of the sandwich samples considered here is the four-point bent test (Figure 15c). To date this is the most popular adhesion test for the microelectronics industry. Two elastic substrates with thin films on them are bonded together with another material (typically Cu, or epoxy). The upper substrate has a notch in it, and a crack propagates through the substrate and kinks into the interface of interest upon loading. At this point the strain energy release rate reaches steady state, which corresponds to the load plateau in the load-displacement curve. The strain energy release rate can be calculated from the steady state fracture plateau load P [75]:

$$G = \frac{21\left(1-\nu^2\right)P^2L^2}{16Eb^2h^3} \quad (1.50),$$

where the geometrical parameters *L*, *b* and *h* are shown in Figure 15c. After passing the lower support line, the crack does not grow stably anymore, and numerical analysis is required to assess *G* [76]. The phase angle for the test at steady state crack growth is approximately 43°. Limitations of the test in terms of the K-dominance region are discussed in [77].

None of the sandwich specimen tests account for the residual stress in thin films. The ideal test should simulate the practical situation as closely as possible, while also being able to extract the value of the practical work of adhesion. The method must explicitly account for contribution of the residual stress to the decohesion process. If the test structure has experienced only low temperatures upon fabrication, using high homologous temperature (T/T_m) processing steps in specimen preparation, such as diffusion bonding, is not desirable, since it severely alters interface adhesion properties.

1.2 MATERIALS CONSIDERATIONS

The objective of this thesis is the investigation of ductile thin film adhesion, primarily Cu and Al as a function of different parameters such as the film thickness, underlayer material, microstructure and test temperature. This has been dictated by the primary application of Cu and Al as the interconnect materials for the microelectronics industry.

MODERN METALLIC INTERCONNECTS

Interconnect lines are used for connecting individual electronic devices (transistors, etc.) in integrated circuits (IC). Interconnects are fabricated by etching certain areas of deposited metallic films. Several layers of interconnect structures are typical in modern ICs.

Al and Al alloys used to be, and still are the most common materials for interconnects in very large scale integrated (VLSI) devices. However, these materials, due to the relatively low melting point of Al, are susceptible to stress and electromigration, which confines interconnect dimensions to a certain limit. To overcome these limitations for future sub-micron VLSIs, copper has been proposed as an attractive material for integrated circuits metallization.

On September 22, 1997 IBM announced new technology, called CMOS 7S. [CNN.com] It is a new semiconductor manufacturing process, which uses copper instead of

aluminum to create the circuitry on silicon wafers. The complementary metal oxide semiconductor (CMOS) manufacturing process integrates six layers of copper on a chip.

Advances in miniaturization allow building of products that are smaller, integrate more complex functions, use less power and require less cooling. As reported by IBM, the width of interconnect copper lines could be as small as 0.20 μm, which allows more complicated circuits to be built and pack between 150 million and 200 million transistors on a single chip. The CMOS 7 device operates at a voltage of 1.8 volts, which makes it very attractive for small power consuming applications.

Right after IBM, on October 1, 1997, Motorola Semiconductor Products Sector said it has developed a processor manufacturing method that incorporates copper into its chips. The company said the method, which it called a dual-inlaid metallization technique, is the result of a two-and-a-half-year research effort. It took more than ten years of research for IBM to incorporate copper in chips. Trends of the interconnect technology in microelectronics are discussed in [78].

Advantages Of Copper As An Interconnect Material

The electrical conductivity of copper is 5.88 $(\text{ohm}\cdot\text{cm})^{-1}$ as compared to 3.65 $(\text{ohm}\cdot\text{cm})^{-1}$ for aluminum [79], which means that for a given cross section of a metal thin interconnect, copper can transport more charge. At the same time thermal conductivity at room temperature is 4.01 $\text{W}\cdot(\text{cm}\cdot\text{K})^{-1}$ for bulk copper and 2.37 $\text{W}\cdot(\text{cm}\cdot\text{K})^{-1}$ for aluminum. The only metal, which has higher values of electrical and thermal conductivity, is silver, but it is susceptible to corrosion [80] and agglomeration problems in presence of weak oxidizing agents such as sulfur.

Electromigration In Metallic Interconnects

Current density in interconnects can reach values of $1\text{-}2\cdot10^5$ A/cm^2 during device operation at 125 °C [81]. Aluminum interconnects, being pushed to their dimensional limits, experience electromigration problems. Discovered 100 years ago, electromigration was rediscovered in the 60's, when the first integrated circuits (IC) were introduced. Initially, ICs failed within the first week of service. Tiny "cracks" several hundred angstroms wide caused

failure, leading IBM to spent almost a billion dollars in 1966 on electromigration research [82].

Electromigration is the transport of a metal due to the momentum transfer between conducting electrons and diffusing metal atoms. There should be enough conducting electrons for electromigration to occur, so it is observed only in metals and heavily doped semiconductors.

Bulk materials cannot withstand high current densities; they simply melt because of Joule heating. Thin films on the other hand are in direct contact with the substrate, which acts like a huge heat sink, so the heat, generated by the current is conducted away into the chip. Current densities in metal interconnects are two orders of magnitude higher than in bulk wires.

Since a perfect lattice cannot exist at temperatures, higher than 0 °K due to crystal defects, and atoms are vibrating at their lattice sites, electrons scatter. When current flows through a thin metal line, the electrons transmit momentum to activated lattice atoms. This results in the so-called wind force ($F = e\rho i Z^*$), which moves atoms in the direction of electron flow (Figure 16). Atomic flux, J, is defined as:

$$J = DC\frac{Z^* e\rho j}{kT} \quad (1.51),$$

where D is the diffusion coefficient, C is the concentration of diffusing atoms, Z^* is a quantity, that represents the sign and the magnitude of the momentum change, ρ is the resistivity, j is the current density.

In order to form a void in a certain region there should be more mass leaving than arriving. Under high-current-density conditions, metal-atom movement causes voids in some regions and metal pileup or hillocks in other regions. Voids can cause open circuits and pileups short circuits, resulting in contact failure. Depletion and accumulation of material takes place in aluminum lines.

One of the most important quantities for the industry, concerning electromigration is the median time to failure (MTF). First it was considered that the MTF follows a 1/j dependence, since it was attributed only to the wind force (equation (1.51)). The mass transport depends on the sum of all the chemical potentials that act on the diffusing metal atoms, and electromigration potential is only one of them. Stress and concentration gradients

are also important contributors to the mass transport process. The empirical formula for electromigration failure that accounts for most contributors is known as Black's Law [83]:

$$t = A\, j^{-2}\, exp\left(\frac{\Delta H}{kT}\right) \qquad (1.52),$$

where t is median time to failure, A is an empirical constant, ΔH is the activation energy for failure. MTF behavior depends on the failure mechanism, whether it is nucleation or growth dominated.

There is also a grain size effect. The grain size of the interconnect line is limited by film thickness. When a line is being patterned out of thin film, there are basically two options in terms of grains: wide lines (many grain boundaries within a line) and narrow or so-called "bamboo" lines (few boundaries within a line) (Figure 17).

For wide lines $1/j^2$ kinetics usually dominates, whereas for narrow lines, $1/j$ kinetics dominates [81, 82]. Since electromigration is a diffusion process, all factors that affect diffusion affect electromigration. Besides current, electromigration depends on other parameters, temperature for example. Since a device operates at a higher temperature, at least half of the melting point of the interconnect material, diffusion at grain boundaries, interfaces and surfaces dominates the mass flux. This happens due to high vacancy concentrations at grain boundaries. It was found that for the same current density and uniform grain size, narrow lines are more reliable in terms of electromigration than wide lines [81, 82]. For narrow lines there are two types of diffusion: slow diffusion inside the grain and fast diffusion along the grain boundary (Figure 18).

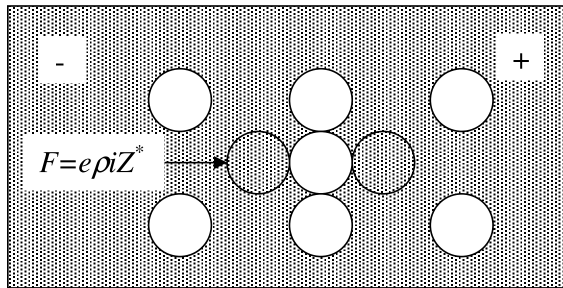

Figure 16. "Electron wind" force.

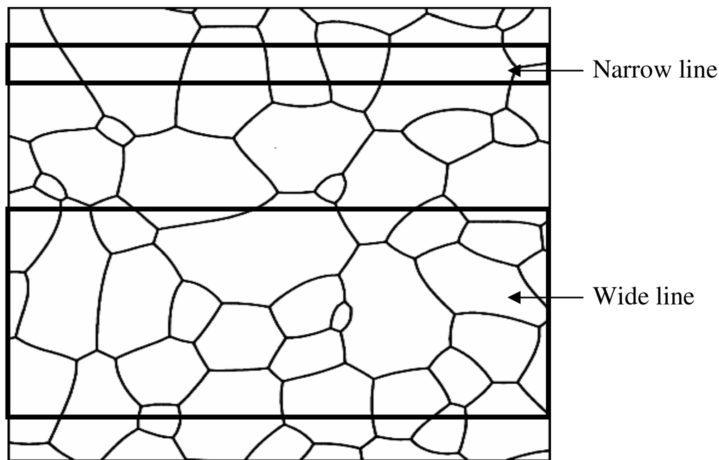

Figure 17. Narrow (bamboo) and wide lines.

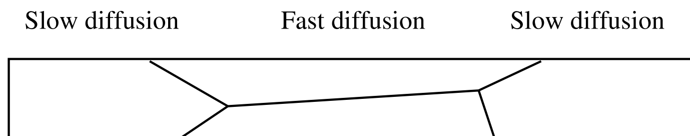

Figure 18. Slow surface diffusion vs. grain boundary fast diffusion.

In the 70's it was noticed that electromigration can be reduced by adding copper to Al. Copper slowed down the grain boundary diffusion in aluminum interconnects. TEM in-situ study of electromigration in Al-Cu showed that copper migrates faster than aluminum, so voiding occurs in regions of copper depletion [85]. Median time to failure was increased by an order of magnitude by using 95% Al 4% Cu 1% Si material for interconnects. Activation energies for electromigration in Al are about 0.5 eV as compared to 1.06 eV in Al (0.5%Cu) [86]. Using Al-Cu instead of Al for interconnects was a great breakthrough in technology, though it did not eliminate electromigration problems.

Electromigration In Cu Interconnects

The operating frequency of an IC is directly related to current density. For Al interconnects there is a $2 \cdot 10^5$ A/cm^2 current density threshold, which limits circuit performance. The idea of using Cu instead of Al in terms of electromigration is based on the fact that smaller lines could be used for higher productivity and reliability.

Electromigration activation energies in Cu were found to be about 1.25 eV as compared to 0.5 eV for pure Al [83]. Since there is an exponential dependence between median time to failure and activation energy for electromigration as in equation (1.52), using copper instead of aluminum will substantially increase MTF. Till recently electromigration in Cu was not extensively characterized due to difficulties in patterning Cu interconnects by reactive ion etching (RIE) because of poor adhesion of Cu and underlying barrier materials to silicon substrates [88]. Copper is a tougher material as compared to aluminum in terms of electromigration, so current densities ($>10^7$ A/cm^2) and higher test temperatures (due to Joule heating) were used to cause visible electromigration effects [89]. It was also observed that copper is subject to corrosion under voltage stressing in atmosphere [90], which increases the interconnects resistance. Due to the mentioned problems, underestimated lifetimes of copper lines were reported. In order to compare electromigration effects in Cu vs. Al, tests should be conducted in vacuum, using comparable current densities and reasonable temperatures.

Unpassivated Cu interconnects with TiN underlayer were tested by means of the Blech-Kingsborn edge-displacement technique in high vacuum, using current density of $6 \cdot 10^5$ A/cm^2 with test temperatures between 175 and 275 °C [87]. As reported in [87], in this

temperature range electromigration-induced ionic drift was three orders of magnitude lower for copper than for aluminum, with an activation energy of 1.25 eV. The value of 1.25 eV agrees with other sources [86] and with the activation energy of Cu grain boundary diffusion ranging from 1.058 to 1.244 eV. The value of –0.7 for Z^* was found for Cu thin film electromigration [87], which is ten times smaller than bulk material value.

There is also a large effect of an underlayer on the activation energy for electromigration in copper. It could be significantly lowered by interfacial diffusion, a mechanism which needs further investigation. Nevertheless, electromigration research shows that Cu will enable higher current densities in ICs as compared to Al interconnects used now. Maximum current densities are limited mostly by Joule heating effects.

Electromigration And Stress

Electromigration and stress in thin films are connected. One can think of electromigration void nucleation in terms of a critical vacancy concentration, or in terms of a critical stress [82]. When atoms accumulate on one side of the conductor, a compressive stress builds up in that region. Higher atomic concentration, C, will result in higher stress, σ:

$$\frac{\partial C}{C} = \frac{\partial \sigma}{E} \qquad (1.53),$$

where σ is a hydrostatic stress component and E is the appropriate elastic modulus.

On the other side of the conductor there is a deficit of atoms, so the vacancy concentration goes up. When the vacancy concentration exceeds the thermal equilibrium concentration, vacancies will disappear, reducing the crystal volume. Since the thin film is attached to the substrate, a volume change will transform into tensile stress.

Tensile stress, in its turn, will affect the vacancy concentration, C:

$$C = C_0 \, exp\left(\frac{\sigma_h \Omega}{kT}\right) \qquad (1.54).$$

Here, Ω is the activation volume (vacancy volume), and σ_h is hydrostatic stress. It is possible to assume that all vacancies that are created are transformed into stress [82].

Sometimes a failure effect, similar to electromigration is observed in thin films without applied current. In this case a stress gradient acts as a driving force for atom motion.

It is called stress migration. Brown, et al. studied thermal stress induced void formation in copper interconnects [91].

Thin film failure in the form of voids will occur when a critical tensile stress is reached. Extrusions or buckles will appear when the critical compressive stress is reached. Stress also affects diffusion, making it easier in the case of tensile stress and more difficult in the case of compressive stress. Both stress and diffusion are functions of temperature.

Complications Associated With Cu As An Interconnect Material

Copper interconnects are more reliable in terms of electromigration as compared to aluminum interconnects. Copper has lower resistivity, which allows higher currents, operating frequencies and smaller interconnect dimensions for IC. There are some problems though associated with copper as a material for interconnects [78, 92].

Copper does not have a protective nonporous oxide layer, as does aluminum. This leads to corrosion problems and affects adhesion. Deposition processes as well as deposition parameters need to be optimized to obtain a desirable copper microstructure. Methods for patterning complex interconnect structures should be enhanced for Cu metallization.

Interconnects exhibit resistance-capacitance coupling, which cases circuit delays. In order to reduce the amount of cross talk between Cu interconnect lines, a good insulator low-K material should be used to passivate lines. The best low-K "material" is air with the dielectric constant of one, but the device must be mechanically stable, so air gaps are not acceptable between the lines. Silicon dioxide with the dielectric constant of 4 has been the standard for the Al-based technology. This is not acceptable for the Cu metallization, and currently materials with the dielectric constant of 2.7 are used. These are typically porous materials with low elastic modulus, sometimes even viscoelastic polymers. This brings up mechanical stability as well as adhesion problems.

Copper diffuses into silicon, reaching active device layers, which makes devices inoperable. A barrier layer is essential to prevent copper diffusion. Good mechanical reliability is needed for stable device operation, so copper stress relaxation mechanisms are to be studied. And finally, copper does not reduce SiO_2, so it does not adhere well. The capital cost of the IC processing equipment is in the order of 1-2 billion dollars per

fabrication, so all problems have to be resolved before full-scale copper interconnect incorporation into IC's would become possible.

Underlayer Materials For Cu Interconnects

There are several reasons why underlayers are needed in case of copper interconnects. Adhesion of copper to silicon is rather poor. Bare copper films on silicon fail the "scotch tape" test. The underlayer is supposed to improve adhesion properties and thus improve mechanical reliability. Copper diffuses into silicon, so the underlayer is supposed to prevent copper diffusion. On the other hand, any additions to copper reduce interconnect conductivity. The underlayer material is supposed to be nonreactive and nonmiscible with copper, but should react with Si at high temperatures. It also should prevent abnormal copper grain growth, assisting good copper texture formation. It should not weaken copper electromigration properties. The underlayer material should be compatible with interconnect patterning processes without adding high additional cost to it. Generally speaking, the barrier material should simultaneously optimize several contradicting requirements.

Reilly, et al. studied the oxidation behavior of thin copper films [93]. The oxide growth rate for sputtered Cu films followed an inverse logarithmic law at intermediate temperatures. Copper thin film oxidation drastically reduced adhesion.

Atomic mixing at the copper-silicon interface of sputtered films was studied by Ektessabi [94]. When energetic particles are involved in the deposition process such as sputtering, interfacial mixing is caused by ion beam irradiation and by diffusion dominated by thermal and chemical effects. Diffusion is different in the case of thin films and bulk materials: atomic mixing in thin films occurs at lower temperatures. For films under a critical thickness the interdiffusion layer increases linearly with sputtering time. Above the critical thickness there is a square root on time dependence. Due to exposure to the plasma the substrate temperature can rise substantially in the case of sputtering. Since diffusivity increases exponentially with temperature increase, diffusion at room temperature is negligible compared to diffusion at the elevated temperatures. Since silicon has a higher activation energy, copper flow into Si is two-three orders of magnitude higher than that of the

silicon. Atomic mixing increases drastically above 550 °K, it also increases with deposition rate decrease and reduced film thickness [94].

Russel, et al. studied copper adhesion via titanium and chromium underlayers [95]. Both Ti and Cr promoted (111) texture in evaporated Cu films and improved adhesion as deposited. Ti and Cr diffuse through Cu, forming TiO_2 and Cr_2O_3 oxides respectively on the free surface. Adhesion was found to drop sufficiently at 400 °C due to intermetallic compounds forming (CuTi and Cu_3Ti). A chemical nature of adhesion improvement was proposed [95], though Cu and Cr have little mutual solubility and do not form intermetallics. Instead of using pure copper, CuTi and CuCr alloys (up to 15% additives) were also used in the study. Though adhesion was also improved in this case, no resistivity measurements were performed on the samples. Spreitzer with coworkers also studied interfacial reactions of electron beam evaporated Cu films on Ti and Cr underlayers by means of Rutherford Backscattering Spectroscopy (RBS) and Auger Electron Spectroscopy (AES) [96]. Similar results for Cr were observed. Cr migration from the Cr/Cu interface was found to be greater than Ti migration from the Ti/Cu bilayer under the same annealing conditions.

TiN is the most commonly used barrier material for Al metallization in VLSI devices. It also works fairly well in the case of copper provided that Cu does not diffuse into TiN through grain boundaries [92, 97]. Thin TiN film on (100) Si wafers is typically formed of small needlelike grains [97]. TiN <111> grains growth direction is parallel to the Si<111> due to similar atomic arrangements and interatomic distances between TiN(111) and Si(111) planes. It was also found that the TiN layer thickness has no effect on the adhesion of copper films [98]. TiN layer performance varies with its deposition and processing techniques.

Ta and its compounds were found to be very effective also. The problem with Ta is that there is no available CVD process for its deposition. A TiW layer was also found to work fairly well in copper interconnects. It is compatible with infrared-assisted reactive ion etching [99]. Adhesive energies for Cu/TiW and Cu/TiN interfaces were measured by means of the contact angle technique to be 2.2 and 1.8 J/m^2 respectively compared to 0.8 N/m for Cu/SiO2 interface [3]. The fact that Cu lines fabricated by infrared light-assisted RIE did not peel from the substrate as opposed to lines on TiN shows better adhesion on TiW.

The performance of standard Al-based metallization materials used as copper interconnects underlayers is summarized in Table 1 [92].

Table 1. Comparison of underlayer materials for copper interconnects.

Barrier Material	Deposition process	Contact Barrier	Drift Barrier	Adhesion on SiO_2
Ta	PVD	Good	?	Fair-good
TaSi	PVD	?	?	Good
TaN	PVD	Very good	Very good	Good
TaSiN	PVD	Excellent	Excellent	Good
Ti	PVD	Poor	Very good	Very good
TiSi	PVD	?	Very good	Very good
TiN	PVD, CVD	Good-very good	Good-very good	Fair
TiSiN	PVD	Very good	Very good	Good
W	PVD, CVD	Fair	Fair	Fair-very poor
WSi	PVD, CVD	?	?	Very poor
WN	PVD	Very good	Very good	Fair-poor
WSiN	PVD	Very good	Very good	Poor, fair
SiON	CVD	Fair	Fair	Very good
SiN	CVD	Good	Good	Very good

1.3 THIN FILM PROCESSING AND CHARACTERIZATION

There are many different processes to produce thin films. Since the final goal of making copper films here was adhesion evaluation, sputtering was chosen as the primary deposition process. Almost any material can be sputtered at a rapid deposition rate and controlled residual stress level. Unlike evaporation, sputter deposition allows the formation of films under a residual compressive stress [111]. In addition, some Cu films prepared at Motorola were electroplated.

Sputter Deposition

Sputtering is a vacuum process in which inert ions are accelerated from a plasma toward a target to eject atoms, which are to be deposited. After evacuation of the chamber an inert gas (Ar) is introduced and serves as the medium in which a discharge is initiated and sustained. A simplified RF sputtering system schematic is shown in Figure 19. The target is a

plate of the high-purity material to be deposited or the material from which film is synthesized. The target is connected to the power supply, and several kilovolts are applied to it. Atoms travel through the plasma and land on the grounded substrate. Secondary excited electrons accelerate away from the target and ionize inert neutrals, sustaining the glow discharge. They also traverse the plasma and heat the substrate due to their high velocity. Usually 75% of the power supplied to the plasma by the power source is dissipated as heat at the target and only 1% generates sputter atoms, the rest heat the substrate. In RF sputtering electrons in the plasma respond to the radio frequency biasing the target, while the heavy ions don't. Due to capacitive coupling of the target a negative self-bias is generated. Positive ion bombardment sputters away atoms from the target for subsequent deposition. A frequency of 13.56 MHz has been reserved for plasma processing by the Federal Communications Commission.

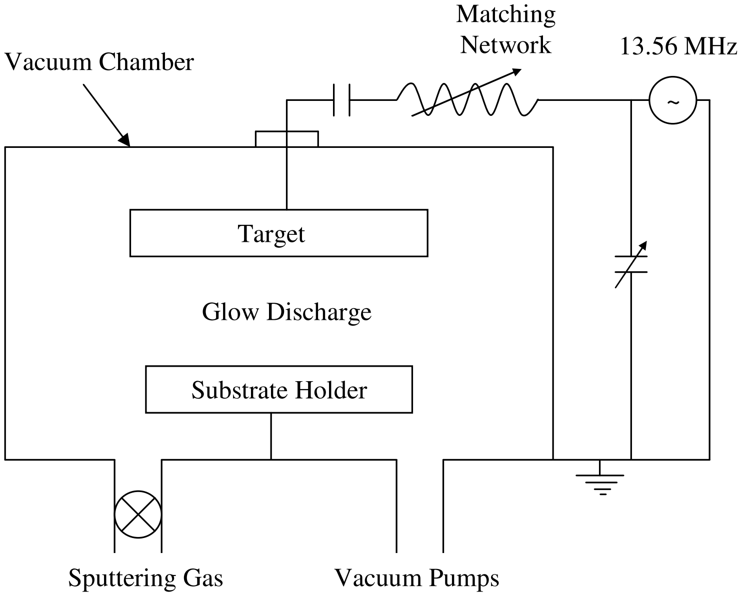

Figure 19. Simplified schematic of RF sputtering system.

Microstructure Of PVD Thin Films

The microstructure of thin PVD (physical vapor deposited) films is highly dependent on the deposition process, as well as on the deposition parameters. Evaporated and sputtered thin films develop similar microstructures. Zone 1 and transition zone (T) structures form as a result of renucleation of grains during deposition and subsequent grain growth. In zone 1 there is high dislocation density, and the internal crystal structure is poorly defined. Zone 2 forms as a result of granular epitaxy and growth, it has columnar structure. In zone 1 grain boundaries are immobile, opposite to zone 2, where grain boundaries are mobile. Zone 3 is characterized by extensive grain growth due to enhanced surface diffusion and porosity decrease (Figure 20).

For sputtering processes inert gas (usually Ar) pressure has to be accounted for. As the gas pressure increases, the zone T temperature range decreases. The microstructure of sputtered films as well as a schematic representation of physical processes are illustrated in Figure 21.

Four mechanisms are involved in the deposition process: shadowing, surface diffusion, bulk diffusion and desorption. Substrate temperature will define which of the mechanisms will prevail. Sputtered films are typically formed at higher temperatures as compared to evaporated films. Shadowing is a mechanism that comes from the geometric constraint imposed by the film roughness and the line-of-sight impingement, forming zone 1 structure. A comparison between zone structures of sputtered and evaporated films is given in Table 2. Thin film grain size typically scales with the film thickness.

One of the advantages of sputtering as compared to evaporation is that it is possible to get residual compressive stresses in sputtered thin films, which is useful in thin films mechanical and adhesion testing. Nanocrystaline sputtered thin films are also typically denser than the evaporated films.

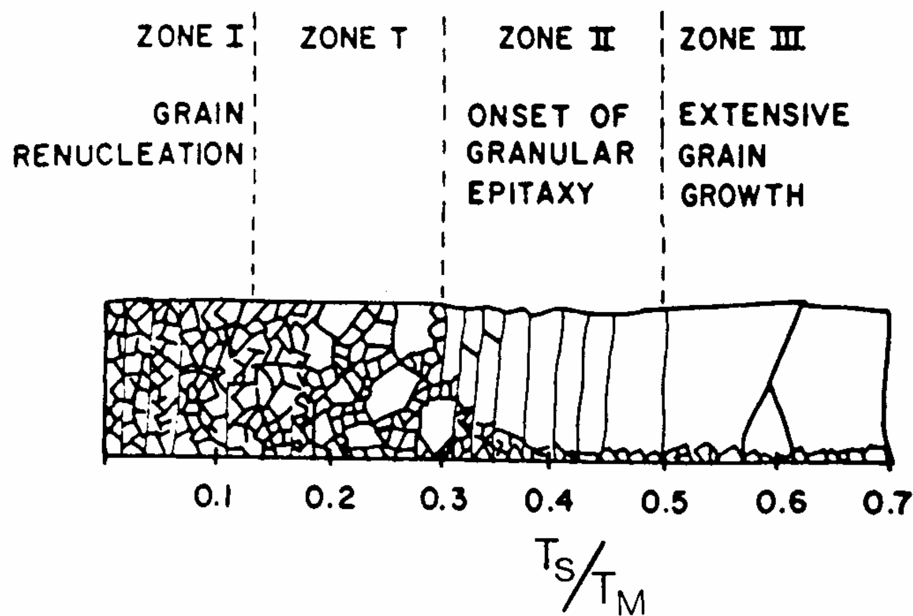

Figure 20. Zone model for thin films. {Schematic reproduced from Hentzell [112]}.

Table 2. Zone structures of evaporated and sputtered coatings [12].

Zone	T_S/T_M	**Structural Characteristics**	*Film Properties*
1 (evaporated)	< 0.3	Tapered crystals, dome tops, voided boundaries.	High dislocation density, hard.
1 (sputtered)	< 0.1 at 0.15 Pa to < 0.5 at 4 Pa	Voided boundaries, fibrous grains. Zone 1 is promoted by substrate roughness and oblique deposition.	Hard.
T (sputtered)	0.1 to 0.4 at 0.15 Pa, ~ 0.4 to 0.5 at 4 Pa	Fibrous grains, dense grain boundary arrays.	High dislocation density, hard, high strength, low ductility.
2 (evaporated)	0.3 to 0.5	Columnar grains, dense grain boundaries.	Hard, low ductility.
2 (sputtered)	0.4 to 0.7		
3 (evaporated)	0.5 to 1.0	Large equiaxed grains, bright surface	Low dislocation density, soft recrystallized grains.
3(sputtered)	0.6-1.0		

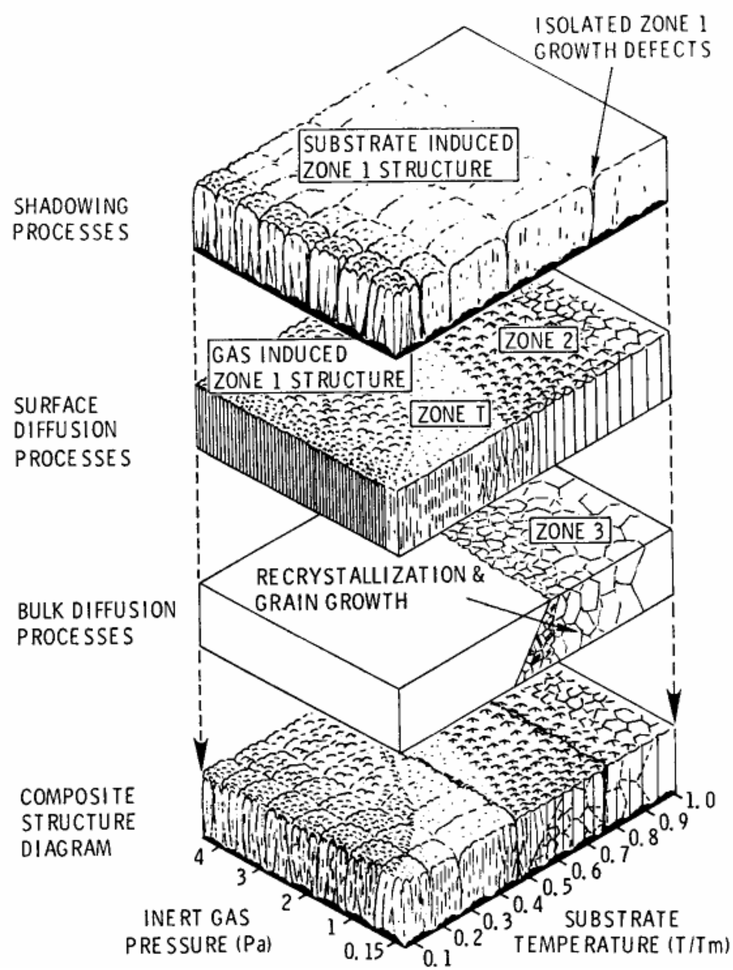

Figure 21. Structural zones and physical processes schematics for sputtering. {Schematic reproduced from Thornton [113]}.

Stresses In Thin Films

Basically, there are four types of stresses in thin films [12, 101, 102, 103] as discussed below:

1) Thermal stresses build up as a consequence of the cooling process after deposition due to the difference in thermal expansion coefficients of the thin film and the substrate. At any temperature, T, thermal stress can be calculated:

$$\sigma_{thermal}(T) = \frac{E_f}{1-\nu_f}(\alpha_f - \alpha_s)\cdot(T_d - T) \qquad (1.55),$$

where E_f is the Young's modulus of the film, ν_f is the Poisson ratio of the film, T_d it the deposition temperature, α_f and α_s are thermal expansion coefficients of the film and the substrate respectively. Whether the film would be in compression or tension (sign of the thermal stress) depends only on the relation between expansion coefficients of the film and the substrate.

The thermal expansion coefficient of $16.6\cdot10^{-6}$ °C^{-1} for copper is relatively small compared to $23.6\cdot10^{-6}$ °C^{-1} for aluminum. The difference in thermal expansion of copper and the silicon substrate ($3\cdot10^{-6}$ °C^{-1}) is smaller, but it is compensated by the higher stiffness of copper. For a given temperature change copper will be under higher tensile stress than aluminum, since the biaxial modulus multiplied by the difference in thermal expansion coefficients is higher in case of copper ($M_{Al}\Delta_{\alpha Si\text{-}Al} = -2.3$ MPa °C^{-1} and $M_{Cu}\Delta_{\alpha Si\text{-}Cu} = -2.6$ MPa °C^{-1}) [105, 106]. The yield stress of Cu is also higher, so residual stresses in copper metallization can reach greater values than for aluminum.

2) "Intrinsic" stresses build up due to solid state reactions like phase transformations or precipitation processes during cooling, associated with a volume change. For a rigid substrate intrinsic stress is given as:

$$\sigma_{int} = -\frac{1}{3}\cdot\frac{E_f}{1-\nu_f}\cdot\sum\Omega_i\cdot c_i \qquad (1.56),$$

where Ω_i is the specific volume change caused by defect i, and c_i is the defect concentration. The effect of interfaces on the intrinsic stresses in polycrystalline thin films is discussed in [104].

3) Epitaxial stresses come from the structural misfit between the nucleated film and the substrate:

$$\sigma_{epitaxial} = \frac{E_f}{1-\nu_f} \cdot \frac{a_f - a_s}{a_s} \quad (1.57),$$

where a_f and a_s are lattice parameters of the film and the substrate respectively.

Since films are thin, the third stress component, the out of plane stress (σ_3) is negligible, and unpassivated films experience a biaxial state of stress ($\sigma_1 = \sigma_2$). Passivated thin films experience a complex triaxial state of stress. The resulting state of stress in a given thin film will depend on the deposition process and parameters.

4) Surface stress evolves with surface modifications and reconstructions:

$$\sigma_{surface} = \frac{\varepsilon_{pl}}{\varepsilon}\gamma + \frac{\varepsilon_{el}}{\varepsilon}\sigma \quad (1.58),$$

where ε, ε_{el} and ε_{pl} are the total, elastic and plastic strains respectively, σ is the elastic stress and γ is the surface energy.

Residual Stress Measurements

The average residual biaxial stresses in the films are calculated from Stoney's equation [114] by means of the wafer curvature technique:

$$\sigma_R = \frac{E_s}{1-\nu_s}\frac{h_s^2}{6h_f R} \quad (1.59),$$

where E_s is the elastic modulus of the substrate, and ν_s is the Poisson's ratio of the substrate, h_s is the substrate thickness, h_f is the film thickness, and R is the radius of curvature of the substrate. The Young's modulus of the film is not required to evaluate the stresses in the film with this method.

The disadvantage of the bow measurement technique is that the whole wafer has to be used for the measurement, and it is not very accurate. Stresses in thin films may vary by 50% throughout the wafer. Usually the film stress is not isotropic, and the substrate curvature varies in different directions, so equation (1.59) takes the following form:

$$\sigma_R = \frac{E_s}{1-\nu_s}\frac{h_s^2}{6h_f R_1}\cdot\left[1+\left[\frac{\nu}{1+\nu}\right]\cdot\left[\frac{R_1}{R_2}-1\right]\right] \quad (1.60),$$

where R_1 and R_2 are the radii of curvature in the x-z and y-z planes respectively. Substrate curvature radii can be measured more accurately with laser deflection and optical lever cantilever beam techniques [115]. This allows constructing a stress map over the whole wafer (Figure 22). This is still a macroscopic average residual stress.

The X-Ray technique is another method for residual stress measurements [12, 105, 117, 118]. It can be applied to continuous as well as patterned films, and provides principal stresses measurements. The drawbacks of this technique are that it can be only used with crystalline materials, and precise measurements are time consuming.

Stress may cause thin film delamination (Figure 23), so stress measurement is a very important part of thin film characterization.

Stress-driven Thin Film Fracture

Tensile residual stress may cause films to crack and debond from the substrate [24, 119, 120]. Thin film fracture or delamination occurs when the crack energy release rate exceeds the interfacial fracture toughness ($G > \Gamma_i$). This behavior is similar to the superlayer test, except that in this case thin film delaminates by itself, which should be avoided. The energy release rate for a crack in the case of delamination can be estimated following [24]:

$$G = Z\frac{\sigma_{res}^2 h}{E} \quad (1.61),$$

where σ_{res} is the residual stress in the film, h is the film thickness and E is the Young's modulus. Z is a dimensionless cracking parameter (Z=1.028 for the crack initiation, Z=0.5 for the steady state). For a given interfacial toughness, residual stress and the film thickness are the two parameters controlling delamination.

Highly compressive residual stress may cause telephone cord delamination through thin film buckling (Figure 23). Thicker films with higher residual compressive stress are more likely to exhibit telephone cord delamination. Mechanics for the compressive stress thin film delamination and buckling is provided in [24]. There are also theoretical attempts to predict pattern formation in the stress-driven thin film failure [121, 122]. High stored elastic

energy in the superlayer due to the high residual compressive stresses is used to promote thin film delamination and buckling in the superlayer indentation test.

Even if the residual stress does not induce thin film fracture and delamination, it may cause other problems such as stress induced electomigration, substrate elastic and even plastic deformation upon its relief. In the real thin film structures residual stress must be minimized in order to avoid these problems. Stress relaxation in Cu thin films is discussed at the end of Chapter 2 of this thesis.

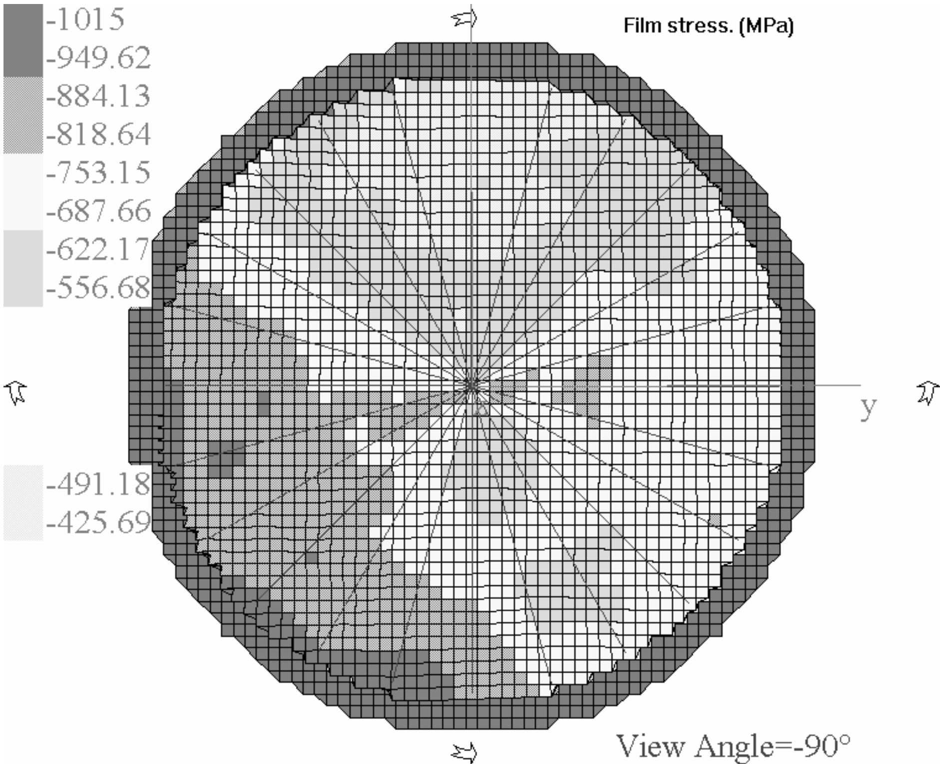

Figure 22. Residual stress map of 1 um W film on a 6” Si wafer.

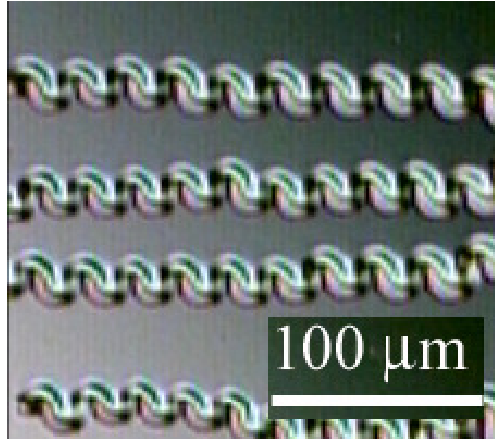

Figure 23. Telephone cord delamination of highly compressed W thin film.

CHAPTER 2. THIN FILM MICROSTRUCTURE AND MECHANICAL PROPERTIES DETERMINATION

2.1 THIN FILM MICROSTRUCTURE

Cu Thin Film Grain Orientation

Cu microstructure is significantly different from aluminum, though both Al and Cu are fcc metals. Aluminum is more3 nearly elastically isotropic, whereas copper exhibits stronger elastic anisotropy. Opposite to Al, which tends to form stable (111) grain orientation, Cu films made by sputtering are usually randomly oriented [123]. Grain orientation in copper films strongly depends on the deposition parameters and on the barrier layer as well [107, 123]. Tracy at al. characterized fiber texture components of copper films [126]. On a Ta underlayer (deposited at 30 °C) three predominant components were observed in sputtered Cu films: (111), (100) and randomly oriented grains. Films deposited at low temperature (30 °C) exhibited predominantly (111) grain orientation. With a temperature increase fiber texture weakened [125], introducing more (100) and randomly oriented grains. On the other hand, for films deposited on a different Ta (100 °C) underlayer, (111) fiber texture strengthened with the deposition temperature. The number of randomly oriented grains tended to decrease as the deposition temperature increased. For films deposited at 100 °C a large number of (200) texture components were found [125].

The fraction of twinned grains decreases with increasing deposition temperature. Twin planes in (111) oriented grains act as a fast diffusion path, lowering electromigration reliability. CVD copper films develop a strong (200) texture, while sputtered copper films develop a very strong (111) texture. CVD (111) textured Cu films could be obtained by using a seed sputtered layer.

Grain growth is usually observed in thin films upon annealing; copper is not an exception [107]. The way copper is different though is that there is (100) abnormal grain growth on Si substrates [123]. Usually abnormal grain growth is associated with surface and interface energy minimization by the elimination of grain boundaries. Grains as large as 10 μm in diameter were observed in copper films on silicon [123]. For fcc metals the theory

predicts the (111) grain orientation for abnormal growth, since these are the planes that are most densely packed. Typical grain orientations for abnormal grain growth in Al are (111), (110) and (112), but not (100) as in copper. Due to copper elastic anisotropy thermal stresses would be different for (111) and (100) orientations. The difference in strain energy density for these two orientations would be:

$$\Delta F_{\varepsilon} = (M_{111} - M_{100})\varepsilon^{2} = 146\varepsilon^{2} \quad GJ / m^{3} \qquad (2.1),$$

assuming isostrain averaging, where ε is the biaxial strain. The driving force is independent of the stress sign. Abnormal grain growth is also observed in electroplated Cu films, but at room temperature, and is considered to be a self-anneal process.

One of the ways to separate thermal and strain effects is to deposit copper films on different substrates. Here, Al, Cu and Si substrates would induce compressive, neutral and tensile stresses in a copper film. Upon heating a Cu film on Si was under compressive stress [123]. The film had a predominant (100) grain orientation. A copper film on an Al substrate supported a tensile stress upon heating. The film responded elastically until the yield point was reached at 100 °C. Abnormal (100) grain growth was observed. As was expected, a copper film on a copper substrate showed no thermal strain upon heating. Film structure was predominantly random oriented with a big portion of (111) grains. Abnormal grain growth was observed in annealed films on Al and Si substrates, but not on a Cu substrate. A larger degree of (100) grain transformation was observed on an Al substrate versus a Si substrate. On an Al substrate, tensile stresses generated by film growth are of the same sign as the thermal stresses, which increases the driving force to its maximum level, limited by plasticity.

Cu Thin Film Grain Size

It is important to measure thin film grain size, since it affects the mechanical properties, specifically yield stress. In the case of a sputtered nanocrystalline thin Cu film its grain size can be measured by means of Atomic Force Microscopy (AFM), where grains evolve on the surface (Figure 24). Measurements from the AFM section analysis provide the average grain size. For example, the average grain size of a 200 nm thick sputter deposited Cu film is about 110 nm. Grain size does not seem to increase much with the film thickness

(Figure 26). Individual grains are better distinguished on the deflection AFM image (Figure 26). Due to the higher surface roughness of thicker films, this technique does not work very well for sputtered films over 1 um thick. This can be resolved with SEM (Figure 25). The same applies to the annealed and electroplated films.

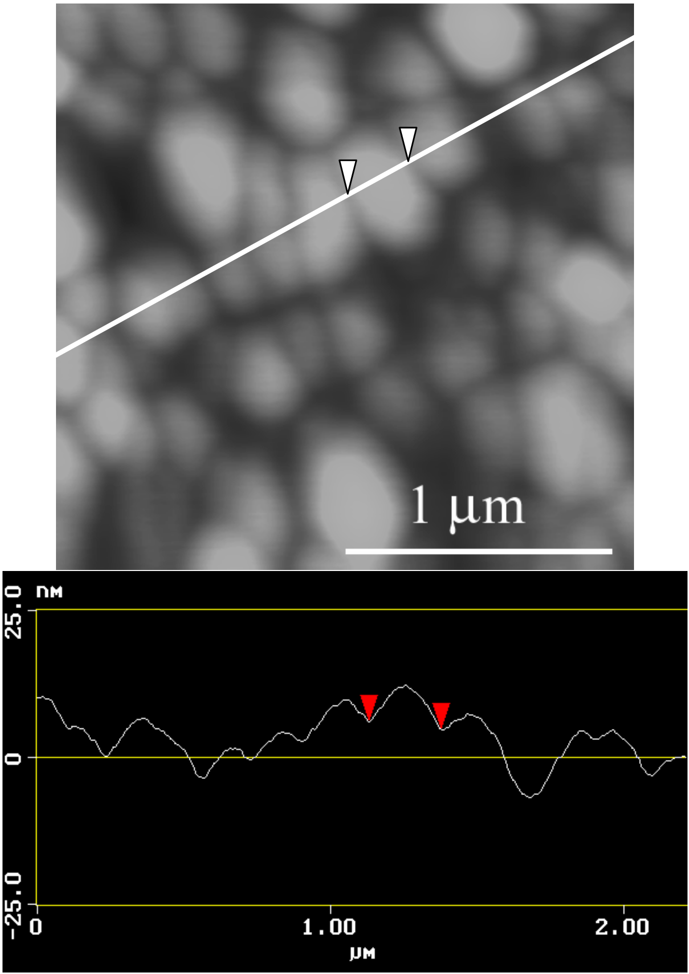

Figure 24. AFM height image of a 200 nm thick sputtered Cu film with a cross-section, showing grain size measurement. {taken by N.I. Tymiak}

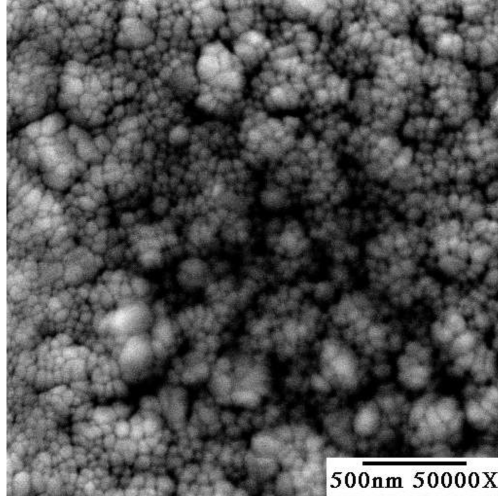

Figure 25. SEM micrograph of a 3 um thick Cu film on Ti. {taken by N.I. Tymiak}

Surfaces of a 200 nm and 2 um thick electroplated Cu films annealed in vacuum at 350 °C for thee minutes are shown in Figure 27. Grains about 350 nm in diameter are distinguishable in a 200 nm thick Cu film; they are covered with smaller oxide particles.

For the 2 um thick Cu films the grains are barely distinguishable even when the section analysis is used due to the higher surface roughness and oxide particle dispersion. Annealing causes grain coalescence through the film thickness, but not necessarily surface reconstruction that would replicate the new bigger grain size. Focused Ion Beam machining (FIB) is a more suitable technique for allowing measurement of the thin film grain size. It is similar to the Scanning Electron Microscopy (SEM), except instead of the electron beam, a focused ion beam is used to raster along the sample surface. FIB can also be used to clean the surface from an oxide by sputtering the film material away. The image is constructed by collecting secondary electrons, which produce a certain contrast according to the grains orientation. FIB images of electroplated Cu films of four thicknesses are presented in Figure 28. It is clearly seen that the grain size increases with the film thickness. The sample is tilted 45° to the ion beam, so all grains appear elongated along the x axis. Grain size can be directly measured off the images in Figure 28. In this particular electroplated sample, AFM would have provided an underestimated value for the grain size compared to FIB.

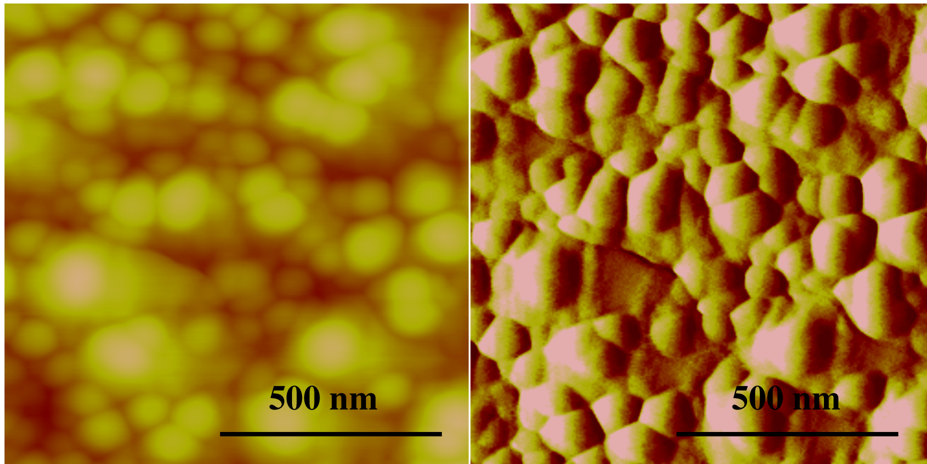

Figure 26. Height and deflection AFM images of sputter deposited 500 nm thick Cu film [143].

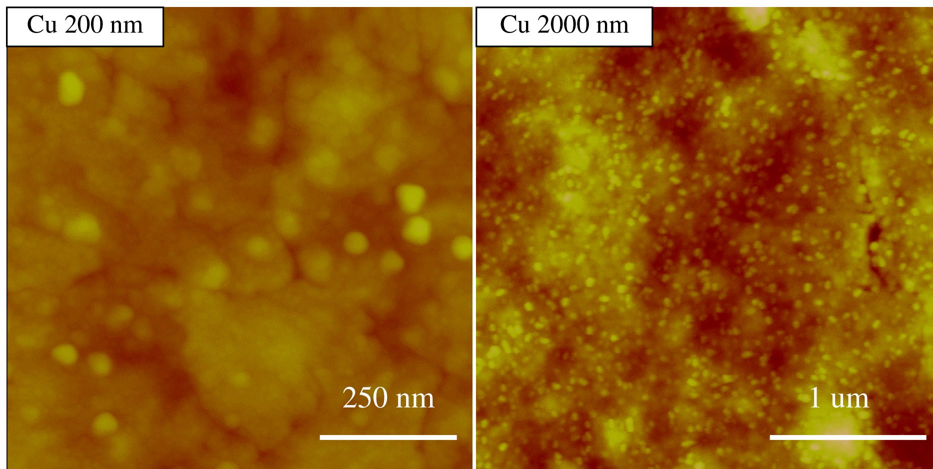

Figure 27. AFM images of electroplated Cu films (100 nm Z range).

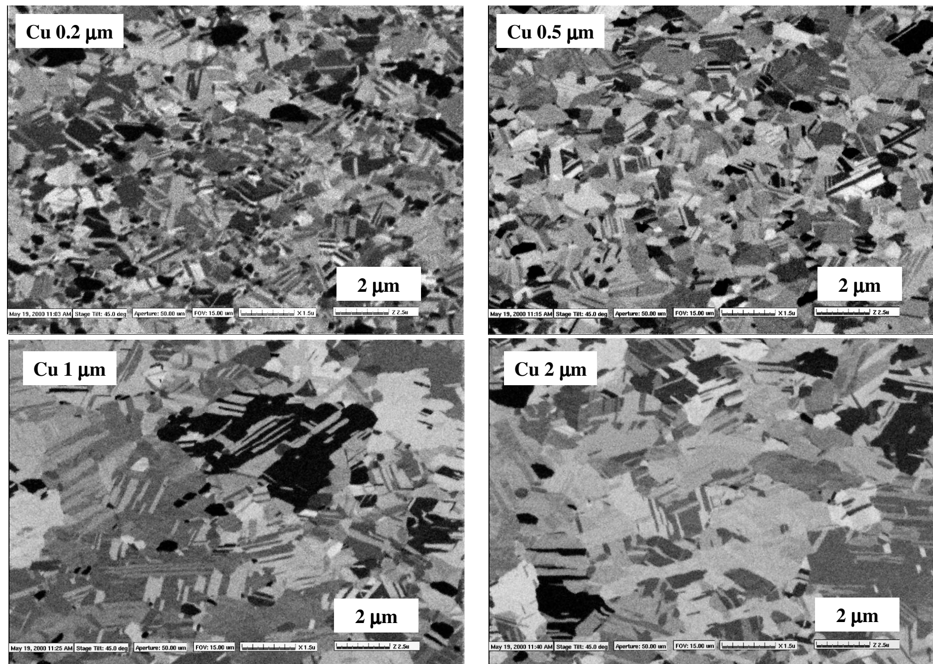

Figure 28. Focused Ion Beam images of electroplated Cu films of different thickness (45° tilt).

2.2 THIN FILM MECHANICAL PROPERTIES

For most of the adhesion tests, knowledge of the thin film constitutive mechanical behavior is required. In Chapter 1 almost every expression for the strain energy release rate has the thin film elastic modulus. The modulus can be measured by the microbeam cantilever deflection technique [127-129], but the easiest way is by means of nanoindentation, since no special sample preparation is required and the same technique can be used for measuring film adhesion. In addition, the yield strength is usually necessary as well, which will be addressed subsequently.

Nanoindentation For Thin Film Mechanical Properties Determination

Nanoindentation is similar to conventional hardness tests, but is performed on a much smaller scale using special equipment. The force required to press a sharp diamond indenter

into tested material is recorded as a function of indentation depth. Since the depth resolution is on the order of nanometers, it is possible to indent even very thin films. The nanoindentation load-displacement curve, similar to one shown in Figure 10 provides a "mechanical fingerprint" of the material's response to contact deformation. Elastic modulus and hardness are the two parameters that can be readily extracted from the nanoindentation curve. Doerner and Nix [130] suggested that a linear fit to the upper 1/3 of the unloading portion of the indentation curve could be used to determine film stiffness $S = dP/dh$, from which the elastic modulus could be calculated for a cylindrical punch:

$$\frac{dP}{dh} = \frac{2}{\sqrt{\pi}}\sqrt{A}\frac{E_r}{1-\nu^2} \quad (2.2),$$

where A is the contact area and E_r is the reduced modulus. Since the indenter itself has finite elastic constants, its deformation contributes to the measured displacement. Reduced modulus E_r is expressed as:

$$\frac{1}{E_r} = \frac{1-\nu^2}{E} + \frac{1-\nu_{ind}^2}{E_{ind}} \quad (2.3),$$

where E and ν, E_{ind} and ν_{ind} are the elastic moduli and the Poisson's ratios of the tested film and the indenter respectively. The technique could be extended for different indenter geometries [131]:

$$\frac{dP}{dh} = \beta\frac{2}{\sqrt{\pi}}\sqrt{A}E_r \quad (2.4).$$

Here, β is the constant for tip geometry. King calculated β values for different tip geometries using final element analysis [132]. Oliver and Pharr have refined the method by using the power law instead of the linear fit into the unloading slope of the load-displacement curve [34].

Hardness H, a material's resistance to plastic deformation is defined as:

$$H = \frac{P_{max}}{A} \quad (2.5),$$

where A is the projected area of contact (a function of the indentation depth) at the maximum load P_{max}. The tip calibration procedure includes an area function determination [34]. In order to avoid substrate effects on the measured mechanical properties, theoretically a film should be indented only up to about 10% of its thickness, which is almost impossible to

achieve on very thin films (< 0.1 μm). There is a large influence of the residual stress and substrate effects that are hard to account for in the analysis [133, 134]. Indentation curve analysis has been extended in the past few years with new FEM-based models being developed [135, 136].

Nanoindentation Apparatus

There are four different indentation devices that have been used in this study: IBM Continuous Microindenter (Micromechanical Tester - MMT) [137], Nanoindenter II™ and Nanoindenter XP™ from Nanoinstruments, and the Hysitron Triboscope from Hysitron Inc. Though the actual configuration differs from one piece of equipment to another, the principle of operation is similar. In the indentation device (Figure 29) the XYZ stage provides coarse sample movement in three dimensions with sub-micron resolution. After the indenter tip is placed in position close to the sample surface, the actuator drives the tip into the sample. For the MMT a piezo acts as an actuator, for the Hysitron a capacitor performs this function, and an electromagnet drives the tip in the Nanoindenter. All indenters can be programmed to perform indents in the standalone regime, without the operator.

In all devices the displacements are measured by means of capacitance probes. The load during indentation is calculated by measuring the displacement and multiplying it by spring constants of springs, supporting the load cell. Load and displacement are recorded continuously by a computer-based data acquisition system. Comparison of different indenters in terms of the load and displacement range is presented in Figure 30.

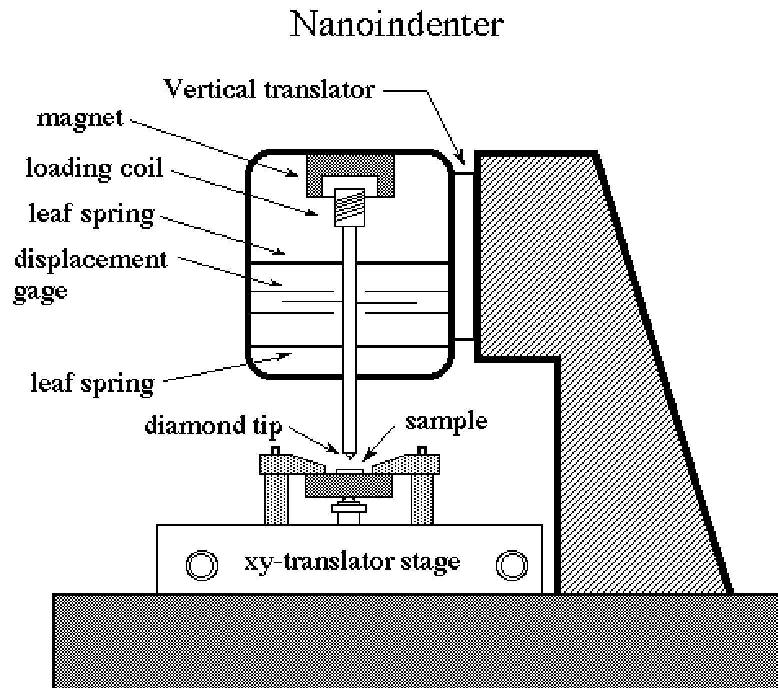

Figure 29. Nanoindenter schematic.

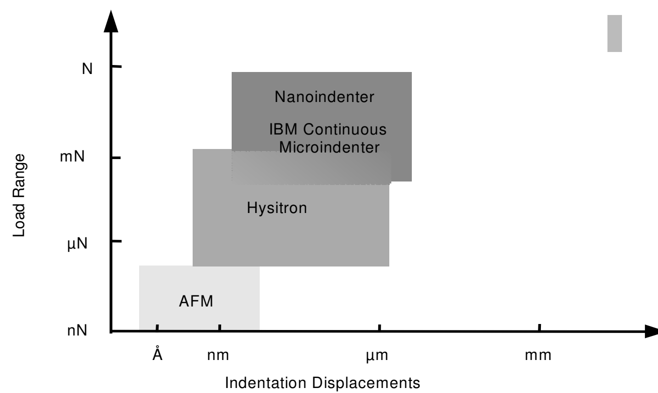

Figure 30. Comparison of indentation instruments.

The MMT and the Nanoindenter have very similar characteristics, except that the Nanoindenter has a continuous stiffness modulation (CSM) option, which allows tip oscillation while indentation is performed. This allows extracting the elastic modulus and hardness at any point of the load-displacement curve. One indentation experiment provides modulus and hardness data as a function of the indentation depth.

The Hysitron Triboscope is a slightly more sensitive device; when attached to an AFM, it allows scanning the surface of the sample with the indenter tip before and after indentation. Surface scanning before the indent helps to select smooth areas for indentation, avoid asperities and microstructural defects on the surface. Post-test scanning allows measuring the extent of plastic pileup around indentation and detecting microcracks and film spallations. However, the maximum indentation load is limited to 50 mN, so this device cannot be efficiently used for thin film delamination experiments for adhesion measurements.

Thin Film Yield Stress

Since there is a contribution of the plastic energy to the fracture process, the maximum amount of this energy would be limited by the film yield stress. In the case of a thin film, the yield stress is typically much higher than for a bulk material. Since thin films are typically nanocrystalline, this is explained by the Hall-Petch type relationship between the film yield stress and its grain size, *d*:

$$\sigma_{YS} = \sigma_i + kd^{-n} \qquad (2.6),$$

where σ_i is some intrinsic stress, independent of the grain size *d*, and *n* is typically between 0.5 and 1. The classic $1/d^{0.5}$ Hall-Petch relationship is not typically observed for thin films due to the substrate effect, limiting thin film plasticity, or due to the dislocation looping along the metal/oxide interface [108]. Similar effects are observed in different nanocrystalline bulk materials and thin films [138, 139]. Since the grain size of a thin film scales with the film thickness, *h*, it can be used instead of the grain size as the scaling parameter [140]:

$$\sigma_{YS} = \alpha\left[1 + \beta h^{-1/2}\right] \qquad (2.7),$$

where α and β are the fitting parameters, and are 400 MPa and 0.287 $\mu m^{-1/2}$ for evaporated Cu films, and 200 MPa and 0.862 $\mu m^{-1/2}$ for diffusion bonded films respectively [140]. Similar approach, based on the film thickness is used by Nix [108] to predict Cu flow stress behavior (equation (2.12)).

For a metal film the yield stress can be taken as the 1/3 of the hardness [141] measured by nanoindentation, or more accurately it can be extracted from the extent of the plastic zone size around the indenter, *c*, measured by AFM (Figure 34) [142]:

$$\sigma_{YS} = \frac{3P_{max}}{2\pi c^2} \qquad (2.8),$$

where P_{max} is the maximum indentation load.

Sputter Deposited Cu Thin Film Mechanical Properties

Tests for measuring sputtered Cu films modulus and yield stress were carried out with the Hysitron nanoindenter [143], A conical 90° indenter with an approximately 400 nm tip radius has been used. Young's modulus and hardness were calculated with the Oliver and Pharr method [34]. An average modulus of 120 GPa has been measured for sputtered Cu films. The yield stress has been estimated as 1/3 of hardness values and evaluated independently from the cross-sectional analysis of the plastic zone radii, using equation (2.8). Only tests at a penetration depth sufficient to neglect roughness effects were used for the analysis. For films from 200 to 500 nm, depths exceeding 1/10 of film thicknesses were required. Substrate effects were apparent for a 200 nm film, as shown in Figure 31, where the measured hardness increases from 3.3 to 4.6 GPa as the penetration depth increased from 50 to 130 nm. Correction for this was accomplished with the Bhattacharya and Nix's method [144]:

$$H_{corrected} = H_s + \left(H_f - H_s\right) exp\left[\frac{\sigma_f E_s}{\sigma_s E_f}\left(\frac{\delta}{h}\right)^2\right] \quad (2.9),$$

where σ_s and σ_f are the yield stresses of the substrate and film respectively, δ is the indentation depth and h is the film thickness. The analysis does not account for material pileup. The hardness ratio H_f/H_s was determined to provide the best fit to the $H_{mesured}/H_{substrate}$ vs. depth/film thickness dependence as shown in Figure 32. Here, the substrate hardness was taken as the hardness of thermally grown SiO_2, 8.1 GPa, determined from indentation into the oxidized Si wafers used for Cu deposition.

Grain sizes estimated with the AFM are presented in Table 3. From this data, it is evident that grain size scales with the film thickness only up to about 200 nm thick films. Grain size estimates from AFM images become less reliable for the films thicker than 500 nm due to increasing surface roughness. FIB measurements could possibly be a better choice in this range. Yield stress vs. grain size dependence for sputter deposited Cu films is shown in Figure 33. It appears that the 1/d dependence provides a slightly better fit for the data compared to the $1/d^{0.5}$ dependence.

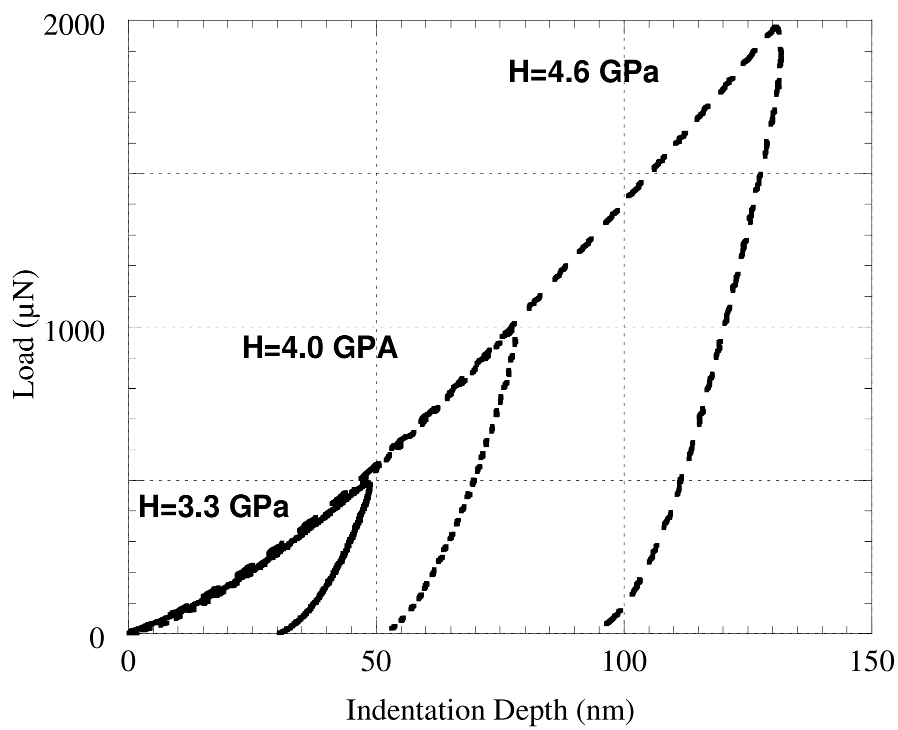

Figure 31. Indentation curves for a 200 nm Cu film.

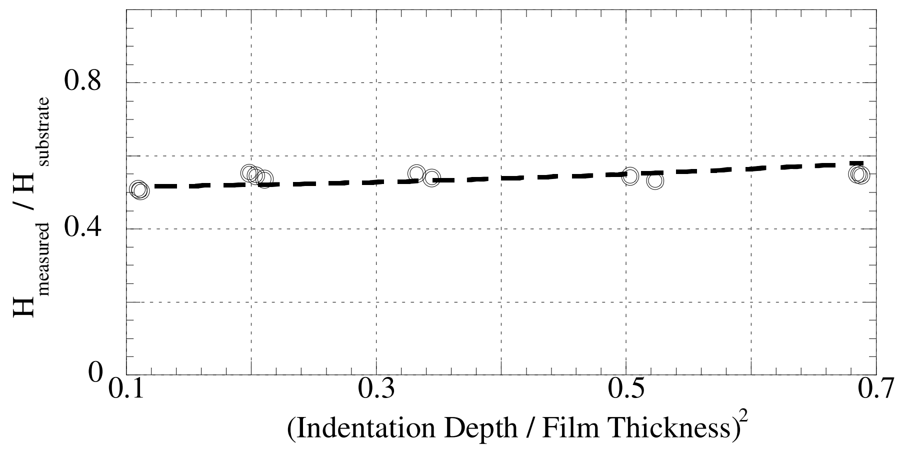

Figure 32. Substrate effect correction. Cu film hardness, H_f is determined from the best fit to the experimental data.

Table 3. Sputtered Cu film grain size and yield stress.

Sputtered Cu Film Thickness, nm	Cu Film Grain Size, nm	Cu Film Yield Stress, GPa
181	110	1.37
505	130	0.89
1056	150	0.84
1930	180	0.8

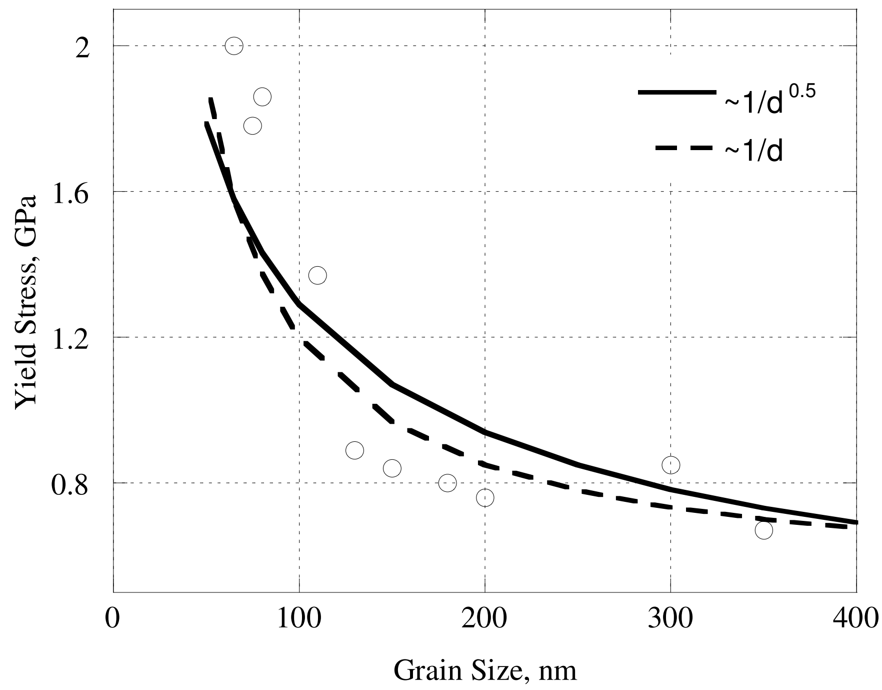

Figure 33. Yield stress dependence on the grain size for sputtered Cu films.

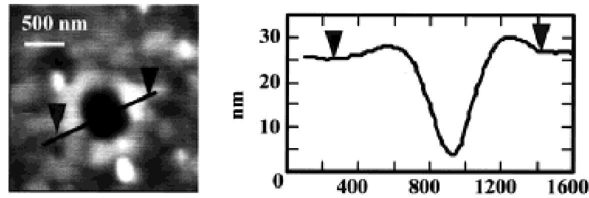

Figure 34. Plastic zone size evaluation for yield stress determination. An AFM image of an indent into a 200 nm Cu film with a corresponding cross-sectional analysis [146].

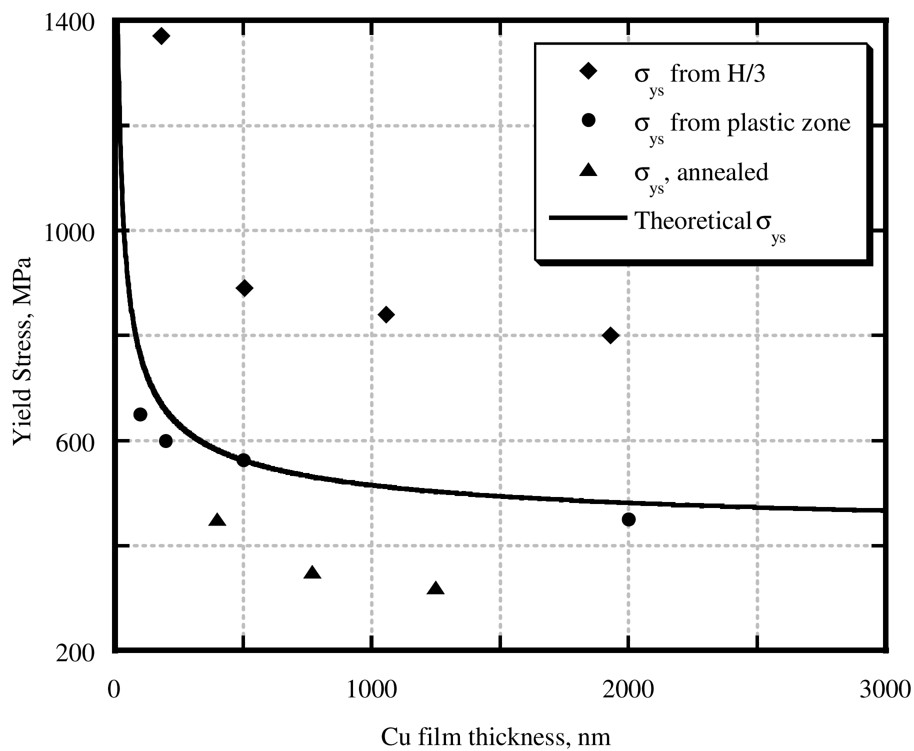

Figure 35. Cu film yield stress based on the hardness and plastic zone size measurements along with theoretical predictions. Annealed Cu data is taken from [106].

Even after a substrate correction, the Cu films yield stress values appeared elevated compared to the predictions from equation (2.7) (Figure 35). For this reason, a more precise plastic zone size measurement technique, based on equation (2.8) has also been used to estimate Cu films yield stresses. The inverse method, described in the previous section, is based on the plastic pile-up measurement around indentation. An AFM image of an indent into a 200 nm thick Cu film is shown in Figure 34 along with the extent of pile-up at the surface obtained from the cross-sectional analysis. The results of these measurements are compared with the previously obtained yield stress data from hardness and with annealed Cu films yield stress [106] in Figure 35. The Cu yield stress data obtained by the inverse method is comparable to the Wei and Hutchinson [140] theoretical predictions, given by equation (2.7). These measurements are intermediate to values approximated from hardness (H/3) and annealed Cu values reported by Vinci et al [106].

Electroplated Cu Thin Film Mechanical Properties

Electroplated Cu film mechanical properties were evaluated with the Nanoindenter XP^{TM}, using a sharp (< 100 nm tip radius) Berkovich tip and the continuous stiffness modulation (CSM) option. Modulus and hardness data for electroplated Cu films of different thickness is presented in Figure 37. Unlike the sputtered Cu films, where the modulus is independent of thin film thickness, the elastic modulus drops from about 133 GPa for a 200 nm thick film down to 110 GPa for a 2 um thick Cu film.

Theoretically, the elastic modulus should not be affected by the film grain size or thickness. In this case the modulus reduction can be partially explained by the fact that thicker films are less dense, so a lower modulus reading may be expected. Compared to sputtered Cu films, the surface roughness increases significantly with the film thickness (Figure 27), which affects the contact area determination in the indentation analysis. The effect of surface roughness on thin films modulus measurements by nanoindentation is discussed in [145].

The yield stress of electroplated Cu was calculated from hardness, measured as a function of indentation depth with the CSM option of the Nanoindenter XP^{TM} (Figure 36). At

low indentation depths a 200 nm thick Cu film appears to be hard due to a surface oxide and/or indentation size effect [184]. The hardness stabilizes at 1.7 GPa at a depth of 20 nm for a 200 nm thick film, exactly 10% of the film thickness. At a depth of 40 nm the tip starts to sense the hard Si substrate, with the hardness elevating accordingly. For each indent the curve minimum (e.g. Figure 36) at 10% indentation depth was taken as the measure of the thin film hardness. Since electroplated Cu films have been annealed during processing, and the grain size is larger compared to the sputtered films, electroplated Cu films appear to be more ductile.

As expected, similar to sputtered Cu films, the yield stress (taken as 1/3 of the hardness) drops with an increase in film thickness (Figure 37). The grain size of electroplated Cu was measured using FIB (Figure 28). The yield stress of electroplated Cu films follows the classical Hall-Petch relationship $\sigma_{YS} = \sigma_i + kd^{-1/2}$ (Figure 39), so for electroplated annealed Cu films the following dependence of yield stress on grain size may be used (Figure 40):

$$\sigma_{YS} = 180MPa + 0.262d^{-1/2} \quad (2.10),$$

where d is the thin film grain size in microns.

Also, the Wei and Hutchinson approach [140] can be used for these films to fit the yield stress data using the film thickness (Figure 41), following equation (2.7):

$$\sigma_{YS} = 230MPa\left[1 + 0.577 \cdot h^{-\frac{1}{2}}\right] \quad (2.11),$$

where h is the thin film thickness in microns. The fitting parameters are close to those for diffusion bonded Cu films [140], which also demonstrates that electroplated films are more ductile compared to sputtered or evaporated Cu films.

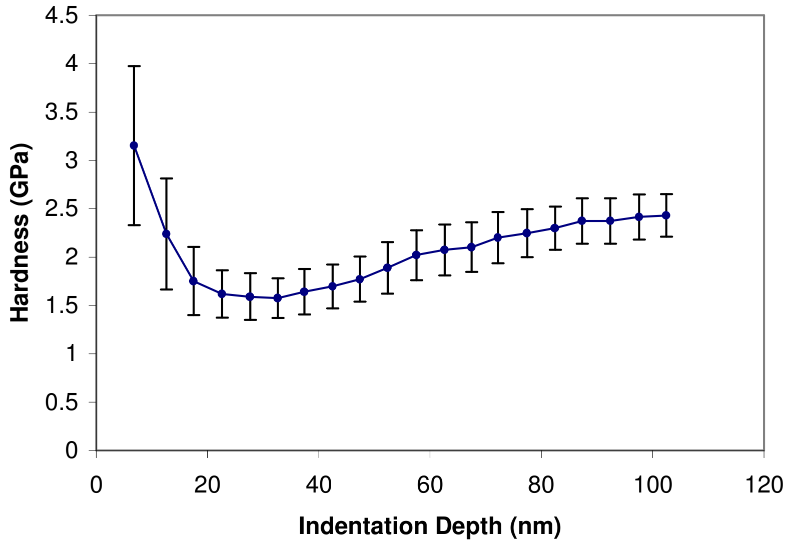

Figure 36. Electroplated 200 nm Cu film hardness as a function of the indentation depth.

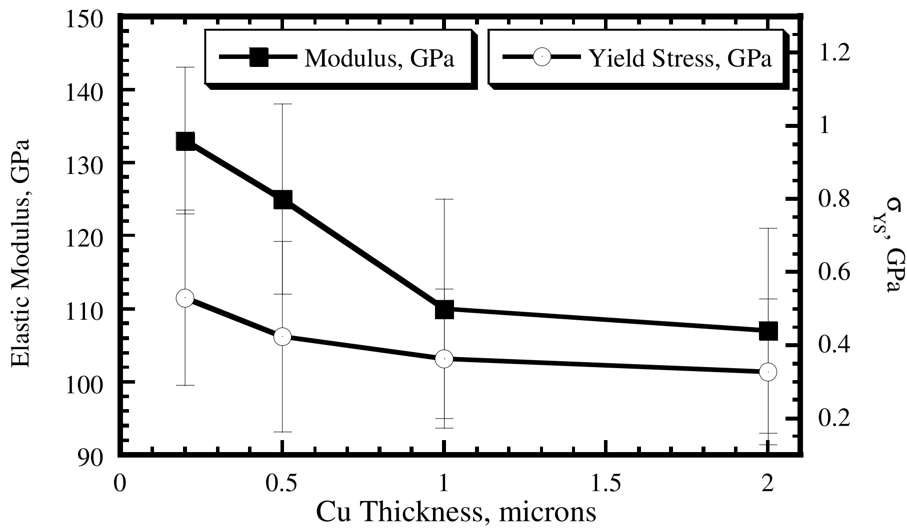

Figure 37. Electroplated Cu elastic modulus and yield stress as a function of film thickness.

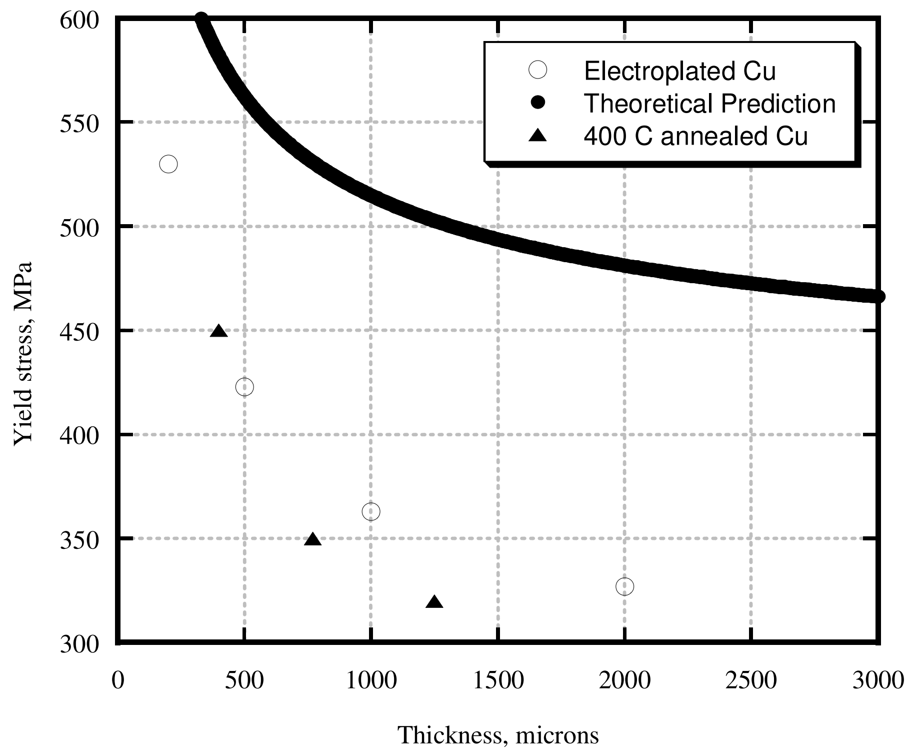

Figure 38. Electroplated Cu yield stress compared to the annealed Cu yield stress from [106] and theoretical prediction from equation (2.7).

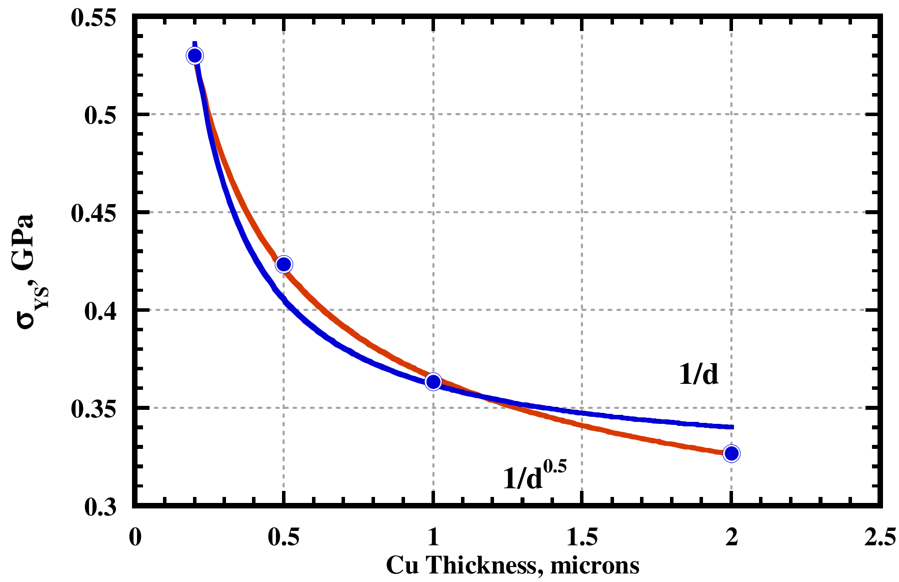

Figure 39. Electroplated Cu yield stress as a function of grain size.

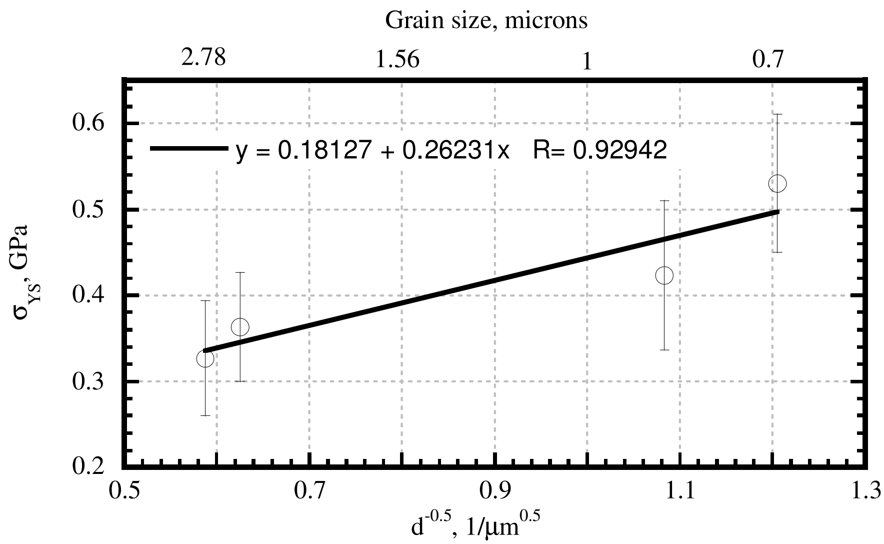

Figure 40. Cu yield stress fit using classical Hall-Petch relationship.

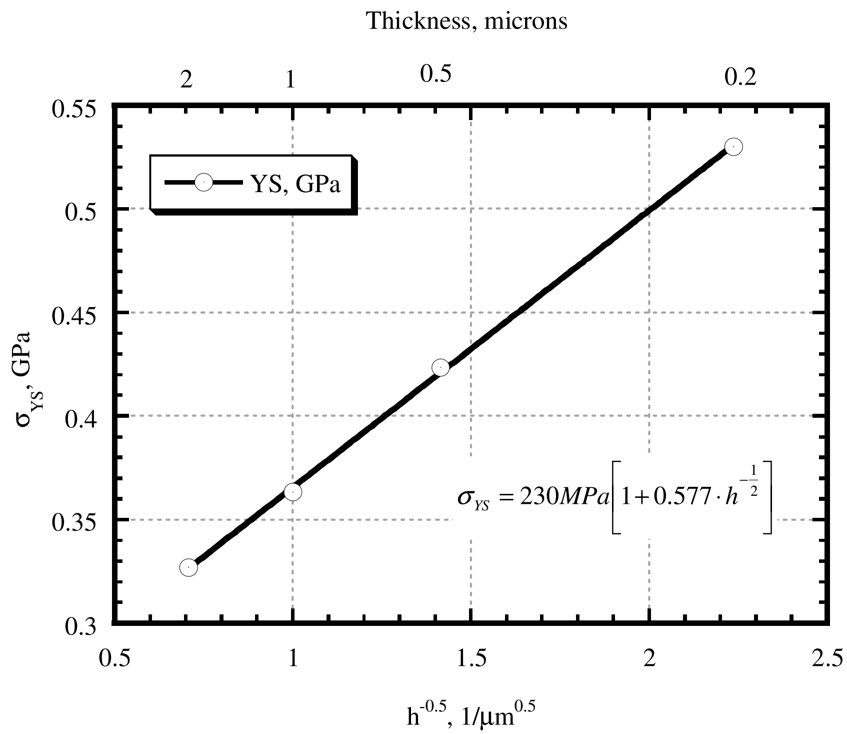

Figure 41. Cu yield stress fit using film thickness.

Stress Relaxation In Copper Thin Films

An inverse relationship between film thickness and flow stress has been observed in metallic films, including copper thin films [107]. There are several explanations to this phenomenon. One of the models, proposed by Nix [108] considers the stress necessary for dislocation glide in surface/film/substrate system:

$$\sigma_{flow} = \frac{sin\phi}{cos\phi\, cos\lambda} \frac{b}{2\pi(1-\nu)h} \left(\frac{\mu_f \mu_s}{\mu_f + \mu_s} ln\left(\frac{\beta_s h}{b}\right) + \frac{\mu_f \mu_0}{\mu_f + \mu_0} ln\left(\frac{\beta_0 t}{b}\right) \right) \quad (2.12),$$

where b is the Burgers vector, h is the film thickness, t is the oxide thickness, μ_f, μ_s and μ_0 are the elastic shear moduli of a film, substrate and oxide layer respectively, β_s and β_0 are constants. Flow stresses in thin films can exceed those in bulk materials by an order of magnitude due to the constraint on the dislocation motion from the film/substrate interface.

Unlike Al, in the case of Cu, there is no tight natural oxide layer on the surface of the film contributing to the dislocation glide, so the last term in the equation could be omitted for an unpassivated Cu film. Note that there is a resolved shear stress term where ϕ is the angle between the film normal and the glide plane normal, and λ is the angle between the film normal and the Burgers vector. These angles depend on the film orientation. The factor $cos\phi\, cos\lambda$ is called the Schmid factor; it determines the shear stress necessary for a dislocation to move on a certain glide plane. The $sin\phi$ term gives the length of the moving dislocation when divided by the film thickness. As this model is mostly athermal, it is not suitable for determining stresses in films upon changing temperature. It also does not account for strengthening mechanisms.

Since thin films usually have fine grain microstructure, grain size strengthening can be applied in the form of the Hall-Petch relation at low temperatures. Thompson enhanced the Nix model by adding grain size strengthening [109]:

$$\sigma_{total} = \frac{sin\phi}{cos\phi\, cos\lambda} \frac{b\mu_f}{4\pi(1-\nu)} ln\left(\frac{d}{b}\right)\left(\frac{2}{d\, sin\phi} + \frac{1}{h}\right) \quad (2.13),$$

There are several stress relaxation mechanisms in thin films that operate simultaneously and are difficult to de-convolute. These mechanisms include, but are not limited to, diffusion creep, dislocation climb, and dislocation glide. Thouless, et al. modified the Frost-Ashby deformation map and used copper bulk properties to predict relaxation

behavior of 1 μm thin copper films (Figure 42) [147]. Here, the film thickness and grain size were introduced into classical equations.

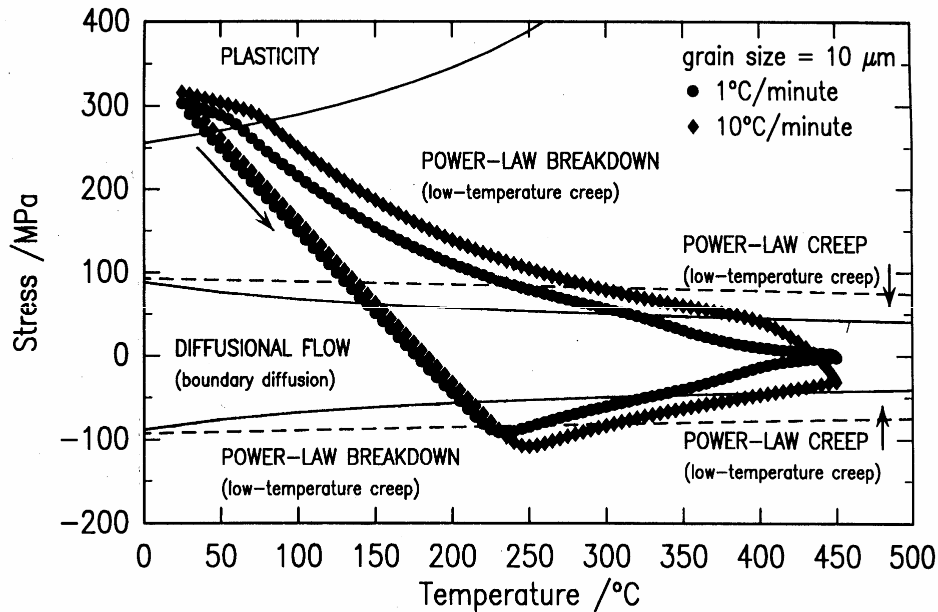

Figure 42. Temperature cycling of 1 μm copper film on silicon. {Schematic after M.D. Thouless}.

Vinci, et al. used the Thouless equations with physical constants for copper thin films [106]:

a) Grain boundary diffusion:

$$\dot{\varepsilon} = \frac{1.282\times10^{-20}\sigma}{Tdh^2} exp\left(\frac{-1.251\times10^4}{T}\right) \quad (2.14);$$

b) Lattice diffusion:

$$\dot{\varepsilon} = \frac{5.127\times10^{-11}\sigma}{Tdh^2} exp\left(\frac{-2.369\times10^4}{T}\right) \quad (2.15);$$

c) Low-temperature plasticity:

$$\dot{\varepsilon} = 5.774\times10^5 \, exp\left[\left(\frac{-2.557\times10^4}{T}\right)(1-2.177\times10^{-9}\sigma)\right] \quad (2.16);$$

d) Power-law breakdown:

$$\dot{\varepsilon} = 46.16\left(\frac{\mu}{T}\right)\left[sinh\left(\frac{458.4\sigma}{\mu}\right)\right]^{5} exp\left(\frac{-2.369\times10^{4}}{T}\right) \quad (2.17);$$

e) Power-law creep:

$$\dot{\varepsilon} = 117.4\left(\frac{\mu}{T}\right)\left(\frac{\sigma}{\mu}\right)^{2}\left[sinh\left(\frac{458.4\sigma}{\mu}\right)\right]^{5} exp\left(\frac{-1.407\times10^{4}}{T}\right) \quad (2.18),$$

where $\dot{\varepsilon}$ is the strain rate, T is the temperature, d is the average grain size, h is film thickness, μ is the shear modulus. These equations could be applied for both tension and compression.

Film thickness was found to have an influence on the strength of copper thin films, since there is dependence between the film thickness and the grain size. The grain size was approximately the same as the film thickness for thin copper films (up to 1 μm) [106].

Films behave differently in the presence of a capping layer. Stresses in thin films are independent of the stresses in the adjacent layers, though the interface created by the capping layer affects deformation processes. Grain growth, diffusional creep and dislocation processes are usually impeded by the capping layer; it changes the microstructure and mechanical properties of Cu films. Unlike unpassivated copper films, there is no thickness dependence of the stress in passivated (capped) films [148]. Since copper is elastically anisotropic and perfectly textured films are difficult to fabricate, there is a significant influence of film texture on the reliability of copper interconnects.

CHAPTER 3. PLASTICITY EFFECT ON Cu THIN FILM ADHESION

For a ductile film such as Cu or Al, one may expect high plastic energy dissipation at the crack tip that would contribute to the practical work of adhesion (U_f term in equation (1.5)). Since the film yield stress decreases with increasing film thickness, a higher amount of plastic dissipation is expected during crack propagation in thicker films. This is due to the larger available plastic volume with larger thickness, as well as the effect of larger plastic zones being possible at lower yield stresses. It has been experimentally observed that thicker ductile metallic films exhibit better adhesion properties [140, 143, 149-154]. Evaluation of the plasticity effects in the measurement of the interfacial toughness with increasing film thickness would require the following:

1. Establishing a theoretical dependence between film thickness and plastic energy dissipation;
2. Experimental evaluation of thickness effects for a broad range of Cu interlayer thicknesses with a comparison to theoretical predictions;
3. Extraction of a true interfacial toughness from the experimental data;
4. Assessment of mode mixity as a function of film thickness;
5. Evaluation of the constitutive properties of nanostructured Cu layers necessary for the analysis of the plasticity effects.

3.1 THEORETICAL CONSIDERATION

Upper Bound Plastic Strip Model

There is always a plastic zone ahead of the crack tip, even in brittle materials, which undergo cleavage fracture [9]. An upper bound model estimates the plastic energy dissipation at the interfacial crack tip by assuming the plastic zone extends through the film thickness. Analysis of scratch tests [155] on Pt and Ti films suggested that over a range of film thicknesses, the whole thickness of metal was plastically deforming during delamination. Even taking into account the difference in the stress-strain states involved during scratch and

indentation, assuming that the plastic zone size is equal to the film thickness appears to be a reasonable first order estimate, at least for an upper bound.

The model is based on the following assumptions:

1) Elastic-perfectly plastic material (no hardening);
2) No plastic deformation in either the substrate or the superlayer;
3) Plastic energy dissipation rate is independent of the crack length;
4) The average stress is equal to the yield stress of the film;
5) The plastic zone only extends to the film/superlayer interface;
6) A burgers vector, *b*, as a cut-off.

The amount of energy dissipated in a plastic strip can be expressed as:

$$U_f = \int \sigma d\varepsilon \cdot dV \quad (3.1).$$

Work per unit fracture area can then be determined as follows, taking this to be equal to the resistance and equivalent to G at crack extension.

$$G = \frac{dU_f}{dA} = \frac{\int \sigma d\varepsilon \cdot dV}{dA} = h\int \sigma d\varepsilon \approx h\overline{\sigma\varepsilon} = h\overline{\sigma}\frac{1}{h-b}\int_b^h \varepsilon(h)dr \quad (3.2).$$

Here, h is the film thickness; $\overline{\sigma} = \sigma_{ys}$, the average stress; $\overline{\varepsilon}$, the average strain; $\varepsilon(h,r)$, the plastic strain at the distance r from the crack tip [156]:

$$\varepsilon(h,r) = \frac{\sigma_{ys}}{E} \cdot \left(\frac{h}{r} - 1\right) \quad (3.3).$$

This relationship had been originally derived for the mode III fracture, using the shear modulus and shear yield stress. We follow the procedure suggested by McClintock [157] for obtaining the mode I analog of the mode III elastic-plastic solution, using the Elastic modulus, E, and tensile yield stress, σ_{ys}.

Substituting (3.3) into (3.2) and integrating yields:

$$G = h\frac{\sigma_{ys}^2}{E}\left\{ln\left[\frac{h}{b}\right] - 1 + \frac{b}{h}\right\} \quad (3.4).$$

The last b/h term is small even for very thin films (b_{Cu}=0.25 nm), giving a first order estimate to be

$$G \approx h \frac{\sigma_{ys}^2}{E} \left\{ ln \left[\frac{h}{b} \right] - 1 \right\} \quad (3.5).$$

This is only an upper bound estimate for the strain energy release rate of a ductile thin film. It clearly does not take into account mode mix, which would result at a bi-material interface, nor does it allow for strain hardening, both of which could increase *G* somewhat beyond this limit.

The thin film yield stress decreases with the film thickness as discussed in Chapter 2. For electroplated Cu films equation (2.11) may be used to estimate the yield stress as a function of thin film thickness. Given the yield stress, the strain energy release rate can be estimated as a function of the film thickness. Both the strain energy release rate and the yield stress for electroplated Cu films are presented in Figure 43. The practical work of adhesion goes as high as 600 J/m^2 for a 100 um thick Cu film with a yield stress of only 250 MPa. High adhesion numbers are typical for very thick films that exhibit almost bulk-like yield properties.

The model considers only the plastic energy dissipation at the crack tip. Figure 44 extends the plot from Figure 43 for the smaller film thicknesses below 200 nm. First consider the smallest film thicknesses on the order of 1 nm. From a practical standpoint, Cu thin films cannot be obtained in continuous form much under tens of nanometers thick. Even though these extremely thin films approach a yield stress of 5 GPa, the small thickness brings the strain energy release rate down below 0.1 J/m^2 (equation (3.5)). Theoretically, however, the strain energy release rate should not fall below the true work of adhesion defined by equation (1.1). The true work of adhesion for the Cu/SiO_2 interface is 0.7 J/m^2, though in may be reduced by segregates and interfacial contamination. This model should not be applied for films thinner than about 20 nm. As discussed below, the application of the model is applicable only for thicker films.

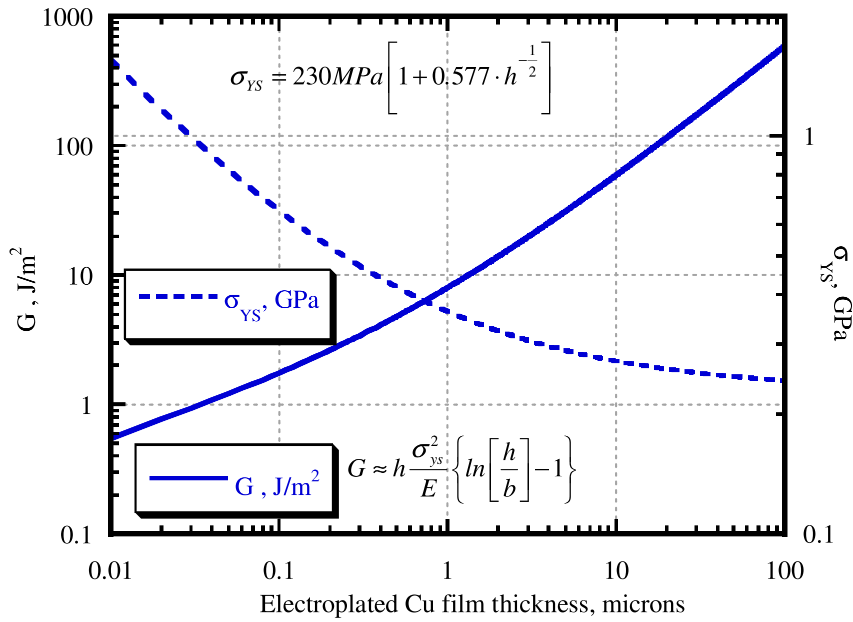

Figure 43. Electroplated Cu yield stress and strain energy release rate upper bound as a function of film thickness.

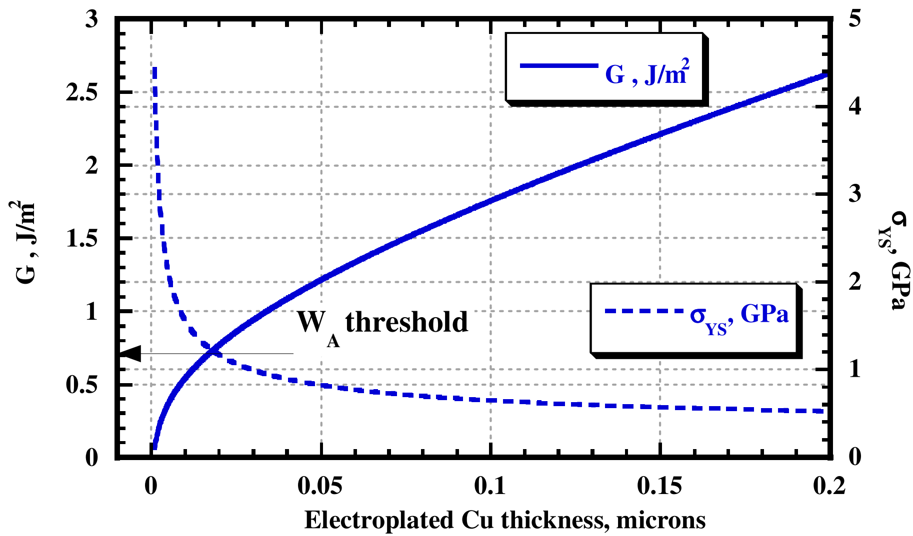

Figure 44. Electroplated Cu yield stress and strain energy release rate upper bound for small film thicknesses.

Crack Tip Plastic Zone Size Estimate

During the superlayer indentation process there are two plastic zones that develop during fracture: first the plastic zone around the indenter occurs followed by crack nucleation and growth with the plastic zone ahead of the crack tip (Figure 45). The plastic zone sizes around an indentation into a single film can be estimated using Johnson's spherical cavity model [159]:

$$C = \sqrt{\frac{3P_{max}}{2\pi\sigma_{ys}}} \quad (3.6),$$

where P_{max} is the maximum indentation load, and σ_{ys} is the film yield stress. Note that this is only approximate and strictly valid for thicker films in the absence of substrate effects. A more thorough analysis is presented in [160].

The plane strain plastic zone size at the crack tip during fracture of a thin film on a substrate with the same elastic constants scales with the following length quantity [158]:

$$c_{SS} = \frac{1}{3\pi(1-\nu^2)}\frac{E\Gamma_{SS}}{\sigma_{ys}^2} \quad (3.7),$$

where E and ν are the thin film elastic modulus and Poisson's ratio respectively, σ_{ys} is the film yield stress and Γ_{SS} is the total steady-state work of fracture. In the presence of elastic mismatch between the film and the substrate:

$$c_{SS} = \frac{2}{3\pi(1-\nu^2)(1-\beta^2)}\left[1+\frac{(1-\nu_s^2)E}{(1-\nu^2)E_s}\right]^{-1}\frac{E\Gamma_{SS}}{\sigma_{ys}^2} \quad (3.8),$$

where E, ν and σ_{ys} pertain to the ductile thin film, E_s and ν_s pertain to the elastic substrate; β is the second Dundurs parameter defined by equation (1.17). Here c_{SS} is an estimate, within a factor of two, of the active plastic zone size at the crack tip.

If the fracture toughness of the interface is known, a plastic strip model described in the previous section can be used for estimating the plastic zone size, c, at the crack tip.

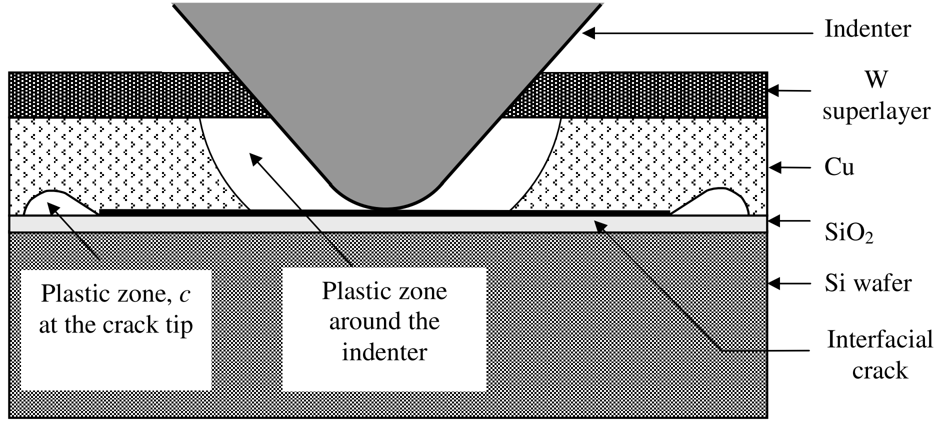

Figure 45. Superlayer indentation schematic. Plastic zones.

Similar assumptions are considered here:

1) Elastic-perfectly plastic material (no hardening);
2) No contribution from substrate or superlayer;
3) Use Burgers vector, *b* as a cut-off;
4) The average stress is equal to the yield stress of the film.

The difference here is that the plastic zone does not necessarily extend through the film thickness, but to some finite distance $c \leq h$. Work per unit fracture area can be determined as follows:

$$G = \frac{dU_f}{dA} = \frac{\int \sigma \ d\varepsilon \cdot dV}{dA} = c\int \sigma \ d\varepsilon \approx c \ \sigma_{ys} \frac{1}{c-b}\int_b^c \varepsilon(r) \ dr \qquad (3.9),$$

where *c* is a finite plastic zone size, *b* is Burgers vector, $\varepsilon(r)$ is the plastic strain at a distance *r* from the crack tip, which can be expressed in a form analogous to equation (3.3):

$$\varepsilon(c,r) = \frac{\sigma_{ys}}{E} \cdot \left(\frac{c}{r} - 1 \right) \qquad (3.10).$$

As for the upper bound model, substituting (3.10) into (3.9) and integrating yields:

$$G = c\frac{\sigma_{ys}^2}{E}\left\{ ln\left[\frac{c}{b}\right] - 1 + \frac{b}{c} \right\} \approx c\frac{\sigma_{ys}^2}{E}\left\{ ln\left[\frac{c}{b}\right] - 1 \right\} \qquad (3.11).$$

Since the plastic zone, c is still much larger than the Burgers vector, the last b/c term can be also omitted in this case. Note that (3.11) reduces to (3.5) at the upper bound where $c = h$. If G is known, equation (3.11) can be solved for c numerically.

3.2 Cu THIN FILM ADHESION

Sample Preparation

All thin film processing was conducted in a clean room environment. Silicon <100> wafers (100 mm in diameter, 0.5 mm thick) were thermally oxidized at 1100 °C in steam to grow 1.5 mm of SiO2. Oxide thickness was measured with a Nanoscope Ellipsometer. Cu films from 40 nm to 3 mm thick were deposited in a 2400 Perkin-Elmer sputtering apparatus. During sputtering the base pressure of the system was 1 μTorr, and the Ar pressure was 12 mTorr. Substrate table rotation was used to achieve uniform Cu film thickness and nanostructure. The maximum temperature during film deposition reached 100 °C after which the system was cooled for one hour without breaking the vacuum in order to prevent film oxidation. The thin film stack schematic for the superlayer indentation adhesion experiments with Cu films is presented in Figure 46. Using a DEKTAK surface profiler (Figure 47), film thickness was assessed and confirmed by RBS measurements assuming a 100% film density (Figure 48). A dummy wafer with a glass cover slide on top of it has been included in each deposition run. A step height has been formed upon removal of the cover slide. The film thicknesses were assessed by measuring the step heights with scanning profilometry with some film thickness measurements confirmed by cross-sectional SEM (Figure 49). Rutherford backscattering (RBS) ion beam analysis was also used to characterize the film thickness, assuming no thin film porosity. The energy loss of deeply penetrating He^{++} nuclei accelerated to 4 MeV was used to characterize the mass per unit depth of the film. If the film density is known, the theoretical fit to the spectrum provides the film thickness. Since the real Cu film is not completely dense and is passivated with W, the theoretical yield Cu spectrum is higher than the measured one (Figure 48). The theory of RBS is relatively well understood [12], and the modern equipment provides adequate measurement accuracy of 5%.

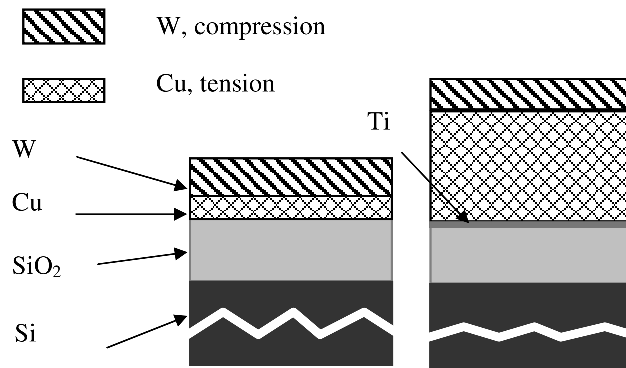

Figure 46. Thin film stack schematic.

Some Cu films were sputtered over a 10 nm thick Ti "glue" layer on top of SiO_2 (Figure 46). Residual stresses in Cu films were measured by the wafer curvature technique employing Stoney's equation, and ranged from 200 to 300 MPa tension. After all Cu films were deposited, a superlayer of 1.1 mm of W with 200-300 MPa compressive residual stress was sputtered over all Cu films in one run. Deposition parameters for the different layers are summarized in Table 4.

While the W superlayer stress was the same for both films with and without Ti, residual tension was slightly higher for the Cu/Ti films as shown in Figure 50.

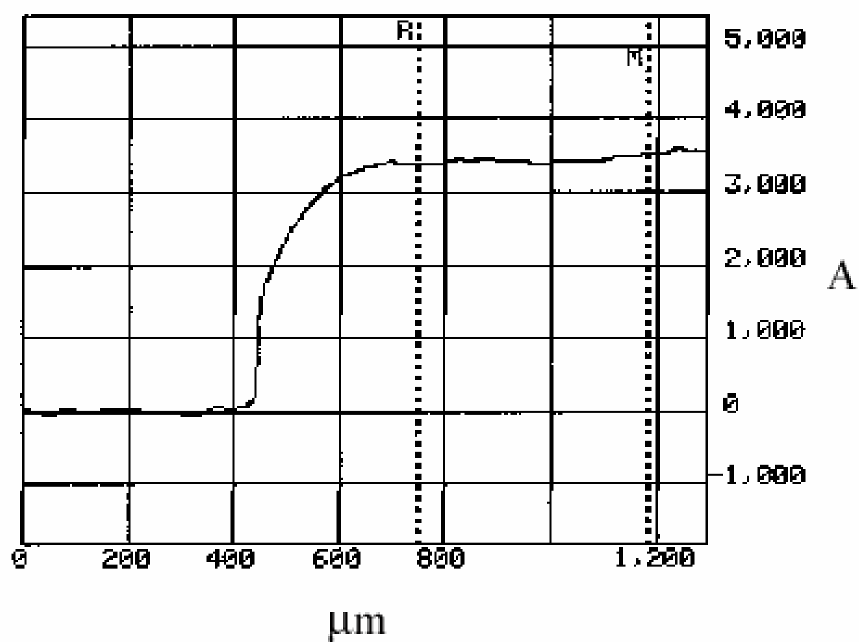

Figure 47. Step profilometry for film thickness determination.

Table 4. Sputtering deposition parameters.

Sputtered Material	Base Pressure, µTorr	Ar Pressure/Flow, mTorr/cm^3 min^{-1}	Pre-sputter time, min	Sputter power, W	Table rotation, rpm
Ti	1	11/9.6	15	1000	3.8
Cu	1	12/12	15	1000	2
W	1	7.4/7	15	1000	3.8

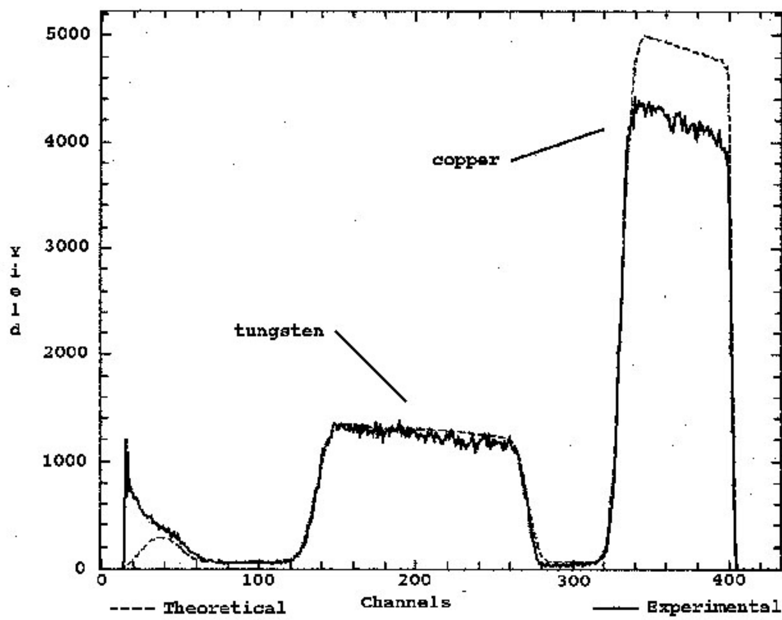

Figure 48. Energy yield spectrum of RBS analysis of W/Cu film.

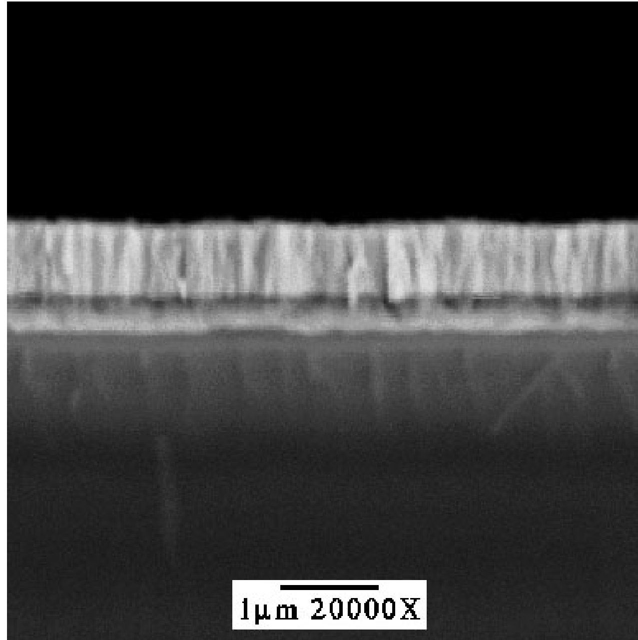

Figure 49. SEM micrograph of a film cross-section.

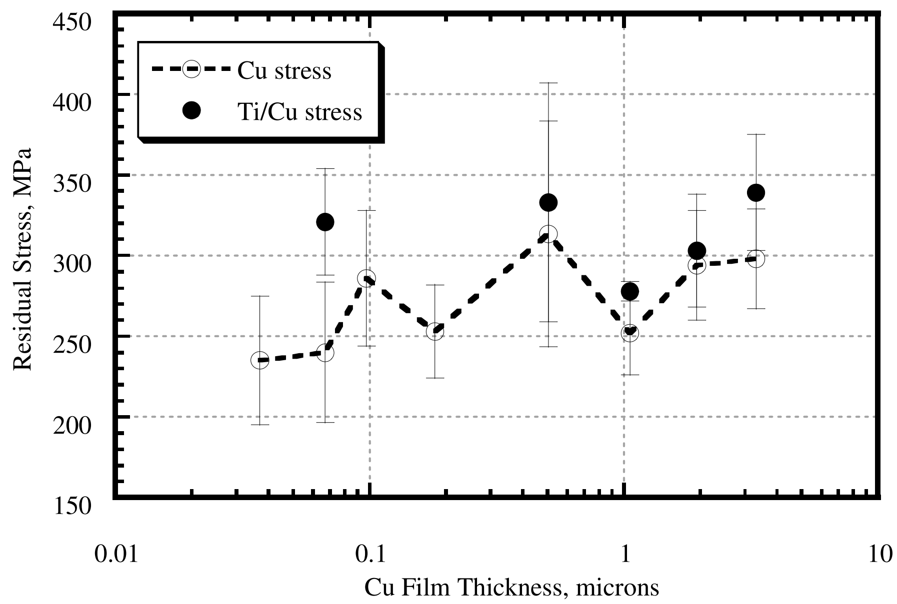

Figure 50. Residual stress levels in the Cu and Ti/Cu films.

Adhesion Assessment

Displacement controlled indentation tests were conducted using the IBM micromechanical tester [137]. A series of indents 100 to 200 um apart to maximum loads ranging from 30 to 250 mN were made with a conical 90° diamond indenter of 1 μm tip radius (Figure 51). There were 3 indents at each load, giving a total of 12 to 18 indents for each film thickness. Generally speaking, there are two measurements that are necessary for strain energy release rate calculations. From the standpoint of blister formation, both indentation depth and blister diameter are required. Blister diameter is measured in the optical microscope with Nomarski contrast (Figure 51). An Olympus optical microscope was calibrated for 50 and 100X magnifications prior to blister diameter measurement with a Tencor surface profilometer being used to verify the measurement accuracy. Load-displacement curves were recorded continuously during the tests. Using the Oliver-Pharr method, the indentation volume was calculated from the indentation depth, as obtained by fitting 65% of the unloading portion of the load-displacement curve. Adhesion values for each indentation experiment were calculated based on the procedure discussed in Chapter 1, using an Excel spreadsheet. A detailed discussion of the spreadsheet is given in the Appendix.

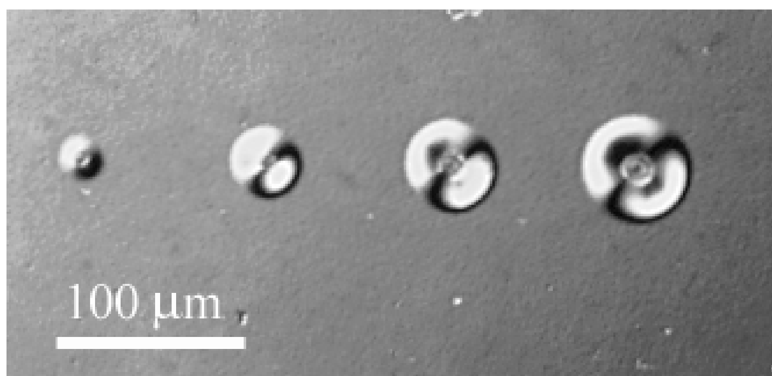

Figure 51. Nomarski contrast optical image of a series of indentations in a 1 um thick Cu film with W superlayer.

Radial Multilayer Cracking

For most of the indents into Cu films without a Ti underlayer, load excursions on the load-displacement curves were observed (Figure 52). Discontinuities on the indentation curve can be attributed to multilayer buckling, unstable crack growth, radial multilayer cracking and substrate cracking. Since the indentation volume is calculated from the residual depth, it will be overestimated for indentations with load excursions, which would result in the higher values for the calculated interfacial adhesion strength. Though the exact nature of the excursions is not clear, it was accounted for in the analysis by subtracting the total excursion length from the residual indentation depth. For shallower indentations, usually no radial cracking or load excursions were observed (e.g. indentation 1 in Figure 52). Increasing the indentation depth caused larger delamination radii, followed with a reproducible load excursion at 120 mN for a 100 nm thick Cu film. From this example it appears that the radial multilayer cracking contributes to the discontinuities on the load-displacement curves. On the other hand, some curvature of Cu/W due to residual stress mismatch or double buckling could lead to a rapid interfacial crack advance followed by radial cracking.

The extent of radial cracks is highly dependent on the residual stress in the W superlayer. Tensile circumferential stress in the delaminated film drives radial cracks initiated at the edge of the contact with an indenter. For a film with a residual compressive stress, the circumferential stress becomes compressive at the edge of a delamination while with tensile residual stresses, the circumferential stress is always tensile. As reported in [161] for a residual compressive stress, the indenter will produce radial cracks in the brittle film (in this case W with 300 MPa compressive residual stress) only up to a half of the delamination radius. This is clearly seen in Figure 52, indentation 2. In the case of tensile residual stress in a W superlayer, radial cracks extend to the delamination radius [162].

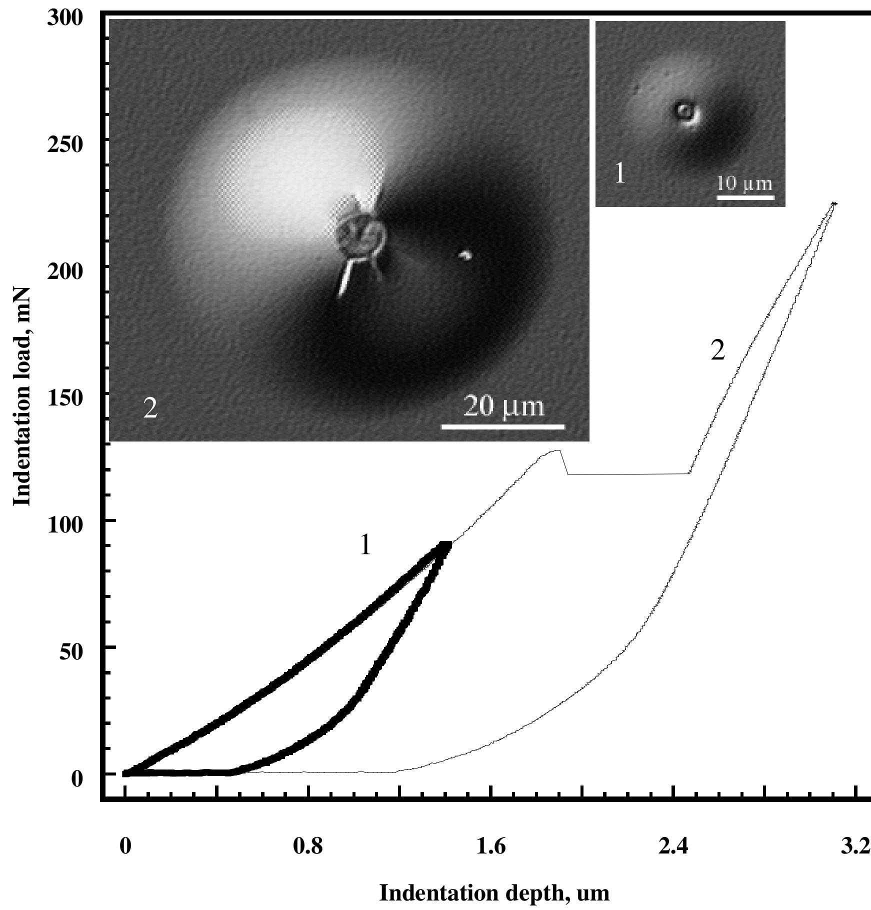

Figure 52. Load-displacement curves and corresponding delaminations for a 100 nm thick Cu film without Ti underlayer.

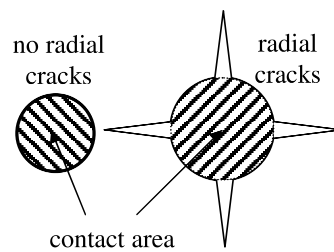

Figure 53. Radial cracking contribution to the increase in the contact area.

For the same indentation load, films with radial cracks around the indenter create a larger contact area than films without cracks (Figure 53). On the other hand, radial cracking combines with buckling to relieve the residual tensile stresses, whereas buckling is the only means to relieve residual compressive stresses.

Ti Underlayer

Several reasons why a thin underlayer is necessary in the case of Cu films were discussed in Chapter 1. From the standpoint of microelectronics, copper diffuses into silicon, reaching active devices. The underlayer is desirable to prevent copper diffusion. On the other hand, any additions to copper reduce film conductivity. The underlayer material is presumably non-reactive and non-miscible with copper, should react with Si at high temperatures but not weaken copper electromigration properties. The underlayer is supposed to improve adhesion properties and thus improve mechanical reliability.

For the current study a thin (10 nm) layer of Ti was used to improve Cu film adhesion to silicon/silica substrates. There are two main reasons why Ti improves Cu adhesion in this case. First, there are two new interfaces that are formed, which are stronger than the original SiO_2/Cu one [163]. Second, in its initial stage of growth, the Ti film has a higher surface roughness than SiO_2, which simply increases the contact area between Ti and Cu and affects the phase angle (Figure 54 and Figure 55). Thus, whatever increase in adhesion with the Ti underlayer must be considered either in terms of roughness or bonding.

A Ti/Cu interface is slightly rougher than the SiO_2/Ti interface as seen in the cross-sectional TEM micrograph (Figure 55). Cu and W appear to have a columnar grain structure. Since the vacuum was broken prior to Cu film deposition, titanium was most likely oxidized [164]. An X-Ray spectrum obtained from the TEM sample is presented in Figure 56, showing distinct C, O, Cu, Si and Ti peaks. The area under the oxygen peak is half the area under the titanium peak, indicating that there is only partial Ti oxidation. The small Cu peaks may indicate some intermixing, since the TEM analysis was performed one year after the sample preparation.

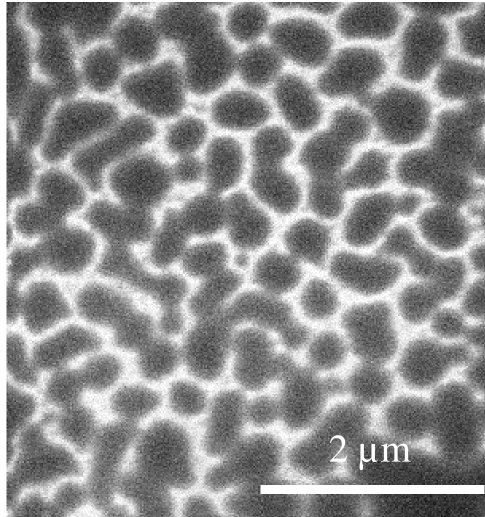

Figure 54. SEM micrograph of Ti underlayer [150].

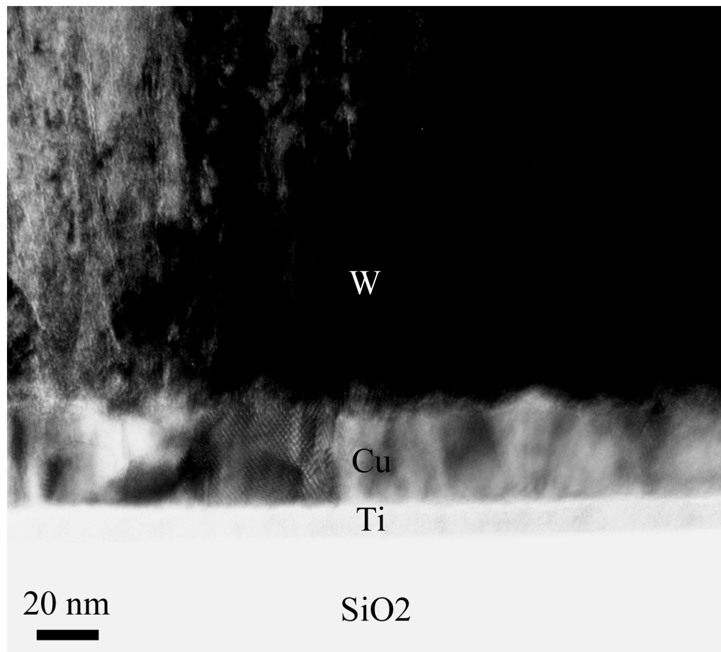

Figure 55. Cross-sectional TEM of the SiO_2/Ti/Cu/W stack {image taken by D. Medlin, Sandia National Lab}.

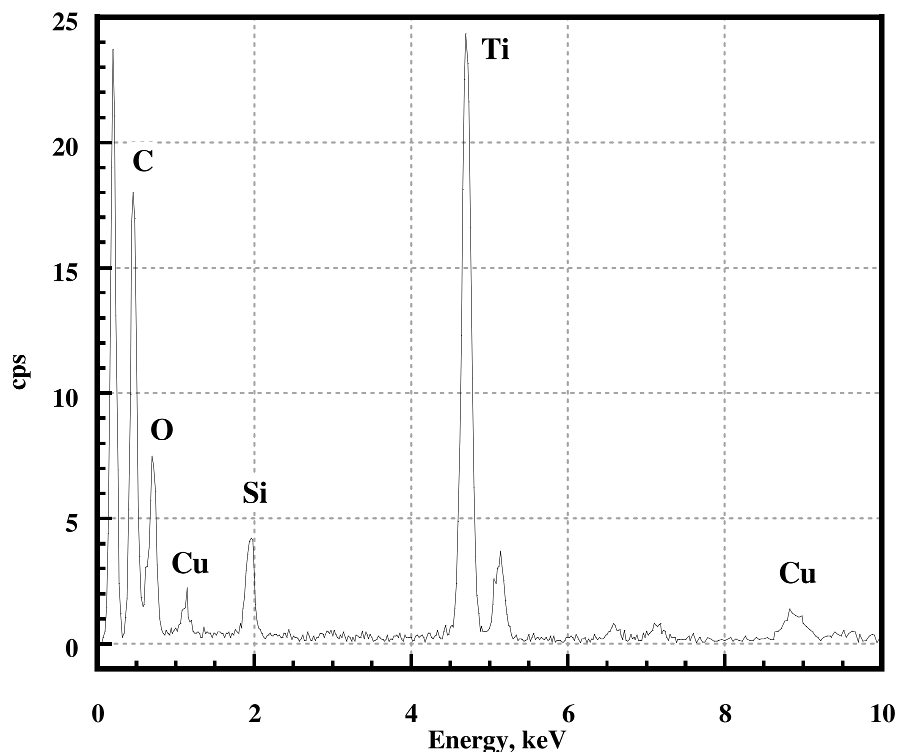

Figure 56. Ti underlayer X-Ray spectra obtained in TEM {D. Medlin, SNL}.

Cu Film Adhesion Results

Interfacial adhesion energies for the sputter-deposited Cu films on SiO_2 are presented in Figure 57. Data set 2 is from the present study, and data set 1 is taken from M.D. Kriese [165] for comparison. As expected, the strain energy release rate increases with the film thickness. This only happens for the films over 100 nm thick, where there is a definite contribution of crack tip plasticity to the practical work of adhesion, which scales with the film thickness. For the thinner films the strain energy release rate appears to plateau, being relatively constant at 0.6 J/m^2. This value translates to a stress intensity of 0.27 $MPa \cdot m^{1/2}$ using a 120 GPa modulus for a Cu thin film. Given a 1.86 GPa yield stress for the 100 nm thick Cu film, the crack tip plane strain plastic zone size is only 22 Å. Since this is practically

the stand off distance for a single dislocation (Burgers vector), it can be assumed that plastic energy dissipation is nil. For comparison, in Fe-3 wt% Si single crystals, the standoff distance of the nearest crack-tip dislocation is given by [166]:

$$c = \frac{\alpha'}{\sigma_{ys}\, ln(\, \beta' K_I\,)} \qquad (3.12).$$

Using the values of $\alpha' = 1.06 \cdot 10^{-5}$ MPa·m and $\beta' = 20/\text{MPa}\cdot\text{m}^{1/2}$ with the above K_I determined to be 0.27 MPa·m$^{1/2}$ gives a standoff distance of 35 Å, which is very close to the 22 Å plastic zone calculated for the 100 nm Cu film. This suggests that the 0.27 MPa·m$^{1/2}$ stress intensity may not be sufficient to emit the first dislocation. This is further supported by Rice and Thompson's original calculation of the local stress intensity, k_{Ie}, for dislocation emission in copper [167]. They estimate k_{Ie} = 0.32 MPa·m$^{1/2}$ for dislocation emission in Cu. This strongly suggests that for thinner Cu films the local stress intensity of 0.27 MPa·m$^{1/2}$ is sufficient to cause film delamination but not sufficient to cause dislocation emission.

For Cu films under 100 nm thick, the average plateau adhesion is 0.6 J/m^2, which agrees with the thermodynamic work of adhesion of 0.7±0.1 J/m^2 (W_A from equation (1.1)) for Cu on SiO_2 measured with the contact angle technique [3]. It can be proposed that the plateau of 0.6 J/m^2 is a true measure of adhesion in absence of plasticity contributions, the true work of adhesion, i.e. the thermodynamic value of fundamental interest.

The upper bound plastic strip model (equation (3.5)) is also presented in Figure 57. Here, the actual yield stress nanoindentation measurements from Chapter 2 are used. It is clearly seen that while being in qualitatively good agreement with the data, the model overestimates the amount of plastic energy dissipation at the crack tip for films under 3 um thick, which means that the plastic zone size does not exceed the film thickness. In fact this is expected if one converts the *G* values to a plastic zone size and compares these values with the film thickness. For example, at a 2 um thickness, the 790 nm plastic zone size calculated is only about 40% of the film thickness while at a 200 nm thickness, the calculated plastic zone of 33 nm is only 17% of the film thickness. Using only a portion of the film thickness for plastic energy absorbtion clearly would place data below the upper bound.

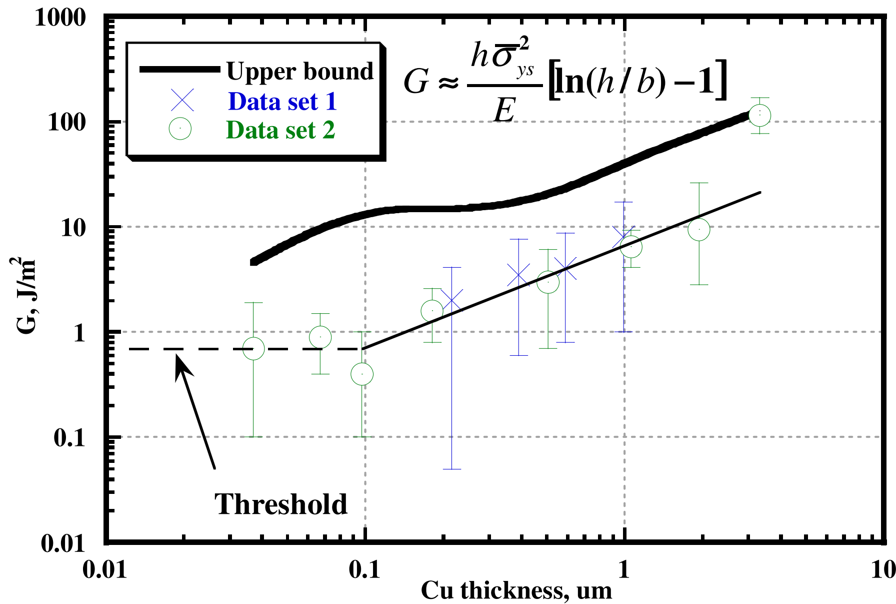

Figure 57. An interfacial energy relationship to the film thickness: theoretical upper bound solution (top solid line) and experimental strain energy release rates.

Results of the crack tip plastic zone size calculations are presented in Figure 58. Here, the calculations are based on the plane strain plastic zone size estimate, approximately twice the value of c_{SS} from equation (3.7), and a modified plastic strip model, using the actual interfacial toughness measurements in Figure 57 and solving equation (3.11) numerically. Both models provide very similar plastic zone size estimates, much less than the film thickness, except for the thickest 3 um Cu film (Figure 58). For the 3 um Cu thick film the plastic zone size extends through the whole film thickness, which results in the elevated interfacial toughness measurement of over a 100 J/m^2 (Figure 57).

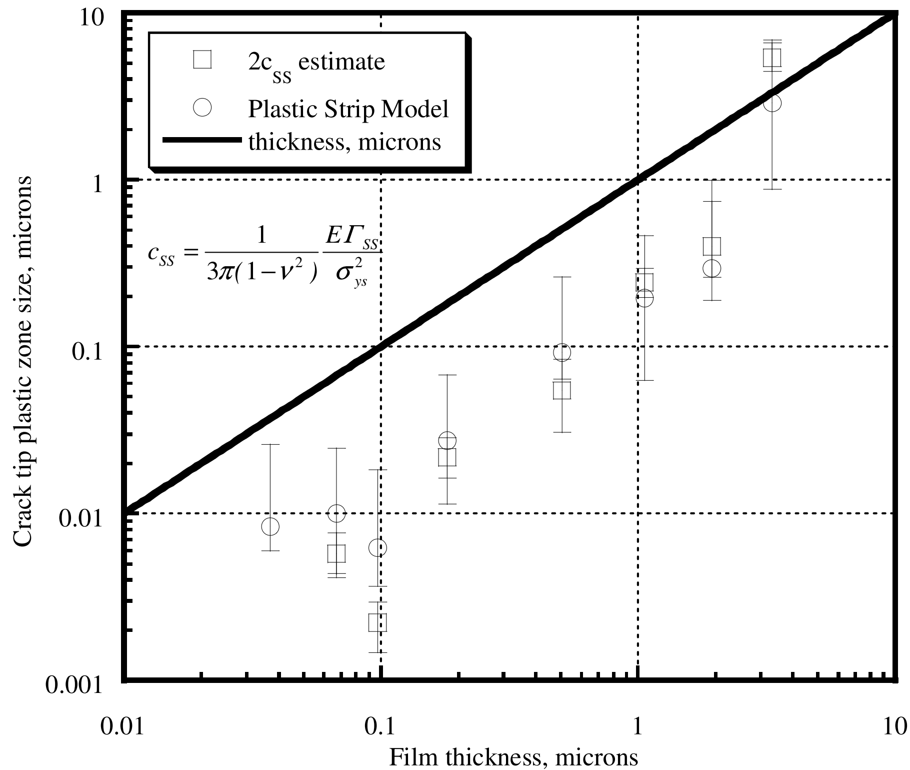

Figure 58. Crack tip plastic zone estimates for Cu films. Straight line corresponds to the plastic zone size equal to the film thickness.

Practical work of adhesion data for Cu films with and without a Ti underlayer are presented in Figure 59. Copper thin film adhesion increases with the film thickness and with the addition of a 10 nm thin Ti underlayer due to the higher plastic energy dissipation at the crack tip. Crack tip plastic zone size estimates, based on the modified plastic strip model (equation (3.11)), are presented in Figure 60 for Cu films with and without a Ti underlayer. These are numerical solutions for the plastic zone size based on the actual strain energy release rate measurements. As in Figure 58, the straight line corresponds to a plastic zone size equal to the film thickness. Here, it is seen that the plastic zone size is always larger with the Ti underlayer, compared to Cu only and is approaching the film thickness. Since the Cu

film adhesion was higher in this case, much more energy was spent on Cu film plastic deformation, approaching the upper bound of Figure 59.

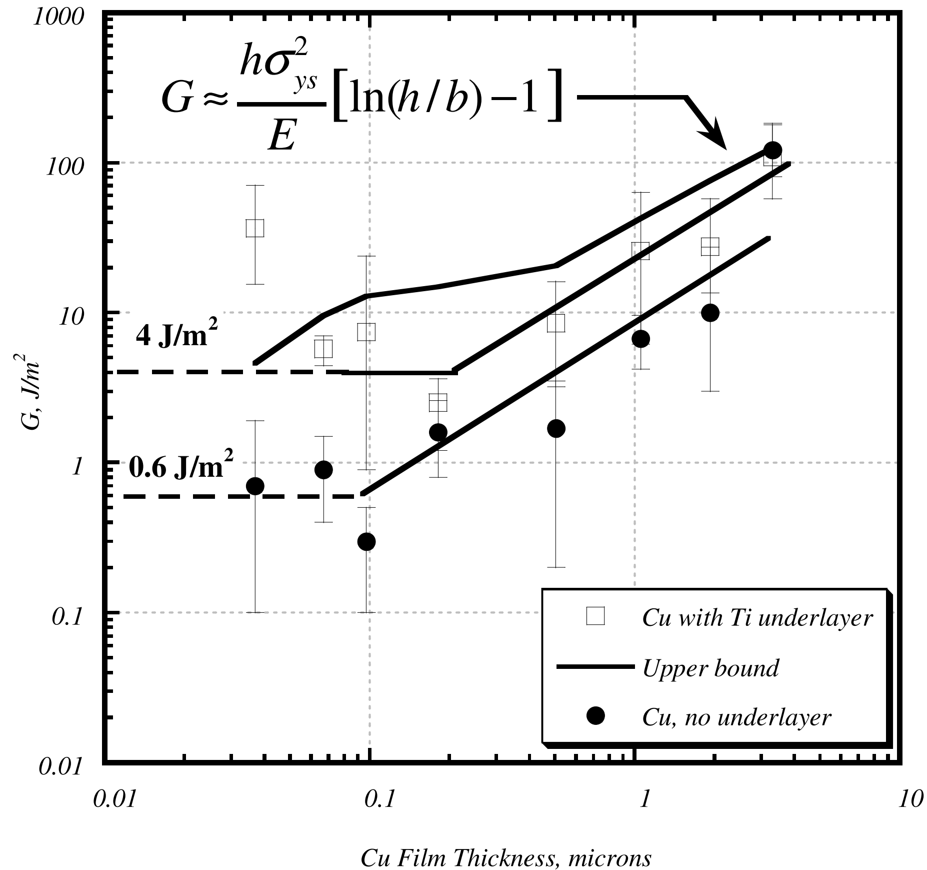

Figure 59. Cu film practical work of adhesion as a function of film thickness.

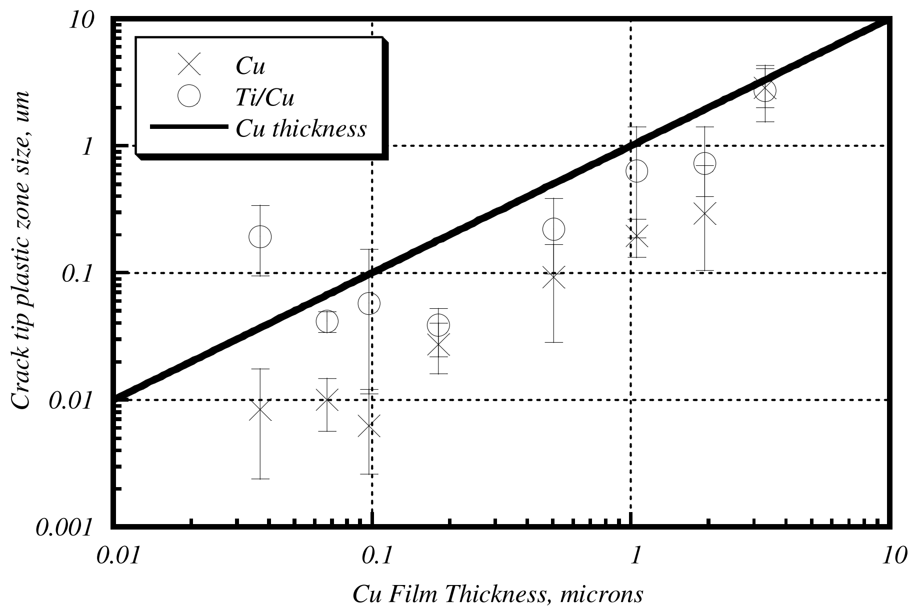

Figure 60. Crack tip plastic zone for Cu films with and without Ti underlayer. Plastic strip model estimates.

Similar to the Cu film adhesion without Ti, the interfacial toughness plateaus for thinner films on Ti (Figure 59). The plateau value is about 4 J/m^2 for a 100 nm thick Cu film. This actually close to the true work of adhesion of Cu on different underlayers measured with the contact angle technique [3, 99, 171]. For example, on TiW the true work of adhesion of Cu scales linearly with the Ti concentration, increasing from 2.1 to 2.6 J/m^2 for 10 and 20 wt % Ti in the TiW underlayer [171]. As mentioned in Chapter 1, high true adhesive energy helps induce plastic energy dissipation terms $U(W_A)$ in equation (1.5). It seems that there may be a plastic term contribution to the measured adhesion values even for the thinnest Cu films on a Ti underlayer.

Sources Of Elevated Interfacial Toughness

Interfacial fracture toughness values of Cu films are compiled in Figure 61 and Figure 62. The plane strain solution for a wedge from [40] is presented for comparison. Elevated values for the strain energy release rate are expected for the delamination radius to contact radius ratios up to five.

There are two components that contribute to the elastic energy in the film that drives interfacial delamination: indenter-induced stress and residual stress in the bilayer. For smaller delamination radii (R/a < 5 in case of a superlayer) there is an indenter-induced stress that drives the crack. For radii ratios over five the residual stress in the superlayer is mostly contributing to the annular crack growth.

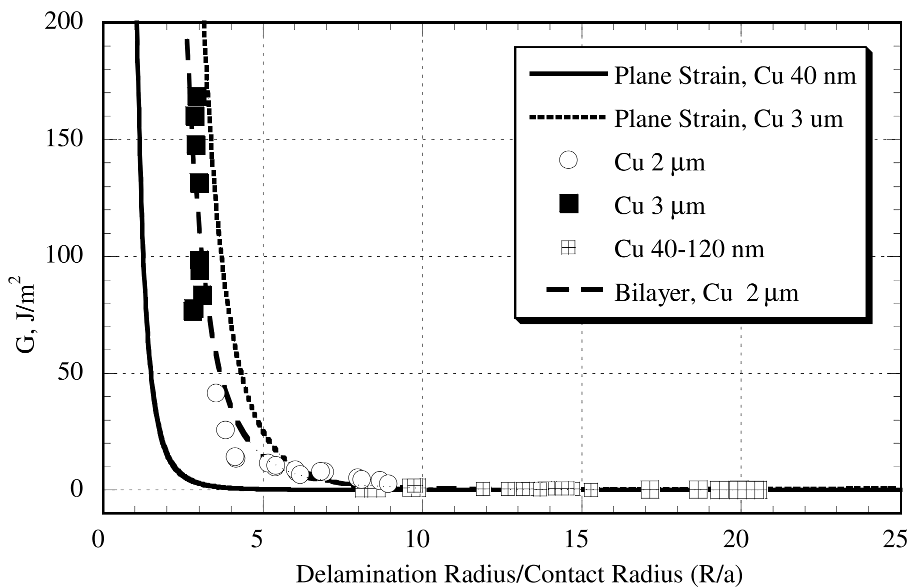

Figure 61. Strain energy release rate as a function of normalized delamination radius for Cu films.

The bi-layer solution for a 2 mm thick Cu film is also presented. This solution is constructed by fixing the indentation depth at 65% of the bilayer thickness and varying the delamination radius. For a given indentation depth and bilayer thickness there will be a unique curve. Both plane strain and bilayer solutions show that for thicker films higher strain

energy release rate values are expected for a given R/a ratio. For R/a < 5, variations in the delamination radius as measured optically will produce significant changes in the measured adhesion. Note that for a given load, bi-layer blisters without Ti are much larger compared to those with the Ti underlayer, as shown in Figure 63. Corresponding indentation curves are shown in Figure 64.

For Cu films with a Ti underlayer, R/a ratios do not exceed 15, compared to 21 without Ti. Improved Cu adhesion in the case of Ti underlayer does not allow blister extensions over R/a ratios higher than 15.

Figure 62. Strain energy release rate as a function of normalized delamination radius for Cu films with Ti underlayer.

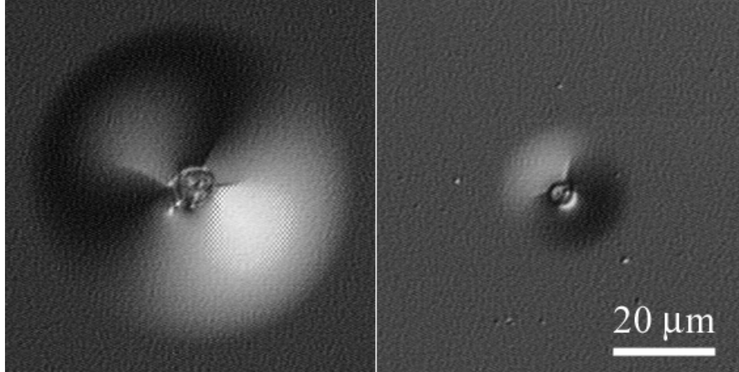

Figure 63. Indentation induced delamination in a 100 nm Cu film with and without Ti underlayer.

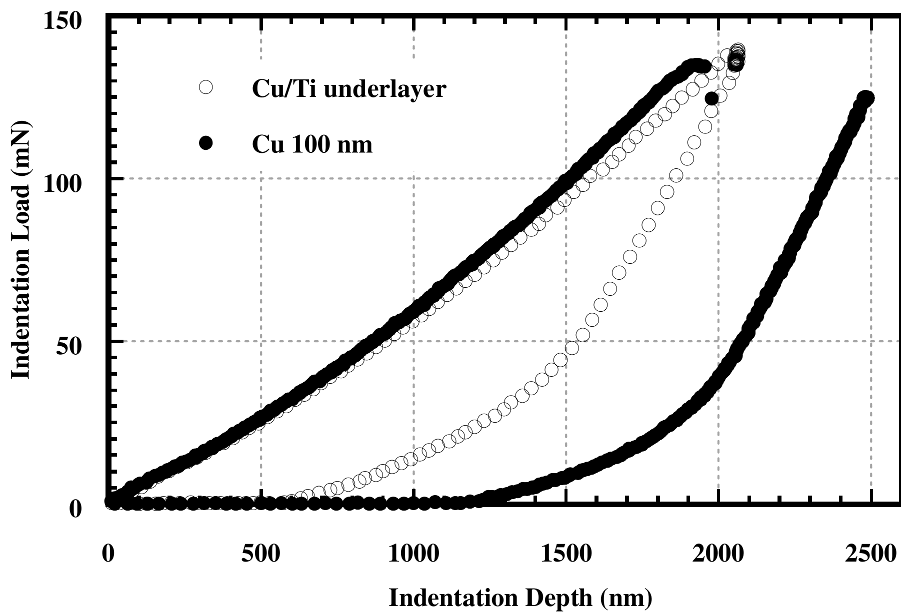

Figure 64. Load-displacement curves corresponding to delaminations in Figure 63.

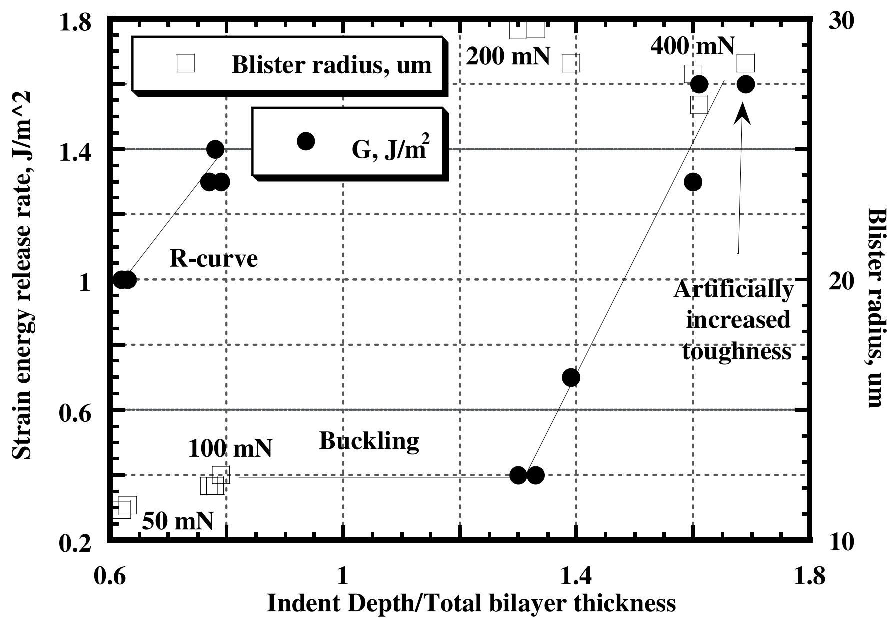

Figure 65. Substrate constraint effect in an 80 nm thick Cu film.

Indenting deeper than the bilayer thickness into the substrate does not increase the blister size substantially (Figure 65), but causes substrate cracking and invalidates the analysis.

In terms of the strain energy release behavior before buckling the superlayer indentation test is analogous to the Precracked Line Scratch Test (PLST). Consider the strain energy release curve for the PLST in Figure 12. Prior to buckling there is an R-curve behavior, where G increases with the crack length. Similar effect is observed for the superlayer indentation test for the depth up to 80% of the total film stack thickness (Figure 65). Here, the strain energy release rate and crack length are plotted as a function of the relative indentation depth. Prior to buckling, which occurs after 80% relative indentation depth, the R-curve behavior is observed. After buckling the G values drop, just like for the PLST (Figure 12, post-buckling G) due to the phase angle decrease. In the PLST the scratch distance, which is analogous to the indentation depth of the superlayer indentation test, is not limited. Unlike PLST though, the indenter motion is limited by the substrate. When the

indenter has reached the substrate, the blister does not grow anymore. This is illustrated in Figure 65, where the load increase from 200 to 400 mN does not cause bigger delamination formation. Nevertheless, the indenter penetrates the substrate, causing its fracture, etc. This results in the higher indentation depth obtained from the load-displacement curve, but since the blister radius does not change, elevated G values are calculated (Figure 65, artificially increased toughness). These effects should be corrected for in the analysis.

Residual stresses in Cu and W layers both affect G values in the case of multilayer buckling. A higher tensile stress in Cu on Ti (Figure 50) would result in increased curvature of the delaminated Cu/W. Thus, with the Ti underlayer, the crack tip would have more Mode I stress. In fact, this prediction is consistent with the phase angle estimates as will be shown in the next section.

Since measured interfacial fracture toughness is strongly dependent on the mode mixity, estimate of phase angle variations with the changing Cu/W film thickness ratio is desirable. This would assist in sorting out whether the improved adhesion was solely due to plastic energy dissipation as opposed to contributions from a change in phase angle.

Bond Strength And Phase Angle Estimates

It is very important in thin film systems to be able to extract the true characteristic of the interfacial strength and identify the phase angle. An estimate of the interfacial bond strength from the measured values of G can be accomplished by extending an approach suggested by Mao et al [172] for pure Mode I conditions. Their approach relies on a model of discontinuous interfacial crack growth, where fracture occurs as normal stress ahead of the blunted crack tip reaches a critical value. This critical stress value, σ_b, is denoted as interfacial bond strength. The crack extends, following a fracture event, until blunting causes arrest. Crack tip blunting results as a consequence of activation of near-tip dislocation sources [173]. This mechanism is applicable only to a relatively weak metal-ceramic interface, since for the stronger interfaces fracture involves void nucleation and coalescence. Based on the model, the strain energy release rate corresponding to the onset of fracture can be determined as:

$$G_0 = \left(\frac{\pi}{8}\right)\frac{\sigma_b^2 \Delta}{E} \quad (3.13),$$

where G_0 is an initiation strain energy release rate; σ_b is the interfacial bond strength, Δ is the crack blunting distance, and E is Young's modulus. The number of dislocations piled-up at a boundary may be given by $N=\Delta/b$ with the Burgers vector, b, and N further defined in terms of the shear stress acting on the boundary [174], giving:

$$N = \frac{\Delta}{b} \approx \frac{\tau_i d}{2A^*} \quad (3.14),$$

where $A^* = \mu b/2\pi(1-\nu)$; d, the pile-up length; μ, as the shear modulus; ν, Poisson's ratio. To first order τ_i can be associated with the maximum shear stress. Since the shear stress at initiation is largely elastic in most cases, this becomes:

$$\tau_i \approx \tau_{max} \approx 0.3 p_0 = 0.45 \frac{P}{\pi a^2} \quad (3.15),$$

where p_0 is the maximum pressure or 3/2 the mean pressure, P is load and a is the contact radius. Since the $P/\pi a^2$ in equation (3.15) is hardness, H, the number of dislocations of interest from equations (3.13)-(3.15) becomes:

$$N = \frac{Hh}{\mu b} \quad (3.16),$$

with the pile-up length, d, being taken as the film thickness, h. Further, taking hardness to be three times the yield strength, σ_{ys}, it is easily shown with (3.13)-(3.16) that

$$\sigma_b = \sqrt{\frac{8E\mu G}{3\pi h \sigma_{ys}^2}} \quad (3.17).$$

There is no direct dependence between the bond strength and the film thickness. The only film thickness dependent term in equation (3.17) is the yield stress, which scales with the film thickness as discussed in Chapter 2. In fact, bond strength values given in Table 5 are almost independent of the film thickness. The magnitude of bond strength seems to be in agreement with values obtained for various metal/oxide interfaces [175].

By measuring G_0 one can estimate bond strength, since σ_{ys}, h, E and μ are known. It should be also noted that in this case σ_b is not a tensile bond strength but rather a measure of the strength corresponding to the particular phase angle Ψ given by:

$$\Psi = tan^{-1}\left(\frac{\tau}{\sigma}\right) \qquad (3.18).$$

Here, σ and τ are normal and tangential stresses at some small distance from the crack tip. As a first order approximation, the tangential stress component at the interface can be estimated as in [176]:

$$\frac{\tau_r}{p_0} = \frac{1}{\sqrt{18}}\left\{-2(1+\nu)\left[1-\frac{r}{a}tan^{-1}\left(\frac{a}{r}\right)\right]+3\left(\frac{r^2}{a^2}\right)^{-1}\right\} \qquad (3.19).$$

In this equation, $p_0 \cong 1.5H$ is mean indentation pressure; $a = \sqrt{\delta R}$, contact radius; δ, penetration depth under maximum load, r, distance to the interface. The later is calculated as $r = h_{Cu} + h_W - \delta_r$ with δ_r being the residual penetration depth; h_{Cu} and h_W are copper and tungsten layer thicknesses respectively. The effective tip radius is defined at $\delta_r + \delta_b$. Here, δ_b is the tip blunting distance, which is 414 nm for a 90° cone indenter with a 1 um tip radius. Equation (3.19) is applicable for penetration depths not exceeding the bi-layer thickness. Interfacial shear stress ranges from 650 to 1450 MPa (Figure 66). This is similar to the results obtained by Dehm et al [177] for the Cu/Al_2O_3 interface. The stress ranged from 400 to 1600 MPa for that interface for a similar Cu thickness range.

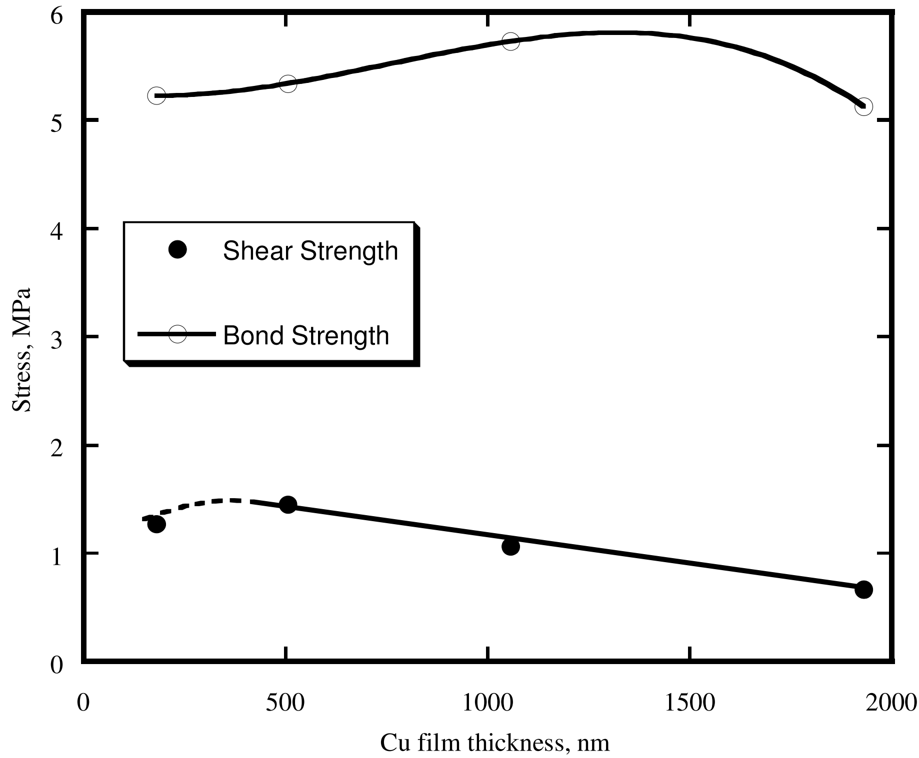

Figure 66. Interfacial shear stress and bond stress dependence on the Cu film thickness.

Determination of the phase angle corresponding to the experimentally measured strain energy release rate would require a knowledge of the normal and tangential stresses at the interfacial crack tip. Assuming that $\sigma_b = \sqrt{\sigma^2 + \tau^2}$, the phase angle can be therefore estimated as:

$$\Psi = tan^{-1}\left(\frac{\tau}{\sqrt{\sigma_b^2 - \tau}}\right) \qquad (3.20).$$

First, the ratio of τ/σ_b is determined using experimentally measured values of G (Table 5). Here we neglect the difference between G_0 and G_s, corresponding to crack initiation and propagation, respectively. Converting this to a phase angle through equation

(3.20) gives the phase angle versus normalized film thickness in Figure 67. The phase angle decreases quite rapidly from about 20 degrees to 5 degrees with increasing Cu thickness compared to the superlayer. This trend is consistent with the following theoretical predictions by N. I. Tymiak [150].

Table 5. Cu film interfacial fracture characteristics.

h_{Cu}, nm	h_{Cu}/h_W	τ, GPa	σ_{bond}, GPa	Ψ, deg.
181	0.165	1.27	5.23	12.7
505	0.459	1.45	5.34	15.2
1056	0.96	1.065	5.73	10.5
1930	1.75	0.663	5.13	7.4

The effects of film thickness and interfacial crack length on the mode mixity for buckling driven delamination in the indented pre-stressed film can be qualitatively evaluated through the parameter $\eta = \sigma/\sigma_c$. Here, σ_c is the critical buckling stress; $\sigma = \sigma_I + \sigma_R$ is the total stress in the film with the σ_i and σ_R being indentation induced stress and residual film stress respectively. As η increases, $|\psi|$ increases with the interfacial crack becoming more heavily under mode II conditions [178]. The parameter η can be determined using values of σ_i and σ_R defined by the Marshall and Evans [35] analysis for a single layer, giving:

$$\eta = \frac{\sigma_i + \sigma_R}{\sigma_c} = \frac{\sigma_R + \beta E V_0 / R^2 h}{\gamma E h^2 / R^2} = \frac{\sigma_R R^2 + \beta E V_0 / h}{\gamma E h^2} \qquad (3.21).$$

Here, $\gamma = 14.68/12(1-\nu^2)$; $\beta = 1/2\pi(1-\nu)$; V_0 is the indentation volume; ν, Poisson's ratio; E, Young's modulus and compression is regarded as a positive stress. In the case of a bi-layer film, σ_R should be replaced with the *effective* residual stress in the laminate. For the Cu/W thickness ratios and residual stress levels considered in the this thesis, the effective σ_R is always positive.

Differentiating (3.21) with respect to the delamination radius yields:

$$\frac{\partial \eta}{\partial R} = \frac{2\sigma_R R}{\gamma E h^2} \qquad (3.22).$$

As follows from (3.22), η increases with the delamination radius if the effective residual stress in the bi-layer is compressive. On the other hand, the derivative $\frac{\partial \eta}{\partial h}$ is always negative providing $\sigma_R > 0$:

$$\frac{\partial \eta}{\partial h} = -\frac{1}{E\gamma}\left(2\sigma_R R^2/h^3 + 3\beta E V_0/h^4\right) \qquad (3.23).$$

Thus, mode mixity decreases with increasing film thickness, which is consistent with the experimental calculations.

The important point is that the material with the titanium underlayer has a slightly lower measured phase angle. This indicates a smaller Mode II component being involved in the delamination process. Since a smaller mode II component should result in a decreased strain energy release rate, the obvious conclusion is that the mode II component is not a controlling factor here. On the other hand, the presence of the Ti underlayer results in approximately doubling in the true adhesion strength as shown in Figure 68. Here, bond strengths for Ti/Cu/W and Cu/W films are given by equation (3.17). Note that estimated values are nearly independent of the film thickness for both types of multilayers. It may be concluded that the increased strain energy release rate observed in Figure 59 with the Ti underlayer cannot be attributed to a phase angle effect. The conclusion, using an admittedly first order calculation of a true bond strength and phase angle, is that the important contribution of the Ti is improved bonding and therefore increased plastic energy dissipation.

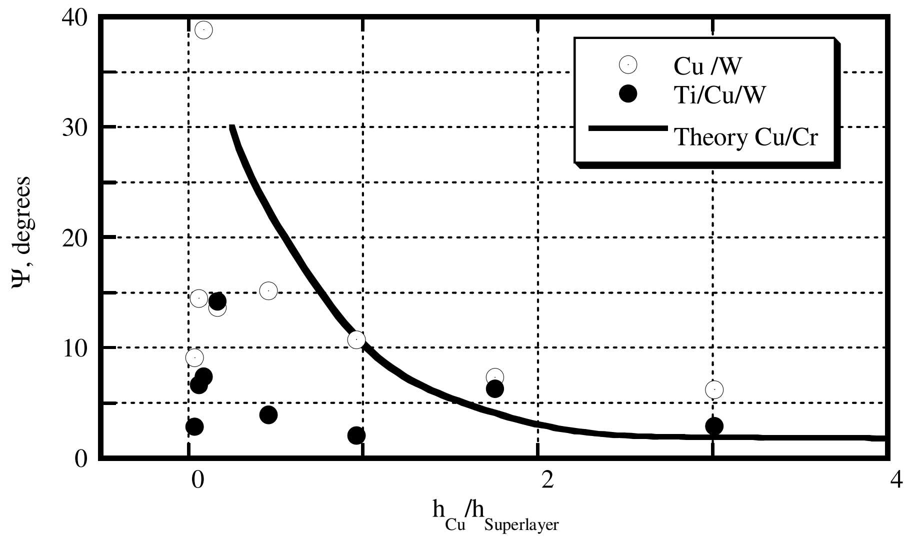

Figure 67. Effect of the relative Cu film thickness on the mode mixity. Solid line is a theoretical prediction from [29].

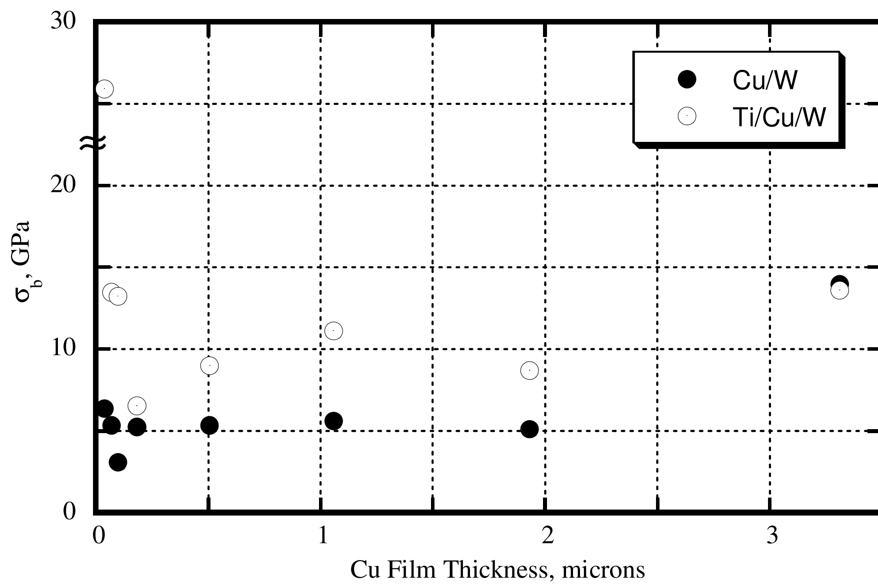

Figure 68. Cu film bond strength.

Regarding the Cu film adhesion measurements, there are three important points to be made:

i) Cu films both with and without a Ti underlayer have increased interfacial energy release rates with increasing thickness;

ii) a Ti underlayer increases both interfacial toughness and interfacial bond strength, but the latter is independent of film thickness;

iii) on both theoretical and experimental grounds, the phase angle decreases with an increasing ductile Cu layer thickness.

These three points taken together are consistent with plastic energy dissipation in the Cu films being the primary contributor to improved adhesion energies. While a Mode II contribution might be a minor factor in all cases but one, the calculated phase angle, $\psi = 15°$ is sufficiently small to reinforce the proposed concept that plastic zone sizes are generally about a factor of two smaller than the Cu film thickness implying that an even stronger bonding agent might further improve interfacial fracture toughness. The one disturbing feature about the data with the Ti underlayer is that strain energy release rate appears to increase with decreasing Cu film thickness below about 100 nm. Presently it is not known whether this is an artifact in our calculated values where R/a is quite small (see Figure 62) or whether some Ti/Cu intermixing at very small Cu thicknesses allows improved bonding to the W superlayer resulting in nonlinear dissipation contributions from the tungsten. The above trends can possibly be attributed to the interfacial friction producing screening of a crack tip from the applied load. As follows from Stringfellow and Freund's [179] theoretical results, screening effects should be negligible at higher film thicknesses but increase with decreasing film thickness. The higher surface roughness of Ti as compared to SiO_2 could possibly result in more effective screening of a crack tip from the applied load. Thus, the adhesion strength of Cu films thinner than 100 nm could be increased via interfacial friction when Ti is present but remain unaffected for the films with no Ti.

Since the practical work of adhesion scales with the ductile film thickness, due to the increased amount of plastic energy dissipation at the crack tip, a similar effect may be achieved by changing the test temperature.

CHAPTER 4. BRITTLE-TO-DUCTILE TRANSITION (BDT) IN Cu FILMS.

It has been long recognized that the BDT in bulk materials may be associated with enhanced plastic energy dissipation. This can be achieved by either changing the state of stress (plane strain to plane stress) or by raising the test temperature (lowering the yield stress). The situation is somewhat different in thin films where the BDT can be achieved by increasing film thickness or in a limited temperature range, by raising the test temperature.

4.1 ELEVATED TEMPERATURE INDENTATION EXPERIMENTS

Elevated Temperature Experimental Setup

With the previous chapter demonstrating that interfacial fracture resistance increased with increasing Cu film thickness, it is of importance to establish how *G* varies as a function of test temperature. For this purpose a resistance heating stage (Figure 69) from Digital Instruments [180] was used in conjunction with the Nanoindenter II. The heating accessory consists of a sample heater and an electronic controller, which allows for setting a desired temperature up to a 130°C with the 0.1° resolution. The heater is a ceramic block that contains an embedded resistive microheater. With a sample glued to a puck using thermoepoxy, this assembly is then clamped onto the top of the microheater with the thermocouple sample clamp (Figure 69). The heating element is thermally isolated from the surrounding atmosphere as the sample is the only surface that conducts heat into the atmosphere. Since the loads used were relatively high (up to 600 mN), operation of the Nanoindenter II was not disturbed with the presence of a heater.

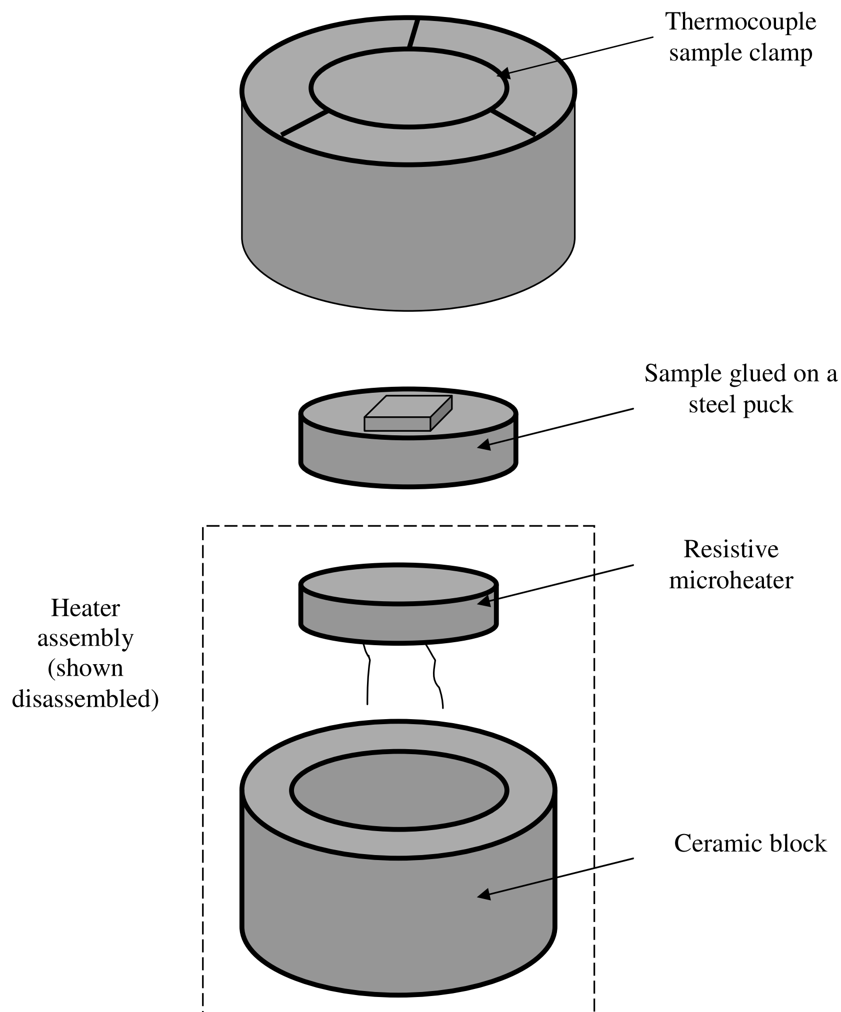

Figure 69. Heater assembly components.

Initially, the original thermocouple sample clamp did not provide enough mechanical force to clamp the steel puck to the heater, which resulted in the sample movement during indentation, producing artifacts in the indentation load-displacement curves for the W/Cu samples (Figure 70). This was fixed by modifying the clamp, and for all further indentation experiments the load-displacements curves obtained with the heater were compared to the curves obtained in the regular Nanoindenter II setup to ensure absence of the sample motion or sliding. All samples mounted on the heater were indented at room temperature prior to and after conducting temperature indentation experiments. The sequence of increasing temperature indentations was performed on each sample, followed by the room temperature experiments to ensure that there were no annealing effects.

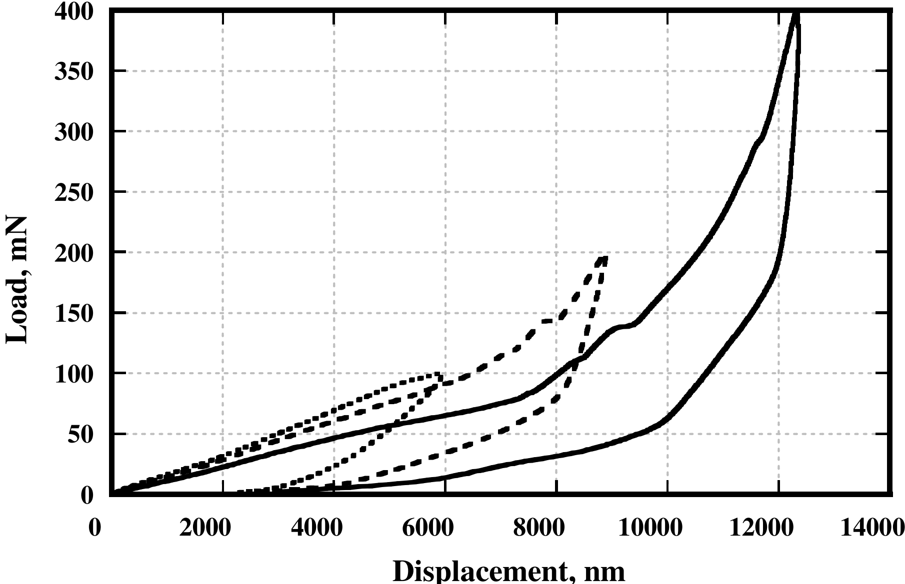

Figure 70. Load-displacement curves reflecting sample motion during indentation.

Thin Film Constitutive Properties At Elevated Temperatures

It was also necessary to establish the constitutive relationship for the yield strength of copper films as a function of thickness and test temperature. Initially, with nanoindentation, Cu film constitutive properties were determined by converting hardness data. Tests were carried out with the Hysitron nanoindenter, an AFM attachment that combines nanoindentation and imaging of a tested area. First, Young's modulus and yield stress were determined from load-displacement curves for all Cu film thicknesses as detailed in Chapter 2. Even after substrate effect corrections, however, yield stress values appeared elevated as compared to these predicted by Wei and Hutchinson [140] and determined experimentally by Vinci et al. [106]. For that reason, the yield strength was measured by the inverse method as had been done before for room temperature data. For Cu, data have been generated from plastic zone size measurements in films of different thickness as a function of temperature. The extent of pile-up at the surface gives consistent and reasonable measures of the yield strength, employing equation (2.8) [142].

Unlike aluminum, copper does not have a dense surface oxide that prevents further thin film oxidation. Copper oxide (Cu_2O) is porous, and does not adhere well to copper; so Cu thin films are known to oxidize even at temperatures below 50 °C [181]. For example, if the sputtering chamber is not cooled down to room temperature before breaking the vacuum after a thin film deposition, films appears to be dark ruby red color, indicating oxidation. For sputtered Cu films the oxidation rate increases with temperature, following an inverse logarithmic rate law [181].

In the case of the dense W superlayer, passivated Cu does not form an oxide, so fracture indentation experiments are safe in terms of the Cu oxidation. However, oxidation is the main obstacle for the constitutive properties determination experiments, since the surface oxide will affect them drastically. For the elevated test temperatures initially data was generated by Neville R. Moody on Au films prepared similar to Cu films with a thickness of 2.7 μm. This film was then indented at depths ranging from about 20 nm to as large as 2000 nm at test temperatures of 20°C to 130°C. Figure 71 shows the elastic modulus change with the apparent test temperature for the gold film. For indentation depths over 1 um the modulus saturates at a 140 GPa, close to the substrate value. At room temperature the

modulus plateaus at about 90 GPa for a 100 nm indentation depth. It drops down to the gold bulk value of 70 GPa at 130 °C. Young's modulus depends on the composition, crystal structure, and bonding. Heat treatment has little effect on the modulus, as long as it does not affect the mentioned parameters. However, the Young's modulus for bulk materials at the melting point is typically between one-half to two-thirds the room temperature value. At elevated temperatures a modulus drop is expected due to thermal expansion and an increased amplitude of atomic vibrations. For example, for bulk Cu, a drop of 20 GPa in modulus corresponds to a temperature increase of a couple hundred degrees [182]. It seems that the apparent temperature has a more drastic effect in nanocrystalline thin films.

The change in elastic modulus is much less pronounced than the yield stress change, since plastic deformation is a thermally activated process (equation (2.16) as an example for thin film low temperature plasticity). As seen in Figure 72, after about a 200 nm contact depth, the apparent yield strength increased due to a substrate effect. The initial plateau was used to estimate the true yield strength of Au as a function of test temperature in Figure 73. A second order polynomial seems to be the best fit to the Au yield stress temperature data. For the 2.7 um Au film the yield stress has the following dependence on temperature, T in Celsius:

$$\sigma_{Au\,YS}(T) \approx 550\ MPa + 0.0112T^2 - 4T \qquad (3.24).$$

As the yield stress of the same thickness Cu film falls on the Au line, and Cu and Au are both face-centered cubic with similar elastic moduli and melting points, to first order one can assume that these nanocrystalline films have a similar thermal component of the yield stress. Knowing the room temperature yield stress of Cu and assuming the same thermal component of the Cu yield stress:

$$\sigma_{Cu\,YS}(T) \approx \sigma_{Cu\,RT} + 0.0112T^2 - 4T \qquad (3.25).$$

Employing equation (3.25), Cu yield strength versus temperature curves are constructed for two film thicknesses of interest (Figure 73).

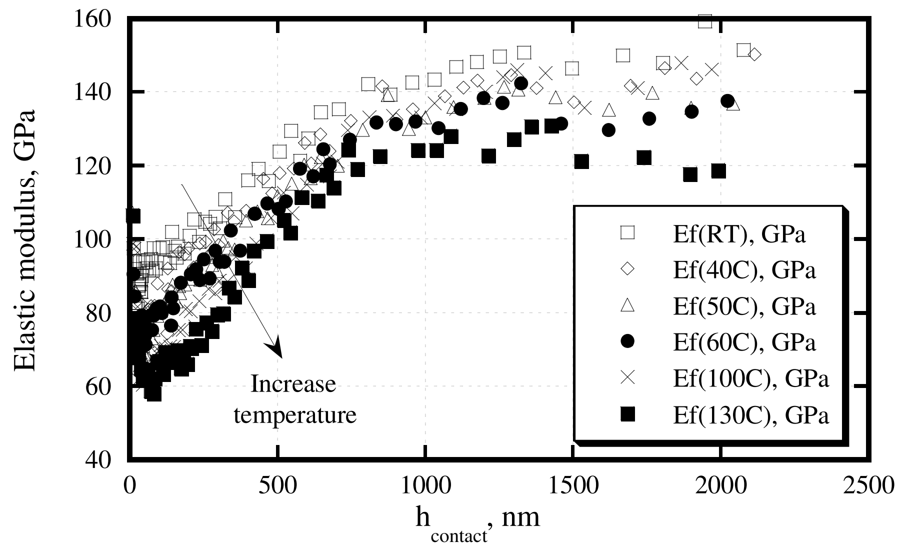

Figure 71. Elastic modulus as a function of indentation depth for Au films at different testing temperatures.

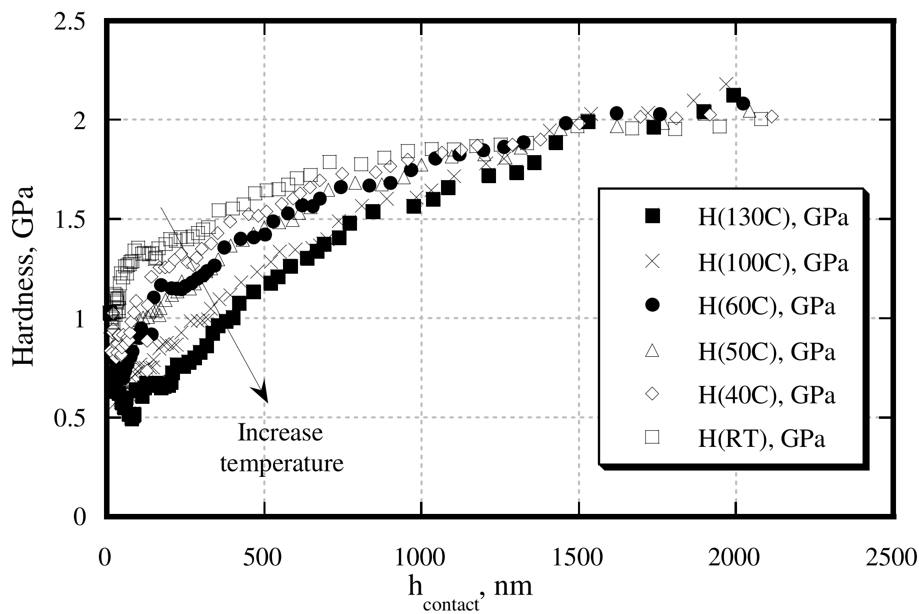

Figure 72. Hardness as a function of indentation depth for Au films at different testing temperatures.

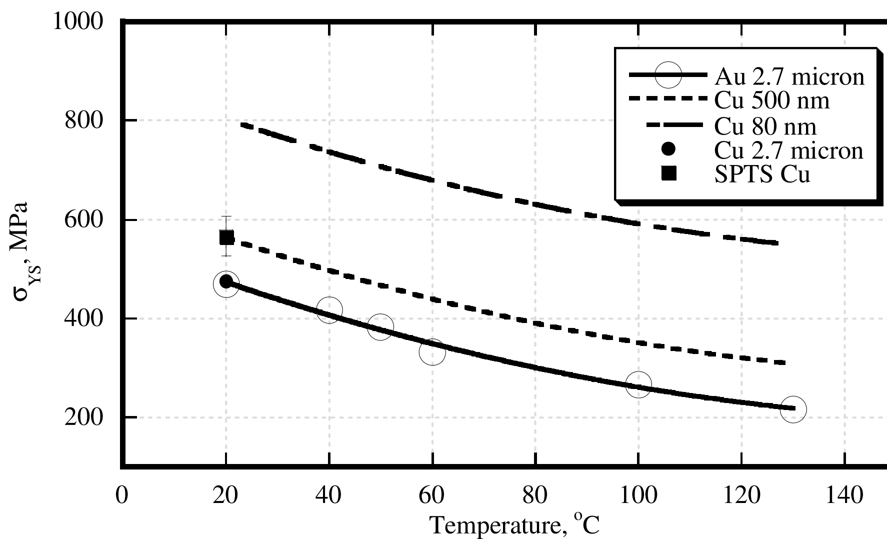

Figure 73. Yield stress variations of Cu and Au thin films.

Jiang, et al. [183] had characterized ultra-fine grained Cu as a function of annealing temperature. That study produced fine-grained Cu by severe plastic torsional straining (SPTS) of rods 12 mm in diameter. These were then tested for microhardness as a function of annealing temperature. Average grain size data of about 150 nm are utilized here as this approximately represents the 500 nm thickness Cu films used in the present study. Taking their room temperature data and superimposing it on Figure 73, it is seen that this agrees reasonably well. Since annealing will decrease the yield strength less rapidly than testing at the same temperature, their slightly higher yield strengths with annealing temperature (e.g. 430 MPa for 130°C anneal versus our 330 MPa for a 130°C test) is expected. This nevertheless points out the need for more careful measurements of yield strength as a function of test temperature in these nanocrystalline thin films. One of the ways to do so would be to perform indentation tests in ultra-high vacuum, which may not be readily available. The other possibility would be to use a protective passivation layer. The layer would have to have similar mechanical properties, high oxidation resistance, and form good bonding with the Cu film. Gold, for example would not work as an oxidation protective layer, since it will rapidly diffuse into Cu.

For the present study a thin 5 nm Pt layer was sputtered on top of 3.2 um thick Cu film for the constitutive properties determination. This prevented Cu oxidation up to the highest test temperature of 130 °C. Hardness was measured by Neville R. Moody at Sandia National Laboratories using the Nanoindenter II with a 300 nm sharp Berkovich tip. Both drift corrected and uncorrected hardness results are shown in Figure 74. Drift correction seems to be a more accurate method for the high temperature experiments, and provides more reliable data, although high Cu hardness values are somewhat disturbing, implying an indentation size effect [184]. The more accurate inverse method described in Chapter 2 should be used for more reliable hardness assessments. Similar to the gold hardness result, a second order polynomial provides almost a perfect fit the data, so as for now, the extrapolated Cu plastic properties are used for further theoretical predictions.

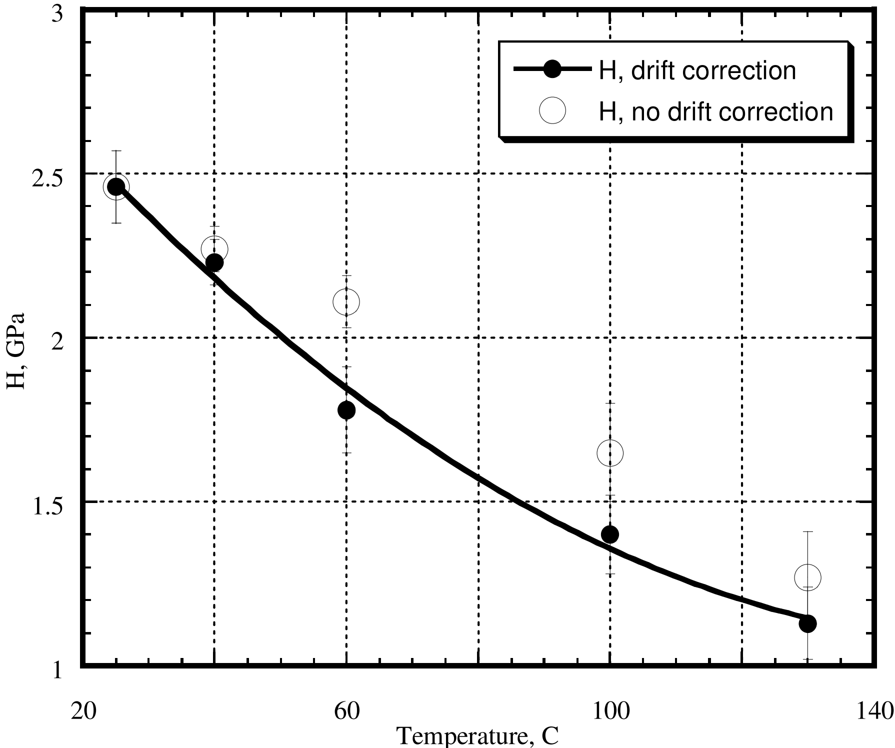

Figure 74. Hardness of a Pt-passivated Cu film as a function of test temperature.

Cu Adhesion At Elevated Temperatures

The superlayer indentation test with a 1 μm tungsten film on top of thin copper films bonded to SiO_2/Si wafers was used to measure Cu film adhesion at elevated temperatures. Initially, 80 and 500 nm thick Cu films have been selected to conduct high temperature adhesion experiments. These films were indented at 20, 60, 100 and 130 °C for the maximum loads of a 100, 200 and 400 mN with a 90° 1 um radius conical tip. There were three indentations performed at each load, resulting in 9 total indents for each test temperature. As the test temperature increased, the delamination radius decreased indicating increased interfacial toughness at elevated temperatures (Figure 75).

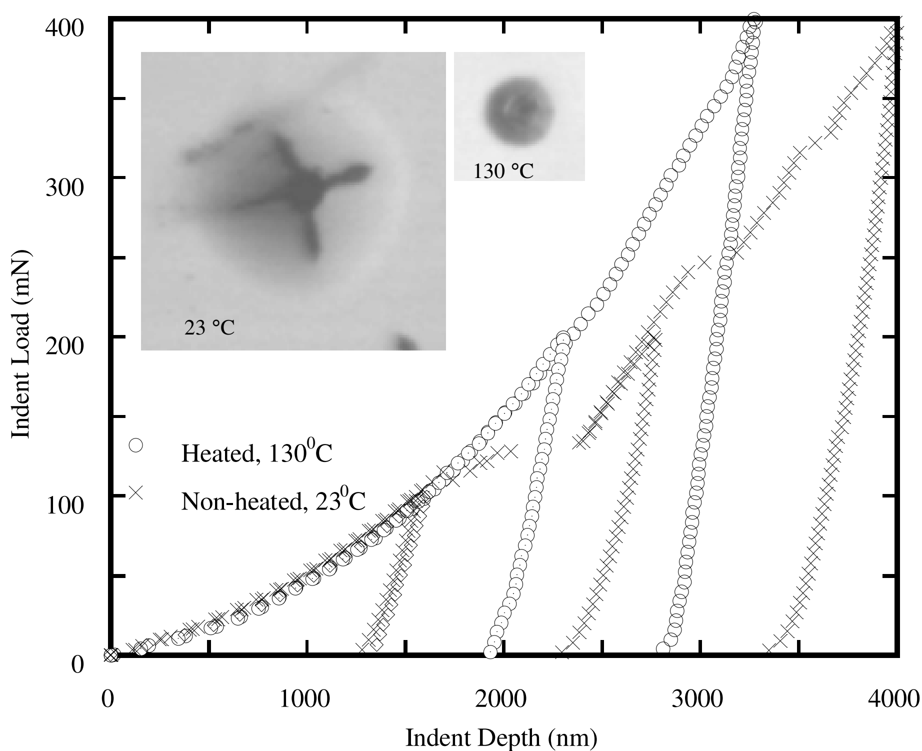

Figure 75. Indentation induced delaminations in a 500 nm thick Cu film at ambient and room temperatures alongside the corresponding indentation curves.

Load-displacement curves with the blisters corresponding to the 400 mN maximum load are presented in Figure 75. The load displacement curves are fairly smooth at 130°C but disrupted by a number of displacement excursions at 23°C. These are believed to be associated with fairly abrupt delamination events although some involvement of radial cracking in the tungsten superlayer could be present as well. At identical loads of 400 mN, it is clear from the insert micrograph that the delamination radius at 23°C was nearly three times as large implying a much lower fracture resistance at room temperature. This is seen in Figure 76 where the strain energy release rate determined from the superlayer driving force concept increases by more than an order of magnitude.

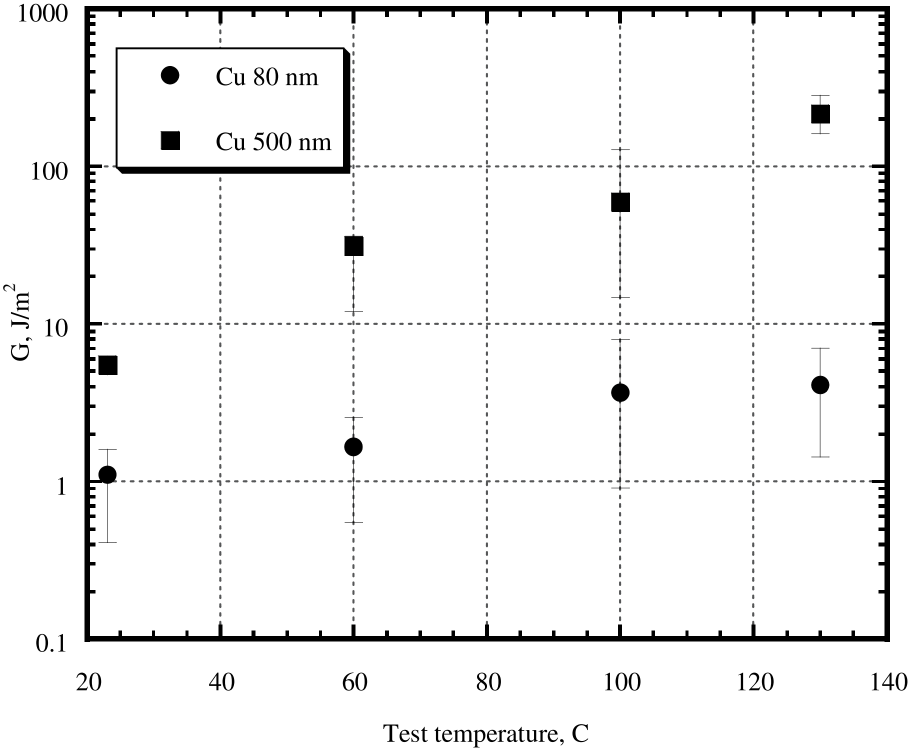

Figure 76. Temperature effects on interfacial toughness for 80 and 500 nm thick Cu films.

As discussed in Chapter 1, except for the constitutive thin film properties, there are two measured parameters representing thin film adhesion: delamination blister radius and indentation depth. As seen in Figure 75, there is no difference in the indentation depth for the lowest 100 mN load indents. However, due to the load excursions, the indentation depth would be greater at room temperature for the higher load indents. For a fixed delamination radius, this would result in higher interfacial toughness. However, the strain energy release rate scales with 1/(blister diameter)^4, so it increases due to the smaller blister size at 130 °C (Figure 75).

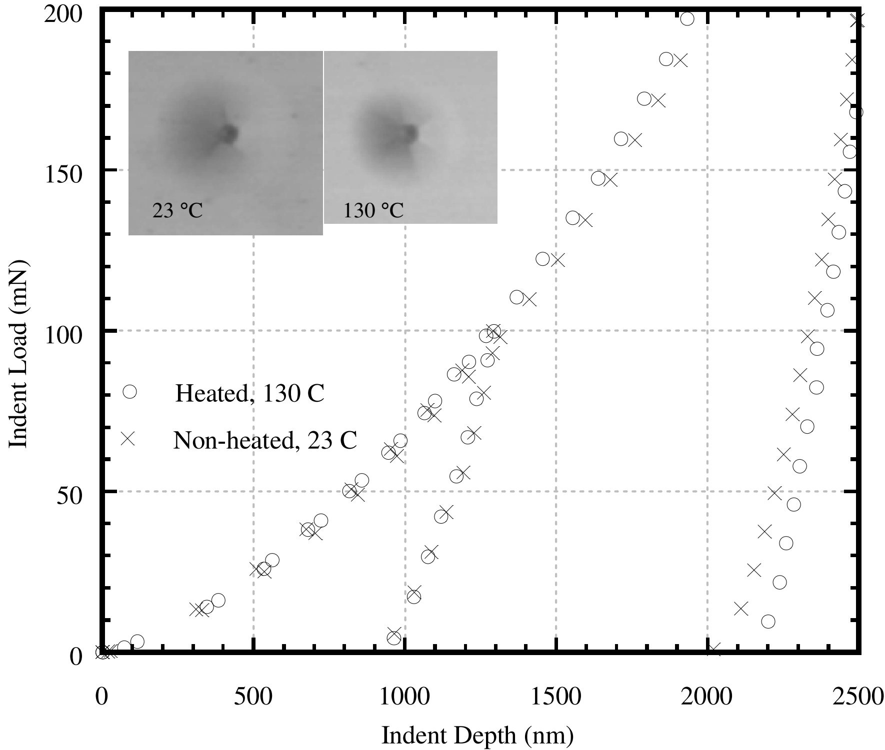

Figure 77. Indentation induced delaminations in an 80 nm thick Cu film at ambient and room temperatures alongside the corresponding indentation curves.

A 500 nm thick Cu exhibits more than an order of magnitude increase in fracture energy from about 5 to 200 J/m^2 as the test temperature is raised from 20°C to 130°C. The room temperature adhesion value of 5 J/m^2 is higher than the one reported in Chapter 3 for the same film thickness, because the load excursions were not subtracted from the indentation depth in this case.

For 80 nm thick Cu films there is almost no difference in the load-displacement curves, though the blister size decreases with the test temperature just like for a thicker film, which results in an adhesion increase from about 1 J/m^2 to 4.1 J/m^2 for the 100 degrees test temperature increase (Figure 76).

4.2 THEORETICAL MODELING

As shown in Chapter 3, the amount of plastic energy absorption during interfacial fracture is limited by film thickness. An order of magnitude change in adhesion with the temperature change of a 100 degrees was unanticipated. The interfacial fracture energy for a 500 nm thick Cu film at a 130 °C translates to a stress intensity of 5 MPa-m$^{1/2}$. In context of the highest possible nanocrystalline Cu yield strength, this represents a plastic zone of nearly 30 μm. This illustrates the quandary associated with explaining such high apparent toughness values as one generally expects plasticity to be truncated by film thickness. Is this associated with:

- Some artifact of assessing local stresses during nanoindentation at elevated temperature;
- Extending the plastic zone in the direction of crack growth much further than the film thickness;
- A shielding mechanism from an organized dislocation array in a ductile film sandwiched between a brittle substrate and a higher yield strength superlayer;
- Some plastic energy dissipation in the superlayer;
- Or by enhanced mode II at higher temperatures?

Following Gerberich, et al [146], some of these will be addressed in some detail with a goal of narrowing the field to the most promising candidates.

Dislocation Free Zone (DFZ) Model

For brittle-to-ductile transitions the original Thomson's analysis [168, 169] and the Rice-Thomson [167] criterion can be applied. The original concept for brittleness was that a local crack-tip stress intensity, k_I, exists and

if $k_I > k_{Ie}$, a crack-tip dislocation emits

if $k_I > k_{IG}$, a brittle crack grows.

With the first condition, a dislocation emission at k_{Ie} leads to crack-tip blunting and ductile behavior. At the second condition, brittle fracture occurs when the Griffith value, k_{IG}, is reached first. This makes sense for the thin-film fracture behavior observed in Figure 57, Chapter 3, where there is a plateau observed at $G_I \sim 0.6\text{-}0.9$ J/m^2 up to film thickness near 100 nm. This could be associated with “brittle” interfacial fracture in the “absence” of dislocation emission. At greater thicknesses, the applied K_I rises necessitating an increase in local k_I, sufficient to trigger dislocation emission at k_{Ie} with attendant localized plasticity. To test the plausibility of such a scenario, the original model of Thomson [168] is invoked, giving

$$k_I = \frac{3}{\pi}\sqrt{\frac{2}{\pi}}\sigma_{ys}\sqrt{c}\left[ln\left(\frac{4R_p}{c}\right)+\frac{4}{3}\right] \quad (4.1).$$

Here, c is the dislocation free zone and R_p is the plastic zone size. Squaring both sides and placing 4/3 inside the argument gives

$$k_I^2 = 0.58\sigma_{ys}^2 c\left[ln\left(\frac{4R_p e^{\frac{4}{3}}}{c}\right)\right]^2 \quad (4.2).$$

The physical picture is schematically shown in Figure 78, where at the transition, a dislocation has just been emitted and is trapped at about $h/3$ between the crack-tip and the

tungsten superlayer. Some intermediate position would be realistic due to the higher modulus superlayer providing an image force of opposite sign to the crack-tip force. A dislocation is shown here on a vertical slip plane between columnar grain boundaries but it could just as easily be on an inclined slip plane or be a grain-boundary dislocation. Such details aren't warranted at this stage of development. The position $h/3$ is reasonable but an *ad hoc* choice since it gives the transition point in Figure 57. Taking the transition to occur at 80 nm, an 80 nm film would have a yield strength of 806 MPa from equation (2.7). For the first dislocation emitted to $c = h/3$ this would be the plastic zone size giving, $R_p = c = h/3$ as the emission condition. This gives

$$k_{Ie}^2 = 0.58\sigma_{ys}^2\left(\frac{h}{3}\right)\left[ln\left(15.2\right)\right]^2 = 1.43\sigma_{ys}^2 h \quad (4.3).$$

For the transition point, this then gives k_{Ie} = 0.27 MPa-m$^{1/2}$. This is also internally consistent with $k_{Ie} = k_{IG}$ as the interfacial fracture energy for the driving force would be

$$G_I = \frac{k_{IG}^2}{E} \approx 0.7\, J/m^2 \quad (4.4),$$

as is observed.

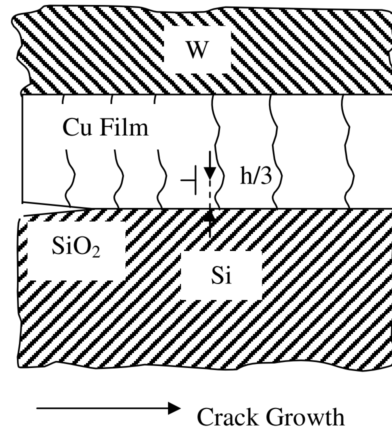

Figure 78. A physical picture corresponding to local crack tip stress intensity, k_I just above a dislocation emission value, k_{Ie}.

This also is consistent with the calculated emission condition for copper cited in the original Rice-Thomson paper [167] to be 0.32 MPa-m$^{1/2}$. Fixing the position of $c = h/3$ for the

transition strongly suggested the following: if this were the nearest dislocation to the crack tip for emission and fracture occurred at this point, then somehow c should remain invariant for all higher thicknesses as well. That is, the interface as it initially is deposited should be of the same morphology and have the same chemistry for a 100 nm film as it does for a 1000 nm film. Since the distance between the crack tip and the nearest dislocation would also fix the local stress, as shown by simulation [185], then the decohesion stress being the same for a 100 nm film compared to a 1000 nm film implies that $c \sim$ constant. The idea is similar to the plasticity-free strip model of Suo, Shih and Varias (SSV) [186]. This hypothesis can be tested by applying the Dugdale plastic zone for R_p, which is

$$R_p = \frac{\pi K_I^2}{8\sigma_{ys}^2} \quad (4.5).$$

With equation (4.1), this gives

$$K_I^2 = \frac{\sigma_{ys}^2 c}{5.96} exp\left\{\frac{k_I}{0.76\sigma_{ys}c^{1/2}}\right\} \quad (4.6).$$

Defining $A = c/5.96$ and $B = 0.76\ c^{1/2}$ and taking the log of both sides one finds:

$$ln\left(\frac{K_I^2}{\sigma_{ys}^2}\right) - ln\,A = \frac{k_{IG}}{B\sigma_{ys}} \quad (4.7).$$

Thus, if the hypothesis that $c \sim$ constant is correct, then a plot of $\ln(K^2_I/\sigma^2_{ys})$ vs. k_{Ii}/σ_{ys} should collapse all data for a given film/substrate combination. Before further describing the deadhesion results, all data representing averages of (~ 10) room temperature tests at each of eight thicknesses and nine tests at each of two thicknesses for each of four temperatures were plotted according to equation (4.7). For this, the value of K_I was taken as $[EG_I]^{1/2}$ from the superlayer driving force calculation. Also, k_{IG} was taken as 0.27 MPa·m$^{1/2}$ and yield strength was calculated for each thickness from (2.7). These are reported in Table 6 and Table 7 for varying test temperature and film thickness respectively. The results in Figure 79 are reasonable with only a few outliers, so the use of $c \sim$ constant in further calculations is appropriate. Admittedly, this is a log scale and one of the outliers could deviate considerably; but the data collapsed sufficiently well to assume invariance in the dislocation free zone size parameter for both film thickness (Table 7) and test temperature (Table 6) variations.

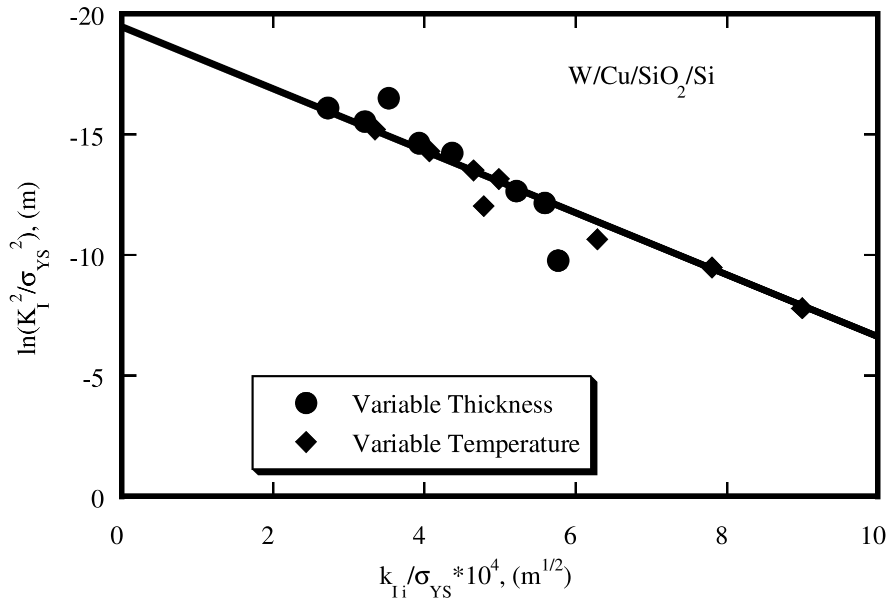

Figure 79. Evaluation of an assumption of a constant DFZ radius.

The dislocation free zone size can be found from a series of experimental/computational studies utilizing discretized dislocation theory for Fe-3wt%Si single crystals [187-189]. The concept was to describe the equilibrium of forces at a crack tip after dislocation emission by utilizing a discretized array of five dislocations at the crack tip with a single superdislocation representing any for field plasticity. The computer solution allowed all dislocations to move and find their equilibrium positions, which finally dictated the closest approach of the nearest dislocation to the crack tip, *c*, as depicted in Figure 80. The numerical simulations for Fe-3wt%Si and Mo single crystals found for an applied stress intensity of 8 MPa-m$^{1/2}$ that *c* ranged from 5 to 70 nm. Values could be even larger for smaller values of K_I. From these, it was found that the crack-tip to nearest dislocation size, *c*, could be given by an analytical solution:

$$c = \frac{\alpha'}{\sigma_{ys} \, ln(K_I \beta')} \qquad (4.8).$$

Using this equation, one was able to predict brittle to ductile transition in Fe-3wt%Si large-grain polycrystals, as repeated in Figure 81. Interfacial toughness is found from equation (4.8):

$$K_I = \frac{1}{\beta'} exp\left(\frac{\alpha'}{\sigma_{ys} c}\right) \quad (4.9),$$

where $\beta' = 20\ \mathrm{MPa^{-1} \cdot m^{-1/2}}$ as used in the original simulation, and α' is about 120 Pa·m, found using $c = 80$ nm as a cut-off for the brittle-to-ductile transition along with the threshold toughness value of 0.7 J/m^2 in Figure 57. With $c = 80$ nm α' is only one-third smaller than the constant used to predict brittle fracture in Fe-3wt%Si. Equation (4.9) represents the Dislocation Free Zone (DFZ) model [146].

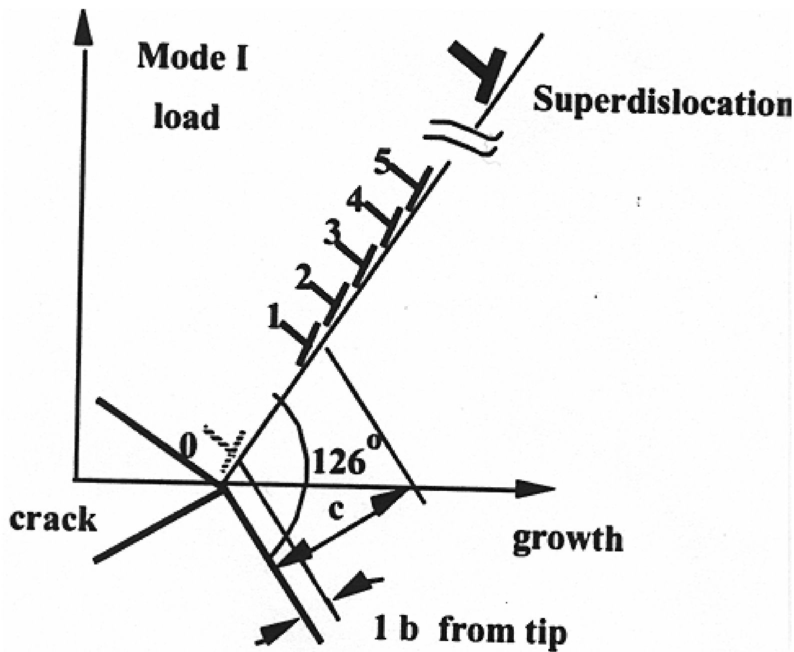

Figure 80. Shielding dislocations at a Mode I crack tip under a far-field K_I in an Fe-3wt%Si single crystal loaded in ⟨100⟩. Single dislocations affect the near-tip local stress intensity, k_{tip}, while the superdislocation representing the far-field plasticity is associated with K_I.

Table 6. Experimental values of k_{Ii}/σ_{ys} and K_I/σ_{ys} obtained from k_{Ii}=0.27 MPa·m$^{1/2}$ and K_I from average G_I values obtained for each test temperature.

	80 nm				500 nm			
	20 °C	60 °C	100 °C	130 °C	20 °C	60 °C	100 °C	130 °C
G_{Ii}	1.1	1.6	3.7	4.1	5.5	30	60	215
K_I	0.363	0.438	0.666	0.701	0.77	1.90	2.68	5.08
σ_{ys}	806	660	580	540	560	430	345	300
$(k_{Ii}/\sigma_{ys})\cdot 10^4$	3.35	4.09	4.66	5.0	4.82	6.28	7.82	9.0
$ln(K_I^2/\sigma_{ys}^2)$	-15.4	-14.6	-13.5	-13.3	-13.1	-10.8	-9.71	-8.16

Table 7. Experimental values of k_{Ii}/σ_{ys} and K_I/σ_{ys} obtained from k_{Ii}=0.27 MPa·m$^{1/2}$ and K_I from average G_I values obtained for each film thickness.

	40 nm	70 nm	100 nm	180 nm	500 nm	1 um	2 um	3 um
G_{Ii}	0.7	0.9	0.3	1.6	1.7	7.0	10	100
K_I	0.290	0.329	0.190	0.438	0.452	0.917	1.095	3.46
σ_{ys}	974	834	763	670	562	515	481	466
$(k_{Ii}/\sigma_{ys})\cdot 10^4$	2.77	3.24	2.54	4.03	4.80	5.24	5.61	5.79
$ln(K_I^2/\sigma_{ys}^2)$	-16.2	-15.7	-16.6	-14.7	-14.2	-12.7	-12.2	-9.8

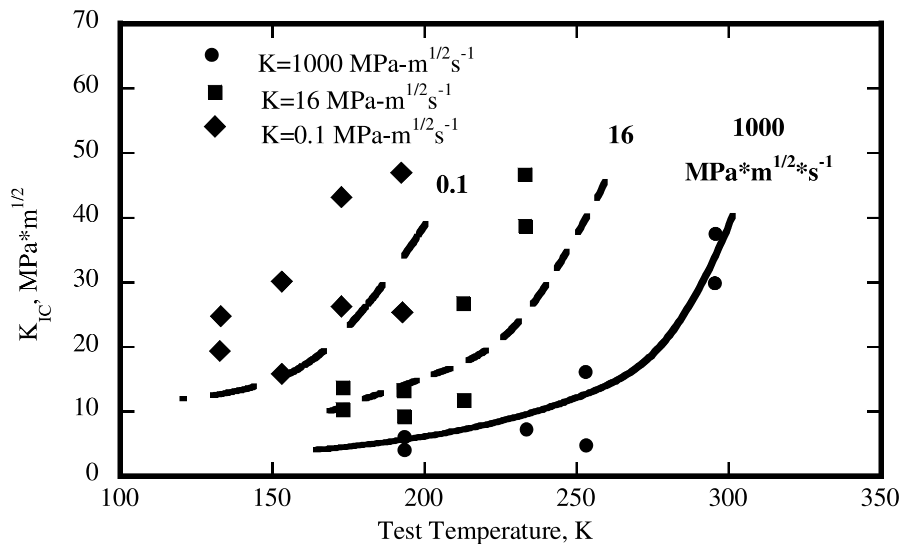

Figure 81. Theoretical predictions (equation (4.9)) for ductile-to-brittle transition in Fe-3wt%Si as compared to experimental data [187].

DFZ Model Validation

In this section a comparison between the DFZ model and the actual interfacial toughness data is made for varying test temperature and film thickness. For the 80 nm thick films, it is seen that the transition is near room temperature and the fracture toughness in terms of strain energy release rate increases by about a factor of five with increasing temperature. This is predicted reasonably well in Figure 82. Similar test data for 500 nm thick Cu films is evaluated. In Figure 83 the strain energy release rate determined from the superlayer driving force concept increases by more than an order of magnitude. This appears to be mimicked quite well by the dislocation concept (DFZ model) represented by the same value of c = 80 nm and yield strength as a function of test temperature using equation (4.9). Since the constants β', α', and c were not changed throughout these calculations, it is seen that the only variation is yield strength. At least to first order, it appears that thin-film delamination of Cu/SiO_2 interfaces is predominantly controlled by yield strength, where this depends on both film thickness and temperature. Of course if the interface strength were changed by different deposition techniques or interfacial chemistry, then one or more of the constants, α', β' and c, would necessarily change.

The DFZ model also seems to predict the Cu film fracture toughness as a function of thickness quite well (Figure 85). It has both the right magnitude and the correct trend with thickness even though thickness is absent in equation (4.9) except through its relationship to σ_{ys} in equation (2.7). This would predict that fracture resistance would plateau for these Cu films at thicknesses greater than about 100 μm where the yield strength would be expected to change further by less than three percent.

As one examines Figure 83, the first aspect that jumps out is to whether one can justify the rapid rise in toughness observed between 100°C and 130°C. A simpler question is whether one can even justify a toughness level of 200 J/m^2 in a 500 nm thick Cu film. With G_I converted to K_I = 4.9 MPa·m$^{1/2}$, a plane strain plastic zone size would be 28 μm in size. This is not possible in a 500 nm thick film unless the zone tunneled in between the W and SiO_2 to an aspect ratio of about 50. Using higher yield strength data somewhat between ours and the annealing data from Jiang, et al [183] or from Figure 74 only slightly improves this implausible picture. On the other hand, perhaps there is actually some crack tip deformation

in the tungsten superlayer at these high toughness levels. From literature values [165] of hardness in similar W films, which give $H \sim 7.5$ GPa, the yield strength is estimated to be 2500 MPa, which would result in a plastic zone of 0.41 μm. This suggests that the 1 μm superlayer is at least partially yielded and this would lead to greater plastic energy dissipation than the Cu itself due to its much higher yield strength. The other concern for the 500 nm thick Cu data is that there could conceivably be a contact plastic zone size/blister-tip interaction. Consider the schematic shown in Figure 84. The W/Cu composite bilayer is shown as a single film with the crack having propagated at the Cu/SiO_2 interface. From equation (2.8), using the yield strength of W (note that the hardness of SiO_2 is similar to W), the calculated value for the indenter plastic zone is 8.7 μm still substantially less than the 12-14 μm blister radius observed. However, these are sufficiently close to justify concern for contact/blister interactions.

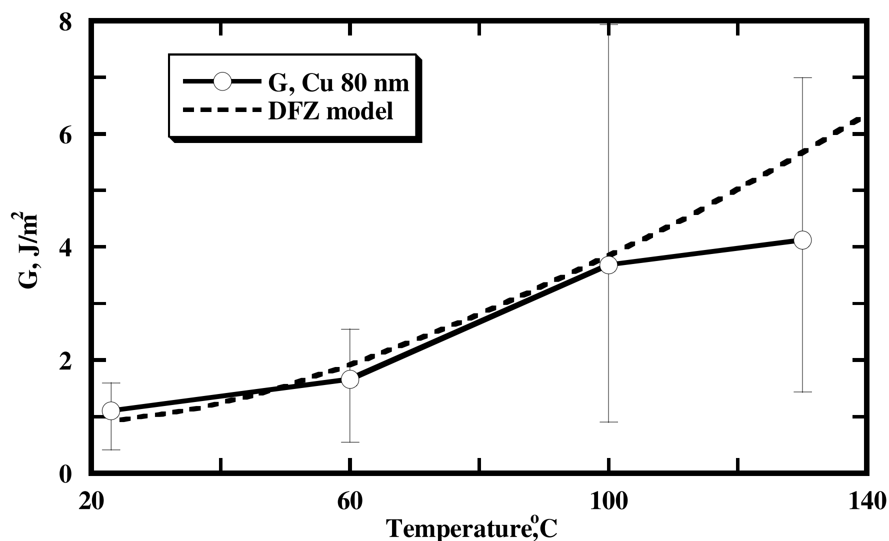

Figure 82. Temperature effects on interfacial toughness for 80 nm thick Cu film. Solid and dashed lines correspond to experimental results and theoretical prediction, respectively.

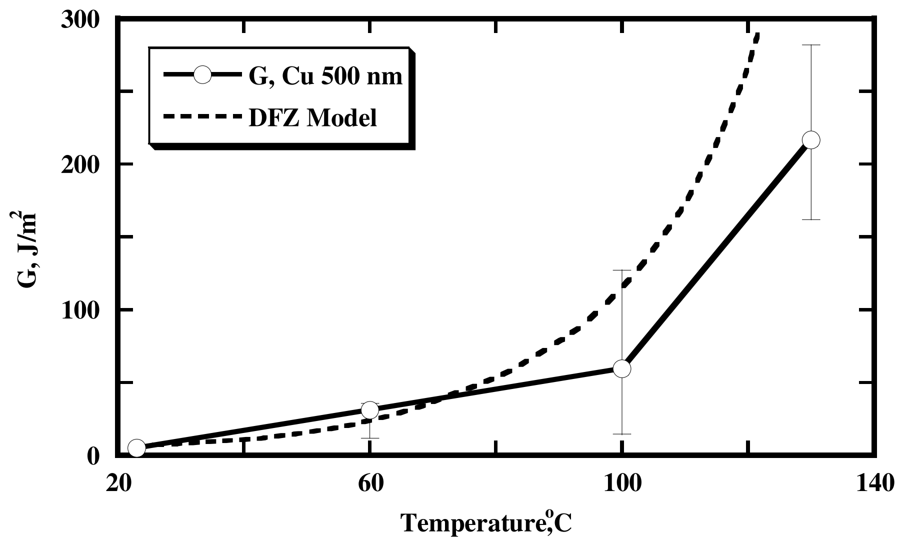

Figure 83. Temperature effects on interfacial toughness for a 500 nm thick Cu film. Solid and dashed lines correspond to experimental results and theoretical prediction, respectively.

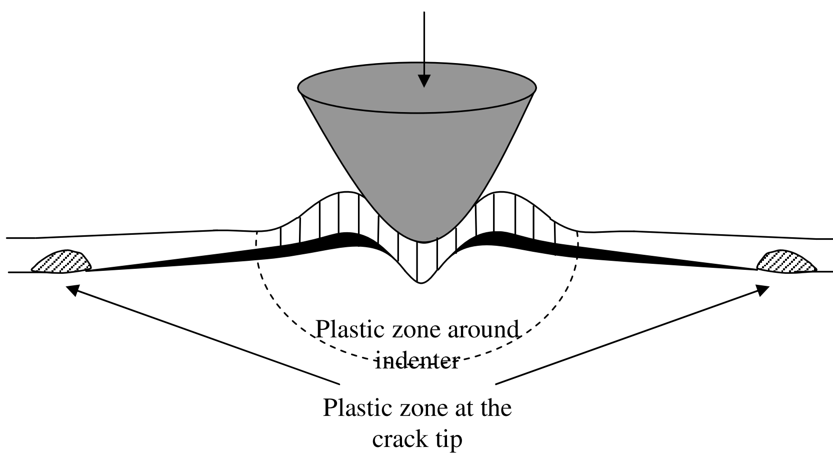

Figure 84. Schematic of an indentation induced delamination. For a strong interface plastic zone around an indenter and crack tip plastic zone may interact.

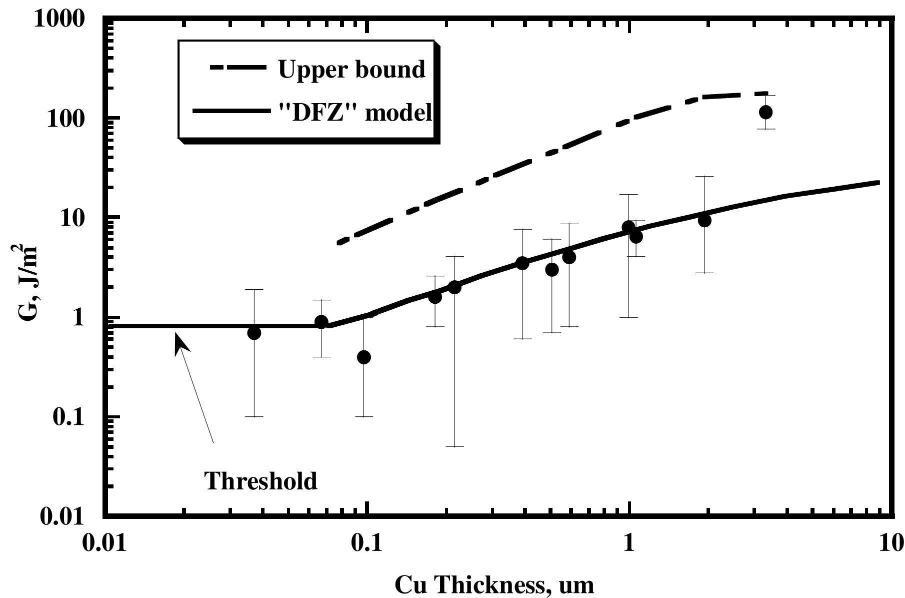

Figure 85. Comparison of experimental strain energy release rates and theoretical predictions as given by both an upper bound and a more precise DFZ model.

The concerns are less for thinner films where the measured driving forces for delamination are less. A determination of K_{Ic} = 0.69 MPa-m$^{1/2}$ at 130°C for the 80 nm thick films coupled with a yield strength of 560 MPa gives a plane strain plastic zone of 160 nm. As this is only twice the film thickness, this size zone could easily tunnel in between the W and SiO_2 as some multilayer computer simulations by Klein [190] have shown. Furthermore, one can show that this level of toughness would only produce an 8 nm plastic zone radius in the W superlayer allowing its effect to be considered secondary if not negligible. Finally, one can calculate the indenter plastic zone size in the W superlayer to be less than one-third of the blister radius suggesting that tip interaction effects are negligible for most of the data of Figure 85. Still, it is important to note that a large deal of the scatter shown in Figure 82, Figure 83 and Figure 85 is because all data have been shown rather than rejecting those which may have had tip-interaction effects. An example of such data shown in Figure 86, which demonstrates the effect as calculated from the bilayer solution compared to calculations from Vlassak et al [40], for the corresponding plane-strain solution. If an area of

the film is particularly well adhered or there is an additional barrier to crack nucleation, the plastic zone from the indentation becomes large prior to delamination. Then, it basically keeps up with the extent of delamination or at least causes a stress field interaction effect. This leads to additional resistance to the extent of delamination and as a result the blister radius is not much larger than the contact plastic zone and consequently, the contact radius. As can be seen in Figure 86, this could represent a nearly runaway toughness value for the smaller ratios of delamination to contact radii. This clearly would justify truncating such a data set and reporting G_I values for a specific range of data greater than a given ratio where such interaction effects can be shown to be negligible. Such approaches have yet to be fully specified.

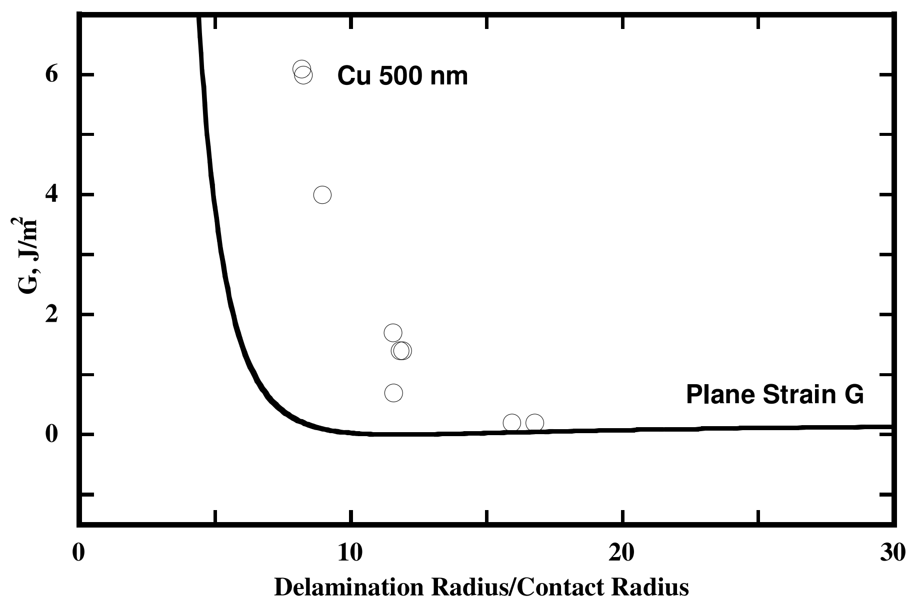

Figure 86. Strain energy release rate as a function of the normalized delamination radius for a 500 nm Cu film.

CHAPTER 5. THIN FILM FRACTURE ACOUSTIC EMISSION

Acoustic emission (AE) is a very powerful method for examining the behavior of materials deforming under stress. This covers fracture, yielding, fatigue, corrosion, creep, etc. in bulk materials, including composites [191]. Several researchers have tried to employ AE for the detection of yielding and fracture events in different thin film systems [192-195]. In the present study, acoustic emission in a Cu film during indentation-induced delamination is considered.

Acoustic Emission Signal

In a typical acoustic emission apparatus signal is recorded when it's level exceeds a certain pre-set threshold limit. The minimal threshold limit along with the sampling rate would define the system sensitivity. Typical parameters obtained from the signal are shown in Figure 87. These are the rise time (time from the detected threshold to the maximum signal level), the duration time, and the signal amplitude (Figure 87). Relative signal energy is calculated by integrating the signal. Some of these parameters reflect certain fracture aspects as discussed below.

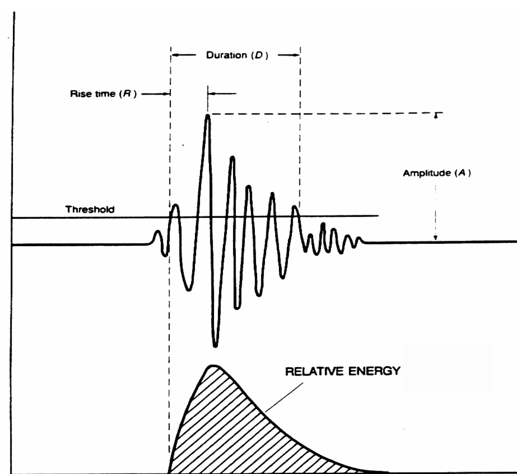

Figure 87. Parameters of a burst-type acoustic emission signal.

5.1 EXPERIMENTAL PROCEDURE

For all the experiments, 5x5 mm samples were bonded with cyanoacrylate to an acoustic emission sensor (100-1000 kHz frequency response range) from Physical Acoustics Corporation. All samples were indented with the IBM Micromechanical Tester (MMT) and the AE waves were recorded with the MISTRAS 2001 system by Physical Acoustics Corp. A schematic of the experimental setup is shown in Figure 88.

Acoustic Emission Setup

The MISTRAS 2001 is a fully digital, computerized, acoustic emission system that performs waveform and signal measurements [183]. The actual waves of the signals above a given threshold were recorded automatically during the indentation test (Figure 90). The preamplifier with a built-in 100-300 kHz filter was set to a 60 dB gain, and the signal was collected at a 10 MHz rate.

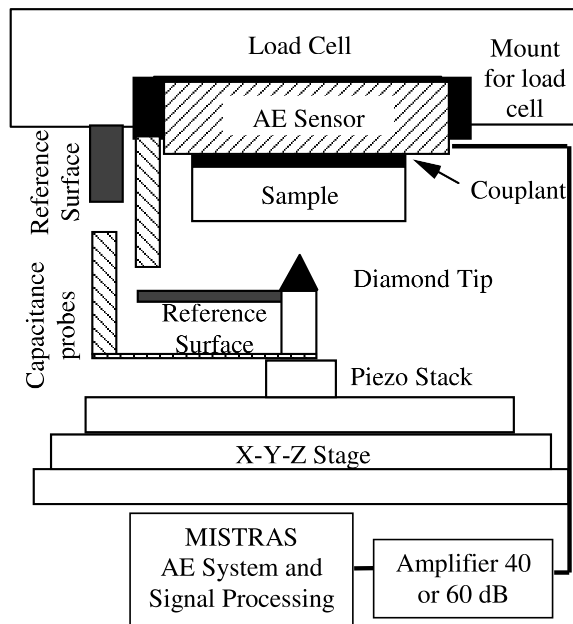

Figure 88. Schematic of the AE experimental setup.

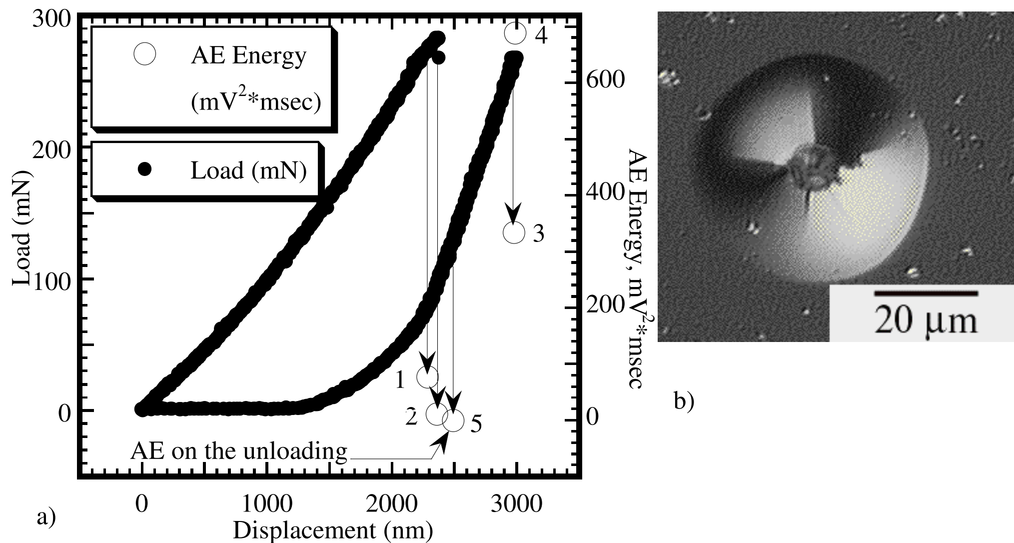

Figure 89. a) Load-displacement curve and acoustic emission events for a Ti/Cu/W indentation; b) Nomarski optical image of the corresponding blister.

5.2 ACOUSTIC EMISSION DURING THIN FILM FRACTURE

Acoustic Emission During Cu And Cu/Ti Film Fracture

Acoustic emission events for an indentation into 120 nm thick Cu film with Ti underlayer are presented in Figure 89. Excursions on the load-displacement curves were observed above a certain load level. For the indentation shown in Figure 89, the load excursion occurs during a constant load hold and four acoustic emission events of different magnitudes are associated with the excursion. One small AE event was observed on the unloading. The actual AE signals are shown in Figure 90. In Figure 91 it is clearly seen that the rise time is much higher for the maximum amplitude signal than for the rest of them. The rise time is not truly indicative of the lifetime of the event, but is a combination of the original signal, its reflections and the piezoelectric detector response. For a fixed energy level, the rate at which the energy is released by a defect in an idealized system is

proportional to the rise time [197]. Here, we find that the total acoustic emission energy changes with the rise time. At this point it is hard to define a functional relationship between the total AE energy and the rise time, but for both film systems, with and without Ti underlayer, the total AE energy increases with the rise time (Figure 91 and Figure 92).

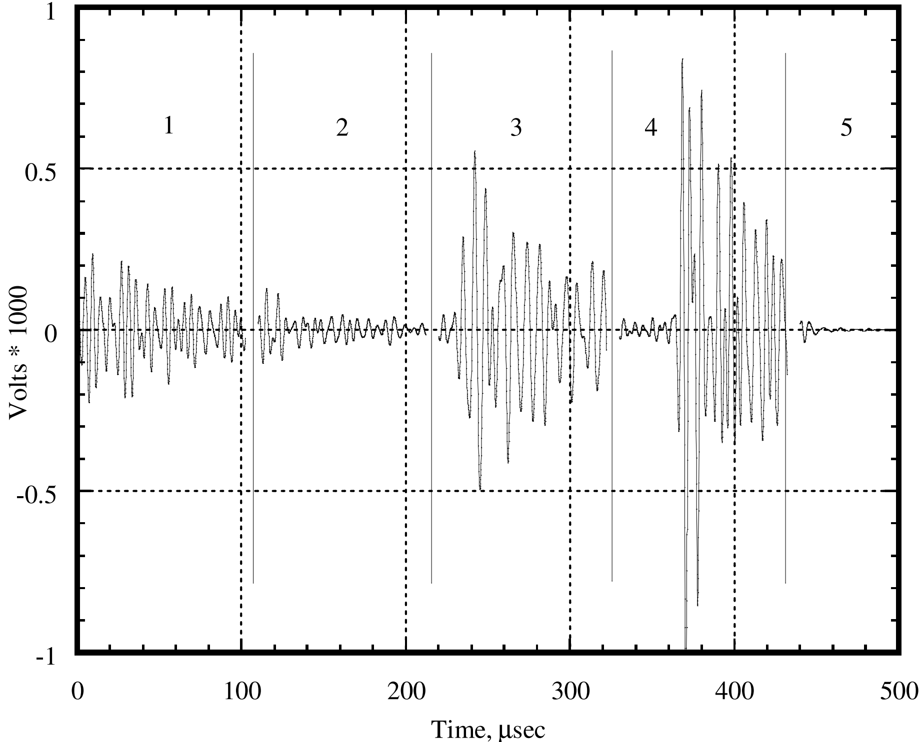

Figure 90. Acoustic emission signals during Ti/Cu/W indentation. Signals are put on the same time scale.

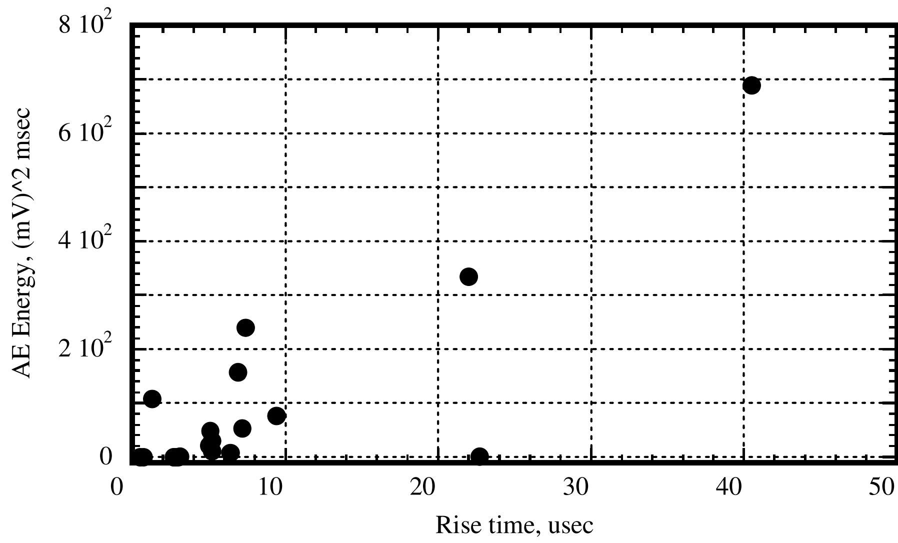

Figure 91. Total AE energy vs. rise time for Cu film with a Ti underlayer.

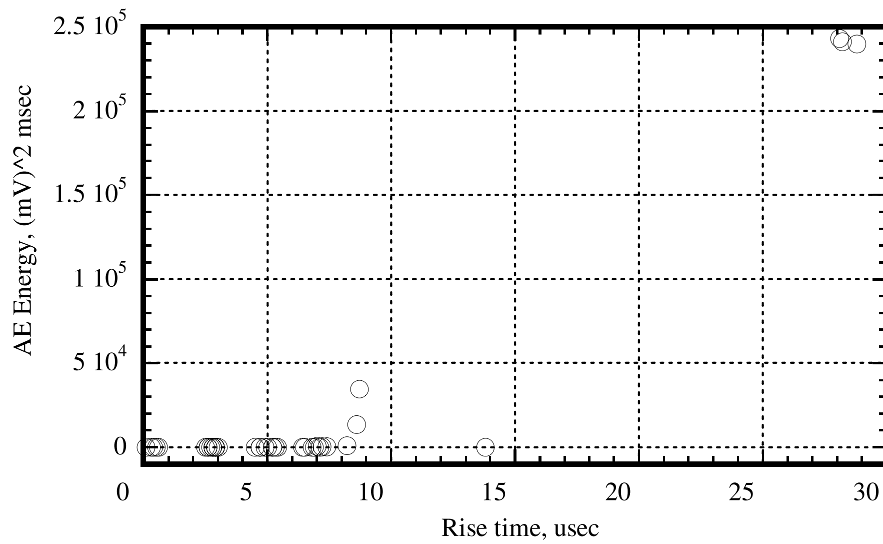

Figure 92. Total AE energy vs. rise time for Cu film without a Ti underlayer.

Acoustic Emission Energy Trends

As expected, the amount of emitted AE energy increased with the load and thus the blister size (Figure 93). What is interesting, though, is that the strain energy release rate, the measure of thin film adhesion, decreases with the total acoustic emission energy emitted. This result is the opposite of what was observed in previous studies on single crystal systems, where dislocation activity governs most acoustic emission [195]. For thin films systems the situation can be different, since the amount of the released acoustic energy is proportional to the crack area [198], and depends on the crack growth rate. In less well-adhered areas of the film (low *G* values) more acoustic energy could be released if delamination occurs in a single event. Alternatively, for the well-adhered areas of the film (high G values) much of the cracking is by subcritical crack growth in such small increments as to be below our detection threshold.

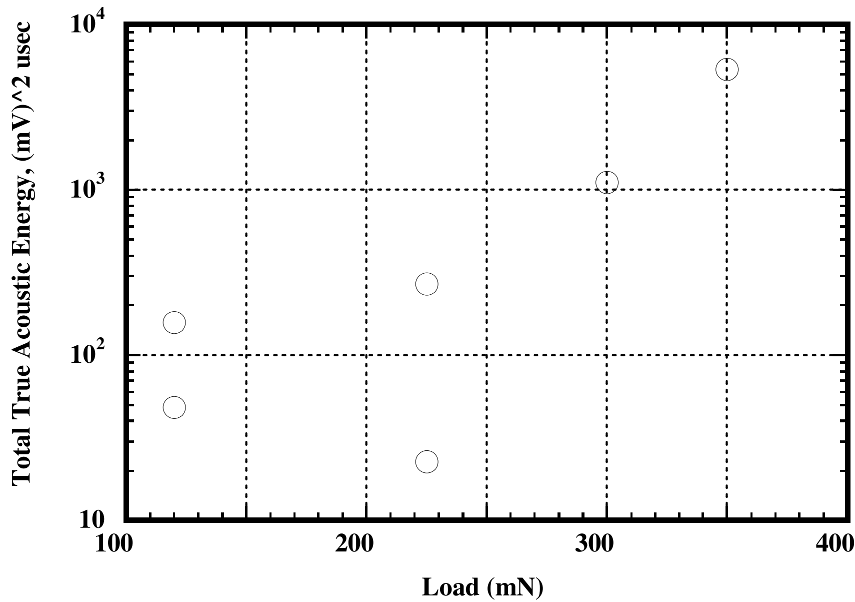

Figure 93. Total AE energy for the films with Ti underlayer.

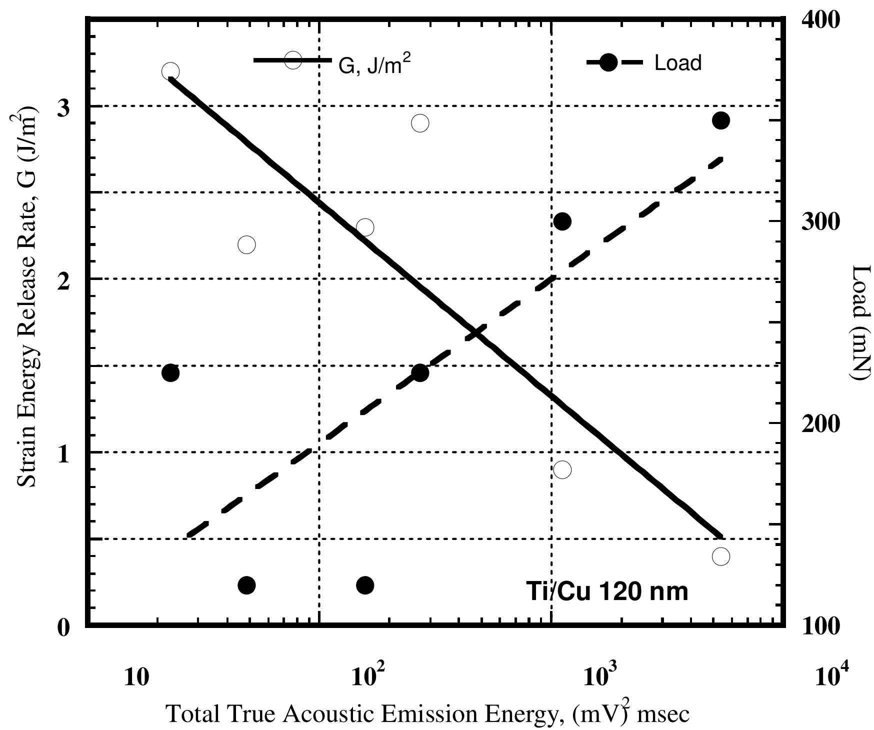

Figure 94. Strain energy release rate for the films with Ti underlayer.

In order to determine that the collected acoustic emission signals are not associated with substrate cracking due to the high normal loads, a plane Cu film without the W superlayer was also indented. For a given load, the distance between the indenter tip and a film/substrate interface is much lower in this case, compared with the W superlayer. Figure 95 shows the total true acoustic emission energy for an uncovered Cu film, and the superlayer structure, with and without the Ti adhesion-promoting underlayer. The magnitude of the total acoustic energy is much higher for the films without Ti underlayer. As discussed in Chapter 3, for the same film thickness Ti increases Cu film adhesion by an order of

magnitude, thus for a given load much smaller blister radii will result, emitting less acoustic energy.

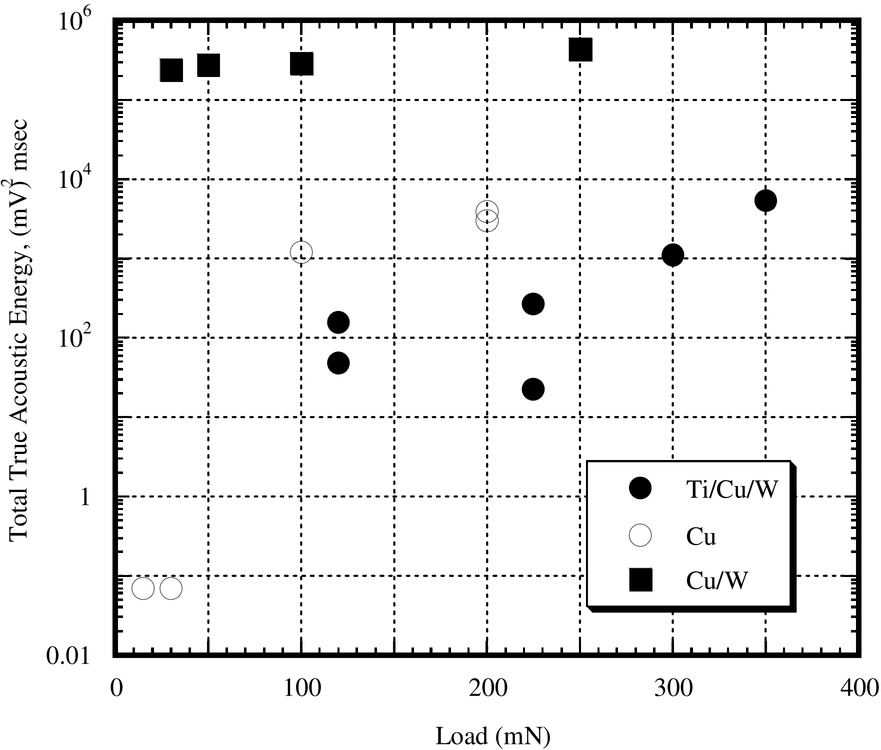

Figure 95. Total true acoustic emission energy as a function of load.

For the thin film system with a Ti underlayer, acoustic emission energy varies inversely proportional to the strain energy release rate. It is proposed that this is due to incremental cracking below the detector threshold. Total AE emission energy is much lower for the system with a Ti underlayer due to improved adhesion. This not only reduces the blister area but also limits the size of incremental crack advance thus reducing the number of detectable acoustic events.

For the same indentation load (e.g. 200 mN) the total acoustic energy increases from 10^2 to $5{\cdot}10^3$ to $3{\cdot}10^5$ for the Ti/Cu/W, Cu and Cu/W systems due to the increased delamination areas.

The AE is low for the low load indents into the Cu film (up to 50 mN). It increases drastically at a 100 mN due to blister formation and substrate cracking. In the case of a W superlayer the indenter does not penetrate the substrate as deep. In this case, the normal loads are not high enough to produce substrate radial cracking. In order to check this blisters were removed so that the SiO_2 surface was exposed for examination.

CHAPTER 6. THIN FILM FRACTURE CHARACTERIZATION

Several indentation-induced blisters in a 120 nm thick Cu film without a Ti underlayer were removed with adhesive tape in order to expose SiO_2 surface for analysis.

6.1 "INSIDE THE BLISTER"

Microscopy Characterization

Optical micrographs did not show any substrate cracking, although there is a permanent impression in Si left by the indenter (Figure 96, substrate side). Radial cracks extended in the film outside the original blister area. These are seen along with the circular cracks on the tape side in Figure 96.

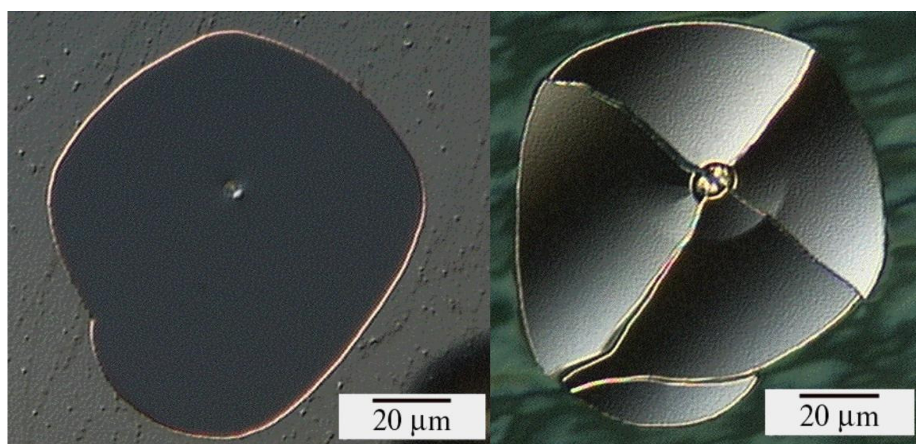

Figure 96. Optical micrographs of the removed blister. Substrate (left) and tape (right) sides.

Figure 97a shows a Nomarski contrast optical image of the original blister of a Cu film without a Ti underlayer. The area under the removed blister is presented in the SEM

image in Figure 97b. The crack propagated further than the original blister size when the tape was removed. No substrate cracking was observed.

In order to determine whether the crack propagated along the SiO_2/Cu interface, Auger electron surface analysis was performed on the SiO_2 fracture surface. Due to the charging problems the spot AES analysis was not possible, so four 100 μm^2 regions were scanned in the delaminated area. The elemental concentration profile is shown in Figure 98. There is a high surface concentration of oxygen and carbon due to contamination and the presence of oxygen in the SiO_2. The oxygen concentration drops from 60 to 40 % upon moving out of the delamination zone to the W surface. The tungsten concentration changes accordingly. A small, almost indistinguishable Cu concentration compared to background inside the blister suggests that the Cu film is almost totally removed during blister formation. An increase in the carbon concentration outside of the delaminated area can be explained by hydrocarbon surface contamination.

Crack Arrest (Fiducial) Marks

Crack arrest marks were found after the blister removal with an adhesive tape. Scanning electron microscopy showed a circle that corresponds to the original blister size in diameter. Two distinct circular marks are clearly seen on the higher magnification SEM image in Figure 97c. We denote those as crack arrest fiducial marks. Atomic force microscopy was performed to measure the feature geometry. Feature width is 1 μm, and it's height ranges from 5 to 15 nm. Contact and deflection AFM images of the blister mark are shown in Figure 99.

It was originally believed that the crack arrest mark is formed by crushed W and/or SiO_2 debris during the indentation. More likely, however, radial cracking allowed laboratory air with moisture, hydrocarbons and surface debris to be sucked into the blister. The exact source of contamination would be identified later, but whatever the source is, relatively mobile moisture, hydrocarbons and small debris particles were sucked into the crack tip leaving the fiducial mark detected in Figure 97b. This is analogous to the method used in the early days of the E24 subcommittee on fracture toughness testing where it was desired to mark the extent of slow crack growth prior to rapid instability in thin sheets. Rather than use

the optical or potential techniques applied later, india ink was placed at the initial crack front prior to increasing the load [199].

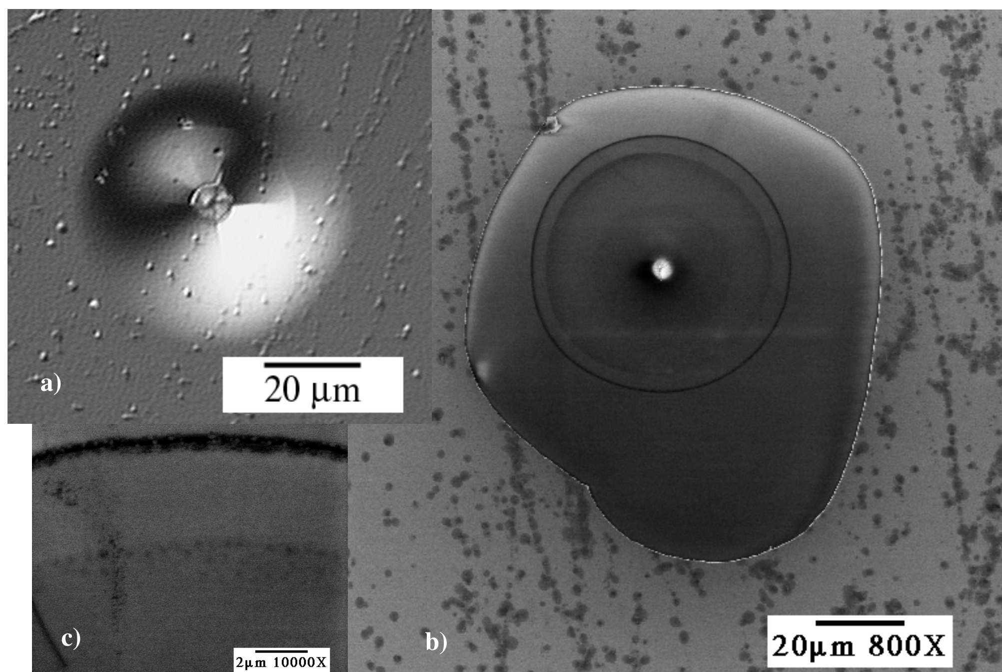

Figure 97. a) Optical image of a blister; b) SEM image of the area underneath the removed blister in a); c) SEM image of a crack arrest mark.

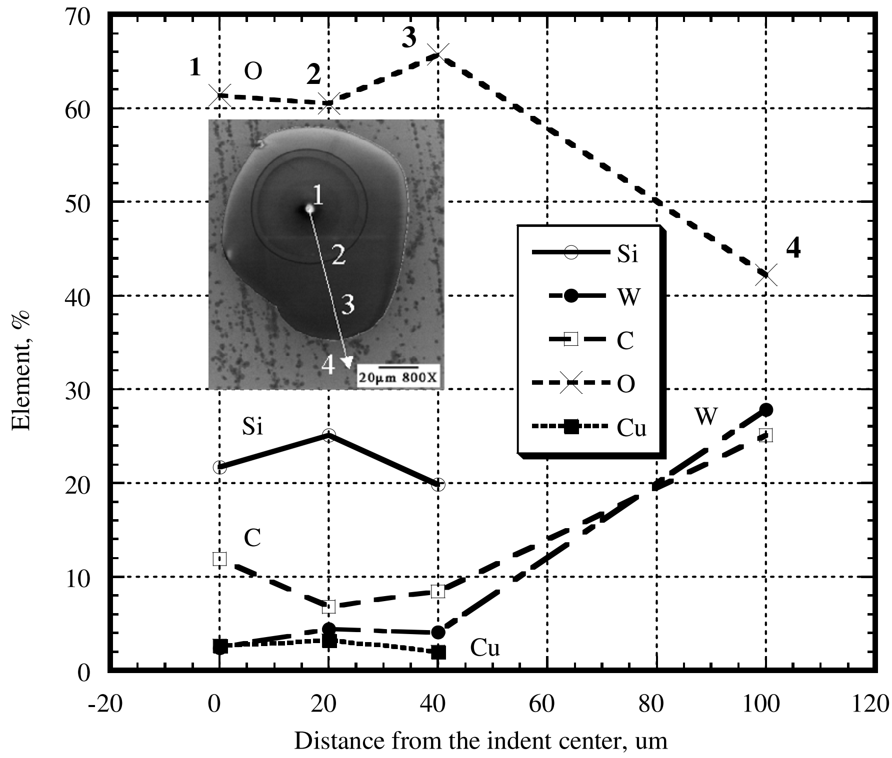

Figure 98. Element concentration profile along with the SEM image identifying analyzed areas.

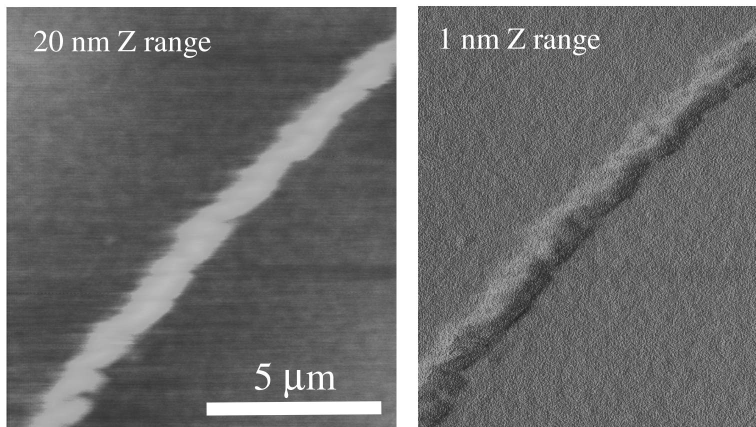

Figure 99. Contact and deflection AFM images of the crack arrest mark.

Upon rising load, as the crack started to grow the new material surfaces formed exposed the fluid to vacuum immediately sucking it into the crack tip. The fluid could not follow, however, the crack front as sonic velocities were approached during unstable crack extension. After separation, india ink outlines of the stable slow crack growth region on the fracture surfaces were impressive but later abandoned due to the finding that this promotes stress corrosion cracking or hydrogen embrittlement. As it is clear that this fiducial mark outlines the crack front, this is used in the next section.

6.2 SLOW CRACK GROWTH ANALYSIS

Crack Tip Opening Angle Measurement

The crack tip angle can be measured by scanning with a profilometer across a blister without its removal, and by measuring the crack arrest mark geometry after a blister removal (Figure 100).

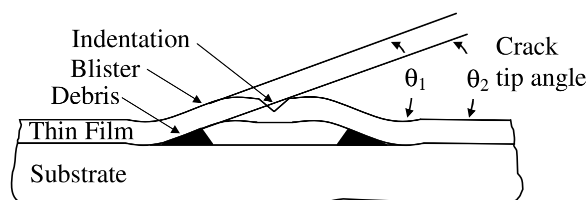

Figure 100. Crack opening displacement angle measurement. θ_1 is the angle measured from the blister angle without its removal, θ_2 is the angle measured from the crack arrest mark geometry.

Slow Crack Growth Approach

For the Cu film without a W overlayer and the Ti/Cu/W system, the acoustic energy for the same load was at least two orders of magnitude lower than the Cu/W system. As the adhesion of the Cu only versus the Cu/W was identical, the only conclusion here is that the higher available stored elastic energy in the Cu/W system grew the crack relatively rapidly during delamination. This gave an easily detectable event(s) as opposed to the Cu only where

the crack must have grown more slowly in many undetectable acoustic events below threshold. The latter is consistent with the more well-adhered Ti/Cu/W system where slow crack growth resulted in many undetectable acoustic events. It is clear then in many cases the crack is growing quite slowly making the Rice, Drugan and Sham (RDS) analysis [200] of the tearing modulus an appropriate model to consider. The RDS model of the tearing modulus, T_0, gives [200]:

$$T_0 = \frac{E\delta_c}{\alpha\sigma_{ys}r_m} - \frac{\beta}{\alpha} ln\left(\frac{e\lambda EJ_0}{r_m\sigma_{ys}^2}\right) \quad (6.1),$$

where δ_c/r_m is the crack-tip displacement at a distance r_m behind the crack tip where it is measured or crack tip opening angle ($CTOA=\delta_c/r_m$), $\alpha \approx 1$, $\lambda \approx 0.2$, e is the natural logarithm base, E and σ_{ys} are modulus and yield strength, $\beta = 5.1$ from the mechanics description and J_0 is the initial value of the J integral at crack initiation. Calculation demonstrated that the first term dominated the second for very high yield strength thin films with toughness less than 100 J/m^2, giving

$$T_0 \approx \frac{E\delta_c}{\alpha\sigma_{ys}r_m} \quad (6.2).$$

Since the steady-state strain energy release rate can be given in terms of the tearing modulus by

$$J_{SS} = J_0 exp\left(\frac{\alpha T_0}{\beta}\right) \quad (6.3),$$

it is seen that combining (6.1) and (6.3) leads to a simple expression for strain energy release rate in terms of the crack-tip opening angle [201],

$$J_{SS} \approx J_0 exp\left\{\frac{E \cdot CTOA}{\sigma_{ys}\beta}\right\} \quad (6.4).$$

With the fiducial mark representing the crack-tip arrest, we suggest that the mark shape may also represent the CTOA as indicated in Figure 100. That is, if the moisture/hydrocarbons/debris mixture is vacuumed into the crack tip and solidifies, this basically represents an internal replica of the crack tip. As noted in Figure 100, this would represent the CTOA in terms of its height divided by its width. Given the 5 to 15 nm height,

this would represent the CTOA in the vicinity of 0.29 to 0.86 degrees. With an average value of 0.01 radians, a modulus of 120 GPa, a yield strength of 1 GPa and $\beta = 5.1$, one finds:

$$J_{SS} = J_0 exp\{0.23\} \approx 1.27J_0 \quad (6.5),$$

which means that during slow crack growth the strain energy release rate has barely increased for this 120 nm thick copper film. This is consistent with Figure 57, which suggests that little if any increase in strain energy release rate over the true surface energy occurs for films less than about a 100 nm thick. This could provide an interesting additional means of assessing film toughness. The feature geometry is proposed to represent the shape of the crack tip, potentially providing the basis for the crack tip opening displacement angle measurement.

6.3 FRACTURE SURFACE AUGER ANALYSIS

Fracture Interface Determination

Conceptually it is important to know along what interface the fracture occurs during the blister formation. For example, it is important to know if Cu film on Ti fails along Cu/Ti interface, or the crack kinks into one of the layers. With this knowledge, correct modeling can be applied.

To evaluate both the film and the substrate fracture surfaces, blisters were removed with carbon conductive adhesive tape for analysis in the Auger apparatus. In order to avoid charging problems, the sample has to be conductive, and has to be electrically connected to the mounting stage. This is achieved by using a conductive media to mount the sample on the stage inside an Auger system. For the same reason carbon conductive tape was used to remove the film.

The substrate side looked just like an oxidized Si wafer upon film removal, and the removed film had a characteristic copper color, which indicated that failure occurred along the Cu/SiO_2 interface. This was confirmed by Auger electron spectroscopy, performed by Miles Clift at Sandia National Laboratories, California, which showed that the failure occurred along the Cu/SiO_2 interface for Cu films without Ti. Spectra corresponding to the substrate and tape sides are presented in Figure 101 and Figure 102 respectively. There are

distinct Si, C and O peaks present on the spectra. Carbon and oxygen come from the surface contamination by hydrocarbons, which typical for surfaces exposed to the atmosphere. One can expect some Cu left on the substrate due to Cu diffusion into SiO_2. However, there is no distinct Cu peak present (Figure 101), but even if there were Cu, its concentration would be less than 2.4% (the detection limit for this element).

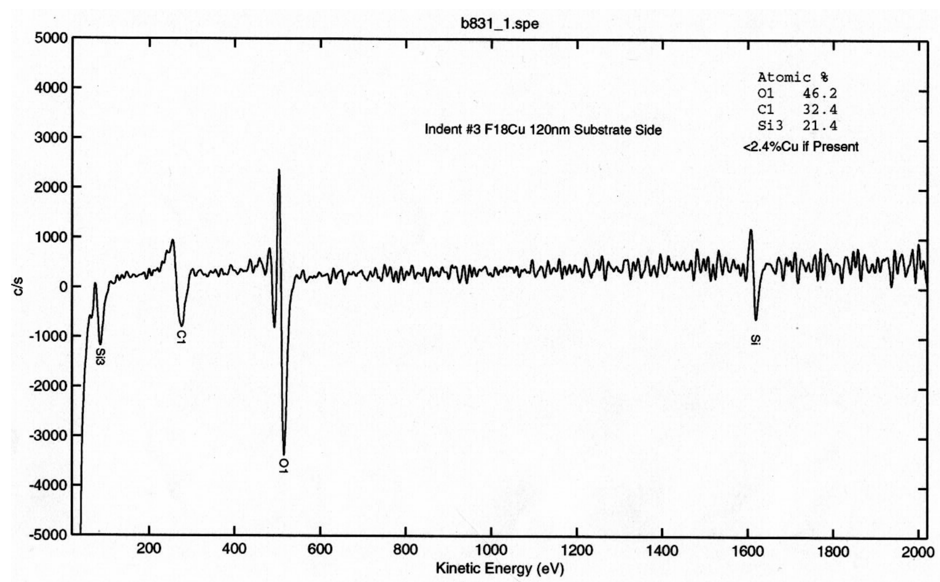

Figure 101. Auger spectrum obtained from the substrate side.

There are three distinct Cu peaks present on the spectrum obtained from the removed Cu film along with some C and O peaks from atmospheric contamination. There is also a small Si peak present, representing less than 1.7% Si elemental concentration.

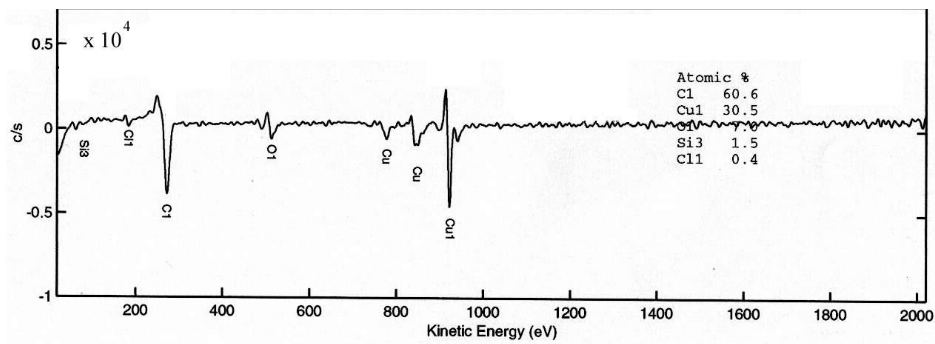

Figure 102. Auger spectrum obtained from the removed Cu film.

From Figure 103 showing AES data for the tape and substrate side, it may be concluded that Cu films with a Ti underlayer failed along the Ti/Cu interface. There is no Cu peak on the substrate side scan, but there are two distinct Ti peaks. Opposite, on the tape side there is Cu, but no Ti.

Contamination levels appear to be different for the substrate and the film sides. For example, oxygen concentration is higher on the substrate side, but carbon concentration is lower. Higher oxygen concentration indicates that the Ti underlayer is at least partially oxidized. There is also a small Cl peak on the tape side, which could have come from the tape adhesive material.

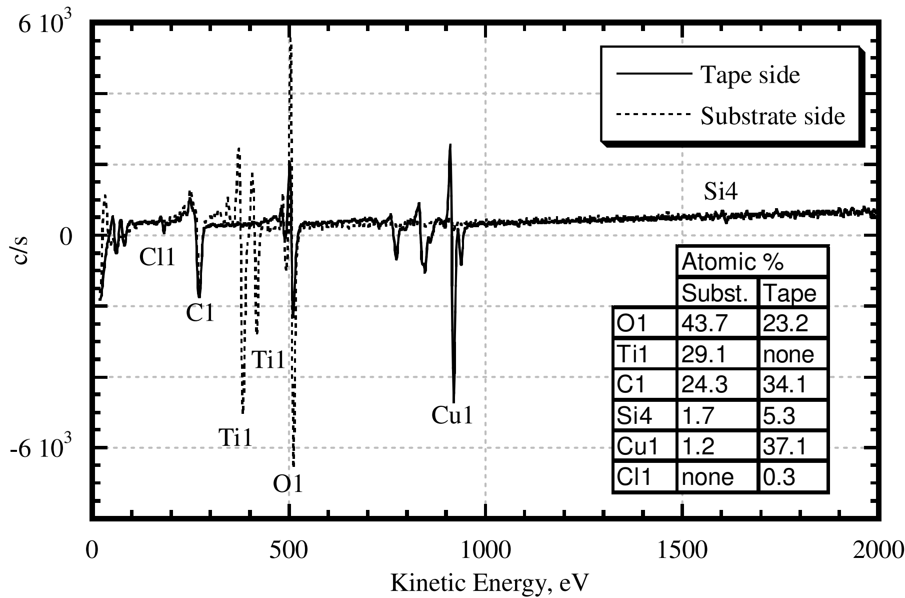

Figure 103. AES scans on the tape and substrate sides for a Cu film on Ti/SiO_2 along with element concentrations.

Electron Beam Surface Damage

For these Auger characterizations, low 5 KeV beam current has been used. Apparently, this is high enough energy to cause surface damage on the substrate side (Figure 104). Even though Ti conducts electricity, it is a very thin Ti layer on SiO_2 dielectric, so heat produced by the beam cannot dissipate, causing the surface modification as seen optically and by AFM (Figure 104). Here, two Auger scan line are placed right next to the residual indent onto SiO_2. For some scans the beam energy was lowered to 2 KeV, which decreased the substrate damage.

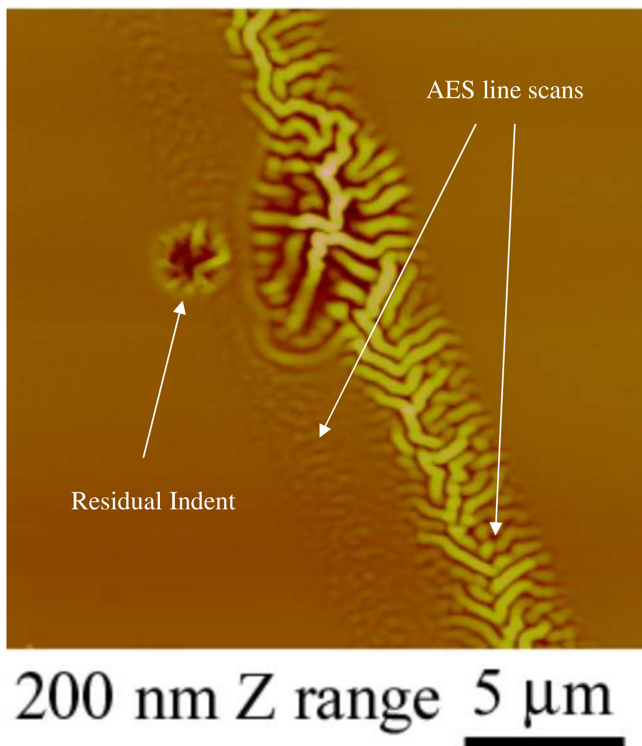

Figure 104. AFM image of the Ti/SiO_2 surface damage due to electron beam scanning.

6.4 FIDUCIAL MARKS CHARACTERIZATION

The delaminated area of a 120 nm thick Cu film after blister removal is shown in Figure 105a. Fiducial marks are clearly seen on the SiO_2 side, and correspond to the original blister diameter. Figure 105b shows the removed portion of the film adhered to tape. Note that inside the blister the light areas on the substrate side correspond to the dark areas on the tape side and visa versa.

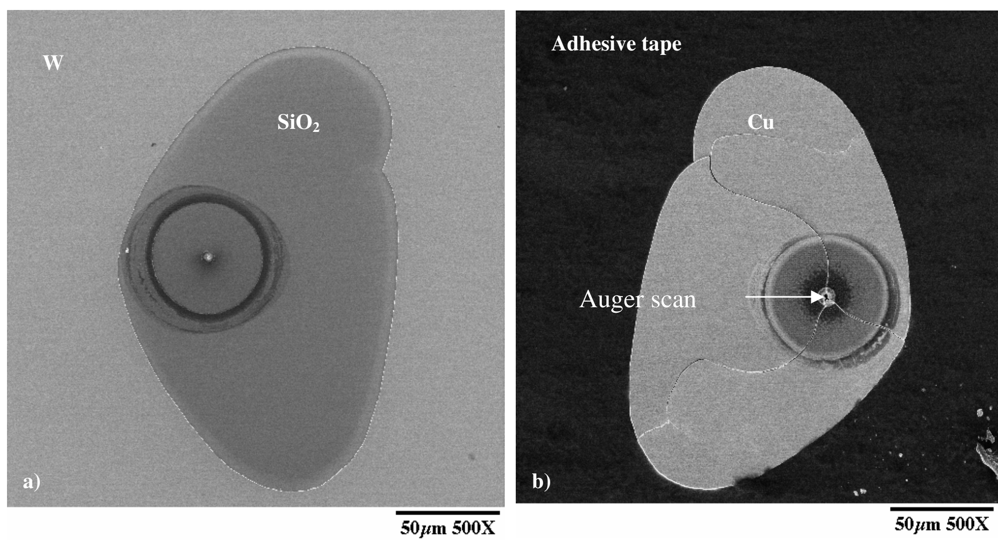

Figure 105. SEM micrographs of Cu 120 nm fiducial marks on the substrate a) and on the tape b) sides.

Fiducial Mark Auger Analysis

Initially Auger electron spectroscopy was used to identify the contents of the fiducial marks on the wafer substrate side, as described in the beginning of this chapter. The results are somewhat inconclusive due to the small volume of the marks' matter and SiO_2 charging problems. In the current situation the removed conductive film contains most of the mark (black area inside the blister in Figure 105b), and it is on a conductive tape. This allowed for a more accurate AES analysis. Figure 106 shows AES line scan data superimposed on the corresponding portion of the SEM image from Figure 105b. The carbon concentration jumps from a background value of 55% to almost 85% inside the mark, at the same time the Cu concentration of 30% drops to about 10% inside the mark. Carbon concentration increases in the darker areas, and decreases in the whiter areas of the mark (Figure 106). Inside the blister the Cu film is covered with a substance that contains carbon.

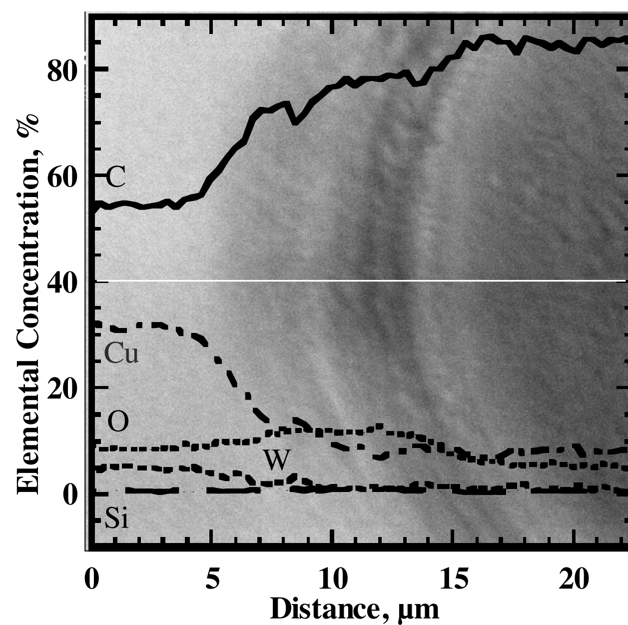

Figure 106. AES scan superimposed on the enlarged SEM image from Figure 101b.

Carbon Contamination Source

There are three possible sources for carbon: adhesive tape, the diamond indenter and hydrocarbons from the atmosphere. Adhesive tape as a contamination source can be eliminated, since several blisters were removed using a micromanipulator, but the marks were still present.

It is known that diamond indenters wear during indentation of "hard" films. Ti as well as W are known to "suck out" carbon from a diamond indenter [202]. Initially it was assumed that a similar process might have occurred in our case. Given a 20 nm thick fiducial mark (from AFM measurements) with a 50 µm blister radius, and assuming fully dense carbon (ρ=12 g/cm^3), one would find $1.9 \cdot 10^{-9}$ grams mass loss per indent. This will result in a significant loss of almost two micrograms for a 1000 indents (a typical number of indents for adhesion testing), assuming that all carbon comes from a diamond tip. On the other hand, W concentration decreases inside the mark, which means that it does not come in the form of a tungsten carbide. One of the ways to find if carbon comes from a diamond tip would be to use a non-diamond tip, and ascertain whether the fiducial marks are still present underneath blister delaminations.

Since the only element besides carbon, which exhibits a concentration increase inside the mark is oxygen (Figure 106), it is possible that carbon contamination comes from hydrocarbons and moisture in the atmosphere. Due to the radial cracking the two newly formed surfaces are exposed to the atmosphere during indentation-induced delamination. The crack itself can suck relatively mobile moisture and hydrocarbons into its tip, leaving behind the fiducial mark (Figure 105). It has also been shown that the test temperature and hydrogen charging both affect Cu film adhesion [146, 203]. Analogous behavior may then exist in the case of fiducial mark formation, where the interfacial toughness may be easily reduced with the contamination present. Indentation fracture experiments in vacuum or in partial pressure of environmental contaminants should resolve the question of atmospheric influence on the fiducial marks formation and Cu film adhesion.

During the course of this study it was found that a similar type of contamination is present in the stress-induced telephone cord delamination, similar to one shown in Figure 23. This happened at Motorola on a different film system than in this study. Films of TiWN

about 1 um thick have delaminated on the corners of several GaAs wafers. SEM micrographs of TiWN removed film and the GaAs substrate are shown in Figure 107 and Figure 108. All images of TiWN films are courtesy of M. Kottke (Motorola). It was initially assumed that this type of delamination is present at the edges of the wafer due to the higher level of surface contamination prior to thin film deposition. However, Auger and RBS analysis did not confirm this assumption. Delamination occurred due to the higher levels of thin film residual stress at wafer edges.

What's interesting here are the traces noted both on the film and substrate surfaces, mimicking the original telephone cord delamination pattern, as seen in SEM (Figure 107 and Figure 108).

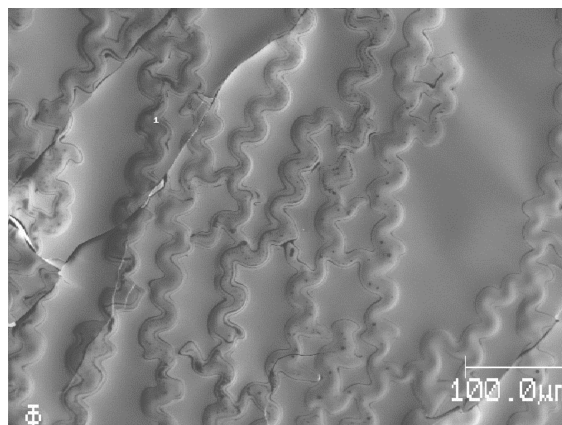

Figure 107. SEM micrograph of the removed TiWN film.

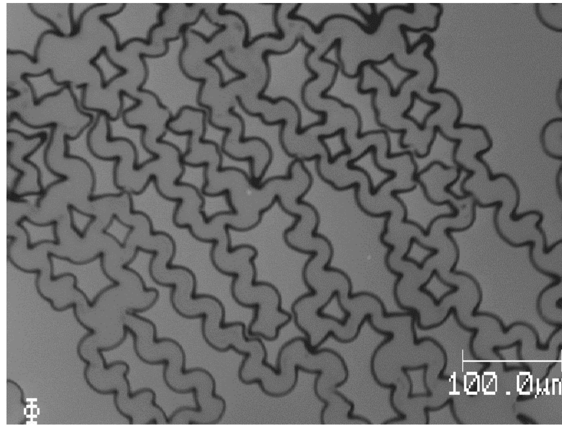

Figure 108. SEM micrograph of a GaAs fracture surface upon TiWN film removal.

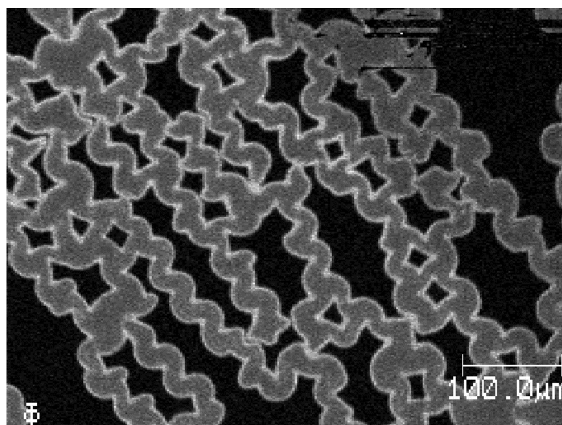

Figure 109. Carbon X-ray map corresponding to the SEM image in Figure 108.

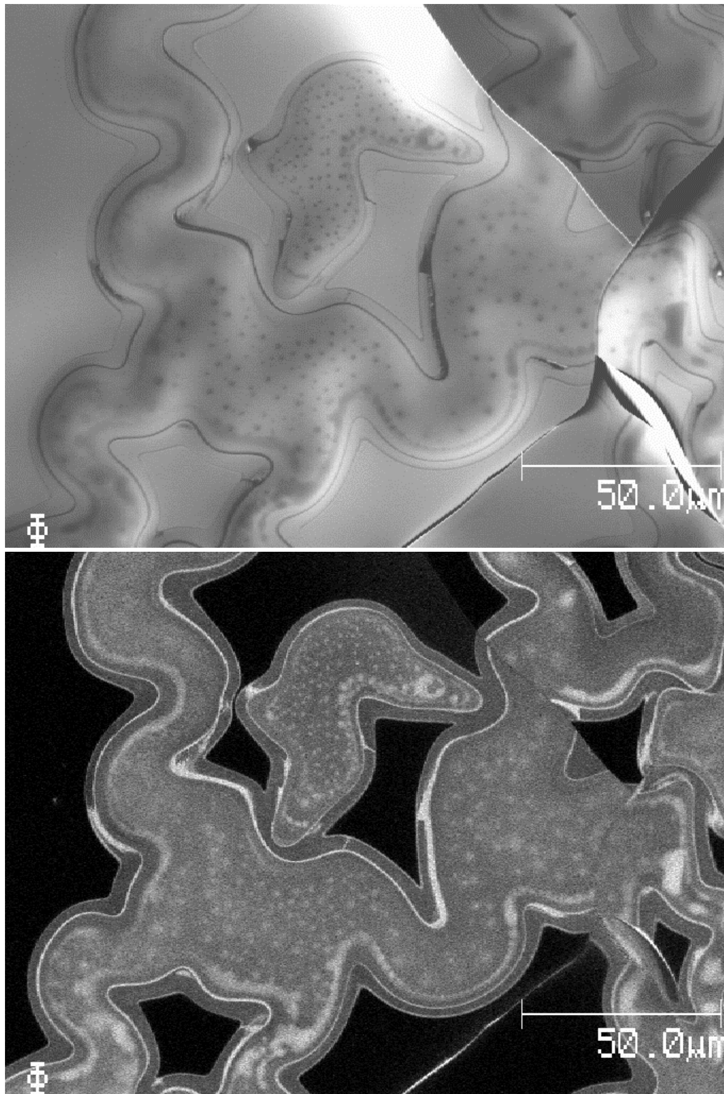

Figure 110. SEM micrograph with the corresponding carbon X-ray map of the delaminated TiWN film.

These are fiducial crack arrest marks like those identified in the beginning of this chapter for the Cu/SiO_2 system. Figure 109 shows a carbon X-ray map, corresponding to the SEM image in Figure 108. Brighter areas correspond to higher carbon concentrations. There is almost no carbon present between the original phone cord delaminated areas (black regions in Figure 109). Most of the carbon goes into the crack tip, outlining the telephone cord topography.

Since there was no indentation performed to induce these delaminations, the diamond tip can be eliminated as the contamination source. One may still argue that carbon comes from the tape used to peel the film. In this case there would be higher carbon concentration around through-thickness cracks present in the removed film in Figure 107 and on the substrate side, right underneath these cracks. As seen from Figure 107, Figure 108, this does not appear to be the case. This is seen even better on the high magnification SEM image along with the corresponding carbon X-ray map in Figure 110. The crack in the film appears to be white on the bottom of the X-ray map, but there is almost no contamination around it. Also, other cracks present in the upper right corner are dark, indicating low carbon concentration. The carbon layer is not uniformly dispersed inside the delaminated areas (Figure 109).

Fiducial Mark Morphology

Just like in the case of TiWN delamination, the carbon contamination layer in Cu/SiO_2 fracture is not uniform. The carbon contamination layer on the Cu film (tape) side has some structure to it. Figure 111 shows the magnified center region of the fiducial mark from Figure 105b. There is a 10 μm diameter circular residual impression left by the diamond indenter with three radial cracks emanating from its center. The fiducial mark starts right around the indentation contact area within a rough region of carbon-containing black particles (Figure 105b). There is a distinct transition at about 20 μm from the indent center in terms of the surface roughness. This is seen even more clearly on the contact mode AFM images of an 80 nm thick Cu film (Figure 112). The Cu film is relatively smooth outside the original blister delamination area. However, the surface roughness increases inside the blister area, and it increases more close to the center of the blister. As the transition zone diameter is

about twice the indenter contact diameter (Figure 105b), it is possible that the roughness transition is associated with the plastic zone in a thin Cu film. Being capped under the W superlayer, Cu undergoes severe plastic deformation upon indentation. As Cu is not allowed to pile-up being constrained by the hard superlayer, the plastic zone "tunnels" in the plane of the Cu film [146]. Even though Cu is capped with the superlayer, the effective yield stress of the bilayer composite, σ_{YS} can be calculated using the plastic zone size model, equation (2.8). A yield stress of about 1.2 GPa would result for a 250 mN indentation and a 10 μm plastic zone size (Figure 112). This seems to be a reasonable number for a W/Cu bilayer, so the fiducial mark transition zone in fact may correspond to the plastic zone size.

Note that these are contact mode AFM images, and a regular sharp SiN contact mode AFM tip does not cause any surface damage. Typically, soft polymers cannot be imaged in the AFM contact mode, since this causes surface damage, the AFM tip sticks to the polymer, and a clear image cannot be taken. On the other hand, when a dust particle is present on the sample surface, it is being moved by the tip operating in the contact mode. These effects are not observed with fiducial marks, which means that these hydrocarbon particles are hard, and adhere well to both Cu and SiO_2. This might be due to the local heating effect at the crack tip. The heat dissipates fast enough so that the whole sample is not heated up, although the local crack tip temperature may increase substantially. This is a very interesting phenomenon that requires further investigation.

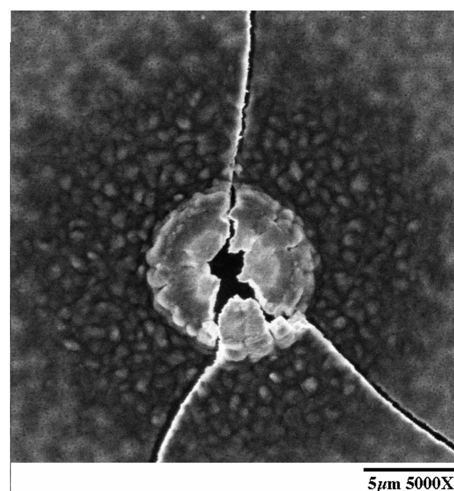

Figure 111. Center of the blister from Figure 105b.

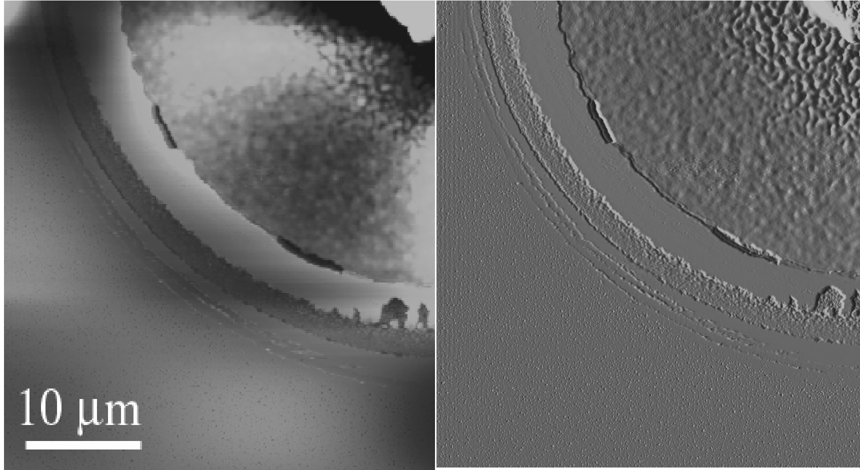

Figure 112. Contact mode AFM height (300 nm Z range) and deflection images of an 80 nm Cu blister.

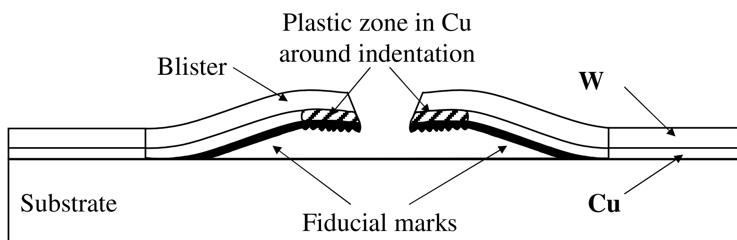

Figure 113. Fiducial mark schematics.

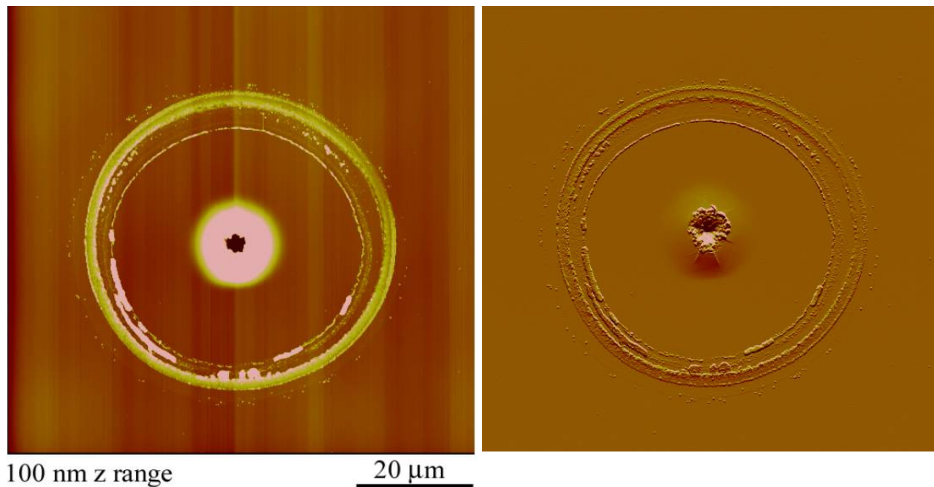

Figure 114. AFM height and deflection images of the fiducial mark left on SiO_2.

Fiducial marks left on the SiO_2 substrate are shown in Figure 114. Here, the inner crack arrest mark corresponds exactly to the original blister size as measured with the optical microscope. These are several bigger concentric marks, which represent crack arrests. This means that the crack growth was not continuous, but rather discreet, in small increments. The crack growth could have happened during indentation, or later due to stress corrosion cracking. There is also a 300 nm high pile-up around the indent present in SiO_2. Currently the superlayer indentation test analysis does not account for the substrate deformation, assuming it is rigid and elastic. Clearly, forming pile-up would dissipate some energy.

Sometimes instead of removing the whole delaminated blister, only a part of it will be removed with the tape with the rest still attached to the substrate (Figure 115). The fiducial mark goes underneath the film, which is clearly seen on the AFM deflection image in Figure 115.

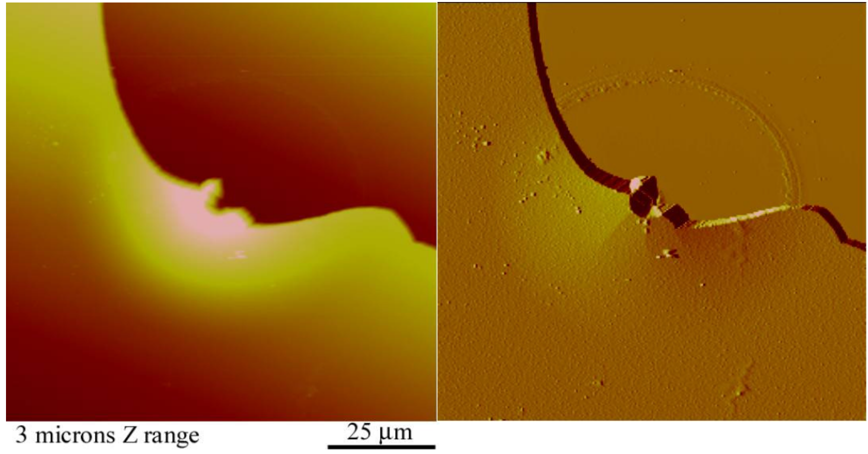

Figure 115. AFM height and deflection images of partially removed blister, showing fiducial mark underneath.

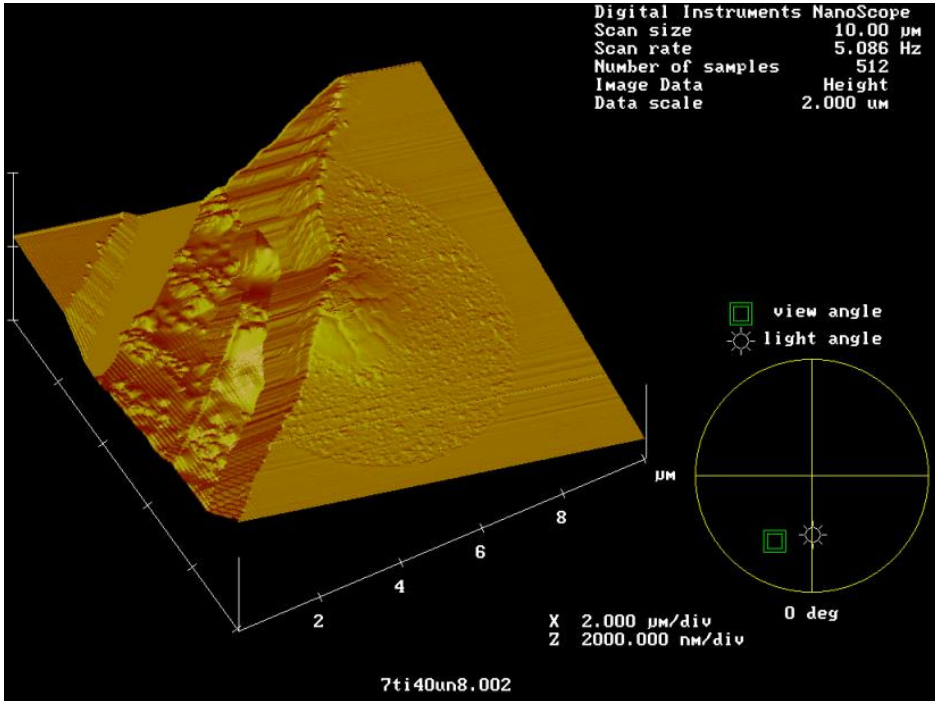

Figure 116. 3D AFM image of the fiducial mark in Ti/Cu film.

For thicker Cu films having strong adhesion (Figure 57), those over 200 nm thick could not be removed with an adhesive tape (they "survived" the pull-off test). The only Cu film with a Ti underlayer removed was a 40 nm thick film. Unlike films without the Ti underlayer, instead of removing islands of film around the blister (Figure 105), the whole film with the Ti underlayer was removed with an adhesive tape. Some Cu films with the Ti underlayer also exhibited fiducial mark formation (Figure 116). However, no fiducial marks were found for indents, where the indenter did not penetrate through the bilayer thickness (Figure 117). Although there is some cracking underneath the indenter in Figure 117, it seems that the delaminating interface has to be exposed to the atmosphere when fracture occurs for the marks to exist. This also identifies atmosphere as a contamination source for the fiducial marks.

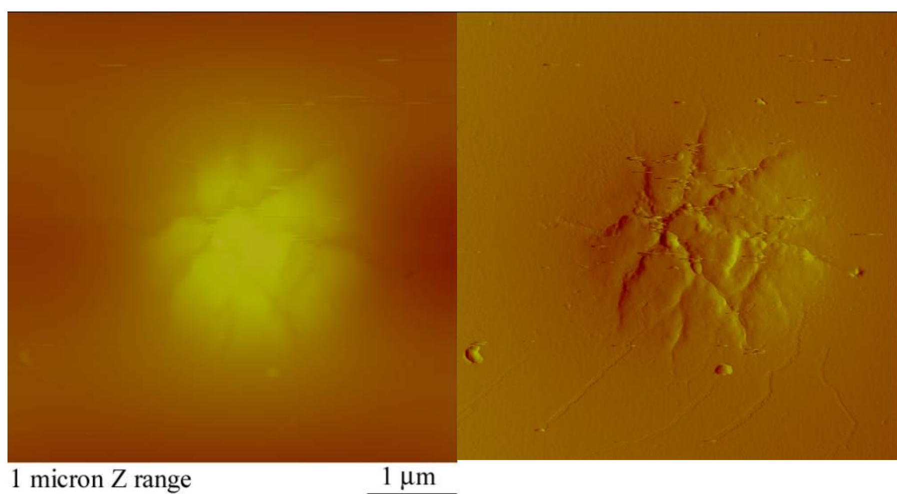

Figure 117. Contact AFM height and deflection images of the small blister indent into a 40 nm Cu/Ti film. No fiducial marks are present.

6.5 PETAL-SHAPED BLEED-THROUGH MARKS

Petal-shaped Marks Discoveries

Stains around indents into SiO_2/Cr/Cu/W stack films [165] have been previously observed (Figure 118). As these have not been reproducible, little attention has been paid to these effects.

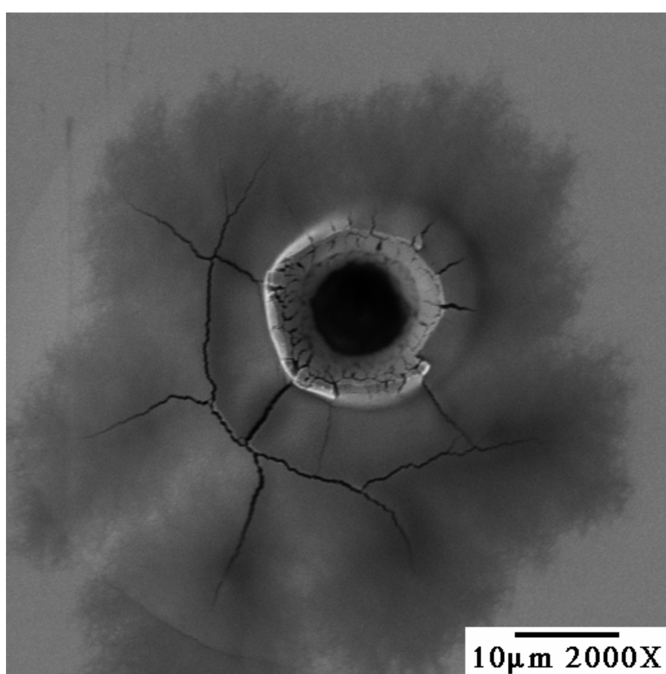

Figure 118. Stains around an indentation into SiO_2/Cr/Cu/W film stack.

For the current adhesion study Cu films with the superlayer were indented both with the MMT at the University of Minnesota and with the Nanoindenter II at Sandia National Laboratories in Livermore, California. Delaminations produced in California exhibited petal-shaped marks around typical radial cracks as seen in the optical microscope (Figure 119).

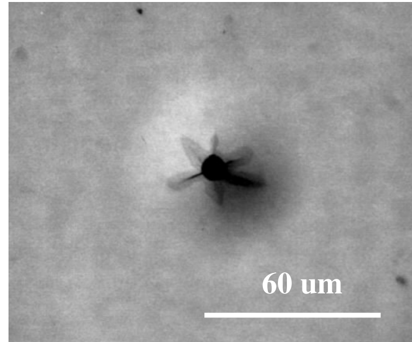

Figure 119. Petal-shaped marks around radial cracks.

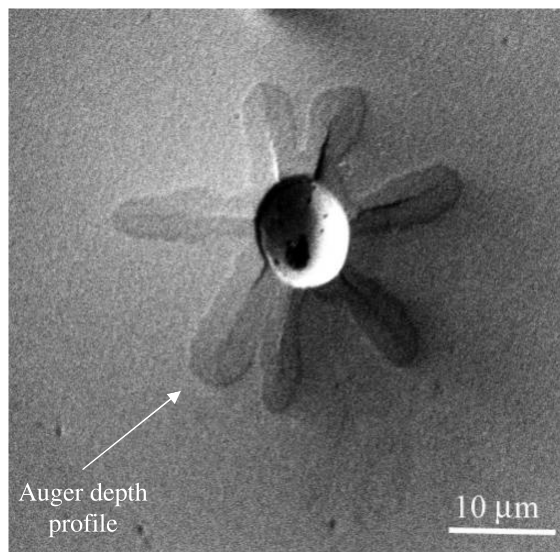

Figure 120. Petal-shaped marks seen in the SEM.

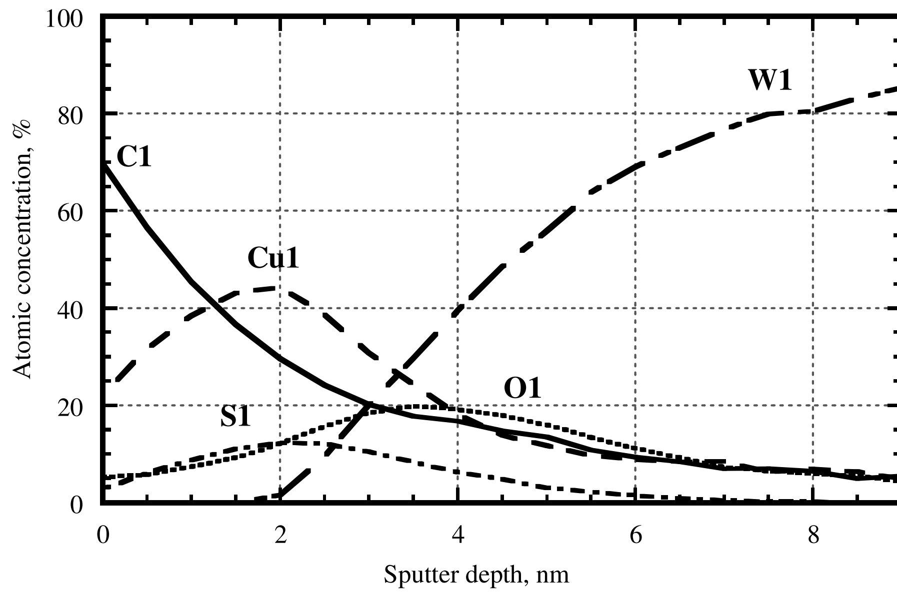

Figure 121. Auger depth concentration profiles taken on the petal-shaped mark from Figure 120.

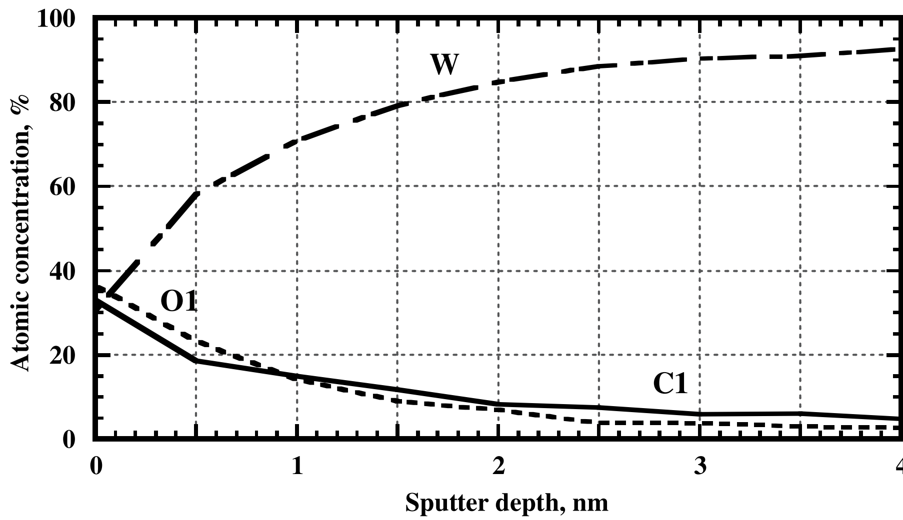

Figure 122. Auger depth concentration profiles taken on the W surface outside the blister area.

Petal-shaped Bleed-through Marks Source

These petal-shaped marks have never been observed on blisters produced in Minnesota (Figure 52 and Figure 63). The marks appear as stains in both the optical microscope (Figure 119) and in the SEM (Figure 120), which imply some sort of a chemical effect. In order to verify the composition and identify the origin of these marks, Auger depth analysis has been performed on these petal-shaped marks. Figure 121 shows the elemental depth concentration profile obtained between the radial crack and the end of the mark as identified in Figure 120. There is a high carbon concentration right at the mark surface, which drops down with the sputter depth. There are also copper and sulfur present on top of the W superlayer, which both have a maximum concentration at about 2 nm depth. The fact that both profiles are almost identical in terms of their shape indicates that Cu and S may have formed a chemical compound, since copper is known to form sulfates. This compound may also contain oxygen. Finally, the W concentration saturates only at about 8 nm depth.

Encyclopedia Britannica identifies sulfur as one of the most reactive of the elements: "It is estimated to be the ninth most abundant element in the universe. In the form of sulfides, sulfates, and elemental sulfur, the element constitutes about 0.03 percent of the Earth's crust. After oxygen and silicon, it is the most abundant constituent of minerals. Sulfur forms compounds in oxidation states -2 (sulfide, S^{2-}), +4 (sulfite, SO_3^{2-}), and +6 (sulfate, SO_4^{2-}). It combines with nearly all elements. An unusual feature of some sulfur compounds results from the fact that sulfur is second only to carbon in exhibiting catenation--i.e., the bonding of an atom to another identical atom. This allows sulfur atoms to form ring systems and chain structures."

The fact that Cu is found on top of the W surface indicates its diffusion along the radial cracks, so the marks are called the Petal-shaped Bleed-through Marks. This may be assisted by a chemical interaction with the atmosphere ("clean" air in California). An Auger depth profile has also been taken outside the blister area on the W surface for comparison (Figure 122). Here, W concentration is almost 90% at a 2 nm depth. The carbon concentration of 10% is almost a constant at this depth, which may indicate some tungsten carbide formation. During the course of this study it was found that some of the blisters did exhibit bleed-through marks formation, which led to the sulfur source identification.

There are many different ways of cleaning a diamond tip. In fact, it is recommended the tip should be cleaned before indenting a new sample. There are chemical methods for cleaning tips in solvents (methanol, acetone, etc), and mechanical methods, such as indenting into Velcro pad or balsa wood. Balsa wood has been occasionally used for cleaning tips in this study. It was noted that the bleed-through marks are not present if the tip is not "cleaned" with balsa wood. Because of this, balsa wood has been identified as one of the tip contamination sources, the second one being human "clean" hands during the tip handling/mounting.

These chemical effects could have also led to stress corrosion cracking. Note that these petal-shaped bleed-through marks are different than the fiducial marks discussed earlier. Observation of fiducial and bleed-through marks in Cu film fracture indicates that there are possible interactive chemical and mechanical effects that may affect adhesion, and should be thoroughly studied.

CHAPTER 7. ALUMINUM FILM ADHESION

Since Al has been a predecessor of Cu in the microelectronics industry for more than 30 years, it was important to consider its adhesion for comparison purposes.

7.1 Al FILMS EXPERIMENTS

Due to Al oxide formation, there is a different type of bonding, so unlike Cu, Al has never exhibited poor adhesion to Si wafers. There are some chemical effects known, for example, when Al acquires oxygen from SiO_2 forming an oxide at the interface [12], but this only enhances Al adhesion by forming a ceramic/ceramic type interface. Interfacial reactions in the Al-Si system are discussed in [12]. Similar to the Cu adhesion experiment, Al films of several thicknesses have been deposited on different underlayers to study the effects of plasticity on Al adhesion.

<u>Al Film Deposition</u>

All thin film processing was conducted in a Class 10 clean room environment. Silicon <100> wafers (100 mm in diameter, 0.5 mm thick) were thermally oxidized at 1100 °C in steam to grow 3 µm of SiO_2. The oxide thickness was measured with a Nanoscope Ellipsometer. Al films from 40 nm to 3.2 µm thick were then deposited onto the oxidized substrates in a Perkin-Elmer DC Magnetron sputtering apparatus. The base pressure of the system was 1 µTorr, and the Ar flow was 10 sccm, which corresponded to 6 mTorr Ar pressure. For Al films from 500 nm to 3.2 µm thick, 5000 Watts of power was applied to the target (Al-2% Si, w/o); for thinner films the sputtering power was reduced to 1000 Watts. Substrate table rotation was used to achieve uniform film thickness and structure. The maximum temperature during film deposition reached 100 °C for the longest deposition run of 3 µm Al, after which the system was cooled for one hour without breaking vacuum. The film thickness was measured using a DEKTAK surface profiler. Using the wafer curvature

technique and Stoney's equation [114], residual stresses measured were found to be tensile ranging from 100 to 200 MPa.

Two sets of Al films of eight thicknesses were coated with two different W superlayers in a 2400 Perkin-Elmer RF sputtering apparatus. The residual stress in sputter deposited films was controlled by varying the working gas pressure [12, 204]. For the first superlayer deposition run the Ar pressure was held at 7.7 mTorr, which produced a compressive residual stress of 1 GPa in the W superlayer. For the second run, the Ar pressure was held at 6 mTorr, which produced a tensile residual stress of 100 MPa.

Al Film Characterization

Sheet resistance of the Al films was measured with a Veeco Instruments Inc. 4-point probe. Reflectance was measured with a Nanometrics Nanospec film thickness measurement system in the reflectance mode, taking a Si wafer as a 100% reflectance reference. As expected, both properties decreased with the film thickness (Figure 123). Al films of 1, 2 and 3 μm thick appeared to produce more scatter than the others due to the higher surface roughness and thicker oxide layer.

The hardness of 0.34 to 2 um thick Al films has been measured using a Nanoindenter II equipped with a 90° conical diamond indenter with a 700 nm tip radius. Here, instead of using the tip calibration function, the hardness was calculated using the actual contact area as measured by AFM. Similar to the Cu plastic properties measurements, the Bhattacharya and Nix approach [144] has been used to account for substrate effect. The results taken from [160] are shown along with the grain size measurements from AFM plan view images.

Table 8. Al film hardness and grain size [160].

Al Film Thickness, um	H, GPa	Grain Size, nm
0.34	2.8	85
0.5	2.2	130
1	2.0	140
2	1.1	250

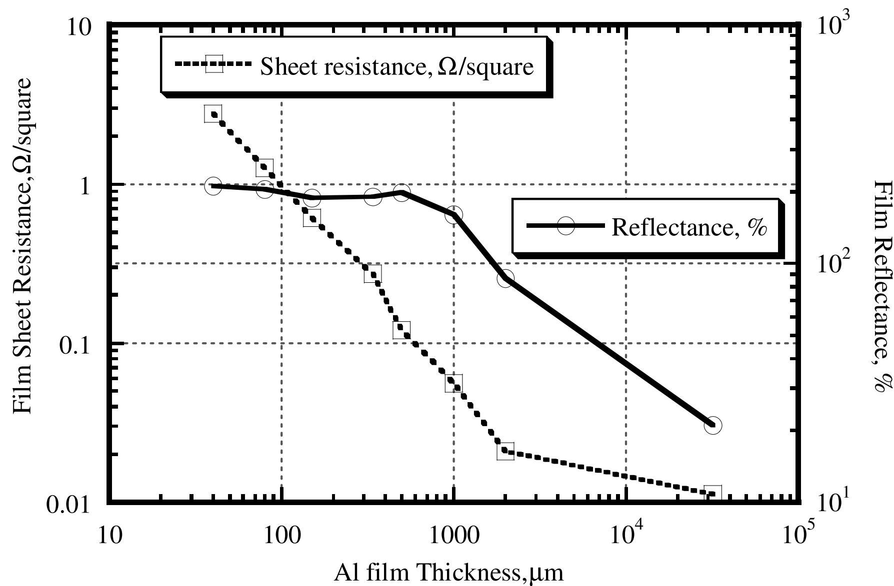

Figure 123. Sheet resistance and reflectance of Al films as a function of film thickness.

Al Adhesion Measurements

All test structures were indented using a conical 90° angle 1 μm radius tip on a Nanoindenter II to six different loads: 25, 50, 100, 200, 400 and 600 mN. There were 3 indents at each load, giving a total of 18 indents for each film thickness. Load-displacement curves were recorded continuously during the tests (Figure 124 and Figure 125). A superlayer indention test spreadsheet (see Appendix for details) has been used to calculate the strain energy release rate for each indentation-induced delamination experiment.

Superlayer Residual Stress

Al films with both tensile and compressive residual stresses in the superlayer have been tested. In the case of the tensile stressed superlayer, the indenter goes deeper into the films for a given load, in agreement with experimental observations and FEM predictions for both bulk materials and thin films [133, 134, 205-207]. This effect is observed on all eight Al

film thicknesses (Figure 124 and Figure 125). For the delamination tests, the first deviation in the loading slope of the load-displacement curve is observed at the depth of 200 nm, with a 10 mN load required for a 40 nm thick Al film (Figure 124). Since a 200 nm depth is still within the spherical region of the indenter tip ($R_{tip} = 1\ \mu m$), the corresponding pressure is 24 GPa.

Zagrebelny and Carter [205] deposited silicate-glass films on pre-bent and strained sapphire substrates to control the residual stress in their films. Here tensile and compressive residual stresses of 0.4 GPa were achieved by substrate bending. Compared to the superlayer indentation, a similar result was observed qualitatively in terms of the loading behavior. The first deviation in the loading slope of their load-displacement curve was observed at a depth of 10 nm with a 0.2 mN corresponding load for a 200 nm thick glass film. Since a sharp Berkovich tip was used (R_{tip}=80 nm), the corresponding indenter pressure appeared to be 120 GPa, well above what would normally be expected even in a sapphire substrate. It is suspected that even in these relatively brittle materials the residual stress affects the resulting contact area through its effect on plastic flow giving the deviation observed.

The residual stress in the case of the superlayer indentations was not achieved by substrate bending as above but rather by changing the sputter deposition parameters. As a consequence, the resulting microstructure, density and properties of the superlayer W films were expected to differ between films in tension and compression. They were also expected to exhibit a difference in load-displacement behavior.

It is worthwhile to note that indentation adhesion measurements involve film debonding from the substrate, which occurs during the loading of the indenter into the film. The loading portion of the load-displacement curve also represents the multilayer compliance, which appears to be higher in the tensile case. Thin aluminum films with tensile stressed superlayers produce radial cracks emanating from the indentations (Figure 124), which increase the tip contact area (Figure 53). Given these differences, one should consider how these might affect the actual adhesion measurements.

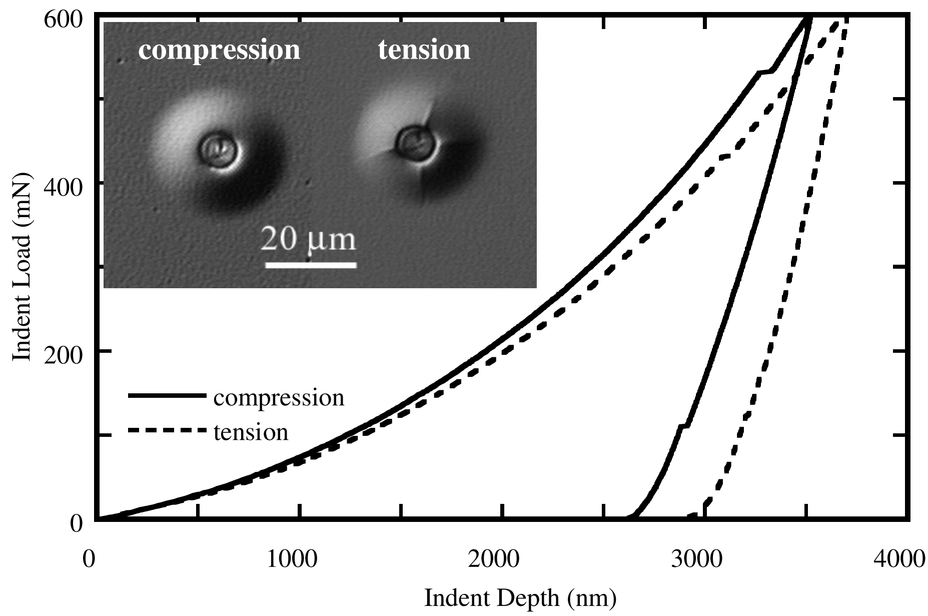

Figure 124. Load-displacement curves and corresponding blister delaminations for a 40 nm thick Al film with compressive and tensile W superlayers.

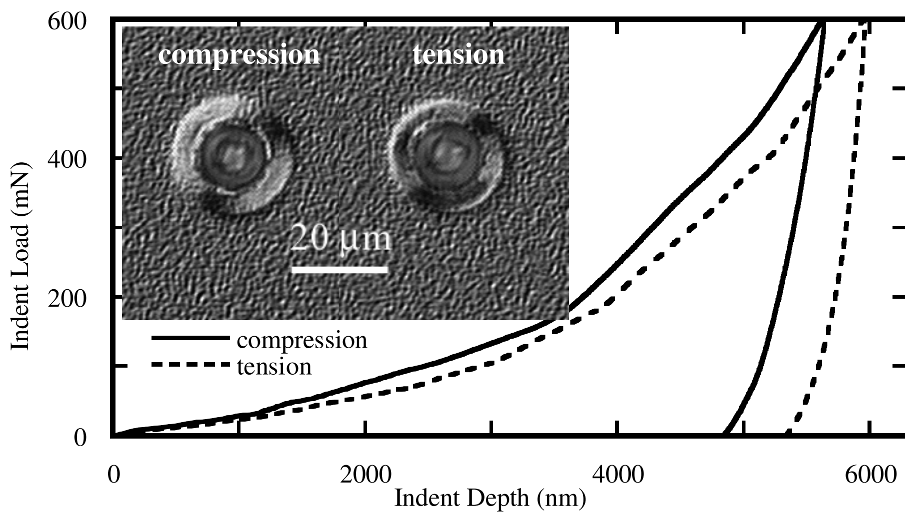

Figure 125. Load-displacement curves and corresponding blister delaminations for a 2 μm thick Al film with compressive and tensile W superlayers.

Al Film Adhesion Results

In the case of a ductile thin film (Cu or Al) on a hard substrate (Si/SiO_2), plastic deformation of the film will contribute most of the energy comprising the practical work of adhesion, as shown in the study of copper films in previous chapters. The amount of plastic deformation at the crack tip and the practical work of adhesion increased with film thickness for copper. Al thin film adhesion as a function of Al film thickness is presented in Figure 128 for both types of W superlayers. Although measured adhesion values range from 4 to over a 100 J/m^2, with one exception at a thickness of 40 nm, there appears to be almost no thickness effect on the practical work of adhesion (30 J/m^2) of Al films up to 1 μm thick. Blister delaminations appear to be smaller and the residual indentation greater for a tensile stressed superlayer (Figure 124). Since the indentation depth is always larger with a tensile stressed W superlayer, one may expect such films to have a higher practical work of adhesion than films with a compressively stressed superlayer. However, this appears to not be the case, since adhesion values start to overlap for 80 and 150 nm thick Al films with both tensile and compressive superlayers. The difference in the practical work of adhesion of nearly 150 J/m^2 for 40 nm thick Al films is also difficult to justify by radial cracking as well, since this effect becomes negligible at greater Al thicknesses.

High Al film adhesion can also be explained by the R-curve behavior (Figure 126). Here, the strain energy release rate keeps increasing with increasing crack length for both types of W superlayers. This also indicates that most of these structures are not buckled, so the crack is mostly under Mode II loading conditions. There is also a mode mixity effect responsible for the broad range of the strain energy release rate values. Although there is no phase angle analytical solution for the superlayer indentation test, one may use a single layer solution (equation (1.18)) for single buckling from Hutchinson and Suo [24] to estimate the phase angle dependence. Figure 127 shows the strain energy release values measured for a 500 nm thick Al film as a function of the calculated phase angle, based on equation (1.18) and using ω=55° [24]. Phenomenological phase angle function form either equation (1.20) or (1.21) are plotted for comparison, assuming λ=0 and Γ_0=4 J/m^2 (the lowest strain energy release rate measured for Al).

Adhesion values converge for both residual tensile and compressive W superlayers for 2 and 3.2 μm thick Al films, reaching on average an extremely large value of 500 J/m^2. Though Ritchie et al [208] measured Al_2O_3/Al toughness of 65 to 400 J/m^2 using a 4-point bend test; we believe that such high values are unreasonable even for a 3.2 μm thick Al film. For these films, the high values can be partially attributed to crack tip interaction effects from overlap of the plastic zones around the indenter and crack tip.

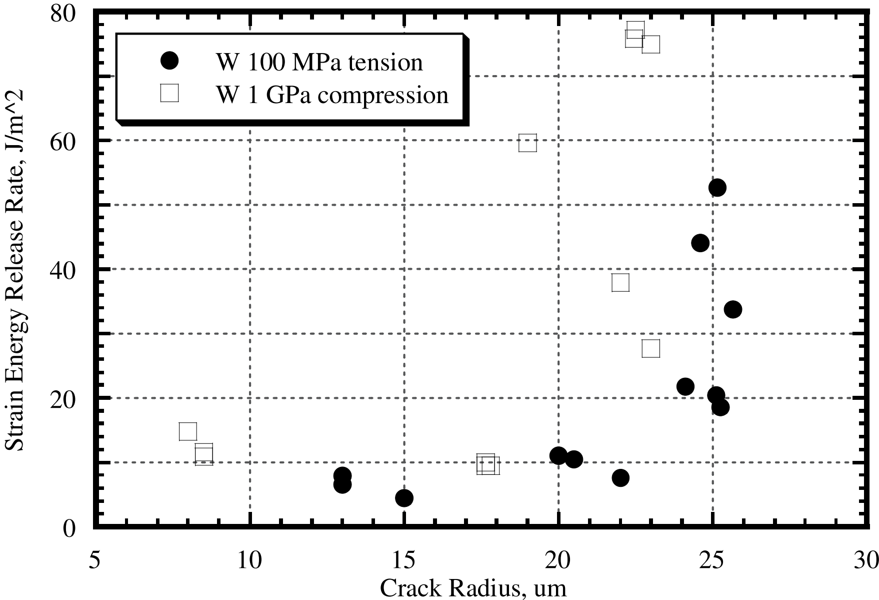

Figure 126. R-curve for a 1 um thick Al film.

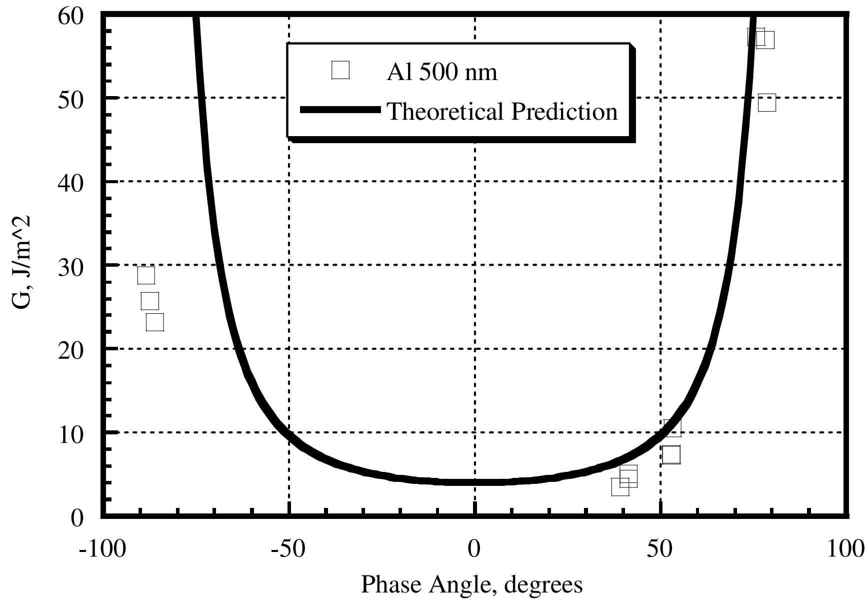

Figure 127. Strain energy release rate dependence on the phase angle for a 500 nm tick Al film. Solid line is a theoretical prediction from either equation (1.20) or equation (1.21), assuming λ=0 and Γ_0=4 J/m^2.

To briefly illustrate the effect, Figure 129 shows the normalized strain energy release rate as a function of distance from the indenter for both plane strain and plane stress. The plane strain solution from Vlassak et al [40] is applicable for a wedge indenter. A corresponding plane stress plot (Figure 129b) is obtained by varying both the indentation depth and the blister diameter using the bilayer solution by Kriese et al [46]. Both solutions are normalized by the appropriate strain energy release rate due to just the residual stress:

$$G_0 = \frac{\sigma_{resW}^2 h}{2E_W} \text{ for plane stress, } G_0 = \frac{\sigma_{resW}^2 h_W (1-\nu_W^2)}{2E_W} \text{ for plane strain} \quad (7.1).$$

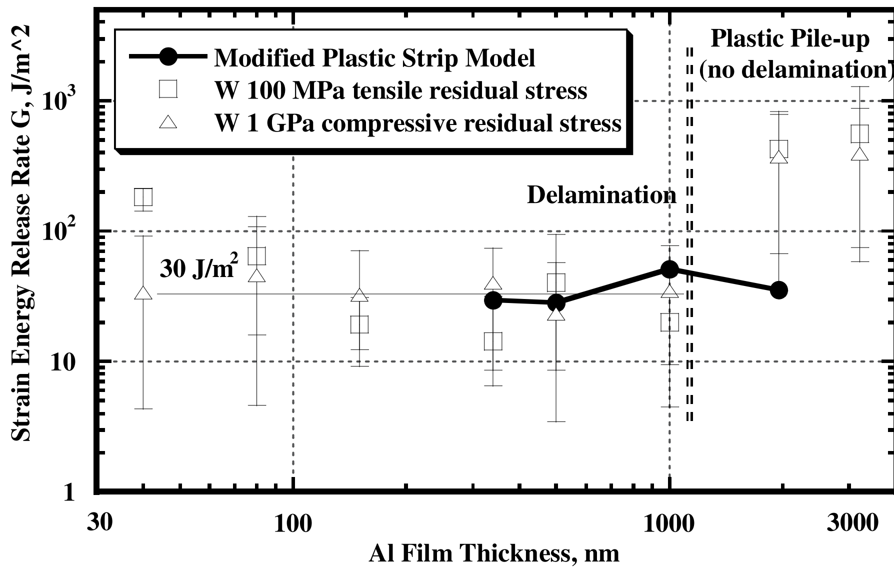

Figure 128. Al thin film adhesion with residual tensile and compressive residual stresses in the W superlayer. Modified Plastic Strip Model is equation (7.4).

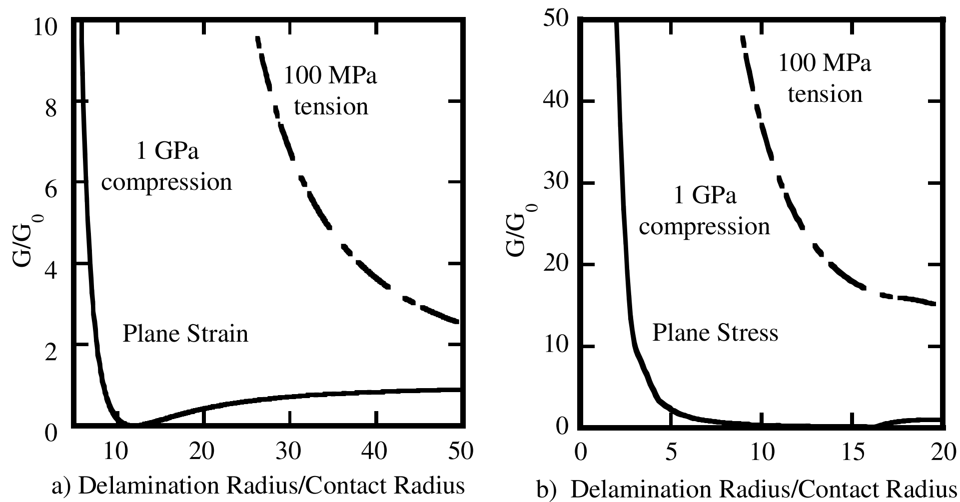

Figure 129. Plane strain a) and plane stress b) normalized strain energy release rate as a function of distance from the indentation for films with residual tensile and compressive residual stresses.

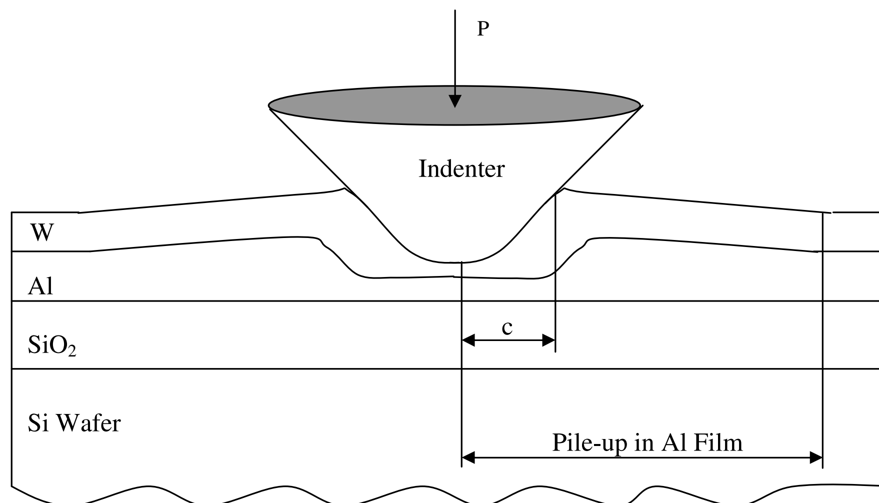

Figure 130. Schematic of the plastic pile-up without interfacial delamination in Al film.

The blister to the indenter contact diameter ratio has to be much greater in the case of a tensile W superlayer compared to compression to avoid this tip interaction effect. Since the radii ratio is only about three for thick Al films (Figure 125), this tip interaction effect is present regardless of the magnitude of the superlayer stress. The only way to solve the problem would be to use a thicker W superlayer, which will store higher elastic energies available for delamination. Given the same test conditions, a compressive residual stress in the superlayer is preferred. Here, the compressive residual stresses in the superlayer are being added to the indentation stress. On the other hand, the indenter has to overcome the tensile residual stress to achieve sufficient compression before a crack can nucleate and grow at the interface. The current analysis does not account for radial cracking, nor for residual stresses prior to film buckling; both may have an effect on the multilayer buckling stress threshold. These require further investigation.

On the other hand, there may be no delamination in thick Al films at all. It is very typical for clean metal/oxide interfaces that the strain energy release rates achieved without failure are well in excess of the critical energy release rate for the oxide [1, 209-211]. There

are examples when 200-400 J/m^2 has been imposed on the metal/oxide interface without failure, despite a very small critical value for the oxide (10-20 J/m^2). We believe that thicker Al films simply did not delaminate from the substrate, since the crack nucleation threshold was too high. This is schematically shown in Figure 130, where high indentation stresses have caused severe plastic deformation in both W and Al layers. Similar behavior has been observed in well-adhered electroplated Cu films on the TiW underlayer. What looked like an indentation-induced blister delamination (Figure 131), was found to be just plastic pile-up (Figure 132) upon cutting the structure with FIB.

The plastic pile-up radius is typically three times greater than the indentation radius. In order to avoid further confusion and expensive FIB characterizations, as well as at least partially the tip interaction effects, blisters smaller than three indentation diameters should not be considered for adhesion measurements. If higher delamination to contact ratios cannot be obtained in a given extremely well adhered thin film system, a thicker superlayer and higher indentation loads should be used to avoid the above mentioned effects.

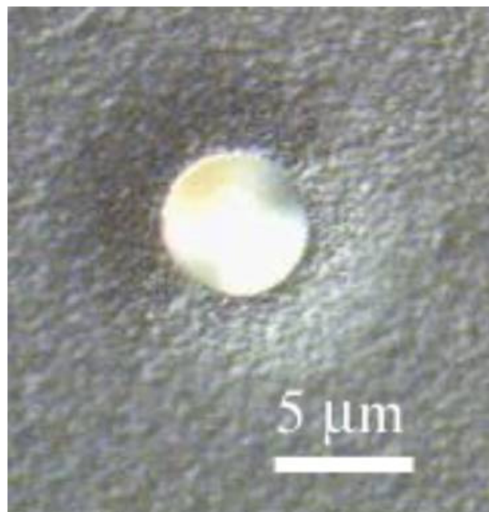

Figure 131. Indentation into TiW/Cu/TiW film stack.

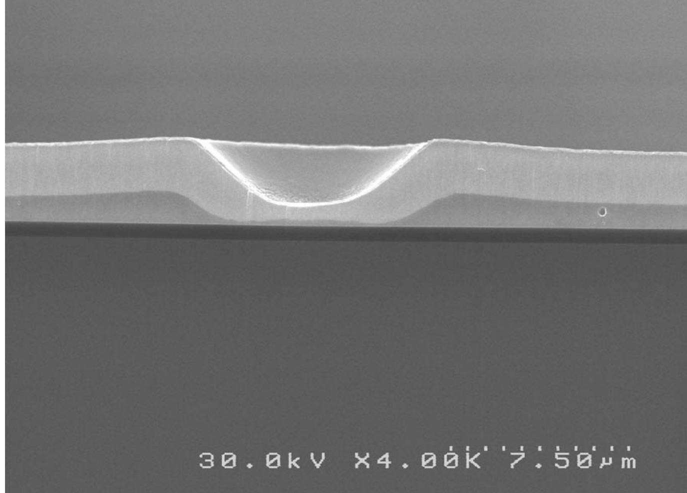

Figure 132. SEM image of the FIB cross-section of an indent in Figure 131, showing no interfacial delamination {courtesy of Motorola}.

Modified Plastic Strip Model

The upper bound plastic strip model presented in Chapter 3 (equation (3.5)) considered only the plastic work contribution to the strain energy release rate. One can add the surface energy term, 2γ:

$$\gamma = \frac{\sigma^2 \pi a}{2E} \tag{7.2},$$

where a is the crack length. At least for the crack initiation stage the $\pi a/2$ term is comparable to the film thickness, and the maximum stress is the yield stress, so

$$\gamma \approx \frac{\sigma_{ys}^2 h}{E} \tag{7.3}.$$

One can add in the surface energy by inserting e into the logarithmic argument of equation (3.4):

$$G = h\frac{\sigma_{ys}^2}{E}\left\{ln\left[\frac{h}{b}\right]-1+\frac{b}{h}\right\}+h\frac{\sigma_{ys}^2}{E}=h\frac{\sigma_{ys}^2}{E}\left\{ln\left[\frac{he}{b}\right]-1+\frac{b}{h}\right\} \tag{7.4}.$$

Even at $h=b$, the strain energy release rate $G=2\gamma=\sigma_{ys}^2 h/E$, which would imply that the local stress associated with debonding would be limited by the yield strength.

The modified plastic strip model is presented in Figure 128 along with the measured Al films adhesion. Here, the experimental values for yield strength of Al films from Table 8 were used for calculating G values, employing equation (7.4). The model passes right through the middle of experimental data for films up to 1 um thick, which means that there is sufficient plastic zone size at the crack tip accompanied with the tip interaction effect. For the 2 um thick Al film the model predictions are well below the calculated G values, which means that these thicker films did not delaminate from the substrate as discussed in the previous section.

The model should be an upper bound, since it assumes that the plastic zone size ahead of the crack tip spreads all the way to the film thickness. The fact that model predictions fall below the measured G values means that there is crack tip plastic zone tunneling, tip interaction and maybe even plasticity contributions from the superlayer. For these reasons, Al adhesion to SiO_2 is very high in the case of a clean interface.

7.2 CONTAMINATION EFFECT ON Al FILM ADHESION

Clean interfaces between Al and ceramic substrates are typically very strong [210]. This drastically changes with the presence of segregates and contaminants at the interface.

Similar to Cu metallization, underlayers are used with Al, though the purpose of putting an underlayer is different. Typically underalyers are used to improve resistance to stress and electromigration in Al, but not to improve Al adhesion, which is good as it is.

Al Films On Cu And C Underlayers

To study the effects of substrate contamination on Al film adhesion, 40 nm thick Cu and C layers have been deposited on wafers prior to Al film deposition (Figure 133).

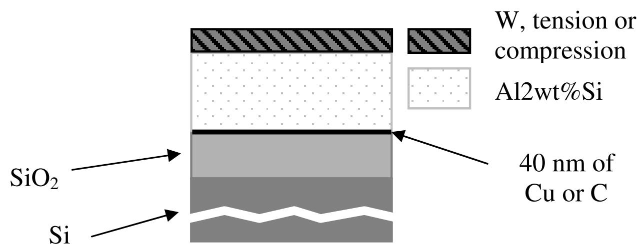

Figure 133. Al film contamination stack schematic.

These adhesion-weakening layers were deposited using a 2400 Perkin-Elmer RF sputtering apparatus. The sputtering conditions for the Cu were as described in Chapter 3, Table 4. Carbon was deposited with the Ar pressure of 14 mTorr, the base pressure of the system was 1 µTorr. Substrate table rotation was used for both Cu and C depositions. Then, Al films of eight different thicknesses from 40 to 3000 nm were deposited on top of the layers just like in the previous section.

Initially, a highly compressed W superlayer (1 GPa residual stress) was deposited on top of all test structures. Due to extremely poor adhesion high W stress caused debonding of Al films thinner than 500 nm from the C underlayer. Thicker films remained attached to the substrate, although occasional telephone cord delaminations, similar to those shown in Figure 136, were present. This necessitated another W superlayer deposition run, which produced a W with tensile residual stress in it.

<u>Al Film Adhesion On Cu And C Underlayers</u>

Strain energy release rates for Al films on Cu and C underlayers are shown in Figure 134. Compared to the non-contaminated Al adhesion, these values are much smaller. For the Al film under 1 um thick on a 40 nm Cu underlayer the strain energy release rate ranged from 0.1 to 3 J/m^2. Plastic energy dissipation effects start to become appreciable for thicker films, increasing the average adhesion values up to 30 J/m^2.

Similar to the non-contaminated Al films, there is the superlayer residual stress effect. The indenter tip penetrated the superlayer stack deeper for a given load in the case of a tensile superlayer residual stress (Figure 135). It appears that in these poorly adhered thin Al films delamination is driven by the superlayer residual stress, rather than by the indentation stress. The indenter acts like a defect nucleation source, inducing telephone cord delamination in some films (Figure 136).

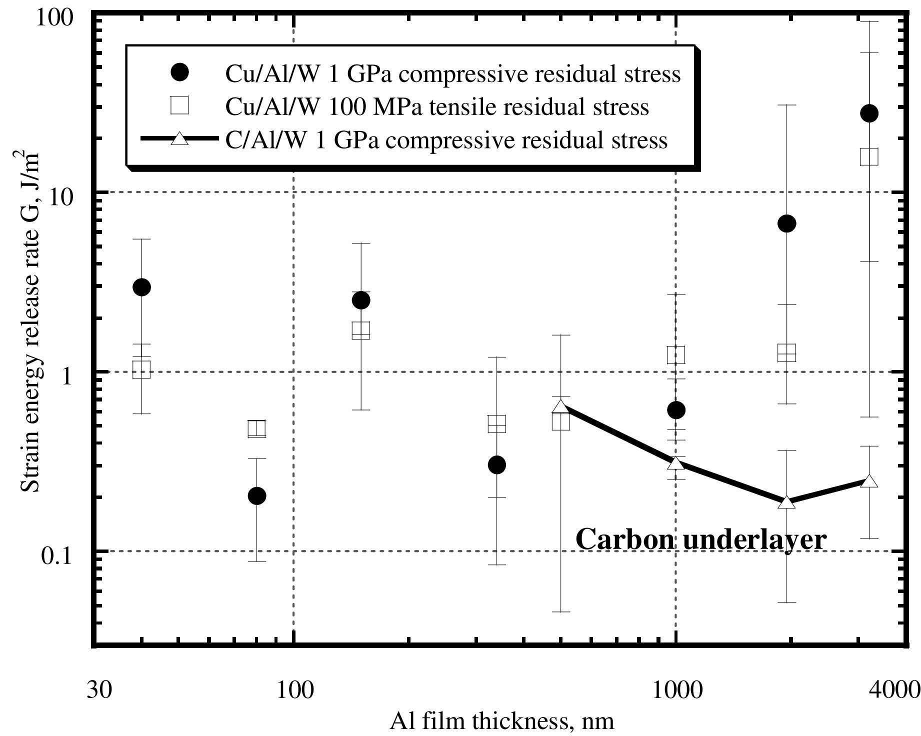

Figure 134. Al film adhesion with Cu and C underlayers.

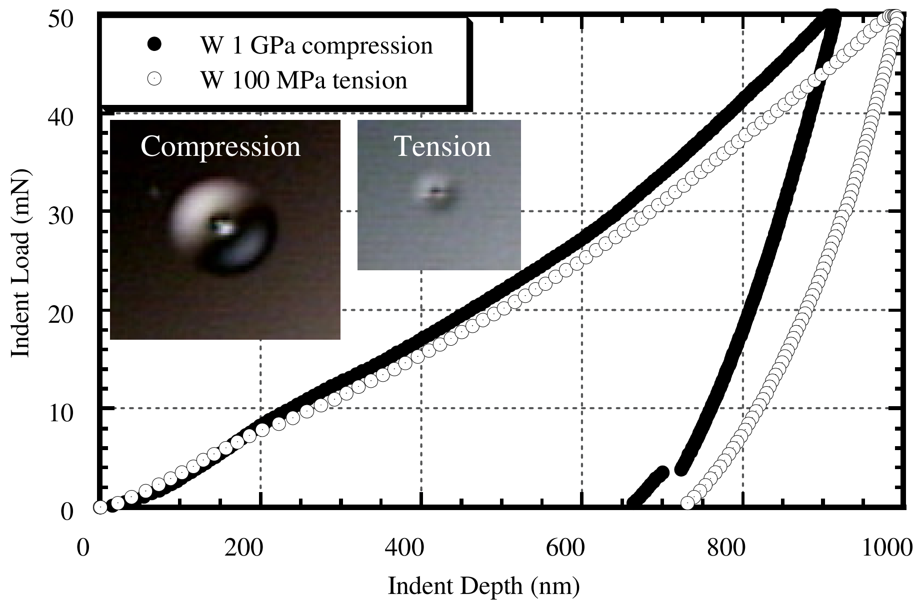

Figure 135. Load-displacement curves with corresponding delaminations in a 340 nm thick Al film on Cu with different superlayers.

Unlike films with a tensile residual stress superlayer, all Al films with a compressed W superlayer did not exhibit the radial cracks formation (Figure 135 and Figure 137). For 340 nm films loaded to 50 mN, larger delamination zone in the compressed superlayer gave a lower toughness than the tensile superlayer in Figure 134. On the other hand, for films 2 um thick loaded to 400 mN, the "tensile" superlayer blister appears to be larger than the "compressed" one, which results in its lower adhesion for this film thickness (Figure 134). Comparing the data for the tensile and compressive superlayers in Figure 134, it does not seem like there is a huge radial cracking contribution effect for the Al films with the tensile W superlayer. For some film thicknesses (40, 150, 2000 and 3000 nm) the adhesion is higher for Al films with the compressed W superlayer.

Although the adhesion between a 40 nm Cu layer and SiO_2 is low, the presence of a more ductile Al layer on top of the Cu contributes to the plastic energy dissipation at the crack tip. This effect is responsible for the thicker Al/Cu films higher adhesion (Figure 134).

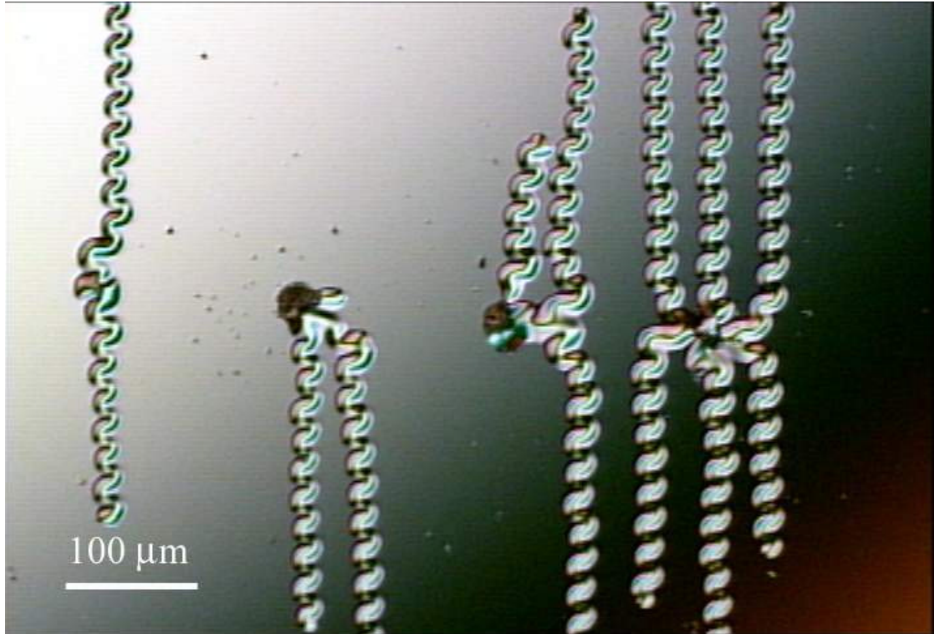

Figure 136. Indentation-induced telephone cord delaminations in a Cu/Al 500 nm thick film.

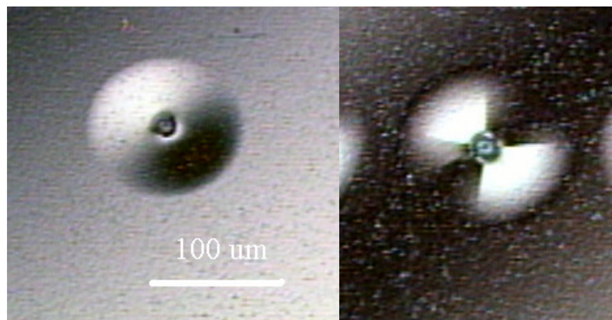

Figure 137. Blister delaminations of a 2 um thick Al film on Cu with the compressive (left image) and tensile (right image) stress in the w superlayer.

Figure 138. Al film spallation and circumferential cracking (Al 340 nm film on Cu, 1 um W 100 MPa tensile residual stress).

Some of the high load indentation-induced delaminations have exhibited circumferential cracking at the edge of the blister along with the film spallation (Figure 138). This supports the argument presented in Chapter 3, which states that there is in fact a limit to which the blister can propagate, no matter how high the load is. The superlayer material cannot transfer the indentation stress over a certain crack length. In this case high bending stresses at the edge of the blister have caused through-thickness film circumferential fracture and partial spallation (Figure 138). The only case when this does not happen is when the high compressive residual stress in the superlayer drives the delamination further, forming telephone cords (Figure 136).

In the case of a carbon contamination layer the Al film adhesion is extremely low, ranging from 0.02 to 0.7 J/m^2. Unlike any other film system considered in this thesis, the adhesion of Al on C decreases with the Al thickness increase. This implies that fracture may have occurred inside the carbon layer, or a 40 nm thick carbon buffer layer reduced dislocation shielding effects.

Here the delamination is driven mostly by the residual stress both in Al and the W superlayer. Recalling equation (1.61), the amount of stored elastic energy scales with the film thickness and square of the residual stress. In this case of a compressive residual stress in the superlayer (W) and tensile stress in the underlayer (Al), both stresses would contribute to the positive bimaterial beam bending moment, thus the total curvature change (Figure 139). A similar situation has been observed in the case of the bimaterial lines debonding [212]. Since the residual stress in Al film is almost independent of the film thickness, film thickness would be the only factor contributing to the strain energy release rate, so thicker Al films on C would have lower adhesion, just like observed experimentally (Figure 134).

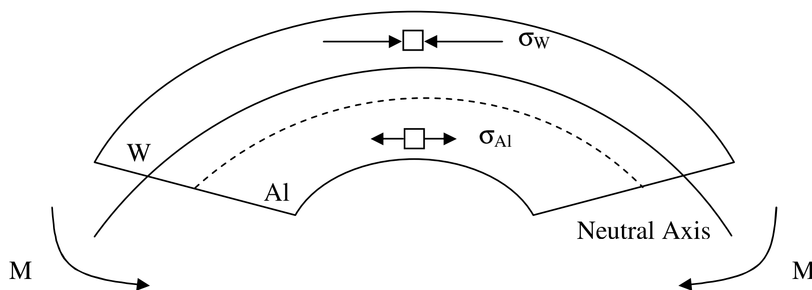

Figure 139. Schematic of a bilayer film bending due to the residual stress in each layer.

Once there is an interfacial defect, the bilayer debonds from the substrate almost without any plastic energy dissipation at the crack tip. The only plastic energy dissipation may occur due to the permanent plastic bending of the bilayer from the residual stress relief.

Perfect blisters without any signs of radial cracking in the W superlayer on top of a 2 um thick Al film are shown in Figure 140. Blister elliptical elongation along the indentation line indicates some stress interaction effects, which should be avoided by placing the indents farther apart. The load-displacement curve for this Al film is shown in Figure 141. Multiple slope changes in the loading portion correspond to several fracture events. Without plasticity effects, the fracture mechanism here is quite different compared to the Cu underlayer.

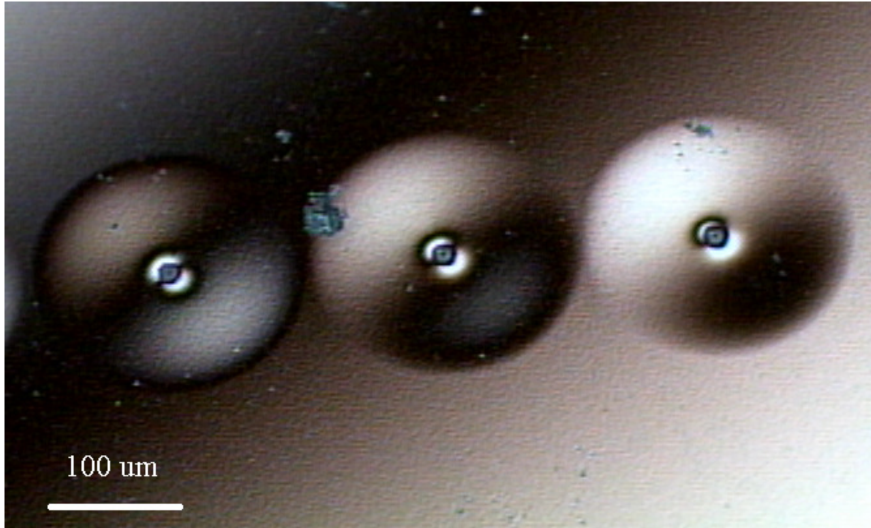

Figure 140. Indentation-induced blisters in a 2 um thick Al film on the carbon underlayer.

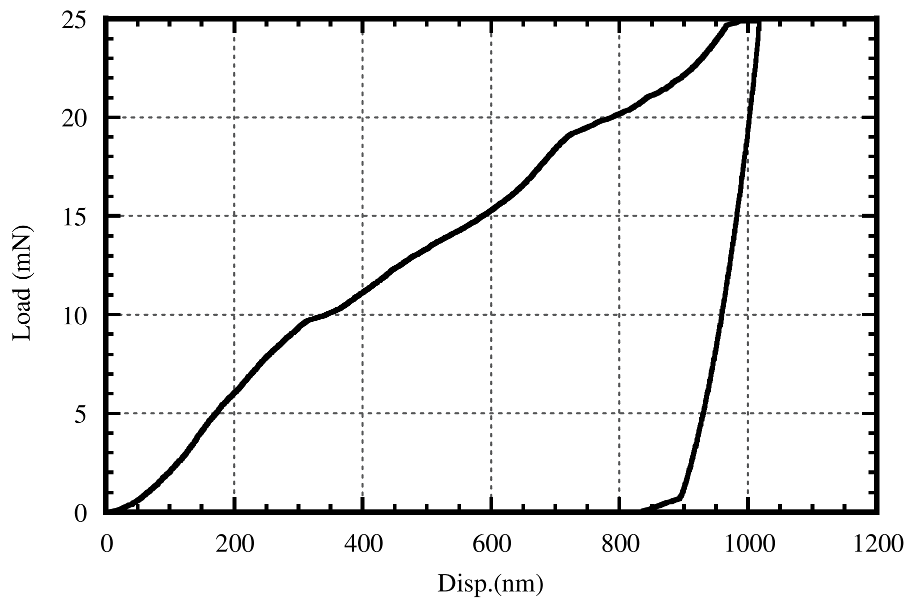

Figure 141. Load-displacement curve for the 2 um thick Al film on carbon.

CHAPTER 8. SUMMARY AND RECOMMENDATIONS

SUMMARY

One of the goals of this thesis was to further develop a rapid inexpensive thin film adhesion measurement technique, which tests films in the as-deposited or as-processed condition, and does not require special sample preparation such as diffusion bonding. Experimental adhesion strength assessment relied on the superlayer indentation technique and axisymmetric bi-layer theory [165].

Plastic energy dissipation effects on the toughness of a thin ductile film/brittle substrate interface have been quantitatively evaluated. Predictions of a proposed theoretical model have been compared to the experimental results for a Cu/SiO_2 interface with and without a Ti underlayer. Values ranging from 0.6 to 100 J/m^2 and from 4 to 110 J/m^2 increasing with the film thickness were obtained for Cu/SiO_2 and $Cu/Ti/SiO_2$ systems, respectively. Observed trends in interfacial toughness vs. film thickness dependencies were in qualitatively good agreement with the theoretical model. Bond strength estimates yielded average values of 10 GPa and 5 GPa for films with and without Ti underlayer, respectively. These values were nearly constant through all the range of Cu layer thicknesses indicating a true adhesion strength independent of the film thickness.

For the Cu films under a 100 nm thick without a Ti underlayer, the strain energy release rate appeared to plateau, being relatively constant at 0.6 - 0.9 J/m^2. This corresponds to the thermodynamic work of adhesion of Cu on SiO_2 and translates to a stress intensity of about 0.27 $MPa \cdot m^{1/2}$. This is less than the estimated 0.32 $MPa \cdot m^{1/2}$ for dislocation emission in Cu, so it was assumed that plastic energy dissipation is nil, and the true thermodynamic work of adhesion is measured for the thinner Cu films. The brittle-to-ductile transition has been identified at this film thickness. This has been also proven by the slow crack growth analysis. Spectroscopy analysis determined that debonding occurred along the Cu/SiO2 interface and with a Ti underlayer, along the Cu/Ti interface, allowing one to properly model fracture of these films.

Estimated phase angle values respectively dropped from 40° to 6° and from 14° to 2° for Cu/SiO_2 and $Cu/Ti/SiO_2$ systems as film thickness increased. Thus in both cases, increasing Cu film thickness resulted in a shift towards Mode I conditions. For the entire range of Cu film thicknesses, estimated plastic zone sizes were higher with the presence of Ti underlayers as compared to the films with no underlayer.

Taking into account the above, plastic energy dissipation has been identified as the mechanism primarily responsible for the observed elevation of the interfacial fracture toughness of Cu films over a 100 nm thick.

The same superlayer indentation approach was used to determine Cu film to SiO_2 adhesion as a function of test temperature. Increasing temperature from 20 °C to 130 °C for an 80 nm Cu film raised the fracture energy from 1 to 4 J/m^2, implying a brittle-to-ductile transition due to the temperature rise. Based on previous studies of fracture in Fe-3wt%Si single crystal, the Dislocation Free Zone (DFZ) model was developed to predict brittle-to-ductile transition in Cu films. The model is in a good agreement with the strain energy release rate experimental data, both as a function of film thickness and test temperature.

AE analysis of an indentation into a superlayer Cu structure was performed. An acoustic emission signal was used to detect both the magnitude and the type of fracture events in thin Cu films. The energy of a given burst AE event was shown to increase with the rise time. For the Cu thin film system with a Ti underlayer, acoustic emission energy varied inversely proportional to the strain energy release rate due to incremental cracking below the detector threshold. Total AE emission energy was found to be much lower for the system with a Ti underlayer due to improved adhesion. This not only reduced the blister area but also limited the size of incremental crack advance thus reducing the number of detectable acoustic events. For all film systems considered the total acoustic emission energy increased with the delamination diameter.

Crack arrest (fiducial) marks were discovered after blister removal with an adhesive tape, and consisted of carbon. The feature geometry was proposed to represent the shape of the crack tip, providing the basis for the crack tip opening displacement angle measurements. The fiducial mark's geometry along with the slow crack growth analysis provides the basis for assessing thin film interfacial toughness, using Rice, Drugan and Sham (RDS) model. Based on the findings of similar delaminations induced by high residual stress in a different

film system at Motorola, the fiducial marks source has been identified as the atmospheric hydrocarbon contamination. Hydrocarbons from the air were sucked into the crack tip upon thin film delamination from the substrate.

Bleed-trough petal-shaped contamination marks were discovered around the radial cracks in the indentation-induced blister delaminations. Being different in nature than the fiducial marks, bleed-though marks contained copper and sulfur. These chemical contamination effects may affect thin film adhesion by inducing stress-corrosion cracking.

Finally, the practical work of adhesion for Al thin films of different thicknesses has been measured using the superlayer indentation technique. Two different W superlayers with tensile and compressive residual stresses were used. Compressive and tensile residual stresses in the superlayer were achieved by changing the sputtering deposition parameters. Films with the tensile W superlayer exhibited radial cracking up to 1 μm thick Al film, so in general a compressive residual stress in the superlayer is preferred. Al film adhesion varied from 4 to a 100 J/m^2 for the films up to 1 um thick, averaging at about 30 J/m^2. The greatest difference of 150 J/m^2 in the measured adhesion values was observed on a 40 nm Al film. Unlike for Cu films, no toughness transition was found for the low film thicknesses. Film thicker than 1 um formed plastic pile-up around indentation and did not delaminate from the substrate. Apparently, the crack initiation threshold is too high for these films. For the indentation-induced delamination the blister radius has to be at least three times greater than the indentation radius, otherwise it may be confused with plastic pile-up. These issues will be addresses in recommendations for future work.

Contamination effects on Al film adhesion were also studied with the use of adhesion-weakening 40 nm thick Cu and C underlayers. In the case of Cu underlayer the strain energy release rate increase is observed for only thicker (> 1 um) Al films. Due to the high compressive residual stresses in the superlayer some films exhibited indentation-induced telephone cord delamination. For the C underlayer the measured work of adhesion decreased with the Al film thickness, since the delamination is driven mostly by the stored elastic energy in the W/Al bilayer. In this case there is almost no crack tip plastic energy dissipation, and delamination is governed by the bilayer residual stress.

RECOMMENDATIONS

Constitutive Properties Determination In Extreme Environments

One of the important aspects of modeling ductile film fracture is the constitutive properties determination. As discussed in this thesis, these may change along with many parameters such as film deposition, film thickness, grain size, test temperature, indentation depth, etc. Since copper, as well as many other metallic films, oxidizes at relatively small temperatures, measuring elastic and plastic properties with the nanoindentation technique in laboratory environment does not give the desired results. In order to solve this problem indentation should be performed in vacuum or neutral gas. For this purpose, the indentation should be conducted under vacuum conditions. If the whole instrument were to be placed in vacuum, this would require all indenter parts to be vacuum compatible. Although the Hysitron indenter has been inside an environmental chamber [213], this is different than using it in vacuum. These are instrumentation issues that have to be resolved.

Indentation is a pioneering field, and it is not standardized yet, so there are also issues that concern the data analysis, substrate and indentation size effects for example.

Radial Cracking

The current superlayer indentation test analysis does not account for radial cracking. There have been some indirect approaches used in the current study such as extracting the length of the load-displacement excursion from the inelastic indentation depth. The proper way to account for this effect would be to incorporate radial cracking into the analysis. One of the ways to account for radial cracking in the superlayer indentation test would be to modify the buckling solution that would account for the pie slice geometry instead of the annular buckling. Just from the theory of elastic stability [214] it is clear that the buckling threshold is lower for the four quarters of a blister than for the whole blister. It is useful to use numerical simulation to account for the radial cracking effect.

Phase Angle Determination For The Superlayer Test

In case of a crack in a bilayer system there is always a mode mixity effect. Strain energy release rate values are not sufficient to fully characterize thin film adhesion. For a given film system the strain energy release rate may vary by an order of magnitude (Figure 127) due to the phase angle dependence. In order to properly address this, information about the phase angle is necessary. There are elastic multiplayer phase angle solutions [29].

Attempts have been made to estimate the phase angle for different film systems considered in this thesis. Although currently there is no analytical phase angle solution for the superlayer indentation test. The problem of estimating the stresses at the crack tip irises from the fact that the stresses are mostly plastic. There are approaches when the characteristic length, L, can be used to calculate the phase angle at any distance, x, ahead of the crack tip [215]:

$$\Psi = \Psi^{*} + \varepsilon \, ln\left(\frac{x}{L}\right) \qquad (8.1).$$

Here, ψ^{*} is the phase angle at a characteristic length L, and ε is the bimaterial real constant defined by equation (1.16). Note that the distance x has to be within the zone of K-dominance. Still since ε is typically small (less than 0.05), even for x=10L the difference in phase angle is less than 7°.

It might be impossible to generate an analytical solution, since the stress state is extremely complicated, especially with the presence of plastic deformation ahead of the crack tip. The stresses ahead of the crack tip can be calculated using the Finite Element analysis (FEA), which would resolve the phase angle determination [216].

Double Indentation

Sometimes it is impossible to induce a crack nucleation by indentation for systems with tough interfaces. These interfaces may withstand extremely high G values (up to a 1000 J/m^2). Instead of delaminating, these would rather form a large plastic pile-up around the indenter. During the course of this study several extremely tough interfaces have been tested. These were thick Al films on SiO_2 and thick electroplated Cu films on TiW underlayer tested at Motorola. Basically, these interfaces did not delaminate from the

substrate. There are three ways to make these delaminate. First, one should use a thicker superlayer, since the amount of the stored elastic energy available for delamination scales with the superlayer thickness (Figure 9). A second approach can be taken by using a superlayer with higher elastic modulus and/or higher compressive residual stress. The third way would be to introduce a pre-crack into the tested structure. For macroscopic fracture experiments, sharp cracks are introduced by fatigue. While not directly applicable to the superlayer indentation test, one might find that repeat loading at the lower loads might introduce microcracks or weaken local interfacial bonding.

One of the ways to separate crack initiation from crack propagation in the superlayer indentation test would be to use double indentations, where there is a low load indentation followed by a higher load indentation into the same spot on a thin film. During the first indentation (preload), the crack is nucleated, and it is propagated during the second indentation. This idea is illustrated in Figure 142, where the two sequential load-displacement curves are shown along with the corresponding blisters in a 120 nm thick Cu film. This would allow to evaluate the strain energy release rates, $\partial U / \partial A$, associated with slow crack growth. The indentation work is proportional to the area under each indentation curve, so the ∂U nominator strain energy release energy term can be calculated. The denominator ∂A area term can be measured from the blisters corresponding to each load-displacement curve. Practically this would be done in two steps, where a single indentation for determining the initial crack length would be followed by the double indentation.

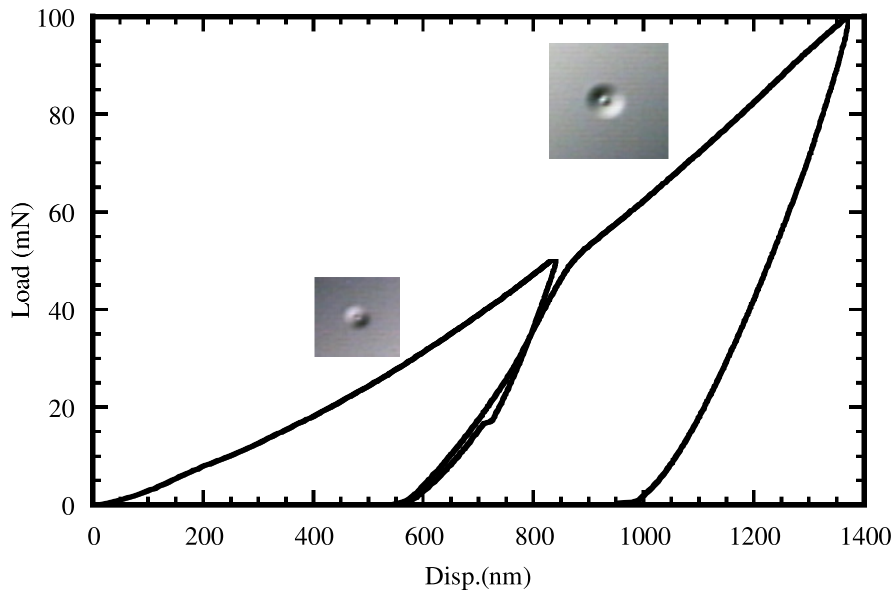

Figure 142. Double indentation into a 120 nm Cu film along with the corresponding blister delamination.

<u>Environmental Fracture Effects</u>

Fiducial and Bleed-through marks have been discovered during the course of this study, implying some chemical effects. This could easily cause stress corrosion problems. This would be extremely important for the thinner films with brittle interfaces. Hydrogen charging effects have been studied for Cu films [203], where they were charged with hydrogen in a solution, and adhesion was measured after charging. Typically charged films had lower adhesion.

Indentation can be performed in-situ with the presence of a corrosive environment [217]. It would be important to perform similar in-situ experiment to study thin film stress corrosion cracking. This can be done as a normal superlayer indentation test setup, where load is applied and instantaneously removed, or like an indentation creep experiment, where interfacial fracture would propagate under load. The diamond tip would have to be

isolated from the corrosive environment, as well as other parts of the indenter. Initially, distilled water can be used to see if there is an effect on adhesion.

The contamination source for the fiducial marks has been identified during this study. A simple experiment can prove that the marks are formed of hydrocarbons in the atmosphere. This can be done on the highly stressed films that form telephone cord delaminations. The telephone cord delamination should be induced either by a manipulator or indenter in vacuum, without the presence of contaminating atmosphere. This can be also done in different environments to enhance the fiducial marks formation.

Superlayer Indentation Test Adhesion Measurement Automation

Currently a picture of each delamination acquired in order to measure the blister size for adhesion calculation. Even though most of the modern microscopes are equipped with the digital image capture devices, the crack area measurement process is a routine and is time consuming. It is also not precise, since the delaminated areas are not always circular. This can be automated and improved with the image recognition software, which would not only take the images automatically, but would also measure the delamination areas.

Acoustic Emission Thin Film Fracture Analysis

Acoustic emission is a useful technique for thin film fracture characterization. With the proper hardware and software tools one should be able to classify fracture events in thin films. Placing an acoustic emission sensor underneath the sample is not the best experimental setup, since the sample geometry will affect the frequency content of collected acoustic emission signal. A better way would be to incorporate the acoustic emission sensor into the indenter tip [218], where the Surface Acoustic Wave (SAW) propagation is monitored in-situ with the indentation experiment. Currently the maximum load is limited to 50 mN for the Hysitron Triboscope, so the acoustic emission monitoring setup can only be used for brittle interfaces, which do not require higher loads for delamination. These experiments along with the Wavelet and short time Fourier transform analysis would provide valuable information about thin film fracture.

Fracture Characterization

It is important to understand the mechanism of crack nucleation and growth. To study the crack nucleation and dynamics one can employ optical microscopy using transparent substrates (glass or sapphire for example). Crack nucleation and propagation can be observed in-situ by using optical microscopy. For this, the microscope objective lens is placed underneath the transparent substrate, and the light beam is focused on the film/substrate interface underneath the indenter. Along with a video capture device this should provide the means of studying crack (interfacial and possibly radial) nucleation and dynamics, with the only limiting factor being the resolution of the optical microscope. These modified indentation devices are being currently built [215]. Since in the course of this study glass substrates were used in each thin film deposition run, samples are readily available for these experiments.

Another, more expensive way to study the superlayer indentation-induced fracture would be FIB ex-situ cross sectioning of blisters. This work is currently underway at Motorola. Figure 143 shows the FIB cut in a high load blister in a 120 nm thick Cu film. After being cross-sectioned with FIB, the sample can be imaged in an SEM.

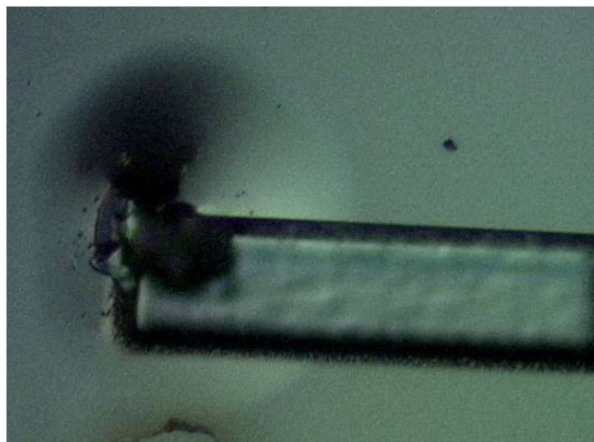

Figure 143. Optical micrograph of the FIB cut in a 120 nm Cu film blister.

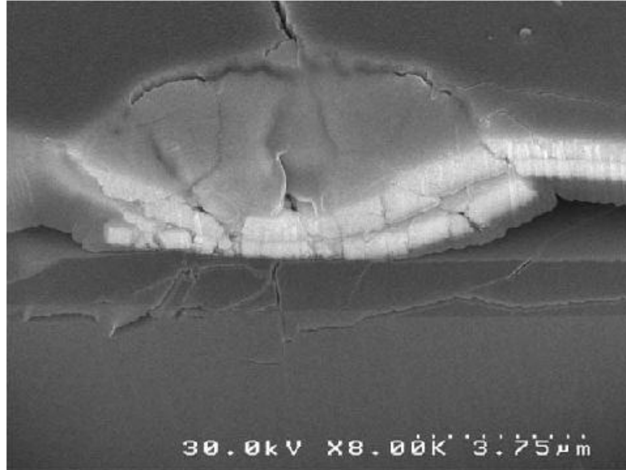

Figure 144. SEM image of the fracture zone underneath the indenter.

The center of the indent in Figure 143 is shown in Figure 144. Due to the high load (600 mN), severe substrate cracking occurs.

These studies provide insight of the fracture process, which would allow more accurate analysis of the superlayer indentation test.

Other Thin Film Systems

Superlayer indentation test is a reliable inexpensive adhesion measuring technique. It was shown to work on different film systems such as:

- Cu, Au, Al on hard substrates with different underlayers (work performed at the University of Minnesota (U of M), Sandia National Labs (SNL), Motorola-DDL)
- Ta, Ta_2N on Si substrates (U of M, SNL)
- Low-K polymer materials on Si substrates with different underlayers, PI on Si substrates (U of M, Motorola-DDL).

Three different superlayers have been utilized: W, TiW and Ta_2N. The superlayer material is not limited to these three choices, it should have high elastic modulus and hardness, and have higher adhesion to the tested film than the interfacial strength of the interface being interest.

Currently there are polymer film systems (PI on Si [220] and Low-K dielectrics on Si) that have been characterized in terms of their adhesion using the superlayer indentation

test. This should be further expanded to other film systems. The only problem with polymers is their low glass transition temperature, which makes these materials incompatible with the superlayer deposition. Films also have to be vacuum compatible for the superlayer sputter deposition. Other ways of low temperature non-vacuum superlayer deposition should be considered.

APPENDIX

EXCEL SPREADSHEET FOR THE SUPERLAYER INDENTATION TEST ADHESION DETERMINATION

Originally, calculations for the superlayer indentation test were performed by the MathCAD program, and later an Excel spreadsheet was developed for calculating interfacial adhesion energies [165]. Calculation requires the knowledge of the elastic properties of the film being tested and the superlayer material. Ideally, these should be measured independently, using the nanoindentation technique, for example. Table 9 shows the left upper portion of the spreadsheet, where the input parameters are defined. These are the elastic moduli and Poisson's ratios for the upper and lower films. Here, the upper film is the superlayer.

Calculations of the indentation volume in the spreadsheet are based on the conical tip shape. The only variable parameter in terms of the indenter geometry is the tip radius. The indentation volume calculations can be changes according to the tip geometry (Currently the volume is calculated in columns N through P). It should be pointed out that the variable parameters are highlighted in red in the spreadsheet, so here underlined cursive font is used to identify these.

Table 9. Materials parameters for the superlayer spreadsheet (Cells A1 through M11).

All units SI unless otherwise noted

Input Parameters				Other Parameters			
						90° conical tip assumed	
Upper Film		Lower Film		µB^2	14.682	tip radius, rt	*1.00E-06*
Modulus E	*4.110E+11*	Modulus E	*1.200E+11*	µ2B^2	42.670	rh	2.93E-07
Poisson's v	*0.28*	Poisson's v	*0.35*			A	7.07E-07
E/(1-v)	5.71E+11	E/(1-v)	1.85E+11	n	3.261		
E/(1-v^2)	4.46E+11	E/(1-v^2)	1.37E+11	n2	3.092		

*positive stress=compressive
*positive strain=compressive

Table 10. Spreadsheet Input parameters for each indent (Cells A26 through M38).

run no.	*Upper Film Thickness*	*Upper Film Resid Stress*	*Lower Film Thickness*	*Lower Film Resid Stress*	*Crack Radius a*	*Indent Depth d*
1	1.10E-06	2.70E+08	9.70E-08	-2.86E+08	6.80E-06	5.46E-07
2	1.10E-06	2.70E+08	9.70E-08	-2.86E+08	6.80E-06	5.55E-07
3	1.10E-06	2.70E+08	9.70E-08	-2.86E+08	1.09E-05	9.41E-07
4	1.10E-06	2.70E+08	9.70E-08	-2.86E+08	1.12E-05	9.52E-07
5	1.10E-06	2.70E+08	9.70E-08	-2.86E+08	2.76E-05	1.34E-06
6	1.10E-06	2.70E+08	9.70E-08	-2.86E+08	2.23E-05	1.34E-06
7	1.10E-06	2.70E+08	9.70E-08	-2.86E+08	8.25E-06	8.30E-07
8	1.10E-06	2.70E+08	9.70E-08	-2.86E+08	9.02E-06	8.19E-07
9	1.10E-06	2.70E+08	9.70E-08	-2.86E+08	8.44E-06	8.05E-07
11	1.10E-06	2.70E+08	9.70E-08	-2.86E+08	7.71E-06	4.70E-07
12	1.10E-06	2.70E+08	9.70E-08	-2.86E+08	3.35E-06	4.88E-07

Table 11. Calculated G values (Cells BM28 through BR50).

Sample: *F5 Ti/Cu 120 nm*

Upper Film		Lower Film	
Thick	1.100 µm	Thick	0.10 µm
Stress	270.0 MPa	Stress	-286.0 MPa
Modulus	411.0 GPa	Modulus	120.0 GPa
Poisson	0.28	Poisson	0.35

**pos stress = compression*

run no.	crack radius	indent dep	dep/thick	indent stress	G
1	6.8 µm	0.546 µm	0.46	2461 MPa	2.2
2	6.8 µm	0.555 µm	0.46	2536 MPa	2.3
3	10.9 µm	0.941 µm	0.79	2980 MPa	3.2
4	11.2 µm	0.952 µm	0.80	2862 MPa	2.9
5	27.6 µm	1.340 µm	1.12	1019 MPa	0.4
6	22.3 µm	1.335 µm	1.12	1546 MPa	0.9
7	8.3 µm	0.830 µm	0.69	3940 MPa	5.6
8	9.0 µm	0.819 µm	0.68	3213 MPa	3.7
9	8.4 µm	0.805 µm	0.67	3539 MPa	4.5
11	3.3 µm	0.488 µm	0.41	8152 MPa	23.9
12	3.3 µm	0.488 µm	0.41	8152 MPa	23.9

Calculation of the strain energy release rates for each indentation is performed in the spreadsheet's rows. For each experiment the film's thickness and residual stresses are

necessary (Table 10). These are typically the same for a given sample. Then, for each individual indentation experiment the delamination radius as measured with optical microscope is required along with the inelastic indentation depth, determined from the load-displacement curve as discussed in Chapter 1. This provides strain energy release values as shown in Table 11. Here, results are shown for 12 indentation experiments conducted on a 120 nm Cu film with a Ti underlayer. It is preferred to use the indentation depth below the total film stack thickness, so experiments 5 and 6 should not be considered in this case. The calculated strain energy release rate values are plotted as a function of the indentation depth/total superlayer stack thickness ratio.

REFERENCES

1. D.M. Lipkin, D.R. Clarke, A.G. Evans, Acta Mater. Vol. 46, No. 13, pp. 4835-4850, 1998
2. C. Lee, K. Lin, Jpn. J. Appl. Phys. 33, p. 2684, 1994
3. A. Furuya, N. Hosoi, Y. Ohshita, J. Appl. Phys. 78 (10), pp. 5989-5992, 1995
4. A.A. Griffith, Phil. Trans. R. Soc. Lond., 1920, A221, p.163
5. R.M. Pilliar, J. Nutting, Phil. Mag., 1967, 16, p. 181
6. W.L. Winterbottom, Acta metal., 1967, 15, p. 303
7. D.M. Lipkin, D.R. Clarke, A.G. Evans, Acta Mater. Vol. 46, No. 13, pp. 4835-4850, 1998
8. A.A. Griffith, Phil. Trans. R. Soc. Lond., 1920, A221, p.163
9. E. Orowan, Trans. Instn. Engrs. Shipbuilders Scot., 1945, 89, p. 165
10. M.L. Jokl, V. Vitek, C.J. McMahon, Acta Metal., 28, p. 1479, 1980
11. A. Pocius, "Adhesion and Adhesives Technology. An Introduction." Hanser Publishers, 1997
12. M. Ohring, "The Materials Science of Thin Films", Academic Press Inc. 1991, p. 444
13. W.T. Chen, T.F. Flavin, IBM J. Res. Develop. 16, pp.203-213, 1972
14. A. Bagchi, A. Evans, MRS Symp. Proc. Vol 383, pp. 183-197, 1995
15. H. Ewalds, R. Wanhill, "Fracture Mechanics", Ewald Arnold publication, London, 1993
16. J. Hutchinson, "Mechanics of Thin Films and Multilayers", Technical University of Denmark, 1996
17. G. Irwin, J. Appl. Mech. 24, p361, 1957
18. Z. Suo, J. Hutchinson, Int. J. Frac., 43, pp. 1-18, 1990
19. J. Dundurs, J. Appl. Mech. 32, p. 400, 1965
20. K.M. Liechti and Y.S. Chai, J. Appl. Mech., 59, 295, 1992
21. H.C. Cao and A.G. Evans, Mech. Mater., 7, 295, 1989
22. J.S. Wang and Z. Suo, Acta Metall. Mater., 38, 1279, 1990
23. H.M. Jensen and M.D. Thouless, Int. J. Solid Structs., 30, p. 779, 1993
24. J. Hutchinson and Z. Suo, Advances in Applied Mechanics, Vol. 29, pp. 63- 191, 1992

25. J.R. Rice, Proceedings of the 1st International Conference on Fracture, Sendai, Japan, ed. T. Yokobuki, T. Kawasaki, and J.L. Swedlow, p. 309, 1966
26. D.M. Lipkin and G.E. Beltz, Acta Mater., 44, 1287, 1996
27. D.M. Lipkin, D.R. Clarke, G.E. Beltz, Acta Mater., 44, 4051, 1996
28. A. Bagchi, G. Lucas, Z. Suo, A. Evans, J. Mater. Res., Vol. 9, No. 7, pp. 1734-1741, 1994
29. A. Bagchi, A. Evans, Thin Solid Films 286, pp. 203-212, 1996
30. A. Kinbara, E. Kusano, T. Kamiya, I. Kondo, O. Takenaka, Thin Solid Films 317, pp. 165-168, 1998
31. H. Ji, G.S. Was, M.D. Thouless, Engineering Fracture Mechanics 61, pp. 163-171, 1998
32. A.V. Zhuk, A.G. Evans, J.W. Hutchinson, J.Mater. Res., Vol.13, No. 12, pp. 3555-3564, 1998
33. G. Xu, M.-Y. He, and D.R.Clarke, Acta Mater. Vol. 47, No. 15, pp. 4113-4141, 1999
34. W.C. Oliver and G.M. Pharr, J. Mater. Res., **7**, pp.1564-1583, 1992
35. D.B. Marshall and A.G. Evans, J. Appl. Phys., 56, pp. 2632-38, 1984
36. L.G. Rosenfeld, J.E. Ritter, T.J. Lander and M.R. Lin, J. Appl. Phys. 67(7), 3291, 1990
37. M.P. De Boer and W.W. Gerberich, Acta Mater. 44 No 8, pp. 3169-3175, 1996
38. M.P. De Boer and W.W. Gerberich, Acta Mater. 44 No 8, pp. 3177-3187, 1996
39. M. De Boer, Ph.D. Dissertation, University of Minnesota, 1996
40. J.J. Vlassak, M.D. Drory and W.D. Nix, J. Mater. Res., 12, No 7, p. 1900-10, 1997
41. M.D. Drory and J.W. Hutchinson, Proc. R. Soc. Lond. A. 452, pp. 2319-2341, 1996
42. L.G. Rosenfeld, J.E. Ritter, T.J. Lander and M.R. Lin, J. Appl. Phys. 67(7), 3291, 1990
43. A.A. Volinsky, J.C. Nelson, W.W. Gerberich, Mater. Res. Soc. Proc. Vol. 563, 1999
44. M.R. Begley, D.R. Mumm, A.G. Evans and J.W. Hutchinson, Acta mater. 48, pp. 3211-3220, 2000
45. J.M Sanchez, S. El-Mansy, B. Sun, T. Scherban, N. Fang, D. Pantuso, W. Ford, M.R. Elizalde, J.M. Martinez-Escanola, A. Martin-Meizoso, J. Gil-Sevillano, M. Fuentes and J. Maiz, Acta Mater. Vol 4, No. 17, pp. 4405- 4413, 1999
46. M.D. Kriese and W.W. Gerberich, J. Mater. Res. 14 (7), p. 3007, 1999
47. M.Y. He, A.G. Evans and J.W. Hutchinson, Acta Metall. Mater., Vol. 44, pp. 2963-2971, 1996

48. P. Benjamin, C. Weaver, Proc. Roy. Soc. London, A 254, p. 163, 1960
49. P. Burnett, D. Rickersby, Thin Solid Films, 154, p. 403, 1987
50. S. Venkataraman, D. Kohlstedt and W.W. Gerberich, J. Mater. Res, 8, p. 685, 1993
51. S. Venkataraman, D. Kohlstedt and W.W. Gerberich, J. Mater. Res, 7, p. 1126, 1992
52. N. Moody, R. Hwang, S. Venkaterman, J. Angelo, D. Norwood and W.W. Gerberich, Acta mater., Vol. 46, No 2, pp. 585-597, 1998
53. M.P. De Boer, M. Kriese and W.W. Gerberich, J. Mater. Res., 12(10), 2673-2685, 1997
54. M.P. De Boer, J.C. Nelson and W.W. Gerberich, J. Mater. Res., 13(4), 1002-1014, 1998
55. J. Vlassak, W. Nix, J. Mater. Res. 7, pp.3242-3249, 1992
56. M.K. Small. J. Vlassak, W. Nix, MRS Symp. Proc. Vol. 239, 1992
57. M.K. Small and W.D. Nix, J. Mater. Res., 7(6), 1553- 1563, 1992
58. V. Paviot, J. Vlassak, W. Nix, MRS. Symp. Proc. Vol. 356, pp. 579-584, 1995
59. R. Hohlfelder, H. Luo, J. Vlassak, C. Chidsey, W. Nix, MRS Symp. Proc. Vol. 436, 1997
60. Kai-Tak Wan, Soon-Chong Lim, International Journal of Fracture 92, pp 43-47, 1998
61. H.M. Jensen, International Journal of Fracture 94, pp. 79-88, 1998
62. ASTM Standard 399-90 pp. 407-436, 1990
63. Z. Suo, J.W. Hutchinson, Mater. Sci. and Eng., A107, pp. 135-143, 1989
64. M. Menningen, H. Weiss, Surface and Coatings Technology, 76-77, pp. 835-840, 1995
65. J.M. McNaney, R. Havens and R.O. Ritchie, J. of Testing and Evaluation, pp. 28- 35, 1997
66. J.M. McNaney, R.M. Cannon and R.O. Ritchie, J. of Testing and Evaluation, pp. 95- 101, 1995
67. M.F. Kanninen, Int. J. Fract. 9, p. 83, 1973
68. F.P. Champonier, in Fracture Mechanics Applied to Brittle Materials, edited by S.W. Freiman, ASTM STP 678 (ASTM, Philadelphia), p.60, 1979
69. H.C. Cao, B.J. Dagleish and A.G. Evans, Closed Loop 17, p. 19, 1989
70. N. O'Dowd, C. Shih, M. Stout, Int. J. Solids Structures Vol. 29, No. 5, pp. 571-589, 1992
71. C. Atkinson, R. Smelser, J. Sanchez, Int. J. Fracutre, Vol. 18, No. 4, pp. 279-291, 1982
72. D. Shetty, A. Rosenfield, W. Duckworth, Engineering Fracture Mechanics, Vol. 26, No. 6, pp. 825-840, 1987
73. Y, Huang, C. Liu, G. Stout, Acta mater. Vol. 44, No. 3, pp. 1223-1232, 1996

74. J. Wang, Z. Suo, Acta metall. Mater. Vol. 38, No. 7, pp. 1279-1290, 1990
75. P.G. Charalambides, J. Lund, A.G. Evans, R.M. McMeeking, J. Appl. Mech. 111, pp. 77-82, 1989
76. I. Hofinger, M. Oechsner, H. Bahr and M. Swain, International Journal of Fracture 92, pp. 213-220, 1998
77. T.L. Becker Jr., J.M. McNaney, R.M. Cannon, R.O. Ritchie, Mechanics of Materials 25 (1997) 291-308
78. R. Liu, C-S. Pai, E. Martinez, Solid-State Electronics, 43, pp. 1003-1009, 1999
79. C. Kittel, "Introduction to Solid State Physics", 7th edition, pp. 160, 1996
80. H. Ono, T. Iijima, N. Ninomiya, A. Nishiyama, Y. Ushiku, H. Iwai, Jap. Soc. Appl. Phys. 40th Spring Meeting, pp.814, 1993
81. J.R. Lloyd, Mat. Res. Soc. Symp. Proc. Vol. 239, pp.667-676, 1992
82. J.R. Lloyd, Semicond. Sci. Technol. 12, pp. 1177-1185, 1997
83. J.R. Black, Proc. 6th Ann. Reliability Physics Symp. (New York: IEEE) p.148
84. I.A. Blech, H.Sello 5th Ann. Symp. On Physics of Failure in Electronics (Columbus, OH) (New York: IEEE), 1966
85. W.C. Shin, A.L. Greer, Mat. Res. Soc. Vol. 356, pp. 417-422, 1995
86. C.-K. Hu, D. C. Edelstein, C. Uzoh and T. Sullivan, VTAIP Conference Proceedings, No. 373. pp. 153-168, 1996
87. R. Frankovic and G. Bernstein, IEEE Transactions on Electron Devices, vol. 43, No. 12, 1996
88. G.C. Schwarts, P.M. Schaible, J. Electrochem. Soc., vol. 130, pp 1777-1779, 1983
89. T. Nitta, T. Ohmi, T. Hoshi, S. Sakai, K. Sakaibara, S. Imai, T. Shibata, J. Electrochem. Soc., vol. 140, p. 1131, 1993
90. R. Frankovic and G. Bernstein, MRS, vol. 391, p. 403, 1993
91. D.D. Brown, P. Borgesen, D.A. Lilienfeld, M.A. Korhonen and C.Y. Li, MRS Symp. Proc. Vol. 239, pp. 701-706, 1993
92. J. Torres, Applied Surface Science 91, pp. 112-123, 1995
93. M. Reilly, X. Jiang, J. Beechinor, S. Lynch, C. Dheasuna, J. Patterson, Applied Surface Science 91, pp. 152-156, 1995
94. A.M. Ektessabi, Thin Solid Films, 236, pp. 135-139, 1993

Comment [AV1]: ***Vinci thesis

Comment [AV2]: http://domino.watson.ibm.com/library/CyberDig.nsf/Home

95. S.Russell, S. Rafalski, R. Spreitzer, J. Li, M. Moinpour, F. Moghadam, T. Alford, Thins Solid Films 262, pp. 154-167, 1995
96. R. Spreitzer, S. Rafalski, D. Adams, S. Russell, Z. Atzmon, J. Li, T. Alford and J. Mayer, MRS Symp. Proc. Vol. 337, pp 631-636, 1994
97. Y. Park, S. Rhee and J. Hong, J. Vac. Sci. Technol. B15(6), pp. 1995-2000, 1997
98. T. Nguyen, D. Evans, MRS Symp. Proc. Vol. 356, pp. 859-862, 1995
99. A. Furuya, N. Hosoi, K. Koyama, Y. Ohshita and Y. Numasawa, IEEE Trans. on Electron Devices, Vol. 42, No. 12, pp. 2302-2303, 1996
100. C.G, Masl, R&D Semiconductor Research, Vol. 42, No. 7, pp. 14-20, 2000
101. H. Oettel, R. Wiedemann, Surface Sci. and Technol. 76-77, pp. 265-273, 1995
102. W.D. Nix, "Mechanical Properties of Thin Films. Course Notes." 1991
103. D. Maugis, Contact, Adhesion and Rupture of Elastic Solids, Springer, 2000
104. F. Spaepen, Acta mater. 48, pp. 31-42, 2000
105. R.P. Vinci, Ph.D Dissertation, Stanford University, 1994
106. R.P. Vinci, E.M. Zielinski, J.C. Bravman, Thin Solid Films 262, pp. 142-153, 1995
107. R.P. Vinci, E.M. Zielinski, J.C. Bravman, MRS Symp. Proc. Vol. 356, pp. 459-464, 1995
108. W.D. Nix, Metallurgical Transactions A 20A, pp. 2217-2245, 1989
109. C.V. Thompson, J. Mater. Res. 8, p. 237, 1993
110. M.D. Thouless, M.E. Harper, J.A. Gupta, J. Mater. Res., 8, p. 1845, 1993
111. W. Westwood, AVS Short Course, MPLS, MN, 1997
112. H.T.G. Hentell, C.R.M. Grovenor, and D.A. Smith, J. Vac. Sci. Tech., A2, p. 218, 1984
113. J.A. Thornton, Ann. Rev. Mater. Sci. 7, p. 239, 1977
114. G.G. Stoney, Proc.Roy.Soc.Lond. **A82** (1909) p.72
115. Frontier Semiconductor Measurements Inc., FSM 128&128L Operation Manual Rev 4/98
116. I. Blech, S. Robles, Solid State Technology, September 1994
117. W.D. Nix, Metall. Trans. A, 20A, pp. 2217-2245, 1988
118. B.D. Cullity, Elements of X-ray Diffraction. 2nd Edition ed. Reading, MA: Addison-Wesley

119. S.J. Hearne, J. Han, S.R. Lee, J.A. Floro, D.M. Follstaedt, E. Chason, I.S.T. Tsong, D.J. Smith, Applied Phys. Lett., Vol. 76, No. 12, pp. 1534-1536, 2000

120. V.K. Tolpygo, D.R. Clarke, Acta Mater., Vol. 47, No. 13, pp. 3589-3605, 1999

121. R.M. Bradley, K. M. Crosby, Phil. Mag. B, Vol. 78, No. 2, pp. 143-153, 1998

122. K. M. Crosby, R.M. Bradley, Phys. Rev. E, Vol. 55, p. 6084, 1997

123. E.M. Zielinski, R.P. Vinci, J.C. Bravman, MRS Symp. Proc. Vol. 391, pp. 103-108, 1995

124. E.M. Zielinski, R.P. Vinci, J.C. Bravman, MRS Symp. Proc. Vol. 356, pp. 429-434, 1995

125. E.M. Zielinski, R.P. Vinci, J.C. Bravman, MRS Symp. Proc. Vol. 391, pp. 303-308, 1995

126. D. Tracy, D. Knorr, J. Elect. Mat. 22, p. 611, 1993

127. T.P. Weihs, S. Hong, J.C. Bravman, and W.D. Nix, J. Mater. Res. 3(5), pp. 931-942, 1988

128. S.P. Baker and W.D. Nix, J. Mater. Res. 9(12), pp. 3131-3144, 1994

129. S.P. Baker and W.D. Nix, J. Mater. Res. 9(12), pp. 3145-3152, 1994

130. M. Doerner and W. Nix, J. Mater. Res. 1, 601, 1986

131. G. Pharr, W. Oliver, F. Brotzen, J. Mater. Res., Vol. 7, No. 3, pp. 613-617, 1992

132. R. King, Int. J. Solid Structures, 23, p.1657, 1987

133. T. Tsui, W. Oliver, G. Pharr, J. Mater. Res., Vol. 11, No. 3, pp. 752-759, 1996

134. A. Bolshakov, W. Oliver, G. Pharr, J. Mater. Res., Vol. 11, No. 3, pp. 760-768, 1996

135. S. Hainsworth, H. Chandler and T. Page, J. Mater. Res., Vol. 11, No. 8, pp.1987-1995, 1996

136. R. Berrich, Scripta Metallurgica et Materialia, Vol. 32, No. 4, pp. 617-620, 1995

137. T. Wu, J. Mater. Res., Vol. 6, No. 2, pp. 407-426, 1991

138. J.B.Savader, M.R.Scanlon, R.C.Camarata, D.T.Smith, and C.Hayzelden, Scripta Mater., pp. 29-34, 1997

139. L. Lu, L.B. Wang, B.Z. Ding, K. Lu, J. Mater. Res., Vol. 15, No. 2, pp. 270-273, 2000

140. Y. Wei and J.W. Hutchinson, J. Mech. Phys. Solids, Vol. 45, No. 7, pp. 1137-1159, 1997

141. D. Tabor, The Hardness of Metals, Claredon Press, United Kingdom, p. 174, 1951

142. D. Kramer, H. Huang, M. Kriese, J. Robach, J. Nelson, A. Wright, D. Bahr and W.W. Gerberich, Acta Mater. 47, p. 333, 1999

143. N.I. Tymiak, A.A. Volinsky, M.D. Kriese, S.A. Downs and W.W. Gerberich, Metallurgical and Materials Transactions A, Vol. 31A, pp. 863-872, 2000

144. A.K. Bhattacharya and W.D.Nix, Int. J. Solid Structures, Vol. 24, No. 12, pp. 1287-1298, 1988

145. W.W. Gerberich, W. Yu, D. Kramer, A. Strojny, D. Bahr, E. Lilleodden, J. Nelson, J. Mater. Res., No. 13, Vol. 2, pp. 421-439, 1998

146. W.W. Gerberich, A.A. Volinsky, N.I. Tymiak, N.R. Moody, Mat. Res. Soc. Symp. Proc. Vol. 594, 2000

147. M.D. Thouless, M.E. Harper, J.A. Gupta, J. Mater. Res., 8, p. 1845, 1993

148. R. Keller, S. Bader, R. Vinci and E. Arzt, MRS Symp. Proc. Vol. 356, pp. 453-458, 1995

149. R.H. Dauskardt, M. Lane, Q. Ma, N. Krishna, Engineering Fracture Mech. 61, pp. 141-162, 1998

150. A.A. Volinsky, N.I. Tymiak, M.D. Kriese, W.W. Gerberich and J.W. Hutchinson, Mat. Res. Soc. Symp. Proc. Vol. 539, pp. 277-290, 1999

151. J.W. Hutchinson, A.G. Evans, Acta Mater. 48, pp. 125-135, 2000

152. A.G. Evans, J.W. Hutchinson, Y. Wei, Acta Mater. Vol. 47, No. 15, pp. 4093-4113, 1999

153. Y. Wei, J.W. Hutchinson, International J. of Fracture 95, pp. 1-17, 1999

154. M. Lane, R.H. Dauskardt, N. Krishna, I. Hashim, J. Mater. Res., 15(1), pp. 203-211, 2000

155. S.Venkataraman, D.L.Kohlstedt and W.W.Gerberich, J. Mater. Res, Vol. 11 pp. 3133-45, 1996

156. F.A. McClintock, J. Appl. Mech, Vol. 25, pp. 582-588, 1958

157. F.A McClintock, and G.R Irwin, Plasticity Aspects of Fracture Mechanics, Fracture Toughness Testing and its Applications, ASTM STP 381, Philadelphia, pp. 84-113, 1965

158. V. Tvergaard and J.W. Hutchinson, J. Mech. Phys. Solids 41, pp. 1119-1135, 1993

159. W. Zielinski, H. Huang, W. W. Gerberich, J. Mater. Res., Vol. 8, No.6, pp. 1300-1310, 1993
160. D.E. Kramer, Ph.D. Dissertation, University of Minnesota, 1999
161. V. Tvergaard, J.W. Hutchinson, J. Mech. Phys. Solids 44, pp. 789-800, 1996
162. M.D. Kriese, N.R. Moody and W.W. Gerberich, Acta Metall., Vol. 46, No. 18, pp. 6623-6630, 1998
163. Y. Shacham-Diamand, A. Dedhia, D. Hoffstetter and W.G. Oldham, J. Electrochem. Soc., 140, p. 93, 1993
164. S.W. Russell, S.A. Raflaski, R.L. Spreitzer, J. Li, M. Moinpour, F. Moghadam, T.L. Alford, Thin Solid Films 262, pp. 154-167, 1995
165. M.D. Kriese, Ph.D. Dissertation, University of Minnesota, 1998
166. P.G. Marsh, W. Zielinski, H. Huang, W.W. Gerberich, Acta mater., 40, p. 2883, 1992
167. J. Rice and R. Thompson, Phil. Mag., 29. p. 73, 1974
168. R. Thomson, Scripta Metall., Vol. 20, p. 1473, 1986
169. I.H. Lin and R. Thomson, Acta mater, Vol. 34. p. 187, 1986
170. W.W. Gerberich, D. Kramer, N. Tymiak, A. Volinsky, D.F. Bahr, and M. Kriese, Acta mater., Vol. 47, No. 15, pp. 4115-4123, 1999
171. A. Furuya, Y. Ohshita, J. Appl. Phys., Vol. 84, No. 9, pp. 4941-4844, 1998
172. S.X.Mao, A.G.Evans, Acta mater., Vol. 45, No. 10, p. 4263, 1997
173. K.J. Hsia, Z. Suo, W. Yang, J. Mech. Phys. Solids, Vol. 42, No. 6, pp. 877-896, 1994
174. A.T. Yokobori, T.Y. Yokobori and H. Nioshi, in Macro-and Micro-Mechanics of High Velocity Deformation and Fracture, IUTAM Symposium, Tokyo, 1985, Springer-Verlag, Berlin, 1987
175. J.R. Smith, T. Hong, D. Srolovitz, Phys. Rev. Lett., Vol. 72, p. 4021, 1997
176. W.W.Gerberich, J.C.Nelson, E.T.Lilleodden, P.Anderson and J.T.Wyrobek, Acta mater, Vol. 44, No 9, pp. 3585-3598, 1996
177. G. Dehm, M. Ruhle, H.D. Conway, R. Raj, Acta mater., Vol. 45. pp. 489-499, 1997
178. J.W. Hutchinson, M.D. Thouless and E.G. Linger, Acta mater., Vol. 40, pp. 295-308, 1992
179. R.G. Stringfellow and L.B. Freund, Int. J. Solids Structures, 30, 239, pp. 1379-1395, 1993

180. Thermal Accessory for MultiMode and Dimensions Scanning Probe Microscopes, Support Note No. 252, Rev. B, Digital Instruments, 1998

181. M.O'Reilly, X. Jiang, J.T. Beechinor, S. Lynch, C. Ni Dheasuna, J.C. Patterson, G.M. Crean, Applied Surface Science 91, pp. 152-156, 1995

182. O.D. Sherby, in Nature and Properties of Materials: An Atomistic Interpretation, J. Pask (ed.), Wiley, New York, p. 376, 1967

183. H.G. Jiang, Y.T. Zhu, I.V. Alexandrov, T.C. Lowe and R.Z. Valev, Mat. Res. Soc. Symp. Proc. Vol. 594, 2000

184. Gerberich, et al, Interpretations of Indentation Size Effects, to be published

185. M.J. Lii, X.F. Chen, Y. Katz and W.W. Gerberich, Acta mater., Vol. 38, p. 2435, 1990

186. Z. Suo, C.F. Shih, A.G. Varias, Acta mater., Vol. 41, pp. 151-157, 1993

187. H. Huang and W.W. Gerberich, Acta mater., Vol. 42 , p. 639, 1994

188. P.G. Marsh and W.W. Gerberich, Acta mater., Vol. 42, p.613, 1994

189. W. Zielinski, M.J. Lii, H. Huang, P.G. Marsh, W.W. Gerberich, Acta mater., Vol. 40, p. 2883, 1992

190. P. Klein, H. Gao, A. Vainchtein, H. Fujimoto, Q. Ma and J. Lee, Mat. Res. Soc. Symp. Proc. Vol. 594, 2000

191. A. A. Pollock, Metals Handbook, 9th ed. Vol. 17, ASM International, PP. 278-294, 1989

192. T.P. Weihs, C.W. Lawrence, B. Derby, C.B. Scruby, J.B. Pethica, Mater. Res. Soc. Proc., Vol. 239, pp. 361-366, 1992

193. J. Kameda, R. Ranjan, Mat. Res. Soc. Symp. Proc., Vol. 356, pp. 853-858, 1995

194. D.F. Bahr, J.W. Hoehn, N.R. Moody, W.W. Gerberich, Acta mater., Vol. 45, No. 12, pp. 5163-5175, 1997

195. D. F. Bahr, W.W. Gerberich, J. Mater. Res., Vol. 13, No. 4, pp. 1065-1074, 1998

196. MISTRAS 2001 AEDSP-32/16 User's Manual, Physical Acoustics Corporation, Princeton, NJ 1995

197. C.B. Scruby, J. Phys. E: Sci Instrum., Vol. 20, p. 946, 1987

198. W.W. Gerberich, C.E. Hartbower, Int. J. Fract. Mech. 3, p. 185, 1967

199. J.E. Srawley and C.D. Beachem, "Fracture of High Strength Sheet Steel Specimens Containing Small Cracks", ASTM Preprint 80a, Philadelphia, p.1, 1961
200. T.L. Anderson, "Fracture Mechanics: Fundamentals and Applications." CRC Press, Boston, p. 219, 1991
201. A.A. Volinsky and W.W. Gerberich, Mater. Res. Soc. Proc. Vol. 563, 1999
202. David F. Bahr, private communications
203. N.I. Tymiak, M. Li, A.A. Volinsky, Y. Katz, W.W. Gerberich, Mater. Res. Soc. Proc., Vol. 563, 1999
204. J.A. Thornton, D.W. Hoffman, Thin Solid Films, Vol. 171, No. 1, pp. 5-31, 1989
205. A.V. Zagrebelny, C.B. Carter, Scripta Mater., Vol. 37, No. 12, pp. 1869-1875, 1997
206. A.V. Zagrebelny, C.B. Carter, Philosophical Magazine A, Vol. 79, No. 4, pp.835-845, 1998
207. S. Suresh, A.E. Giannakopoulos, Acta Mater., Vol. 46, No. 16, pp.5755-5767, 1998
208. R.O. Ritchie, R.M. Cannon, B.J. Dalgleish, R.H. Dauskardt, J.M. McNaney, Mater. Sci. and Eng., A166, pp. 221-235, 1993
209. G. Elsnner, D. Korn, M. Ruhle, Scripta mater., Vol. 31, p. 1037, 1994
210. J.M. McNaney, R.M. Cannon, R.O. Ritchie, Acta mater., Vol. 44, p. 4713, 1996
211. F.A. Gaudette, S. Suresh, A.G. Evans, G. Dehm, M. Ruhle, Acta mater., Vol. 45, p. 3503, 1997
212. H. Ji, G.S. Was, M.D. Thouless, Engineering Fracture Mechanics 61, pp. 163-171, 1998
213. Xinyun (Sherry) Xia, Ph.D. Dissertation, University of Minnesota, 2000
214. S.P. Timoshenko, Theory of Elastic Stability, McGraw-Hill, New York, 1961
215. J.R. Rice, Z. Suo, J.-S. Wang, Metal-Ceramic Interfaces, eds: M. Rhule, A.G. Evans, M.F. Ashby, J.P. Hirsh, Oxford, Permagon Press, pp. 269-294, 1990
216. P. Gu, M. Dao, R.J. Asaro, J. of Applied Mechanics-Transactions of the ASME, Vol. 66, No., pp. 101-108, 1999
217. N.I. Tymiak, J.C. Nelson, D.F. Bahr, W.W Gerberich, Corrosion Science, Vol. 40, No. 11, pp. 1953-1975, 1998
218. A. Daugela, Acoustic Emission Sensor: In-Situ Acoustic Emission Monitoring of Nanoindentation. Application Notes, Hysitron, Inc. 2000

219. R.F. Cook, private communication

220. M. Li, C.B. Carter, M.A. Hillmyer, and W.W. Gerberich, Microscopy and Microanalyisis, 6 Suppl. 2, pp. 722-723, 2000

View publication stats